Studies on the magnetostrictive properties of metal substituted sintered cobalt ferrite $Co(Fe,M)_2O_4$ (M = Al, Ga, In, Mg, Mn, Zn)

Thesis Submitted to AcSIR For the Award of the Degree of

DOCTOR OF PHILOSOPHY

in

Chemical Sciences

By
Mr. Anantharamaiah P N

Registration Number: 10CC11A26002

Under the Guidance of

Dr. P A Joy

Physical and Materials Chemistry Division
CSIR-National Chemical Laboratory
Pune-411008, India

June 2017

सीएसआईआर - राष्ट्रीय रासायनिक प्रयोगशाला
(वैज्ञानिक तथा औद्योगिक अनुसंधान परिषद)
डॉ. होमी भाभा मार्ग, पुणे - 411 008, भारत

CSIR - NATIONAL CHEMICAL LABORATORY
(Council of Scientific & Industrial Research)
Dr. Homi Bhabha Road, Pune - 411 008, India

Certificate

This is to certify that the work incorporated in this Ph.D. thesis entitled "**Studies on the Magnetostrictive Properties of Metal Substituted Sintered Cobalt Ferrite $Co(Fe,M)_2O_4$ (M = Al, Ga, In, Mg, Mn, Zn)**" submitted by **Mr. Anantharamaiah P N** to Academy of Scientific and Innovative Research (AcSIR) in fulfillment of the requirements for the award of the Degree of **DOCTOR OF PHILOSOPHY in Chemical Sciences**, embodies original research work under my guidance. I further certify that this work has not been submitted to any other University or Institution in part or full for the award of any degree or diploma. Research material obtained from other sources has been duly acknowledged in the thesis. Any text, illustration, table etc., used in the thesis from other sources, have been duly cited and acknowledged.

Mr. Anantharamaiah P N
(Ph D Student)

Dr. P A Joy
(Supervisor)

Date: 14-06-2017

Place: Pune

Communication Channels
NCL Level DID : 2590
NCL Board No. : +91-20-25902000
EPABX : +91-20-25893300
: +91-20-25893400
FAX
Director's Office : +91-20-25902601
COA's Office : +91-20-25902660
SPO's Office : +91-20-25902664
WEBSITE
www.ncl-india.org

DECLARATION BY RESERCH SCHOLAR

I hereby declare that the work incorporated in this thesis entitled "**Studies on the magnetostrictive properties of metal substituted sintered cobalt ferrite $Co(Fe,M)_2O_4$ (M=Al, Ga, In, Mg, Mn, Zn)"** submitted for the **Degree of Doctor of Philosophy** in **Chemical Sciences** to the Academy of Scientific and Innovative Research (AcSIR), has been carried out by me at the Physical and Materials Chemistry Division, CSIR-National Chemical Laboratory, Pune-411008, India, under the supervision of Dr. P A Joy (Research Guide). The work is original and has not been submitted in part or full by me for any degree or diploma to this or any other University. All the materials from other sources have been duly acknowledge in the thesis.

Date: **Anantharamaiah P N**

CSIR-National Chemical laboratory

Pune-411008

Dedication:

This work is lovingly dedicated to

My beloved parents:

Nadikeraiah

Lakshmamma

Acknowledgements:

At this rejoiceful moment, it's my utmost duty to express the sincerest gratitude to each and everyone, who have helped me, directly or indirectly at different phases, in completing my doctoral thesis. First and foremost I thank Almighty God for giving me the strength, determination, and patience to work all these years.

I would like to convey my deepest gratitude to my research supervisor Dr. P A Joy, for introducing myself to the contemporary materials science research field by providing unconditional support, unprecedented guidance, and profound freedom to carry out my research activities in his esteem laboratory. I truly admired of his sea of scientific and technical skills due to which many characterization techniques and the software to acquire the data are designed in the lab. More importantly, despite the fact that those techniques were assembled 10 to 15 years ago, still they are functioning with the high degree of accuracy; such durability is hard to anticipate from commercially available techniques. Constant thought-provoking discussions with him indeed helped a comprehensive understanding of my research topic as well as other related scientific areas that drive me to give my best. Irrespective of any circumstances, he keeps an everlasting smile and tremendous patience that is unique. For instance, while writing my thesis, even though I was making simple mistakes in multiple times (which I should not have made at this point of time), in each time he corrected those mistakes very patiently. When I was experiencing very difficult time at some stage of my research journey, the advice, the motivation and the life lesson given by my sir are priceless and I wish to keep those words in my heart forever. I always think that if I could able to install 20 to 25% of his patience, critical data analysis, teaching and scientific writing skills in myself, certainly I can be a good research as well as a teacher somewhere in the academics.

I am grateful to all my doctoral advisory committee (DAC) members, Dr. B L V Prasad sir, Dr. Nandini Devi and Dr. C S Gopinath sir, for their precious time to evaluate my research progress at different levels. I could able to learn many more scientific concepts and improve my presentation skills based on their advice and suggestions rendered at the time of my research work presentations.

I wish to acknowledge all my coursework teachers including Dr. Rajesh Gonade sir, Dr. Rahul Banerjee sir, Dr. Sreekumar sir, Dr. B L V Prasad, sir, Dr. P A Joy Sir, Dr. Nandini Devi, Dr. Ajithkumar sir and many more. By attending those coursework classes, I could able to fetch immense knowledge about rudimentary concepts of nanotechnology, materials science, and X-Ray diffraction, etc. I truly inspired from the way in which the complex scientific concepts are meticulously planned and taught in a concise fashion by the teachers of respective courses. Similarly, I wish to acknowledge all my teachers starting from the first standard to PG course for sharing their knowledge.

I sincerely thank my senior Dr. K K Mohaideen for his kind help and sharing his knowledge on magnetostriction characteristics and other experimental techniques. By capitalizing on the knowledge given by him, I could able to produce better results and are incorporated in this thesis. Similarly, I am grateful to all my seniors Dr. Mangesh, Dr. Bindhu Baby, Dr. Lenin, Dr. Govind, Dr. Jayaprabha, Ramsundar and Anjali for their timely help in analyzing and plotting the data and fruitful scientific discussions, particularly at the time of weekly seminars. I would like to extend my heartfelt thanks to fellow labmates Manjunath, Mohan, Arun Dadwal and Anupriya for their valuable support.

During the course of my work, I had the pleasure of working with several project students, Deepa, Ojaswini, and Sharath. Their assistance is gratefully acknowledged at this moment.

I must thank the former directors of NCL, Dr. Sourav Pal sir and Dr. Vijayamohanan sir, and the present director Prof. Ashwini Kumar Nangia sir, for the infrastructures and the facilities to carry out my research work in this prestigious laboratory. Similarly, I thank the former divisional head Dr. Anil Kumar sir for the various divisional facilities rendered to me during the course.

My special thanks to staff members of AcSIR, here at NCL, for their timely help in processing the various documents in a stipulated period.

I am thankful to University Grant Commission (UGC), Government of India, for providing me a fellowship to pursue my research career here at NCL.

I take this opportunity to thank my close friends, here at NCL, Hemender Chand, Sachin Tawarkar, and Sandeep K Singh who treated me as their own brother and their immense care and help when it is required a most. Hostel friends, divisional and other divisional friends including Sharath, Bishnu, Umesh, Bharath, Punith, Praveen, Krishna Prasad, Shivakumar, Gowdappa Gowda, Ashok, Dr. Harshitha, Dr. Jijil, Hanuman Prasad, Dr. Amit Nagare, Dr. Balanagalu, Kundan K Singh, Tiwari M, and many more are also acknowledged. The happiest moments I spent with them by discussing scientific and non-scientific matters are indelible and I always thankful to their friendship.

Eventually, my backbone and pillars of my life are my parents, Nadikeraiah and Lakshmamma, to who I am dedicating this thesis. The love, care, constant support and the encouragements rendered to me through all these years are unparallel and I am always grateful for their patience and believing in myself throughout my journey. I can't imagine a life without their support, love, and blessings. I would like to extend my thanks and utmost respect to my family members and relatives who nothing shorter than my parents when it comes to love and support.....

..... ***Anantharamaiah P N***

Contents

List of Tables

List of Figures

List of abbreviations

Å: Angstrom

BE: Binding Energy

eV: Electron Volt

FCC: Face Centered Cubic

H: Magnetic Field

H_c: Coercivity

JCPDS: Joint Committee on Powder Diffraction Standards

K: Kelvin

K_1: Magnetocrystalline Anisotropy Constant

λ: Magnetostriction Coefficient

dλ/dH: Strain Sensitivity

M: Magnetization

M_s: Saturation Magnetization

Oe: Oersted

PCW: Powder Cell for Windows

PVA: Polyvinyl Alcohol

SEM: Scanning Electron Microscopy

SQUID: Superconducting Quantum Interference Device

T: Tesla

T_C: Curie temperature

TEM: Transmission Electron Microscopy

VSM: Vibrating Sample Magnetometer

XRD: X-Ray Diffraction

XPS: X-Ray Photoelectron Spectroscopy

Abstract

Magnetostriction is the change in dimensions of a magnetic material on the application of an external magnetic field. The performance of a magnetostrictive smart material is mainly characterized by two important parameters viz, magnetostriction strain (λ) and strain sensitivity ($d\lambda/dH$). Among all the metal oxide based magnetostrictive materials, cobalt ferrite, $CoFe_2O_4$, manifests high magnetostriction both in single crystal (-600 ppm) and sintered polycrystalline (-150 to -400 ppm) forms at room temperature. This is due to high positive magnetocrystalline anisotropy governed by the spin-orbit coupling of Co^{2+} located at octahedral sites in the spinel lattice of cobalt ferrite. Therefore, the material has been studied as a suitable alternative for the currently used, high-cost, alloy based magnetostrictive materials such as Terfenol-D and its derivatives. Chemical composition, microstructure, magnetic domain configuration, magnetic anisotropy, synthesis and processing conditions, etc, are some of the major factors which affect the magnetostriction parameters of sintered polycrystalline cobalt ferrite.

The high magnetostriction strain, with low strain sensitivity, only at higher magnetic fields, associated with sintered polycrystalline cobalt ferrite makes the system unsuitable for torque and stress sensor applications. Constant efforts are being made to enhance the strain sensitivity without reducing the magnetostriction strain. Substitution by magnetic and nonmagnetic metal ions in place of Fe or Co in $CoFe_2O_4$ lattice is one of the possibilities. Many reports are available in the literature pertaining to magnetostrictive properties of different metal substituted cobalt ferrite. The strain sensitivity has been reported to be improved on substitution, but with much reduced magnetostriction strain for the substituted compositions. However, systematic studies on the role of the substituted ion, such as its valency, ionic size and site preference in the spinel lattice, on the magnetostrictive properties of cobalt ferrite have not been made so far. The main objective of the present study is to enhance the strain sensitivity of cobalt ferrite by substitution of metal ions in place of Fe in $CoFe_2O_4$, without affecting the magnetostriction coefficient and to obtain higher values at low magnetic fields.

Higher magnitude of magnetostriction parameters reported for the cobalt ferrite samples sintered from nanocrystalline powders against the samples sintered from the bulk counterparts. Similarly, higher $[d\lambda/dH]_{max}$ without any drop in the value of λ_{max} compared to that of the unsubstituted counterpart has been reported for Mn-substituted cobalt ferrite compositions sintered from nanocrystalline powders. Therefore, in the present study, we have adopted wet chemical methods to synthesize nanosized powders of different metal ions substituted cobalt ferrite, to obtain higher strain sensitivity for the sintered products, without affecting the magnetostriction strain on substitution. Nonmagnetic ions having different sizes and valencies are selected to understand the role of these parameters.

Introduction to magnetism, crystal structure and magnetic properties of spinel ferrites, magnetostriction and magnetostrictive materials (both alloys and oxides based) is presented in **chapter 1**. Detailed information on the different synthesis methods used for the preparation of materials and the techniques exploited to characterize the materials is provided in **chapter 2**.

Chapter 3 reports studies on the impact of substitution of divalent metal ions Mg^{2+} and Zn^{2+} for Fe^{3+}, in $CoM_xFe_{2-x}O_4$ (M= Zn, Mg, $0 \leq x \leq 0.2$), on the magnetostrictive properties. Magnetic and Raman spectral analysis indicated that Mg is substituted at the octahedral sites whereas Zn is substituted at the tetrahedral sites of the spinel ferrite lattice. Mg-substituted samples ($x<0.1$) showed higher strain sensitivity without affecting the magnetostriction coefficient even at lower magnetic fields. However, in the case of Zn-substituted samples, λ_{max} is found to be decreased with larger enhancement in the strain sensitivity. In both the series, the magnitude of λ_{max} is decreased at a faster rate for $x>0.1$ and this is attributed to the presence of Co^{3+} at the octahedral sites. In both the systems, the magnetostriction parameters are found to vary distinctly in the composition above and below $x=0.1$. XRD, Raman and magnetic parameters also exhibited a noticeable variation in the compositional range $x<0.1$ and $x>0.1$. This suggests the role of induced local structural distortion in the systems for compositions below $x=0.1$, due to inhomogeneous distribution of the substituted metal ions in the cobalt ferrite lattice.

Chapter 4 describes the role of size effect and site preference of trivalent nonmagnetic substituted metal ions (Al^{3+}, Ga^{3+} and In^{3+}) for Fe^{3+} in $CoFe_2O_4$ on the magnetostrictive properties. Detailed structural, Raman and magnetic characterizations indicated that Ga^{3+} and In^{3+} ions are substituted at the tetrahedral sites whereas Al^{3+} ions are occupied both the tetrahedral and octahedral sites with relatively larger amounts at the octahedral sites. The compositions with $x=0.1$ from three series showed higher λ_{max} than for the other compositions including the unsubstituted counterpart. All the substituted compositions showed higher strain sensitivity at lower magnetic fields than for the unsubstituted sample. Despite the large differences in the size and site preferences of the substituted ions, the magnetostriction parameters are nearly comparable for the same value of 'x' in the studied series. These observations suggest the role of local structural distortions, at lower levels of substitution, rather than the size and site preferences in determining the magnetostriction parameters.

Chapter 5 describes studies on the effect of co-substitution of two different metal ions $CoM_{x/2}M'_{x/2}Fe_{2-x}O_4$ (M,M'=Ga,Mn; Ga,Al; and Zn,Mg) on the magnetostrictive properties of cobalt ferrite. GaMn and GaAl co-substituted compositions showed higher λ_{max} up to $x=0.1$ at lower magnetic fields, than for the unsubstituted compound. On the other hand, ZnMg co-substituted compositions showed decrease in λ_{max} with small decrease up to $x=0.05$ and faster decrease at higher values of 'x'. In all the studied series, strain sensitivity is observed to be increased almost linearly up to the composition $x=0.1$, and above this composition, the sensitivity is decreased at faster rate for

ZnMg co-substituted series whereas further increased for the GaMn and GaAl co-substituted series. The structural, magnetic and Raman spectral parameters are found to exhibit distinguishable variation above and below x=0.1. The observed variation in the magnetostriction parameters for all the three co-substituted series above and below x=0.1 is likely to be associated with inhomogeneous distribution of the substituted metal ions in the lattice of cobalt ferrite.

Chapter 6 reports studies on sintered self-composites prepared by sintering mixed powders of different initial particle sizes (nanosized powders of size <5 nm and bulk powder of size >1 μm) of the same composition. The sintered self-composites are found to exhibit higher magnetostriction parameters than that for the sintered individual components. Such a higher magnetostriction displayed by the self-composites is attributed to changes in the microstructure. The self-composites (80 % nano + 20 % bulk) of the compositions $CoM_{0.1}Fe_{1.9}O_4$ (M=Ga, In, Mn) showed λ_{max} more than -300 ppm, with relatively high strain sensitivity at lower magnetic fields and these are the highest magnetostriction parameters so far reported for any metal ion substituted sintered polycrystalline cobalt ferrite. The magnetostriction parameters of the self-composites are further enhanced by magnetic field annealing.

Chapter 7 compares the magnetostriction characteristics of different metal ion substituted cobalt ferrite compositions. It has been observed from the current thesis work that trivalent metal ions are more suitable candidates for substitution for Fe in $CoFe_2O_4$ to enhance the magnetostriction parameters over divalent metal ions due to their isovalent nature with Fe. Regardless of the size effect and site preference of the substituted metal ions, higher magnetostriction characteristics are observed at lower magnetic fields for the compositions x=0.1 in $CoM_xFe_{2-x}O_4$ against that for the parent compound, indicating the role of local structural distortion induced in the spinel crystal structure, at low levels of substitution, due to the inhomogeneous distribution of the substituted metal ions.

Chapter 1

Introduction

1.1 Materials science

Materials are mostly solid substances that are intended to be used for specific applications in various fields including aerospace, electrical, mechanical, metallurgical, etc. [1]. In this contemporary world, materials play a vital role in designing high-performance technologies that greatly improve the lifestyles of the humans. A systematic study of materials is called materials science, and it is an interdisciplinary area, covering different branches of science including crystallography, thermodynamics, chemistry, engineering, physics, biology, etc., which primarily deals with the structure-properties relationship of materials [1,2]. Materials are found to exhibit different properties like thermal, chemical, optical, magnetic, electrical, mechanical, etc., and these properties strongly depend on the structure of the parent material. Therefore, by a comprehensive understanding of the fundamental aspects of a verity of materials, such as their structure-properties relationship, it is possible to develop new materials with enhanced properties. Materials science and engineering primarily deals with the structure-properties-processing-performance relationship of materials [3-6] and the relationship between them is shown in Figure 1.1.

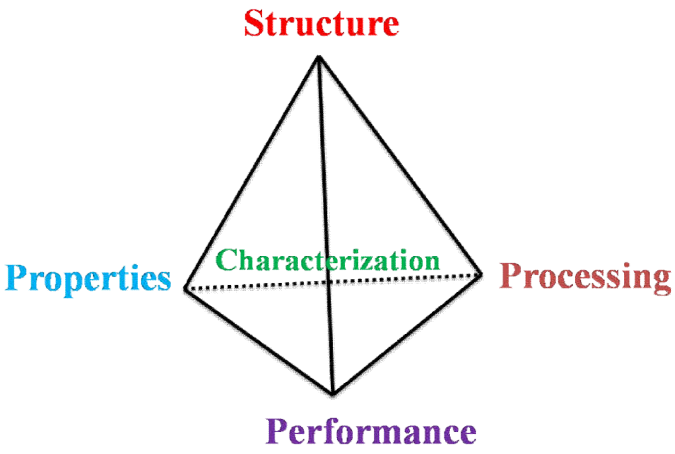

Figure 1.1*: Pictorial representation of the four components of materials science and engineering, and their inter-relationship.*

Ever since nanotechnology came into limelight, materials science received significant attention because the known materials began to manifest new properties at the nanoscale regime which are different from those of the corresponding bulk counterparts. This brought about a new scientific revolution to play with the synthesis as well as fabrication of materials to achieve desirable properties and also to design devices which are compact in size with high performance [3]. In the recent years, much attention has been focused on composite materials

and the optimization their processing to obtain the desired properties. Composite materials are prepared by combining two or more materials, and the individual material can work together to generate unique properties that are different from those of the individual components of the composite [4].

An important class of materials is called smart materials, and they are designed materials that have one or more properties that can be significantly altered in a controlled fashion by external stimuli such as mechanical stress, temperature, electric field, magnetic field, etc. [6,7]. Mainly four types of smart materials are often used for applications as sensors and actuators, and they are:

- **Piezoelectric materials**: They generate electrical signals on the application of mechanical stress or when a force is imposed on them. Conversely, they can also undergo volume expansion or contraction in response to an applied electric field or voltage [8].
  Examples: Barium titanate ($BaTiO_3$), lead zirconate titanate ($PbZr_{1-x}Ti_xO_3$), lithium niobate ($LiNbO_3$), lithium tantalate ($LiTaO_3$), aluminium phosphate ($AlPO_4$), etc.
  Applications: Ultrasonic detector, frequency generator, gas lighter, microphones.

- **Shape memory alloys**: As the name suggests, these materials remember their shape at a particular temperature. Structural changes at the atomic level or molecular level predominantly contribute to this unique property of the materials [9].
  Example: Nitinol (Ni-Ti alloy), Cu-Zn-Al, Au-Cd, Cu-Al-Ni, etc.
  Applications: Automotive, medicine, robotic, aircraft or spacecraft, etc.

- **Electrorheological and Magnetorheological fluids:** These are viscous liquids prepared by suspension of solid particulates in a liquid matrix. They manifest a substantial change in their viscosity in the presence of a magnetic or electric field. As soon as the field is removed, the fluids regain their original configuration [10].
  Examples: Ferrofluids, carbon/silica dispersed in oil,
  Applications: Coolants in electronic devices, vibration controller, shock absorbers, hydraulic valves, clutches, flexible electronics.

- **Magnetostrictive materials**: Materials that undergo a change in dimensions (shape and size) under the application of an externally applied magnetic field. Conversely, magnetostrictive materials also manifest a change in magnetization in response to a change in mechanical stress [11]. Due to the conversion of magnetic energy into mechanical energy or vice versa, these materials can be used both as sensors as well as actuators.

  Examples: Terfenol-D ($Tb_{0.3}Fe_{1.9}Dy_{0.7}$), Galfenol ($Ga_{0.2}Fe_{1.8}$), cobalt ferrite ($CoFe_2O_4$), Nickel ferrite ($NiFe_2O_4$), etc.

  Application: Vibration and noise control, linear motors, adaptive optics, position and mechanical torque sensors, ultrasonic generator, controlled fuel injection, etc.

1.2 Magnetism and magnetic materials

Magnetism in solids originates from the motions of electrons. There are two types of electron motions, namely spin and orbital, and each type has a magnetic moment associated with it [12]. The magnetic moment of an electron from its orbital motion or spin motion is given by [13,14],

$$\mu_{orbit} = \mu_{spin} = \frac{eh}{4\pi mc} \tag{1.1}$$

where the term *e* is the charge of an electron (1.62×10^{-19} C), *h* is called Planck's constant (6.625×10^{-34} m^2kg/s), *m* is the mass of an electron (9.21×10^{-31} kg) and *c* is the velocity of light (3×10^8 m/s). On substitution of all the values in the above equation, the magnetic moment due to the spin and orbital motion of electrons is equal to 9.27×10^{-24} J/T, and this constant value known as a Bohr magneton and denoted by the symbol μ_B.

The magnetic moment is one of the fundamental quantities in the magnetism. It is defined as the torque acting on a bar magnet having pole strength 'p' at each end and separated by a distance 'q' when it is placed perpendicular to a uniform magnetic field of strength 1 Oe. Thus, the magnetic moment is expressed numerically as [14],

$$m = pq = pq\sin\theta = (pH\sin\theta)\left(\frac{q}{2}\right) + (pH\sin\theta)\left(\frac{q}{2}\right) \tag{1.2}$$

where 'm' is the magnetic moment and $\theta = 90^{o}$. The magnetic moment per unit volume is called magnetization, M, and is given by

$$M = \frac{m}{v} \left(\frac{emu}{cm^3}\right) \tag{1.3}$$

where *v* stands for volume of the material. The specific magnetization, σ, is the magnetic moment per unit mass of the sample and is given by [14],

$$\sigma = \frac{m}{w} = \frac{m}{\rho v} = \frac{M}{\rho} \left(\frac{emu}{g}\right) \tag{1.4}$$

where *w* is the mass and ρ is the density of the material. It is more convenient to express the magnetization in terms of specific magnetization than volume magnetization because the mass of a material can be measured more accurately than its volume and also mass is independent of temperature but not volume. Therefore, magnetic moment per unit mass is generally used to specify magnetization.

The magnetization per unit magnetic field is called magnetic susceptibility, χ, represented by [14],

$$\chi = \frac{M}{H} \tag{1.5}$$

Based on the response of magnetic materials to an externally applied magnetic field, magnetic materials are classified into five categories viz diamagnetic, paramagnetic, antiferromagnetic, ferromagnetic, and ferrimagnetic.

Diamagnetism is an inherent property of all types of materials and always makes a small contribution to a material in response to an applied magnetic field [15]. Atoms or molecules consisting of closed shell electronic configurations are meant to have zero net magnetic moments and are considered as diamagnetic materials [15]. When a magnetic field is applied to such materials, extra current will be generated in the materials due to the effect of electromagnetic induction and the resultant current will oppose the applied magnetic field lines [15]. Therefore, they exhibit negative magnetization for positive applied field or *vice versa*. The magnitude of the negative magnetization of a diamagnetic material is proportional to the strength of the applied magnetic field, as shown in Figure 1.2(a). The susceptibility of a diamagnetic material is temperature independent, as shown in Figure 1.2(b). The inert gases He, Ne, etc., diatomic gases like H_2, Cl_2, N_2, etc., covalent salts like NaCl, KCl, etc.,

covalently bonded materials such as C in diamond form, Si, Ge, and most of the organic compounds as well as superconductors are examples for diamagnetic materials.

Paramagnetism is a weak magnetic phenomenon exhibited by atoms, ions, molecules comprised of unpaired electrons [14]. Due to the presence of unpaired electrons, the paramagnetic materials possess permanent magnetic dipole moments and these dipole moments show a strong response to an applied magnetic field. Eventhough the paramagnetic materials consist of magnetic dipole moments, the moments are randomly oriented due to the effect contributing from thermal energy, as depicted in Figure 1.3. With increasing applied magnetic field, the magnetization of the paramagnetic material increases linearly, as shown in Figure 1.2(a), this is because the applied field acts against the thermal energy and tries to orient the magnetic moments in its direction and hence the linear increment in the magnetization with the field. However, as soon as the applied field is reduced to zero, the material loses its magnetization instantaneously due to the randomization of the moments by the thermal energy [16]. Unlike diamagnetic materials, the paramagnetic materials have a positive value of susceptibility, $\chi>0$, with the magnitude of 10^{-2} emu/g/Oe [16].

Ferromagnetic materials such as Fe, Co, Ni and alloys including FeNi, CoNi, etc., show spontaneous magnetization even in the absence of an external magnetic field. This is because the atomic moments are aligned in a particular direction through the exchange energy [14,17]. The alignment of the atomic moments in a ferromagnetic material is illustrated in Figure 1.3. Since the atomic moments are aligned in the same direction, the ferromagnetic materials, in response to an applied magnetic field, show very high positive susceptibility, $\chi>>0$. The ferromagnetic materials transform to the paramagnetic state at a critical temperature called Curie temperature (T_C). Pierre-Ernest Weiss extended his molecular field concept to interpret the phenomenon of ferromagnetism, and he made the assumption that the molecular field acts in the ferromagnetic material above as well below its T_C [14]. Below the T_C, the strength of the molecular field is very strong that can magnetize the material to saturation even in the absence of an external magnetic field. However, due to the formation of magnetic domains (described in the proceeding section), a ferromagnetic material will be in an unmagnetised state. When a small magnetic field is applied to the material, the internal molecular field of the material then reinforces with the applied magnetic field in magnetizing the material, and hence higher magnetization is obtained at the very low magnetic field.

Above the critical temperature, T_C, the susceptibility of the ferromagnetic materials obeys Curie-Weiss law, $\chi = C/(T-\theta)$ with a value of θ approximately equal to the value of T_C. The θ for ferromagnetic materials is very large and positive, as shown in Figure 1.2(b).

Similar to ferromagnetic materials, antiferromagnetic materials also exhibit ordered magnetic phenomenon, but they have zero net magnetization. This is because the antiferromagnetic crystals consist of two sublattices and the magnetic moments in the each sublattice are ordered ferromagnetically but between the sublattices, the moments are aligned opposite to each other with equal magnitude, as shown in Figure 1.3 and hence the zero net magnetization. Using the Weiss molecular field theory, Louis Neel developed the theory of antiferromagnetism in 1932 [14]. Shull and Smart showed the first experimental evidence of antiferromagnetic ordering using neutron diffraction experiment made on MnO crystal [18]. Antiferromagnetic materials show a small positive susceptibility, $\chi>0$, and χ increases with increasing temperature and reaches a maximum value at a critical temperature called Neel temperature, T_N, followed by a decrease for $T>T_N$. Above T_N, the materials will be in the paramagnetic state and obey Curie-Weiss law with a negative value of θ, as shown in Figure 1.2(b), indicating that the molecular field acts against the externally applied magnetic field to disalign the moments. Examples: MnO, FeO, NiO, Cr, Cr_2O_3, NiF_2, etc.

Similar to antiferro- and ferromagnetism, ferrimagnetism is also an ordered magnetic phenomenon, but the net magnetization of the ferrimagnetic materials is much larger than that of antiferromagnetic and smaller than that of ferromagnetic materials. In general, ferrimagnetic materials consist of crystallographically distinguishable sub-lattices (sites or voids) in which metal ions are located [14,16]. Within each sublattice, the magnetic moments are aligned in the same direction and between the sublattices, the arrangement of the magnetic moments is antiparallel as shown in Figure 1.3. Due to the large difference in the magnitude of the magnetic moments of the neighboring sub-lattices, a partial cancellation of the magnetic moments results in a net magnetization in the ferrimagnetic materials. Ferrimagnetic materials exhibit a substantial spontaneous magnetization, similar to the ferromagnetic materials, and their spontaneous magnetization vanishes at a transition temperature called Curie temperature, T_C. Above the T_C, the material behaves like paramagnetic and obeys Curie-Weiss relation, as shown in Figure 1.2(b). Examples: Ferrites like cobalt ferrite ($CoFe_2O_4$), Iron oxide (Fe_3O_4), nickel ferrite ($NiFe_2O_4$), strontium ferrite ($SrFe_{12}O_{19}$), barium ferrite ($BaFe_{12}O_{19}$).

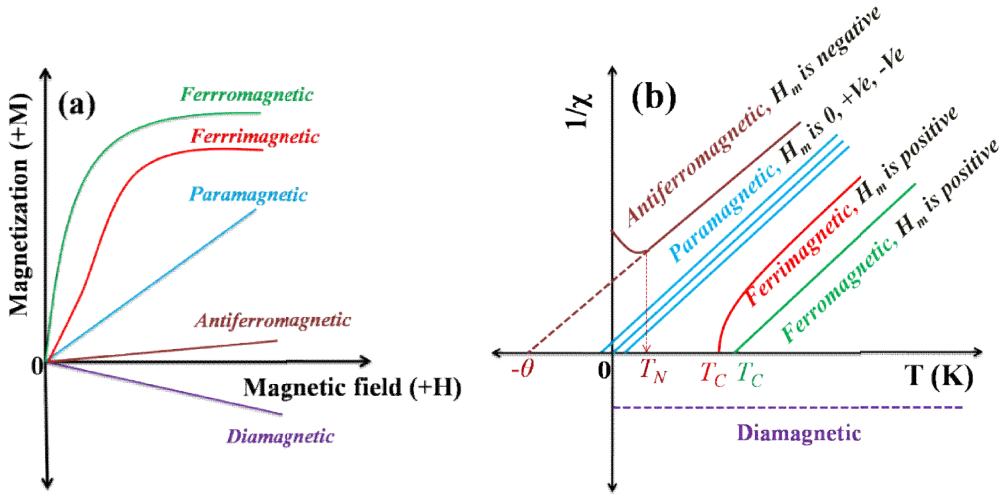

***Figure 1.2**: Comparison of (a) magnetization vs. field and (b) inverse susceptibility vs. temperature of various types of magnetic materials. In* (b), H_m stands for the molecular field [14].

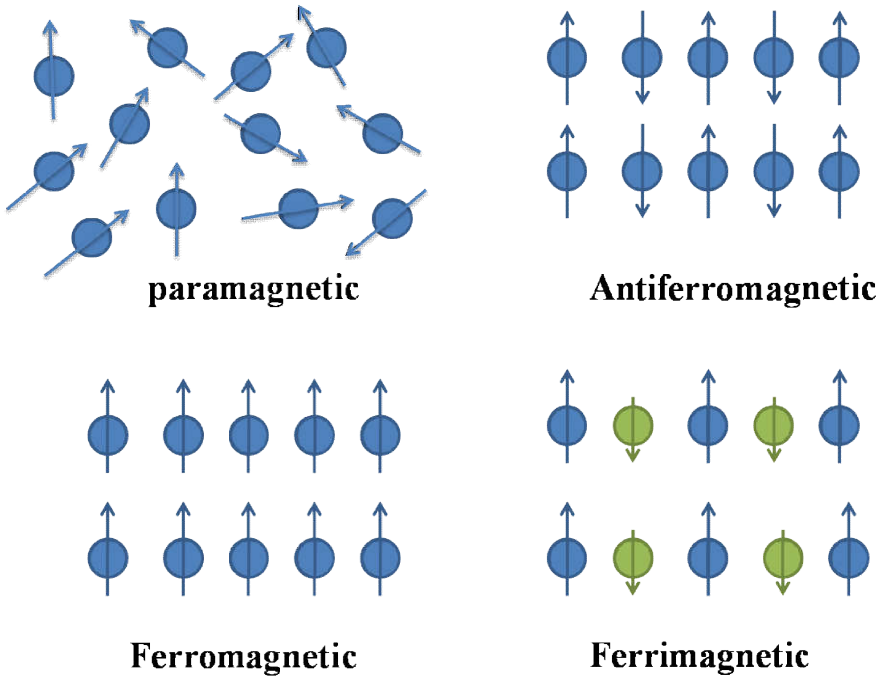

***Figure 1.3**: Arrangements of magnetic moments in different types of magnetism.*

1.2.1 Magnetic domains and magnetization process

A magnetic domain is a region within ferro- or ferrimagnetic materials in which the magnetic moments are aligned parallel to one another [15]. The domains in the magnetic materials will be generated to minimize the total magnetic energy of the system [15]. Both the exchange and magnetostatic energies will contribute to the total magnetic energy, out of them magnetostatic energy is the principal driving force for the domain formation. A magnetic crystal with single domain configuration, as shown in Figure 1.4(a), will be a source of large magnetization field due to the free poles on the ends. Thus, the crystal possesses higher magnitude of magnetostatic energy which in turn put the crystal into a magnetically unstable state. The magnetostatic energy of a single-domain crystal is given as [14],

$$E_{ms} = \frac{1}{2} N_d M_s^2 \tag{1.6}$$

where N_d is the demagnetizing factor of the crystal, and its value depends on the shape of the crystal. The magnetostatic energy will be reduced by a factor of two when the crystal splits into two domains whose magnetization vectors are opposite to each other, as shown in Figure 1.4(b), because this domain configuration brings the north and south poles closer to another. If the crystal splits into four domains, as represented in Figure 1.4(c), the corresponding magnetostatic energy will be reduced further to one-fourth of its initial value, and the formation of smaller and smaller domains continues until an equilibrium domain size is achieved [14]. The adjacent domains are separated by a thin layer called ‘domain wall’ and inside the wall, the magnetic moments are aligned at different angles with respect to the direction of the magnetization vectors of the adjoining domains as shown in Figure 1.5.

The concept of domain wall was first introduced by Weiss in 1906, and Bloch theoretically examined the structure of a domain wall, and hence a domain wall is called as ‘Bloch wall’. Magnetocrystalline anisotropy inside a domain wall is relatively larger than it is in the adjoining domains due the orientation of the magnetic moments (or spin) away from the easy direction. A domain wall has a definite structure with nonzero width because of the competitive action of anisotropy and exchange energies on spins of the domain wall. The crystal anisotropy energy tries to reduce the thickness of the domain wall in order to decrease the number of spins aligned away from the easy direction whereas an exchange energy tries to make the wall as wide as possible by decreasing the angle between the neighbouring

spins [14]. In bulk polycrystalline magnetic materials, each grain may consist of hundreds of domains, and the magnetization vectors of the domains are randomly oriented. Also, the direction of magnetization in a domain would vary depending upon the size and shape of the grains (spherical, elongated) of polycrystalline materials [19-21].

Due to the random orientation of the magnetic domains inside the ferro- or ferrimagnetic materials, the material will be in the unmagnetized state with almost zero magnetic field strength. However, the magnetization of the domains can be altered, and high magnetization can be induced in the specimen under the influence of an applied magnetic field. The response of the magnetic domains of a crystal to the external magnetic field strength is illustrated in Figure 1.6. When a small external magnetic field is applied to a system in the unmagnetized state, the domain whose magnetization vector is nearly close to the direction of the applied field starts growing at the cost of the other domains whose magnetization vectors are oriented away from the direction of the applied field. With further increase in the applied field, the volume of the domain magnetization driven by the field increases and attains single domain configuration at relatively higher field strength. The magnetization vector of the resultant single domain is then rotated forcefully along the applied field direction only at very high magnetic field strength.

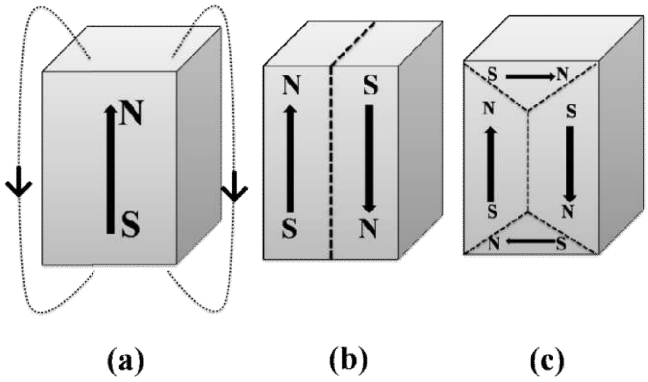

***Figure 1.4**: Schematic representation of the breakup of a magnet into domains. (a) Single domain, (b) two domains, (c) closed domains.*

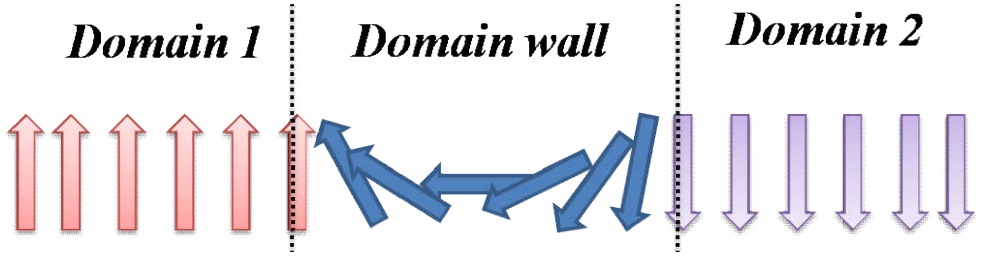

***Figure 1.5**: Schematic representation of domains separated by a domain wall.*

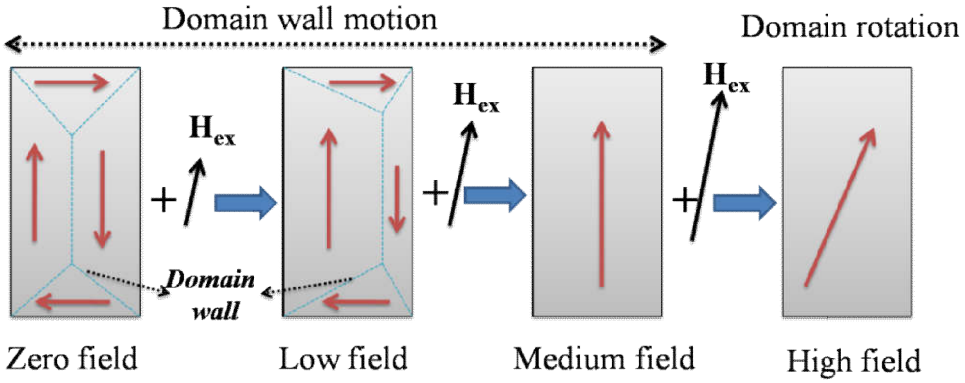

***Figure 1.6**: Schematic representation of domain wall motion in an applied magnetic field.*

A nonlinear behavior is observed when the magnetization of an isotropic ferro- or ferrimagnetic material is recorded as a function of applied magnetic field. This nonlinear behavior of M vs. H curve could be described based on the interaction of the magnetic domains with the external magnetic field. The magnetization of a ferro- or ferrimagnetic material arises due to the contribution of domain wall motion and domain rotation triggered by the application of an external magnetic field. As shown in Figure 1.7(a) for the initial magnetization curve against the field, domain wall motion is predominant at low fields and domain rotation at the higher fields. Both reversible and irreversible wall motions contribute to the magnetization curve at different applied field regions (Figure 1.7(a)). A small increase in the magnetization at the very low applied field is due to the reversible domain wall displacement and at this point when the applied field is turned off then the magnetization of the system would be reduced to its original state (unmagnetized). If the magnetization is purely by domain rotation, then it is said to be reversible because the applied field works against the anisotropy field of the material [14]. A typical magnetization vs. magnetic field (M-H) hysteresis loop is depicted in Figure 1.7(b). When all the magnetic moments are aligned in the direction of the applied magnetic field, the magnetization M of the system becomes constant or saturates, and it is known as saturation magnetization, M_s. The magnetization will not be reduced to zero even after the applied field is reduced to zero because the material possesses a certain amount of residual magnetization and it is termed as remnant magnetization or remanence, M_r. To reduce the remnant magnetization to zero, a negative magnetic field need to be applied and the magnitude of the field at which the magnetization becomes zero is called the coercive field or simply coercivity, H_c. The M_s, M_r, and H_c are the characteristic parameters used to determine the magnetic properties of materials. The area under the M-H loop is proportional to the hysteresis loss, i.e., energy loss during the process of magnetization and demagnetization.

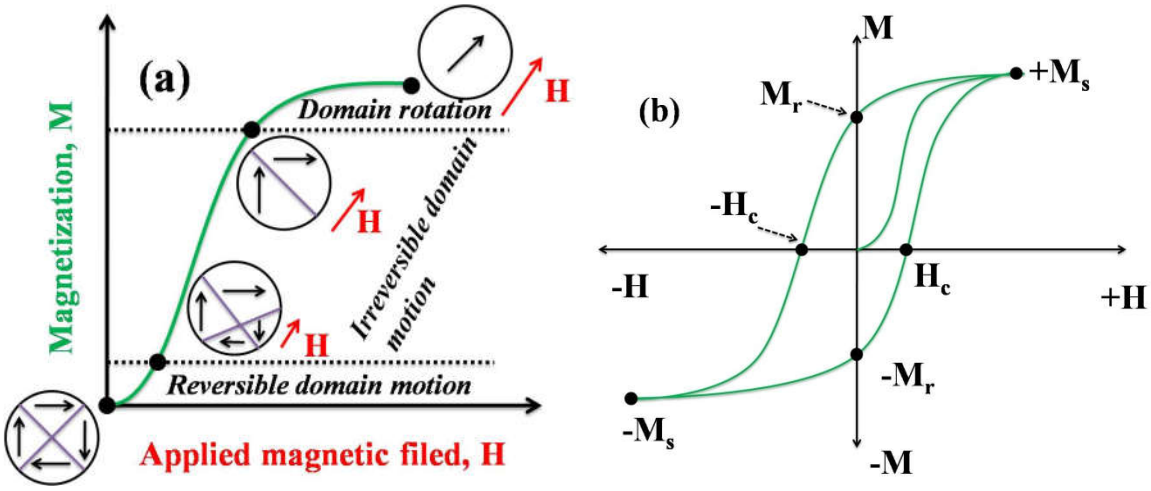

***Figure 1.7**: Schematic representation of (a) initial magnetization curve and (b) magnetic hysteresis loop.*

The concept of magnetic anisotropy helps to understand why certain ferro- and ferrimagnetic materials are magnetically soft and others are magnetically hard. Magnetically soft materials possess higher magnitude of saturation magnetization and low coercivity and are easily magnetizable by applying a small applied magnetic field whereas hard magnetic materials are characterized by high coercivity, high remanence, and moderate saturation magnetization apart from that high field strength is required to saturate them magnetically [14]. Also, magnetic anisotropy is one of the prime factors that define the shape of the magnetization vs. field curve of a magnetic material [15].

1.2.2 Magnetocrystalline anisotropy

Magnetic materials exhibit different types of magnetic anisotropies, such as crystal anisotropy or magnetocrystalline anisotropy, stress anisotropy, shape anisotropy, the anisotropies induced by magnetic annealing, elastic deformation, irradiation, and exchange anisotropy [14]. Among them, the most dominant contribution is emanating from the magnetocrystalline anisotropy, followed by stress and shape anisotropies. Crystal anisotropy is a force which tends to hold the magnetization vectors in certain crystallographic directions in a crystal [14]. Therefore, it is envisaged that the nature of the magnetization curve will be different along the different crystallographic directions when it is measured as a function of

applied magnetic field. For example, single crystal Fe, which belongs to body-centered cubic structure, requires a small strength of magnetic field (a few tens of Oersteds) to achieve saturation magnetization along the <100> direction, which is accordingly called the easy direction of magnetization. However, along the <111> direction, more field strength (several hundred Oersteds) is necessary to obtain saturation, and thus this direction is called the magnetically hard direction. In the case of single crystal Ni, which has face centered cubic structure, <111> and <100> are magnetically easy and hard directions, respectively. It has been attributed that atomic density along those directions is responsible for easy and hard directions of magnetization [13,14]. For instance, in Fe crystal structure, atomic density along the <111> direction is the highest and consequently is the magnetically hard direction, whereas, the atomic density is the lowest in the direction <100> and consequently is the easy direction [13,14]. Easy magnetization along the <100> directions in Fe and <111> direction in Ni is because crystal anisotropy holds the magnetic moments along those directions and hence less field is required for saturation. However, along the other directions, the applied magnetic field has to work against the force of crystal anisotropy, which is usually strong.

The amount of energy required to rotate the magnetic moments away from the easy direction is called as the crystal anisotropy energy, E [14]. Akulov showed that E could be expressed in terms of a series expansion of the direction cosine of saturation magnetization relative to the crystal axis [14]. For a cubic crystal, anisotropy energy can be expressed as,

$$E = K_o + K_1(\alpha_1^2\alpha_2^2 + \alpha_2^2\alpha_3^2 + \alpha_3^2\alpha_1^2) + K_2(\alpha_1^2\alpha_2^2\alpha_3^2) + \cdots \quad (1.7)$$

where K_o, K_1, K_2,... are anisotropy constants for a particular material and are expressed in erg/cm^3 or J/m^3. $\alpha_i = \cos\theta_i$ and θ_i are the angles between the magnetization and the easy axes. Since K_o is angle independent, it is usually ignored. The direction of the easy magnetization is estimated from the sign of the anisotropy constant K_1 provided K_2 is zero. If K_1 is positive then <100> is the easy direction of magnetization and <111> is the hard direction because exchange energy falls in the order $E_{100}<E_{110}<E_{111}$. Similarly, if K_1 is negative, then $E_{111}<E_{110}<E_{100}$, and <111> is the easy direction. When K_2 is not zero, the values of both K_1 and K_2 are used to determine the easy direction of magnetization [14].

Physical origin of crystal anisotropy

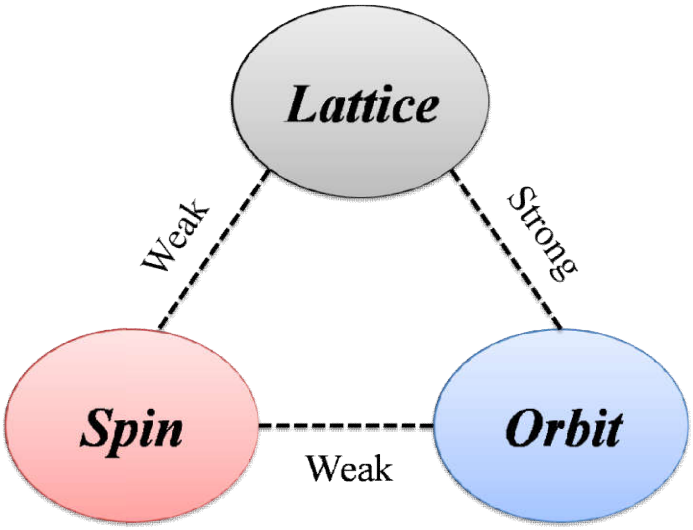

***Figure 1.8**: Spin-lattice-orbit interaction [14].*

Spin-orbit coupling is responsible for crystal anisotropy of a magnetic material [14,15]. Although spin-spin coupling, which acts to keep neighboring spins parallel or antiparallel to one another, is very strong, it will not contribute to the crystal anisotropy because the associated exchange energy between the spins is isotropic in nature and depends only on the angle between the adjacent spins. Similar to spin-spin coupling, the orbit-lattice coupling is also strong because the orbital orientations are fixed firmly to the crystal lattice by the crystal field created by the adjacent atoms, and hence even large fields cannot change their orientations. Other interactions/couplings such as spin-orbit and spin-lattice are also possible, but their strength is weak when compared to that of orbit-lattice interactions. The relationship between the spin, orbit and lattice interactions is summarized in Figure 1.8. In the case of spin-orbit coupling, when an externally applied magnetic field makes an attempt to orient the spin of an electron, the orbit of that electron also tends to be reoriented because of the coupling. Since the orbit is strongly coupled with the crystal lattice, there will be a strong resistance to rotate the spin by the field. To overcome that resistive force, extra energy is required, and it is called anisotropy energy which eventually acts against the spin-orbit coupling. Therefore, the magnetocrystalline anisotropy arises from the spin-orbit coupling which connects the magnetic moments to the atomic lattice through the electron orbits. The importance of spin-orbit coupling under the influence of an applied magnetic field is illustrated in Figure 1.9. As shown in Figure 1.9(a), magnetic moments are aligned along the easy (vertical) direction with the orbital components aligned along the horizontal direction. The orbital components are spherical in nature due to spin-orbit coupling. For this particular

crystal, the orbital configuration is energetically favorable. When a magnetic field is applied perpendicular to the easy magnetization direction, the applied field forces the magnetic spin to align along the horizontal direction, and the orbital component aligns along the vertical direction, due to the coupling, and it is shown in Figure 1.9(b).

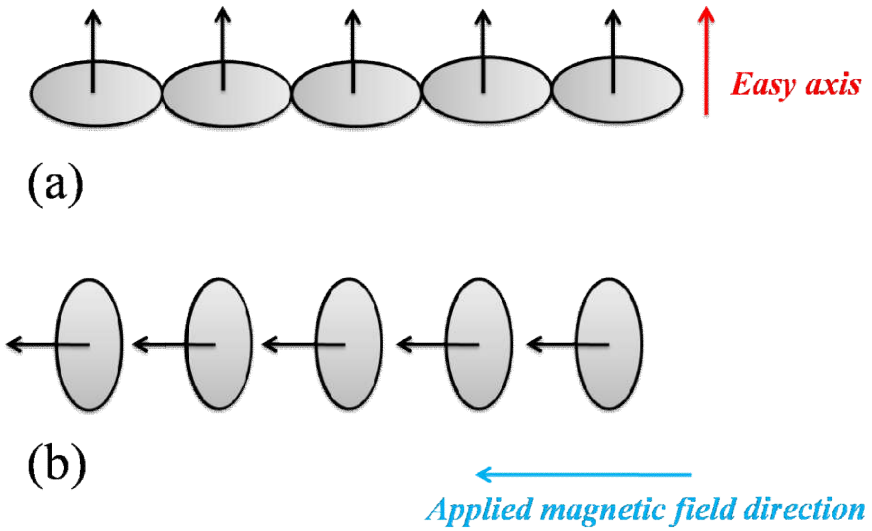

***Figure 1.9**: Interaction between spin and orbit degrees of freedom [15].*

1.3 Spinel ferrites

Ferrites are ferrimagnetic ceramic oxides consisting of Fe_2O_3 as a major chemical constituent and are well known for their unique magnetic and electrical properties [16,22]. Apart from the magnetic and electrical properties, recently multiferroic properties have been discovered in some of the complex ferrite systems [23-26]. Due to the ionic in nature with stable oxide crystal structure, ferrites are also known for their high electrical resistivity, low eddy current, and dielectric losses. Therefore, ferrites are ideal candidates for numerous technological applications including microwave components, computers, telecommunication devices, high-frequency devices, high-density magnetic data storage, magnetic refrigerators, etc., they also find applications in sensors and actuators [22,27-30]. Spinel ferrites have the general chemical formula AFe_2O_4 where A stands for divalent metal ions such as Co^{2+}, Fe^{2+}, Mg^{2+}, Zn^{2+}, Cd^{2+}, Mn^{2+}, Ni^{2+}, etc. Examples are $FeFe_2O_4$, $CoFe_2O_4$, $MnFe_2O_4$, $NiFe_2O_4$, $ZnFe_2O_4$, etc.

1.3.1 Crystal structure

The crystal structure of spinel ferrites is derived from the mineral spinel, magnesium aluminate ($MgAl_2O_4$ or $MgO.Al_2O_3$), which belongs to cubic crystal system [28,31]. The crystal structure of cubic spinel, with the general formula AB_2O_4, is displayed in Figure 1.10. The unit cell of a spinel consists of 32 oxygens and are arranged in a cubic close-packed (ccp) fashion to form a face-centered cubic (fcc) lattice. This arrangement generates two crystallographically distinguishable sites or voids, namely tetrahedral sites, surrounded by four oxygens (A-sites) and octahedral sites, surrounded by six oxygens (B-sites), as shown in Figure 1.10. The unit cell of a spinel contains 64 A-sites and 32 B-sites. Among them, only 8 A-sites and 16 B-sites are occupied by metal ions. The crystal structure is described by subdividing the unit cell into 8 octants with edge ½*a* where '*a'* is the unit cell length of the cubic spinel lattice [28]. Each octant contains four oxygen ions on the body diagonals, and they lie at the corners of a tetrahedron [28]. Each oxygen ion is located at a distance equal to one-fourth of the length of the body diagonal from alternate corners of the octant. The positions of the metal ions are different in the two octants sharing a face. Each octant is made up of four octahedral metal ions, and these are situated at the sites similar to those of the oxygen ions. Octahedral metal ions form four interpenetrating FCC lattice with the edge '*a*.' In the crytal structure, each oxygen ion is surrounded by one tetrahedral ion (A-site) and three octahedral ions (B-site). Each tetrahedral site is surrounded by 12 nearest neighbor octahedral sites, and each octahedral site is surrounded by only six tetrahedral sites [28].

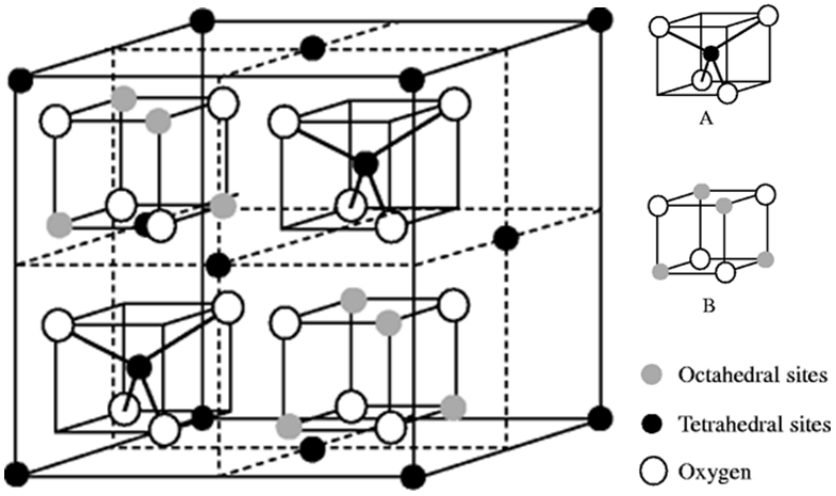

Figure 1.10*: Unit cell of AB_2O_4 spinel structure with tetrahedral and octahedral geometries as shown in the right side [22].*

Depending on the distribution of the cations among the tetrahedral and octahedral sites, the spinel ferrites are classified into three categories as represented below.

Normal spinel: $(M^{2+})_A[Fe^{3+}]_BO_4$; A-sites = $8M^{2+}$, B-sites = 16 Fe^{3+}.

Inverse spinel: $(Fe^{3+})_A[M^{2+}Fe^{3+}]_BO_4$; A-sites = $8Fe^{3+}$, B-sites = $8Fe^{3+}$, $8M^{2+}$.

Mixed spinel: $(Fe_x^{3+},M_{(1-x)}^{2+})_A[M_x^{2+}Fe_{(2-x)}^{3+}]_BO_4$;

A-sites = $8xFe^{3+}$,$8(1-x)M^{2+}$, B-sites = $8xM^{2+}$, $8(2-x)Fe^{3+}$.

1.3.2 Factors affecting the cation distribution in spinel ferrites

The structural, magnetic, optical and electrical properties of the spinel ferrites depend not only on the type of cations present in the lattice of the spinels but also on their distribution over the tetrahedral and octahedral sites.

Ionic size**:** The **s**ize of the tetrahedral site is considerably smaller than that of the octahedral site and therefore it is envisaged that smaller ions will prefer to occupy at the tetrahedral sites whereas larger ions prefer the octahedral sites. The trivalent ions are smaller than the divalent ions, and this leads to the inverse spinel structure.

Valency and oxygen parameter (Electrostatic energy)**:** The chemical bonding in the spinel ferrite is regarded as purely ionic. Hence both Coulomb energy and Born repulsion energy primarily contribute to the lattice energy [28]. The lattice energy calculation revealed that the combinations of size, the valency of the cations and oxygen anion parameter are crucial for the determination of cations distribution [28]. Larger divalent cations preferentially occupy the tetrahedral sites whereas the smaller trivalent cations occupy the octahedral sites owing to the favorable polarization effect. If the A-site ions have a lower valency and B-site ions have a higher valency, then the oxygen anion will be polarized toward the B-sites, and the polarization yields the normal spinel configuration. In an ideal cubic close-packed lattice, the position of the oxygen lattice is u=3/8=0.375. Calculations carried out by Verwey *et al*. [32,33] indicated that the lattice energy would be the lowest for the inverse spinel structure (more stable) when 'u' (oxygen parameter) is lower than 0.379 whereas for the normal spinel structure lattice energy is the lowest when u>0.379.

The factors described above alone are insufficient to provide a complete insight on the observed cation distribution in the spinel compounds. For example, even though both Co^{2+}

and Zn^{2+} are isovalent and their sizes are nearly comparable at both the tetrahedral and octahedral sites, $CoFe_2O_4$ crystallizes in an inverse spinel configuration, while $ZnFe_2O_4$ in the normal spinel structure. In a similar fashion, $NiFe_2O_4$ is completely inverse, $NiCr_2O_4$ is normal, and $NiAl_2O_4$ is mixed spinel although the ionic sizes satisfy the condition of the polarization effect, i.e., $Al^{3+}<Cr^{3+}<Fe^{3+}$. Thus, certain cations have strong site preference for a certain crystallographic site. For instance, Zn^{2+} and Cd^{2+} have a strong preference for the tetrahedral site due to the formation of a strong covalent bond between the 4s, 4p, and 5s, 5p electrons with the 2p electrons of an oxygen ion, respectively [16]. As a result of this, four bonds are oriented towards the corner of a tetrahedron. Ni^{2+} and Cr^{2+} have a tendency to occupy octahedral site due to favorable charge distribution in an octahedral crystal field. Even though Mg^{2+} is isovalent with Zn^{2+} with almost same sizes, Mg^{2+} has a tendency to occupy both the tetrahedral and octahedral sites. This is due to utilization of the empty higher energy orbitals of Mg^{2+} for the coordination bonding. A similar explanation is likely to be valid for the Al^{3+} as well.

***Crystal field stabilization energy*:** Romeijn was the first to suggest the use of the crystal field theory (CFT) to understand the cation site preference in the spinel systems [34]. To understand the site preference of magnetic cations in the spinel oxides, two important theories have been designed based on the chemical bonding in the spinel oxides. Dunitz and Orgel [35], and also McClure [36], have exploited CFT, which is based on the ionic type of bonding between oxygen and the transition metal ions, whereas Blasse [37] has used a simplified molecular orbital (MO) approach by considering the covalent bonding betweenthe oxygen and the transition metal ions. According to CFT, the difference between the octahedral and tetrahedral stabilization energies is a semi-quantitative estimation of the site preference energy [28]. The system with d^3electronic configuration has the highest octahedral site preference energy followed by d^4, d^8, d^6, d^9, d^7 and d^1 [28]. The system with d^0, d^5 and d^{10} configurations have zero crystal field stabilizing energy and therefore no site preference. Blasse obtained a set of site preference energies based on the molecular orbital approach. There is inconsistency in some cases with the values obtained from CFT. According to this approach, the system with d^5, d^6, d^7, d^9 and d^{10} configurations have tetrahedral site preference. Interestingly, both approaches (CFT and MO) are consistent with the d^3 electronic configuration.

1.3.3 Magnetic properties of spinel ferrites

Magnetic properties of the spinel ferrites depend strongly on the types of magnetic cations located at the A- and B-sites of the spinel lattice, chemical composition and relative strength of the possible interactions. Also, the properties are also dictated by the distribution of the cations among the sub-lattices which in turn is affected by the history of the sample preparation and processing parameters [16,22,28]. Three important types of the magnetic superexchange interactions are possible between the magnetic cations located at the A- and B-sites mediated through oxygen, and they are A-O-B, B-O-B and A-O-A interactions. Among the three interactions, A-O-B is known as predominant followed by the B-O-B and A-O-A as the weakest [14,16]. Neel proposed the two sub-lattice magnetization model to elucidate the magnetic properties of the spinel ferrites [14]. According to the model, the net magnetization of a spinel ferrite is the numerical difference between the net magnetization of the two sublattices, as represented by [14],

$$M = \sum M_B - \sum M_A \tag{1.8}$$

where, ΣM_B and ΣM_A are net magnetization of the B- and A-sites, respectively.

Eventhough the magnetic dipole moments in the A- and B sublattices are opposite to one another, the magnitude of the magnetic moments at the respective sites is unequal, and as a result of this, the spinel ferrite compounds can show net magnetization due to the partial cancellation of the magnetic moments. This difference in the magnitude of the moments arises mainly due to the difference in the oxidation state of the metal ions. For example, Fe_3O_4 is an inverse spinel consisting of both Fe^{2+} and Fe^{3+} where Fe^{3+} has a higher magnetic moment ($5\mu_B$) than for Fe^{2+} ($4\mu_B$), and all Fe^{2+} are present at the B-sites whereas Fe^{3+} are equally distributed among the A- and B-sites. Therefore, the net magnetic moment of the compound will be $9\mu_B - 5\mu_B = 4\mu_B$. The experimentally observed net moment for the Fe_3O_4, obtained at nearer to -273 ^oC (0 K), is closer to the theoretical value [16]. In a similar fashion, the net magnetic moments can also be estimated for other members of the spinel ferrite family, provided the distribution is known. Use of various techniques to acquire information on the distribution of cations over the A- and B-sites in the spinel ferrites are reported in the literature [38-42]. Among them, X-ray diffraction, neutron diffraction, and Mössbauer spectroscopy are the most commonly used techniques. Recently, Raman spectroscopy was also exploited as a complementary tool to Mössbauer technique to estimate the distribution of

the cations [43,44]. Apart from the mentioned techniques, a net saturation magnetic moment of the spinel ferrites can also be estimated from the saturation magnetization (M_s) data recorded at a temperature closer to absolute zero [16].

Magnetic properties of the spinel ferrites can be effectively tuned by chemical substitution of various magnetic and nonmagnetic metal ions. In the case of the metal ions substituted samples, the magnitude of the saturation magnetization (M_s) depends on whether the substituted metal ion is occupying at the A- sites or the B-sites in the spinel crystal structure, amount of substitution and also on nature of the metal ions (magnetic or non-magnetic). The M_s of the metal ion substituted spinel ferrite sample will be higher than that of the parent compound when the A-site is substituted by a nonmagnetic cation. This is due to magnetic dilution of the A-sites by the nonmagnetic cation, as a result of which the magnetization of the B-site will be larger than that of the A-site in the substituted samples compared to the parent counterpart and hence the higher magnetization. However, increase in the M_s with the amount of substitution occurs only up to a particular substitution level and M_s is decreased with higher levels of substitution. For example, substitution of A-site by nonmagnetic cations such as In^{3+} and Ga^{3+} for Fe in $CoM_xFe_{2-x}O_4$ leads to increased M_s up to a particular composition ($x \leq 0.4$) followed by a decrease for $x > 0.4$ [45,46]. It has been suggested that decreased in the M_s at a higher amount of substitution is due to the magnetic dilution at the B-site by the substituents. Similarly, substitution at the B-site by non magnetic ions such as Al^{3+} and Mg^{2+} in cobalt ferrite reduces the net magnetization of the B-site to a greater extent than at the A-site [47-50]. Therefore, overall magnetization decreases as the substituent concentration increases in the spinel lattice. It is expected that if the substituted nonmagnetic ion dilutes both the A- and B-sites of the spinel ferrite by an equal magnitude, then the net magnetization of the substituted sample will be almost comparable to that of the unsubstituted counterpart.

1.3.4 Exchange interaction

The magnetic exchange energy between the cations via oxygen in the ferrites is of purely indirect or superexchange type [15,16]. Negative exchange energies are predominant in the ferrites systems, and the magnitude of the negative exchange energies depends on the distance of the metal ions from the oxygen, through which the superexchange occur, and on the angles [16]. It has been shown that angle of 180^o leads to the strongest exchange energy, and the exchange energy decreases with increasing the bond distance [16].

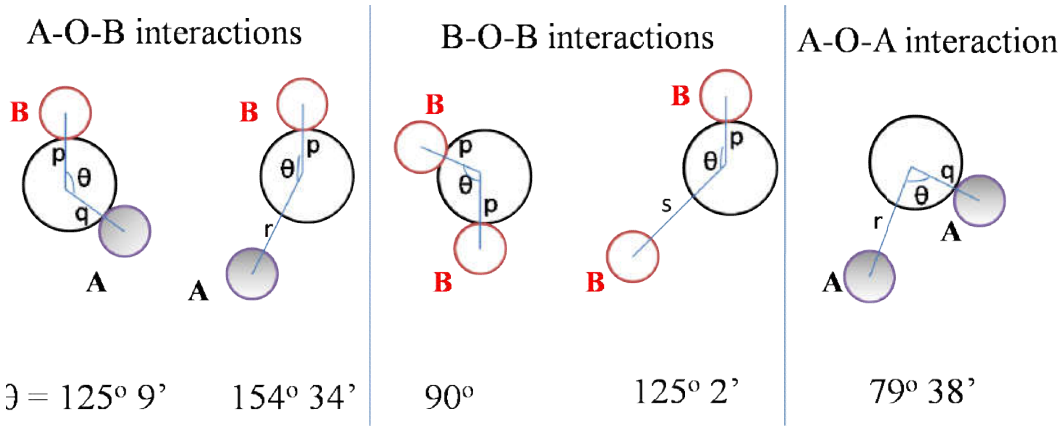

***Figure 1.11**: Most favorable types of superexchange interactions in spinel ferrites [16].*

By comparing the bond angles and bond lengths of various configurations as depicted in Figure 1.11, the A-O-B exchange interaction is strongest over the others. Among the two possible configurations of A-O-B interactions as shown in the figure, the first configuration has maximum interaction due to the shorter bond distances (p = O-B and q = O-A) and fairly larger angle ($\theta \approx 125^{o}$), but in the second configuration, although the angle is larger, longer the O-A bond distance makes the interaction less effective compared to the first. Similarly, first B-O-B configuration has maximum exchange interaction. The weakest configuration is A-O-A because of the longer bond distance (r) and unfavorable bond angle ($\theta \approx 0^{o}$). The oxygen parameter (u) for most of the ferrites is greater than its ideal value, 0.375 [16,28]. Thus, the magnitude of the exchange energy is affected by the parameter 'u' in such a way that the A-O bond distance is increased whereas B-O distance is decreased and also the bond angle is decreased. On the other hand, A-O-A interaction is decreased further due to the increase in the bond lengths and B-O-B interaction is increased due to reduction in the bond lengths. The magnitude of the exchange interactions controls the saturation magnetization, and Curie temperature of the spinel ferrites and the exchange interaction is, in turn, controlled by the distribution of the cations.

1.4 Magnetostriction

Magnetostriction is a property of ferro-and ferrimagnetic materials, which is a change in their shape or dimension during the process of magnetization, particularly in the direction of the applied magnetic field, as represented in Figure 1.12. The magnetostriction effect was first observed by James Joule in 1842 while investigating an iron sample in the presence of a magnetic field [51]. Hence, this effect is often referred to as the Joule effect. The magnetostriction coefficient (λ) is expressed as,

$$\lambda = \frac{\Delta L}{L} \tag{1.9}$$

where,

L is the length of the material in its unmagnetized state,

ΔL is the fractional change in length after the magnetization by the magnetic field,

λ can be either positive or negative depending on the expansion or contraction along the direction of the applied magnetic field.

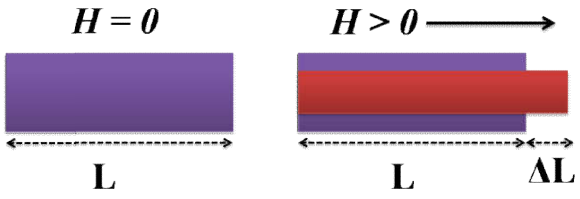

***Figure 1.12**: Schematic representation of the change in length of a ferromagnetic rod in the presence of a magnetic field.*

Magnetostriction effect is a reversible feature because when the external magnetic field is tuned off, the material regains its original shape. Similar to the Joule effect, which is an inverse effect, other effects related to magnetostriction are also reported [52]. Inverse Joule effect is called Villari effect that describes when a mechanical stressis imposed on a magnetostrictive material, the magnetization of the sample changes [52,53]. By measuring the change in the magnetic flux density using pickup coils, the amount of stress imposed on the sample can be estimated. Since the effect is reversible, itis used in sensors applications. Another effect is called Wiedemann effect [54] which describes a change in the shear strain in a sample in response to an applied magnetic field. The physical origin of this effect is

almost identical to the Joule effect, but instead of forming compressive strain, theshearing strain will be generated which results in a torsional displacement of the ferromagnetic sample. The inverse Wiedemann effect is called Matteucci effect [52,55], and it is widely applicable for torque sensors. When an alternating current is passed through a coil that generates a longitudinal magnetic field in a sample, a magnetic flux density is createdin the sample. Under such conditions, torque or twisting of the magnetostrictive sample induces a change in the magnetization of the sample which results in a changein the rate of change of the magnetic flux density. By detecting the magnetizationchange using a pickup coil, the change in shear stress can be evaluated, and as aresult, the magnitude of the applied torque can be calculated. Under extream operational conditions, the volume of the magnetostrictive material changes with an applied magnetic field and this additional magnetostrictive effect is called the Barret effect [52]. However, under normal operational conditions, the change in volume of the material in response to an applied magnetic field is very small, and hence it can be neglected. Inverse Barret effect is called Nagaoka-Honda effect, which is a change in volume of a material under extreme pressure like hydrostatic pressure causing a change in the magnetic state of the material [56,57]. Both these effects, Barret and Nagaoka-Honda, are operational and detectable under extreme conditions and hence they are not widely been used in applications.

1.4.1 Mechanism of magnetostriction

The cause of change in dimension due to magnetostriction is the result of the rotation of magnetic domainsin a material. The rotation and reorientation of the domains cause internal strains in the material structure leading to the elongation of the material in the direction of the applied magnetic field [57]. A pictorial representation of the magnetostriction curve, as a function of magnetic field (along the positive and negative directions to the applied field), is shown in Figure 1.13. The strain curve along the positive field direction is divided into three regions. As discussed in a previous section, magnetic materials in an unmagnetized state possess domains whose magnetization vectors are oriented in random directions leading to zero magnetization and hence zero magnetostriction in the same state. In the region 0 to 1, a slight increase in the magnetostriction under the application of small magnetic field strength is observed. This will be the result of the slight orientation of the magnetic domains along the applied field direction, as depicted in Figure 1.14. In the region between 1 and 2, a large change in the magnetostriction is observed, and in this region, both the applied magnetic field

and the resultant magnetostriction strain are related linearly. Because of this linear relationship, energy loss during the conversion of magnetic energy into mechanical energy or vice versa will be minimum, and therefore most devices are designed to operate in this linear region [57]. Beyond point 2, the magnetostriction curve becomes nonlinear again as a result of the fact that most of the domains have become aligned in the direction of the applied magnetic field. At point 3, magnetostriction becomes saturated and no further increase in the strain despite the increased field strength. In a similar fashion, when the magnetic field is applied in the reverse direction, the negative field produces the same shape of the magnetostriction curve as that produced by the positive field. The shape of the curve is reminiscent of a butterfly and often referred as a butterfly curve.

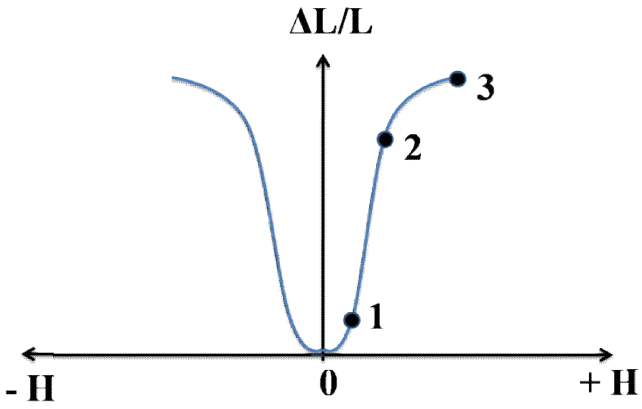

***Figure 1.13**: Pictorial representation of strain curve as a function of applied magnetic field (H) [57].*

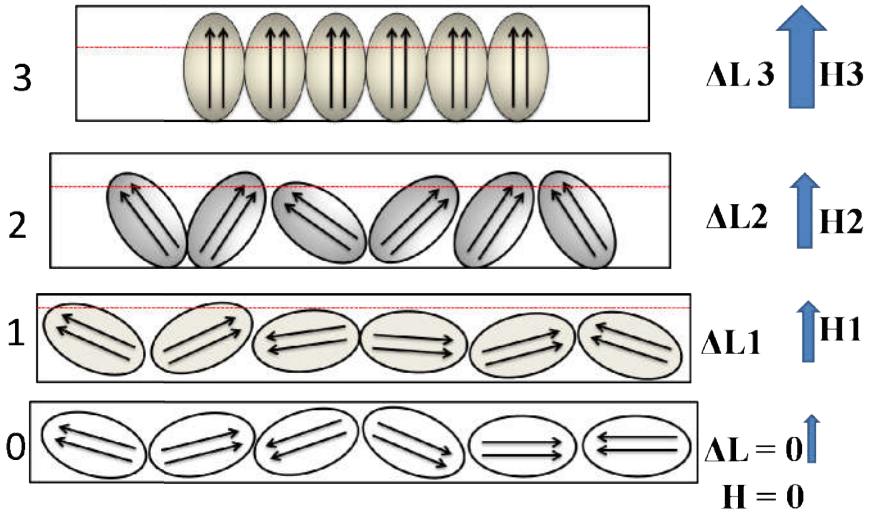

***Figure 1.14**: Pictorial representation of the response of the magnetic domains to the applied magnetic field, at three different field strengths, H_1, H_2 and H_3 [57].*

It is to be noted that all ferro- and ferrimagnetic materials will not manifest the same magnitude of the magnetostriction strain eventhough they are highly magnetic in nature. This is because the magnetostriction depends not only on the response of the magnetic domains to the applied magnetic field but also on the domain structure due to the difference in the magnetocrystalline anisotropy governed by the spin-obit coupling. As discussed earlier, when an externally applied magnetic field tries to rotate the spin of an electron, the orbit of that electron would also tend to be oriented because of the coupling. Since the orbit is strongly bound to the crystal lattice, an attempt to rotate the spin axis by the applied magnetic field is resisted. Therefore, the field has to overcome that resistance to rotate the spin. This eventually leads to changes in the lattice dimensions giving rise to small dimensional changes. The anisotropic magnetostriction in a cubic single crystal is given by [58],

$$\lambda_s = \frac{3}{2}\lambda_{100}\left(\alpha_1^2\beta_1^2 + \alpha_2^2\beta_2^2 + \alpha_3^2\beta_3^2 - \frac{1}{3}\right) + 3\lambda_{111}\left(\alpha_1\alpha_2\beta_1\beta_2 + \alpha_2\alpha_3\beta_2\beta_3 + \alpha_3\alpha_1\beta_3\beta_1\right) \quad (1.10)$$

where λ_s is the saturation magnetostriction. The terms α and β are the direction cosines of the saturation magnetization and strain measurementrelative to the crystal axes, respectively, λ_{100} and λ_{111} are the magnetostriction coefficients along the <100> and <111> crystallographic directions, respectively.

In a polycrystalline cubic material, the saturation magnetostriction is given by [14],

$$\lambda_s = \frac{2}{5}\lambda_{100} + \frac{3}{5}\lambda_{111} \quad (1.11)$$

where λ_s is a saturation magnetostriction, and its value depends on the magnetostrictive properties of the individual grains and also on the way in which these grains are arranged in the sample. If the polycrystalline sample consists of grains with different shapes and sizes, then each grain will strain along the direction of the applied magnetic field. The magnitude of magnetostriction contributing from one grain will be different from its neighbors because of its different orientation and shape [14]. Studies on the nature of the magnetostriction λ vs. H curves of Fe_3O_4 and its solid solution containing few percentage of $CoFe_2O_4$ revealed that Fe_3O_4, at room temperature, showed a positive magnetostriction at low applied field strength [59]. However, the sign of the magnetostriction changed to negative when the sample was cooled below 160 K, and at that temperature, even the easy direction of magnetization switched from <111> to <100> indicating a change in the sign of anisotropy constant (K_1) from negative to positive.

The initial part of the λ vs. H curve depends on the sign of λ in the easy direction, and the latter part of the curve shows the effect of the sign of λ in the hard direction [59]. Similarly, in the case of sintered polycrystalline cobalt ferrite, the initial part of the λ vs. H curve is due to the dominant contribution of easy axis of the magnetostriction coefficient (λ_{100}) and the later part, at higher fields, is due to the contribution of the hard axis of magnetostriction coefficient (λ_{111}) [45,60,61]. The sign of the magnetostriction coefficients (λ_{100} and λ_{111}) depends on the sign of the first order magnetocrystalline anisotropy constant (K_1) as well as the chemical composition [59]. For example, Ni has negative anisotropy that makes both the coefficients to attain negative value. However, after making an alloy of Ni with different percentages of Co, the sign of the λ_{100} and λ_{111} are changed without changing the sign of the anisotropy constant [59]. Similarly, 60% Ni-Fe alloy has positive K_1 and also the same sign of λ_{100} and λ_{111}, but in the case of 2% Si-Fe alloy eventhough K_1 is positive, λ_{100} is positive whereas λ_{111} is negative.

For polycrystalline materials with cubic symmetry, the angle-dependent magnetostriction can be expressed as [14,61],

$$\lambda(\theta) = \frac{3}{2}\lambda_s\left(\cos^2\theta - \frac{1}{3}\right) \tag{1.12}$$

where θ is the angle between the direction of the applied magnetic field and the strain measuring direction, and λ_s is the saturation magnetostriction. Since this equation is derived for an isotropic material, it is applicable for polycrystalline samples with no preferred orientation or magnetically non-interacting isolated grains.

For the measurement along the parallel direction, $\theta=0^o$ and then

$$\lambda_{par} = \lambda(0) = \lambda_s \tag{1.13}$$

For the measurement along the perpendicular direction, $\theta = 90^o$

$$\lambda_{per} = \lambda(90) = -\frac{\lambda_s}{2} \tag{1.14}$$

Therefore, the total magnetostriction obtained under the influence of an applied magnetic field is,

$$\lambda_{total} = \lambda_{par} - \lambda_{par} = \frac{3\lambda_s}{2} \tag{1.15}$$

1.4.2 Strain sensitivity

In the strain vs. magnetic field curve, the slope is highest in the linear region between 1 and 2 (see Figure 1.13), and this slope is called field derivative or strain derivative or strain sensitivity, $d\lambda/dH$. This is also sometimes referred to as magneto-mechanical coupling factor, d_{33} [57]. Strain sensitivity of a magnetostrictive material is an important parameter that decides the sensitivity of the material in its application as an actuator and also determines how the material would behave in stress or torque sensors. The relation between strain derivative and sensitivity of its magnetic induction to applied stress is described as [62,63]

$$\left(\frac{dB}{d\sigma}\right)_{\lambda} = \left(\frac{d\lambda}{dH}\right)_{\sigma} \tag{1.16}$$

where, the term on the left side is the change in the magnetic flux (dB) with respect to change in the stress ($d\sigma$), at constant magnetostriction strain. The above relation is derived based on the Le Chatelier's principle, and it indicates that material that would be sensitive in sensor capability would also be sensitive in actuation capability [45]. The importance of strain sensitivity regarding energy efficiency can be understood by comparing the hypothetical magnetostriction strain curves of two samples, as shown in Figure 1.15. For any given field strength in Figure 1.15, sample 1 shows the higher magnitude of magnetostriction than sample 2. At lower fields, sample 1 has a higher slope than that for sample 2 and hence $(d\lambda/dH)_1 >> (d\lambda/dH)_2$. $H_{1,max}$ and $H_{2,max}$ are the maximum fields required to achieve maximum amplitude of the magnetostriction coefficients λ_1 and λ_2 for the samples 1 and 2, respectively. H_1 is the field required for the sample 1 to achieve the same amplitude of magnetostriction strain λ_2 of sample 2 and the field is nearly three times lower than that of $H_{2,max}$. Therefore, the currents needed to magnetize these two samples would be in the ratio [64],

$$\left[\frac{I_{mag\,1}}{I_{mag\,2}} \propto \frac{H_1}{H_{2,max}}\right]_{\lambda=\lambda_2} \tag{1.17}$$

where I_{mag1} and I_{mag2} are the currents needed to generate field H_1 and $H_{2,max}$, respectively. Since power usage depends on the square of the current, the power needed to reach the same strain amplitude for sample 1 is only one ninth of that needed for sample 2. This is an important consideration for energy efficient devices.

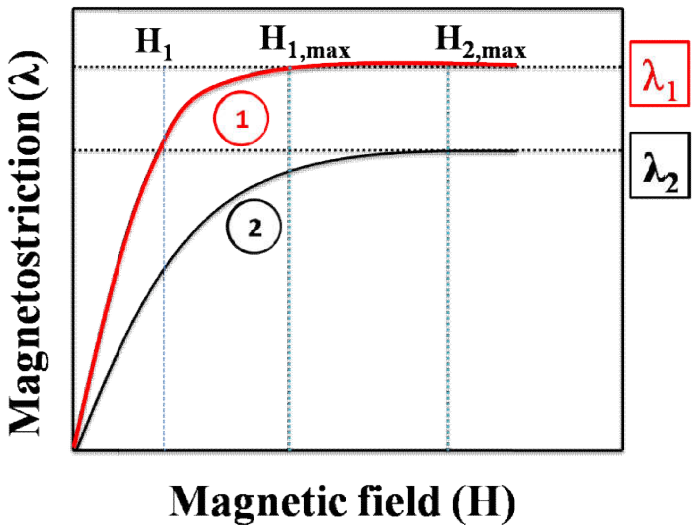

***Figure 1.15**: Illustration of the importance of strain sensitivity as a useful figure of merit for magnetostrictive applications [64].*

1.4.3 Applications

Magnetostrictive materials have been used in almost in every industry, ranging from aerospace to acoustic and MEMS (Micro-Electro-Mechanical Systems). Some of the commercial applications of magnetostrictive materials are listed below [11,56,65-67].

***Table 1.1**: List of applications of magnetostrictive materials.*

1. Sensors	**2. Actuators**
❖ Position sensor ❖ Non-contact torque sensor ❖ Magnetic field sensor ❖ Liquid level sensor ❖ MEMS bio and chemical sensor	❖ Linear and rotary motors ❖ Fuel injection system ❖ Inchworm actuator ❖ Position controller ❖ Hydraulic actuators such as servo valves and pumps ❖ Optical scanning system
3. Vibration control	**4. Acoustic devices**
❖ Vibration damper ❖ Image stabilizer ❖ Platform stabilizer ❖ Energy harvester	❖ Sonar ❖ Hydrophone ❖ Ultrasonic shaker for cleaning and mixing ❖ Ultrasonic friction welding

The concept of magnetostriction is also useful to investigate the basic magnetism and the development of a complete atomic level theory of magnetism and magnetic materials. Static and dynamic magnetostrictive measurements, together with magneto-inductive and magneto-transport measurements are the basic tools for the determination of magnetic properties. Also, magnetostrictive smart materials have been studied as one of the active components in the multiferroic magnetoelectric hybrid composites comprising of piezoelectric and magnetostrictive components, to achieve better magnetoelectric coefficient (α_{ME}) for various applications including magnetic field sensors, wireless powering systems, dual electric field and magnetic field tunable devices, etc [68-70].

1.5 Magnetostrictive materials

1.5.1 Alloy based materials

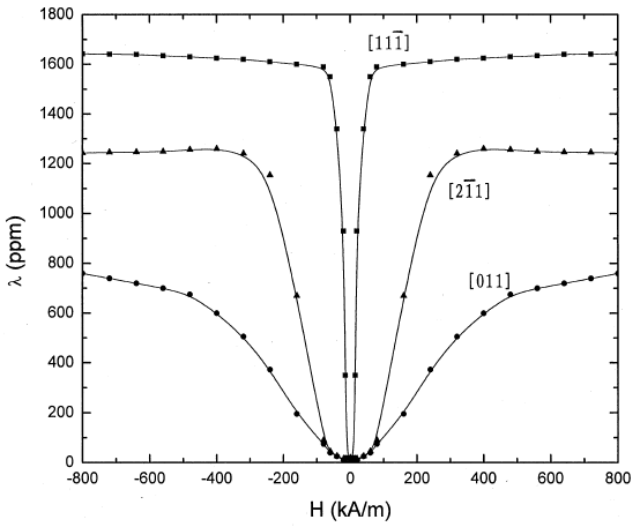

***Figure 1.16**: Magnetostriction curves of single crystal Terfenol-D measured along different crystallographic directions with respect to applied magnetic field. Taken from ref. [71].*

Although the phenomenon of magnetostriction effect was discovered in the 1840s, magnetostrictive materials were not used for any applications until much later. At the time of world war II, nickel based alloys having magnetostriction of ~50 ppm were exploited to design transducers for sonar applications. In the 1960s, giant magnetostriction (~10000 ppm) has been found in the rare-earth elements terbium and dysprosium, but at very low temperatures [11,72]. However, at room temperature, they don't manifest such remarkable

magnetostriction because of their low Curie temperatures. To develop magnetostrictive materials with a higher magnitude of magnetostriction at room temperature, rare-earth elements were alloyed with 3d-transition elements such as Fe that exhibit higher Curie temperature (770 ^{o}C) and also magnetically soft. In that attempt, two intermetallics rare-earth Fe alloys such as $TbFe_2$ and $DyFe_2$ showed higher T_C (>400 ^{o}C) and also found to exhibit magnetostriction coefficient of 2630 and 650 ppm, respectively [72]. Since very large magnetocrystalline anisotropies are associated with these alloys, very larger magnetic fields were needed to drive them to saturation. However, the magnetocrystalline anisotropies of the alloys could be attenuated by replacement of other rare earth elements with the same sign of magnetostriction and opposite sign of anisotropy constant. It was found that replacement of Tb by Dy was the most effective way to curtail the magnetocrystalline anisotropy with minimal drop in magnetostriction amplitude [73]. This led to the development of Terfenol, $Tb_{0.27}Dy_{0.73}Fe_{1.95}$, commercially known as *Terfenol-D* by researchers at the ***N***aval ***O***rdinance ***L***aboratory, which showed magnetostriction as high as 1600 ppm in single crystal form, at room temperature. The magnetostriction curves of single crystal Terfenol-D, measured as a function of the magnetic field along the different crystallographic directions are shown in Figure1.16. The magnetocrystalline anisotropy and the field required to saturate the magnetostriction of Terfenol-D are much lower than that for either $TbFe_2$ or $DyFe_2$. A detailed description of the magnetostrictive properties of Terfenol-D and other alloys are reviewed in the book by Engdahl [11]. Polycrystalline Terfenol-D shows the better magnetostriction coefficient and very low strain sensitivity at very high magnetic fields [65]. Many attempts were made to improve the mechanical strength and to reduce the cost of the polycrystalline Terfenol-D by making a composite with other materials like polymers and $NaPO_3$ glass matrix [65]. Improved mechanical strength and low cost of production are achieved in those composites but at the cost of the amplitude of magnetostriction. Even though single crystal Terfenol-D shows better magnetostriction at room temperature, plenty of limitations are associated with the material, like the high cost of raw materials, the requirement of single crystal, high brittleness and unable to withstand a substantial amount of tension.

To surmount the limitations of the Terfenol-D alloys, iron-gallium alloys, $Fe_{1-x}Ga_x$ (x=0.20-0.35), were developed as alternative materials to Terfenol-D by Clark *et al.* and the materials exhibit moderate magnetostriction (~400 ppm) in single crystal form even at very low magnetic fields of 100 Oe (≈8 kA/m) [74,75]. The high tensile strength and

minimum temperature dependence of magnetostriction behavior of Galfenol alloys were reported by Kellogg *et al.* [76,77] indicating that these alloys can withstand shock loads and harsh operating environments. Similar to Galfenol alloys, magnetostrictive characteristics of alloys of Fe with Aluminium and Beryllium are also reported [78,79], but the magnetostriction (λ_{100}) of Alfenol, $Fe_{1-x}Al_x$, is nearly two times lower than that of $Ga_{1-x}Fe_x$ for x=0.19. Although the magnetostriction of $Fe_{1.89}Be_{0.11}$ is similar to that of Galfenol, FeBe alloys are hard to process due to the toxicity of Beryllium. Studies on the magnetostrictive characteristics of Terfenol-D and Galfenol in thin film and polycrystalline forms are also reported, but the magnitude of the magnetostriction is lower than that of the single crystal counterparts and high fields are required to saturate the magnetostriction amplitudes [11,65,80-85]. Apart from that, many authors have made several attempts to improve the magnetostriction properties of polycrystalline Terfenol-D and Galfenol alloys by aligning the powder particles in the presence of magnetic fields during compaction [11,81,86-88].

1.5.2 Oxide based materials

Unlike alloy based magnetostrictive materials, oxide based magnetostrictive materials have advantages such as the high resistance towards corrosion, low cost of raw materials as well as production, chemically stability, have the ability to function at a higher frequency and can be processed into any shape and thin film form to design technological devices. Despite the facts that the magnetostriction coefficient is not as high as that of alloy based compounds, the oxide-based materials are very interesting due to their associated advantages as mentioned above. Many researchers have studied the magnetostrictive properties of some of the complex metal oxides such as hexagonal ferrites, garnets, spinels and perovskite materials in both single crystal and polycrystalline forms. Sayetat has studied the magnetostriction properties of single crystal garnets such as $Tb_3Fe_5O_{12}$, $DyFe_5O_{12}$, and $Ho_3Fe_5O_{12}$ and found to exhibit very high magnetostriction up to 2400, 875, and 450 ppm, respectively, at a temperature close to -269 °C [89]. However, the magnetostriction strain is found to vanish at ambient temperature. Licci *et al*. have made systematic studies on the magnetostriction properties of different types of sintered polycrystalline hexagonal ferrites such as W-, Y- and M-types [90]. Among all the studied systems, highest magnetostriction has been shown for Co_2-W type ferrite ($Ba_2Co_2Fe_{12}O_{22}$) with a magnitude of -74 ppm along the parallel direction and +24 ppm along the perpendicular direction to the applied magnetic field.

A colossal magnetostriction either at lower temperatures or higher applied magnetic field has been reported in some of the manganites based perovskite structured systems [91, 92]. In the perovskite manganites, e_g electron in Mn^{3+} is responsible for double-exchange interactions, superexchange interaction and Jahn-Teller distortion. Also, strong magnetoelastic effects in the manganites perovskite are accompanied by coupling of charge-lattice and spin-lattice. Ibarra *et al*. [91] have shown an increase in the volume magnetostriction from 0 ppm at -203 ^oC to -1200 ppm at -103 ^oC, but with further increase in the temperature, the magnitude of magnetostriction decreased at a faster rate. The authors proposed two mechanisms above and below the transition temperature, T_C = -103 ^oC. The magnetostriction in the paramagnetic state, above T_C, was suggested to be due to the contribution of charge localization and the observed large magnetostriction in the crossoverregion was attributed to charge-lattice and spin-lattice interactions. Dabrowski *et al.* have performed magnetostriction measurements on $La_{1-x}Sr_xMnO_3$ (x=0.11, 0.13, and 0.165) series of compositions in magnetic fields up to 12 T (1T ≈ 800 kA/m) [93]. In this study, the authors have observed a larger magnetostriction effect at the ferromagnetic transition temperature and suggested the coupling of the local spin moments and charge carriers to the crystal lattice [93]. Demin *et al*. studied anomalies of magnetostriction which was attributed to magnetic phase separation in a $La_{0.7}Sr_{0.3}MnO_3$ single crystal [94]. According to the authors, the essential contribution to the anisotropic magnetostriction at low temperature is from the Jahn–Teller effect associated with magnetic field driven changes in the orientation of the Jahn–Teller structural domains. Kuwahara *et al.* have investigated the magnetostrictive properties of single crystal $(Nd_{1-x}Sm_x)_{0.5}Sr_{0.5}MnO_3$ with x=0.25, 0.50, and 0.94 and observed clear hysteresis and abrupt changes in the magnetostriction for increasing and decreasing magnetic fields just above the ferromagnetic transition temperature [95]. Although the crystal structure remains unchanged, the lattice parameters abruptly changed at T_C. According to the authors, the magnetic field does not directly affect the crystal lattice but does so indirectly through localized spins with t_{2g} states of Mn^{3+}. Thus, these structural changes induced by a magnetic field reveal a strong coupling between the spin and charge degrees via Hund's–rule coupling, as well as the charge and lattice coupling via general electron–lattice coupling, or Jahn–Teller coupling.Similar to these studies, there are several reports on the magnetostriction properties of manganites and the related cobaltites [96-99].

Apart from garnets, hexagonal and perovskite materials, higher magnitudes of magnetostriction coefficient at room temperature as well as at low applied magnetic fields are

reported for some of the spinel ferrite materials. Bozorth *et al.* studied the magnetostrictive properties of single crystals of various spinel ferrites by measuring the strain along different crystallographic directions [59]. Magnetostriction coefficients of -19, -590, -210, -200, -36, -35 and -14 ppm are reported for the ferrite compositions Fe_3O_4, $Co_{0.8}Fe_{2.2}O_4$, $Co_{0.3}Zn_{0.2}Fe_{2.2}O_4$, $Co_{0.3}Mn_{0.4}Fe_{2.0}O_4$, $Ni_{0.8}Fe_{2.2}O_4$, $Mn_{0.28}Fe_{1.86}O_4$ and $Mn_{0.6}Zn_{0.1}Fe_{2.1}O_4$, respectively, along the <100> direction. Atif *et al.* reported the magnetostrictive properties of Zn-substituted nickel ferrite in $Ni_{1-x}Zn_xFe_2O_4$ ($0 \leq x \leq 0.6$) [100] and showed a decrease in the maximum magnetostriction coefficient from -28 ppm for x=0 to -5 ppm for x=0.6. The effect of substitution of Zn by Ni in $Zn_{1-x}Ni_xFeO_4$ on the magnetostrictive characteristics has been studied by Adhikari *et al.* [101]. It has been shown from the studies that the magnetostriction coefficient is almost zero up to 25% substitution of Ni and increased to +7 ppm for 50% substitution. The sign of the magnetostriction coefficient changed to negative after the 50% substitution of Ni and reached the maximum value of -35 ppm when Ni replaces all Zn. The observed variation in the magnetostriction with Ni content has been speculated based on the cation inversion where initially Ni is substituted for Zn at the tetrahedral sites and later for Fe at the octahedral sites. Bharathi *et al.* reported the magnetostriction values of -34 and -24 ppm when 7.5% of Fe in $NiFe_2O_4$ had been substituted by Sm and Ho, respectively, against the value -25 ppm for pure nickel ferrite. The authors have stated that higher negative magnetostriction of Sm is responsible for higher magnitudes of the magnetostriction in the Sm-substituted sample [102].

1.6 Magnetostriction studies on cobalt ferrite

Among the spinel ferrites, cobalt ferrite is known to exhibit distinguishable magnetic properties such as high positive magnetocrystalline anisotropy, high coercivity, moderate saturation magnetization and high Curie temperature [14, 61,103,104]. Prince *et al*. reported cobalt ferrite as inverse spinel structure based on the neutron diffraction analysis [105]. From various techniques, many authors have shown that it is not completely inverse spinel and rather is a mixed spinel in which Co^{2+} and Fe^{3+} are randomly distributed among A- and B-sites and the degree of distribution depend on the synthesis methods and processing conditions [106-108]. Also, cobalt ferrite shows better magnetostriction properties at room temperature [59] making the system as one of the technologically important ferrites in the magnetic ceramic category. Cobalt ferrite is known to exhibit remarkably higher magnitude

of magnetostriction both in single crystal and polycrystalline forms. The remarkable magnetic and magnetostrictive properties associated with cobalt ferrite is mainly due to the high positive magnetocrystalline anisotropy originating from the spin-orbit coupling of Co^{2+} ions located at the octahedral coordination site in the spinel crystal structure [109]. In the recent years, many researchers are projecting sintered polycrystalline cobalt ferrite as a suitable alternative candidate for the currently available high-cost alloy based magnetostrictive materials such as Terfenol D and its composites [65]. Although the magnitude of magnetostrictive strain is relatively low for cobalt ferrite, the material offers plenty of economical advantages over the alloy based materials because of its ability to function at high-frequency based devices, no contribution of eddy current due to its high electrical resistivity (105 Ω-m), low thermal conductivity (~0.005 W/m-K), high permeability, no corrosion effect due to its oxide nature, low cost and easy processability and also its good mechanical properties enable to operate in the tensile regime without losing its magnetic performance [65]. There were constant efforts to reduce the production cost and enhance the mechanical robustness of Terfenol-D by making composites with suitable materials [65,110]. However, after making the composite of Terfenol-D with several polymer and other materials, a significant drop in the production cost with increased mechanical robustness is attained but at the cost of magnetostriction amplitude and magneto-mechanical coupling factor (strain sensitivity) [110]. By comparing with the Terfenol-D composites, sintered polycrystalline cobalt ferrite has a high magnetostrictive strain at low magnetic fields with better magneto-mechanical coupling factor [110]. These superior advantages of cobalt ferrite over Terfenol-D and its composites will make it a better material for technological applications in the future.

Bozorth *et al*. [59] have investigated the magnetostriction properties of single crystal cobalt ferrite having the chemical composition $Co_{0.8}Fe_{2.2}O_4$, by measuring the strain along the different crystallographic directions as a function of field, as shown in Figure 1.17. A high negative magnetostrictive strain of ~-600 ppm (before magnetic field annealing) is reported along the <100> direction by applying the measuring field in the same direction [59]. However, by applying the field perpendicular to the <100> direction, the strain is positive with the magnitude much lower than that in the other direction. After annealing the crystal along <100> direction, magnetostrictive strain has been increased to ~850 ppm along the same direction but the measuring field is applied perpendicular to the <100> direction. Even for the single crystal, magnetostriction is almost zero along the different crystallographic

directions at lower magnetic fields, H<3000 Oe (239 kA/m). A similar feature of negligible magnetostriction at low fields is reported by Sato-Turtelli*et al*. for single crystal cobalt ferrite of similar chemical composition [111]. In the reported study, the response of the magnetostrictive strain to the applied magnetic field is measured at -269 ^{o}C along the two different crystallographic directions, <100> and <111>. The magnitude of the magnetostriction obtained along the <100> direction is almost comparable to that reported by Bozorth *et al* [59]. The magnetostrictive strain of single crystal cobalt ferrite not only depends on the crystallographic direction along which the strain is measured but also strongly on the chemical composition of the crystal. For example, the magnetostriction along <100> direction, λ_{100}, is reported as -250 ppm and -590 ppm for the chemical compositions $Co_{1.1}Fe_{1.9}O_4$ and $Co_{0.8}Fe_{2.2}O_4$, respectively [59].

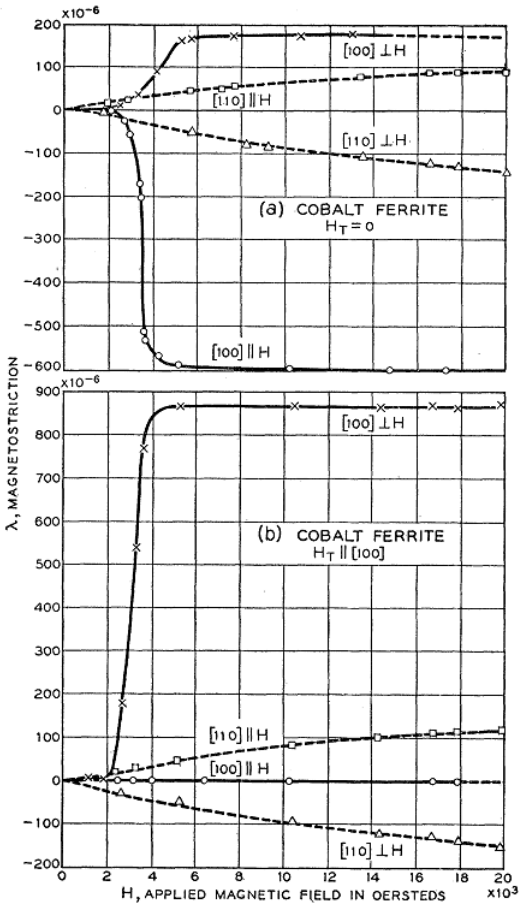

Figure 1.17*: Magnetostriction strain curves of single crystal cobalt ferrite ($Co_{0.8}Fe_{2.2}O_4$) measured along the different crystallographic directions, before and after magnetic field annealing. Taken from ref. [59].*

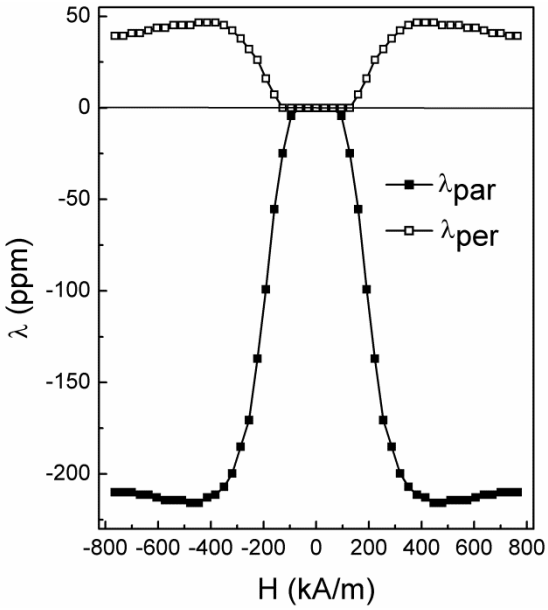

***Figure 1.18**: Magnetostriction strain curves of a sintered polycrystalline cobalt ferrite compact measured at room temperature by applying field along the parallel (closed symbols) and perpendicular (open symbols) directions to the cylindrical axis of the compact. This graph is part of current thesis work.*

The use of single crystal cobalt ferrite for the practical applications is limited due to its high cost of production, and also it is hard to grow the crystals with different shapes which are necessary and recommended for designing technological devices. Therefore, more attention has been devoted to developing high performance sintered polycrystalline cobalt ferrite due to the ease of preparation of the sintered materials and the cost effectiveness apart from the good mechanical properties. Typical magnetostriction strain curves of sintered polycrystalline cobalt ferrite compact, measured as a function of applied magnetic field along the parallel and perpendicular directions to the cylindrical axis of the sintered compact, are shown in Figure 1.18. Along the parallel direction, the large negative slope at lower magnetic fields is due to the dominant contribution from the easy axis magnetostriction coefficient, λ_{100}, and the small positive slope at higher magnetic fields is from the contribution of hard axis magnetostriction coefficient, λ_{111}, as reported [45,60,61]. Similarly, along the perpendicular direction, the positive slope in the lower magnetic field region is possibly due to the contribution from λ_{100} and the negative slope in the higher field region is from the contribution of λ_{111}. Much similar to the magnetostriction strain curves of single crystal cobalt ferrite, even for the sintered polycrystalline cobalt ferrite, the magnitude of magnetostriction is almost negligible at the low measuring magnetic field, indicating the dominance of the magnetocrystalline anisotropy of the material. The magnitude of the

maximum magnetostriction strain [λ_{max}] of the sintered polycrystalline cobalt ferrite is reported to vary from -150 ppm to -400 ppm [112-117]. These values depend on various factors such as stoichiometry, cation distribution, the density of the sintered compacts, and microstructure, which are effectively influenced by the synthesis methods and processing conditions.

McCallum *et al*. have studied the magnetostrictive properties of metal-bonded sintered polycrystalline cobalt ferrite composites and the magnetostriction strain curves are compared with that of the Terfenol-based composite materials [110]. The λ_{max} and $[d\lambda/dH]_{max}$ as high as -220 ppm and -1.3×10^{-9} m/A**,** respectively, are reported for the cobalt ferrite composites, and these values are higher than that of most of the studied Terfenol composites, at lower magnetic fields [110]. Moreover, it has been shown that the metal bonded cobalt ferrite composites have excellent mechanical and corrosion resistance properties over the Terfenol composites. Bhame and Joy have shown that the magnitude of λ_{max} of the sintered cobalt ferrite samples, prepared by various synthesis methods and heat treated at different temperatures and sintering time, strongly depends on the initial morphology of the ferrite particles used for sintering and the microstructure of the final sintered compacts [115,117]. From the studies, it has been concluded that the presence of smaller and uniform grains with minimum porous structure in the sintered materials are the crucial parameters to have higher magnetostriction properties.

Nlebedim *et al.* have made an effort to study the effect of heat treatment on the magnetostrictive properties of sintered cobalt ferrite samples quenched in water from the different sintering temperatures [60]. The highest value of $[d\lambda/dH]_{max}$ (-4.34×10^{-9} m/A) has been obtained for the furnace cooled followed sample with a lower λ_{max} (~-145 ppm). However, the authors have observed a decline in the magnitudes of λ_{max} and $[d\lambda/dH]_{max}$ with increasing annealing temperatures by subsequent quenching from the respective temperature. It has been concluded from the study that the decrease in the magnetocrystalline anisotropy due to the migration of large amount of Co^{2+} from the octahedral sites to the tetrahedral sites with increasing annealing temperature is responsible for the decrease in the magnetostrictive parameters.

Muhammad *et al.* have systematically investigated the effect of compaction pressure applied during the pelletization on the magnetostrictive properties of cobalt ferrite [116]. The authors compacted the prepared ferrite powder sample at various compaction pressures and

sintered at 1350 ^{o}C for 24 hours followed by furnace cooled to room temperature. The magnetostriction measurements indicated marginally higher magnetostriction parameters (λ_{max} = ~-200 ppm and $[d\lambda/dH]_{max}$ = -0.6 × 10^{-9} m/A) for the sample compacted at a pressure around 150 MPa. It has been suggested that the redistribution of Co^{2+} and Fe^{3+} among the tetrahedral and octahedral sites of the spinel lattice induced by the compaction pressure is a major contributing factor for such variation in the magnetostriction parameters. Very high λ_{max} of -400 ppm with the $[d\lambda/dH]_{max}$ of -1.2 × 10^{-9} m/A is shown after annealing the sintered sample in a magnetic field of 10 T (1T ≈ 800 kA/m) for 3 hours against the values ~-200 ppm and ~-0.6 × 10^{-9} m/A, respectively, for unannealed sample.

Nlebedim and Jiles investigated the magnetostrictive properties of cobalt ferrite samples, prepared by solid state method, compacted at two different pressures (87 MPa and 127 MPa) and sintered at three different temperatures (1250, 1350 and 1450 ^{o}C) by holding the samples at the respective temperatures for 24 and 36 hours each [118]. The authors have reported the highest λ_{max} (~-210 ppm) for the sample compacted at 127 MPa and sintered at 1350 ^{o}C for 24 hours and the lowest (~-70 ppm) for the sample compacted at 87 MPa and sintered at 1350 ^{o}C for 36 hours. The authors also observed a decrease in the amplitude of the magnetostriction coefficient with an increase in the holding time at any given sintering temperature for any of the compaction pressures and the decrease has been correlated to the increase in the porosity with an increase in the holding time but not with cation distribution. Moreover, samples compacted at 127 MPa and sintered at any given temperature for any of the holding times exhibited relatively higher $[d\lambda/dH]_{max}$ (~-2.2 × 10^{-9} m/A) compared to those compacted at 87 MPa and sintered at the same temperatures and holding time. It has been summarized from the study that the magnitudes of both λ_{max} and $[d\lambda/dH]_{max}$ of the sintered polycrystalline cobalt ferrite strongly depend on the processing parameters. The effect of vacuum sintering temperature and time on the magnetostrictive properties of cobalt ferrite is studied by Nlebedim *et al.* [119]. It has been shown that the samples sintered in vacuum developed a second phase that reduced the overall magnetostriction and also the magnetostriction is largest for lower sintering temperatures and longer sintering times.

Recently, Wang *et al.* have achieved a very high $[d\lambda/dH]_{max}$ of -7.7 × 10^{-9} m/A and λ_{max} of -277 ppm for the textured cobalt ferrite sample [120]. In the study, the authors have pelletized the semi-solid slurry of ferrite powder made with 5% polyvinyl alcohol by applying a pressure of 150 MPa and aligned along the axial direction by the application of a

DC magnetic field of strength 2 T (1T≈800 kA/m) for 30 seconds followed by sintering at 1350 ^{o}C for 6 hours. Higher magnetostriction has obtained for the magnetic field oriented cobalt ferrite sample at lower magnetic fields compared to the non-oriented sample (-142 ppm and -2.2 × 10^{-9} m/A) and it has been attributed to the redistribution of grain orientation along a particular crystallographic direction [120]. Even the magnitudes of the maximum λ (~-250 ppm) are reported to be almost comparable for the samples aligned at different magnetic fields (0.5 T, 1 T and 1.5 T) (1T≈800 kA/m) [121].

Aubert *et al.* reported the magnetic and magnetostriction properties of polycrystalline cobalt ferrite prepared by three different methods [122]. In one method, the sample was prepared by the conventional solid-state method using oxides of the corresponding metal and sintered at 1250 ^{o}C for 10 hours. In the second method, the prepared spinel compound from the first method was sintered using spark plasma sintering (SPS) process under a pressure of 100 MPa at 980 ^{o}C for 2 minutes. In the third method, the cobalt ferrite sample was prepared as well as sintered using the SPS process, where the synthesis was performed at 500 ^{o}C for 5 minutes and sintering at 750 ^{o}C for 3 minutes, both at 100 MPa pressure. Presence of secondary phases, higher sintered density (97%) and smaller sized grains are shown for the SPS samples. Higher λ_{max} of -229 ppm at the low field is obtained for the sample prepared and sintered from the SPS over the other samples and has been attributed to induced uniaxial anisotropy of the sample. It has been suggested that when the preparation of the spinel ferrite sample is performed under higher uniaxial pressure and at a temperature below its T_C, the applied stress influences the position of Co^{2+} at the octahedral sites leading to an induced uniaxial anisotropy in the direction of the pressure.

Lo *et al.* reported the improvement in the magnetostriction parameters for the sintered polycrystalline cobalt ferrite after annealing the sample at 300 ^{o}C for 36 hours in the presence of a DC magnetic field 318 kA/m [123]. The results showed the λ_{max} increased from -200 ppm to -250 ppm when the magnetostriction measured along the hard axis by applying the field on the same direction and the $[d\lambda/dH]_{max}$ also increased to -3.9 × 10^{-9} m/A from the value -1.5 × 10^{-9} m/A at lower field. Induced uniaxial anisotropy along the annealing direction was confirmed by measuring the magnetization hysteresis loops along the easy and hard directions higher magnetization at low field is observed in the former case.

Zheng *et al.* investigated the effect of magnetic field annealing on the magnetic and magnetostrictive properties of sintered polycrystalline cobalt ferrite after rapidly heating the

sample to 400 ^{o}C in a magnetic field ~360 kA/m and kept at that temperature for 30 minutes followed by slowly cooled to room temperature [124]. The uniaxial behaviour was observed in both magnetization and magnetostriction curves measured as a function of field. The magnetostriction curves of the field annealed sample were measured by applying the field along the parallel and perpendicular to the field annealed direction and reported the λ_{max} of only -50 ppm and -278 ppm along the respective directions, against the value -194 ppm for un-annealed sample. Such variation in the magnitudes of the λ_{max} in the field annealed sample was interpreted based on response of the magnetic domains to the magnetic field applied along the different directions, similar to the magnetostriction of field annealed single cobalt ferrite reported by Bozorth [59]. But compared to the single crystal, the non-zero magnetostriction coefficient has been shown along the easy axis when the measuring field is also in the same direction and it is suggested that not all domains have been fixed on easy axis by the annealing field; therefore the domain rotation in the polycrystals would contributes to that non-zero magnetostriction.

Khaja and Joy compared the magnetostriction parameters of polycrystalline cobalt ferrites sintered from the compacts made up of nanosized and bulk powders [113]. The sample sintered from the nanocrystalline powder of particle size <5 nm showed a large enhancement in the λ_{max} of about -315 ppm and $[d\lambda/dH]_{max}$ of -1.97×10^{-9} m/A compared to the values of -150 ppm and -0.56×10^{-9} m/A for the sample sintered from the bulk powder. In another study, the role of the initial particle size on the magnetostrictive properties of sintered cobalt ferrite derived from the nanocrystalline powders synthesized by an autocombustion reaction method was investigated [125]. It has been shown that high values of the λ_{max} and $[d\lambda/dH]_{max}$ for the compacts sintered from particles of very small sizes (<5 nm) are obtained, and also a close correlation between the magnetostriction and microstructures of the sintered compacts is observed. Magnetostriction parameters are further enhanced at lower magnetic fields after annealing the samples in magnetic field of strength 0.5 T (~400 kA/m) for 30 minutes.

The influence of the microstructure on the magnetostrictive characteristics of cobalt ferrite sintered at different conditions is reported [126]. It has been shown from the studies that the compacts made from the nanocrystalline powders and sintered at 1450 ^{o}C for a very short period exhibit very high magnetostriction coefficient compared to the samples heat treated for prolonged duration. Moreover, the magnitude of λ_{max} decreased with decreasing

the sintering temperatures from 1450 ^{o}C. The authors have observed a direct correlation between the magnetostriction characteristics and density as well as intragranular pores of the sintered products. The magnetostriction coefficient is found to be further improved to -330 ppm after sintering the nanocrystalline cobalt ferrite compacts in two stages. It has been concluded that two-stage sintering process, at relatively lower temperatures, is very effective in improving the magnetostriction characteristics of polycrystalline cobalt ferrite by achieving uniform grain size with relatively higher sintered density compared to the single stage sintering process [127]. Magnetostriction parameters are further enhanced at lower magnetic fields after annealing the samples in magnetic field of strength 0.5 T (~400 kA/m) for 30 minutes.

A novel concept of enhancing the magnetostriction coefficient of sintered cobalt ferrite by making self-composites from nanosized and bulk powders with different particle sizes of the same material as components has been reported [114]. The studies showed higher magnetostrictive characteristics for the sintered self-composite products compared to the products sintered from the individual powders [114]. The λ_{max} obtained for the samples sintered from the individual 3 nm, 40 nm, and the bulk powders are -315 ppm, -250 ppm and -150 ppm, respectively. However, a large enhancement in the magnetostriction coefficient,up to -400 ppm at a field of 800 kA/m, has been shown for the sintered polycrystalline cobalt ferrite compact made up of an appropriate weight percentages of different initial particle sizes of the same material (80% of 3 nm +10% of 40 nm +10% of bulk powders). In fact, saturation magnetostriction was not reached even at the highest measuring field (~800 kA/m) revealing a further possible increment in the magnetostriction coefficient at high fields. This is the highest magnetostriction coefficient, without magnetic field annealing, so far reported in the literature for sintered polycrystalline cobalt ferrite. Although higher magnetostriction coefficient is achieved from the self-composite technique, no significant improvement in the $[d\lambda/dH]_{max}$ (-2.0×10^{-9} m/A) has been reported. Magnetostriction parameters are further enhanced at lower magnetic fields after annealing the samples in magnetic field of strength 0.5 T (~400 kA/m) for 30 minutes.

Similar to the above mentioned self-composite studies, the dependence of the magnetostrictive properties of cobalt ferrite on the distribution of the initial powder particle sizes (~1- 2 μm), derived from the solid state synthesis method has been investigated [128]. The results revealed no significant improvement in the magnetostrictive characteristics.

1.7 Magnetostriction properties of substituted cobalt ferrite

The concept of substitution in cobalt ferrite was introduced to achieve a higher magnitude of strain sensitivity at lower magnetic fields, which is an essential requirement for the applications in sensors and actuators. Chemical substitution of various magnetic and nonmagnetic metal ions in place of Fe or Co in $CoFe_2O_4$ has been reported to affect the magnitude of both magnetostriction strain and strain sensitivity. This is because, the magnetostriction properties of cobalt ferrite depend not only on the concentration of the Co^{2+} ions located at the octahedral sites but also strongly on the magnetocrystalline anisotropy, A-O-B superexchange interactions, cation distribution, magnetic and structural parameters and these parameters are perturbed by the effect of the chemical substitution. Valency of the substituted ion (di-, tri-, tetravalent), the size of the substituted ion, amount of substitution and site preference (tetrahedral or octahedral) of the substituted metal ions are the crucial and dominant factors in tuning the magnetostriction parameters. Apart from these factors, similar to unsubstituted cobalt ferrite, various synthesis methods and processing conditions adopted to fabricate the samples of different metal ions substituted cobalt ferrite also influence the magnetostriction parameters significantly. Substitution of nonmagnetic cations into the cobalt ferrite lattice effectively weakens the A-O-B superexchange interactions due to the complete absence of the magnetic interaction between the magnetic and nonmagnetic cations mediated through oxygen in the spinel structure. Several studies on the magnetostriction properties of metal ion substituted cobalt ferrite, synthesized by different methods, are reported in the literature. An overview of the studies on metal ions substituted cobalt ferrite is presented below.

1.7.1 Divalent metal ion substituted cobalt ferrite

Somaiah *et al.* and Nlebedim *et al.* have studied the magnetostrictive properties of $CoZn_xFe_{2-x}O_4$ and $Co_{1-x}Zn_xFe_2O_4$ systems, respectively, synthesized by an autocombustion method and sintered at 1300 ^oC for 12 hours [129,130]. The studies on $CoZn_xFe_{2-x}O_4$ revealed that relatively high value of $[d\lambda/dH]_{max}$ for x=0.1 (-1.32×10^{-9} m/A) than the parent compound x=0 (-0.71×10^{-9} m/A) with λ_{max}=-148 ppm for x=0.1 and -183 ppm for x=0 [129]. However, the magnitude of λ_{max} is progressively decreased with increasing the Zn content. Similarly, studies by Nlebedim *et al.* on the magnetostrictive characteristics of the $Co_{1-x}Zn_xFe_2O_4$ showed a decrease in both the magnetostriction parameters with increasing Zn content with the λ_{max} and the $[d\lambda/dH]_{max}$ of ~-150 ppm and ~-0.5×10^{-9} m/A, respectively,

for the composition x=0.09 against -210 ppm and -0.71 × 10^{-9} m/A for x=0 [130]. Eventhough both substituted systems are prepared and processed under identical conditions, such a large variation in the strain sensitivity in the case of the $Co_{1-x}Zn_xFe_2O_4$ is due to the decreased content of Co^{2+}, as suggested [130]. The studies clearly indicated that it is possible to enhance the strain sensitivity when the substitution was made in place of Fe not for Co in $CoFe_2O_4$. However, contradictory to the above systems, the study by Nlebedim *et al*. [131] on the magnetostrictive properties of $CoMg_xFe_{2-x}O_4$ synthesized by a solid state reaction method showed a larger drop in both λ_{max} and $[d\lambda/dH]_{max}$ by increasing the Mg content in the spinel lattice. The possible reason for the large variation in the magnetostriction parameters for the Mg- and Zn-substituted samples, both substituted in place of Fe, is due to the difference in the synthesis methods and processing conditions.

Sekhar *et al.* have investigated the magnetostrictive properties of Cu-substituted cobalt ferrite, $Co_{1-x}Cu_xFeO_4$ ($0 \leq x \leq 0.25$), prepared by the citrate-gel autocombustion method and sintered at 1050 ^oC for 4 hours [132]. The study showed that λ_{max} of the composition with x=0.025 is almost comparable to that of the unsubstituted counterpart (-170 ppm) but at a lower magnetic field. However, for a higher amount of Cu-substitution, a large drop in λ_{max} has been reported. It has been suggested that the decrease in the value of λ_{max} with x is due to the Jahn-Teller type of distortion caused by the presence of copper ions in the spinel lattice and such type of distortion arises due to the coexistence of various oxidation states of Cu (+1 and +2) in the crystal structure. Unlike $Co_{1-x}Zn_xFeO_4$ system reported by Nlebedim *et al.*, $[d\lambda/dH]_{max}$ of $Co_{1-x}Cu_xFeO_4$ has been shown to increase from -0.25 × 10^{-9} m/A for x=0 to the value -4.52 × 10^{-9} m/A for x=0.15 and declined for higher values of x. The initial increment in $[d\lambda/dH]_{max}$ is attributed to the reduction in the anisotropy of the samples [132]. Here again, both $Co_{1-x}Zn_xFeO_4$ and $Co_{1-x}Cu_xFeO_4$ systems were prepared by different wet chemical methods and processed under different conditions, and therefore such a variation in the magnetostriction properties is anticipated. Also, Zn has a stable oxidation state with a strong preference for the tetrahedral coordination site whereas Cu exhibits variable oxidation states and has the ability to present at both the crystallographic sites leading to a large structural distortion.

The magnetostriction properties of $Co_{1-x}Ni_xFeO_4$ samples prepared by a coprecipitation method and sintered at a very low temperature, 600 ^oC, for 8 hours, are studied by Mathe and Sheikh [133]. A very low value of λ_{max}, -64 ppm, has been reported for the unsubstituted

cobalt ferrite and λ_{max} is found to be decreased with increasing the Ni content. Recently, Xin and Xi have investigated the magnetostrictive characteristics of different compositions in $Co_{1-x}M_xFeO_4$ (M=Ni, Cu, Zn) synthesized by a sol-gel autocombustion method and sintered at 1450 ^oC [134]. The authors have shown a better magnetostriction strain in the case of the Ni- and Cu-substituted cobalt ferrite samples, at a lower amount of substitution (x=0.1), over the Zn-substituted samples.

1.7.2 Trivalent metal ion substituted cobalt ferrite

The Jiles' group has reported systematic studies on the magnetostrictive properties made on the systems $CoM_xFe_{2-x}O_4$ (M=Al, Ga, Cr, Mn), synthesized by solid state reaction method and sintered at 1350 ^oC for 24 hours [135-138]. Despite having different sizes and site preferences for Mn, Cr, Al and Ga in the cobalt ferrite lattice, where Cr, Mn and Al are substituted at octahedral sites whereas Ga at the tetrahedral site, λ_{max} decreased with x in all cases from the value of -212 ppm for x=0, with improvement in $[d\lambda/dH]_{max}$ ranging from -2.5 to -3.4×10^{-9} m/A for $x \leq 0.4$ against the value -1.37×10^{-9} m/A for x=0 [135-138]. Although both Mn and Cr, which are magnetic cations, are substituted at the octahedral sites, the rate of decrease of λ_{max} is faster for the Cr-substituted samples over the Mn-substituted samples. Even for the same degree of substitution, x=0.2, a marginal variation in the magnetostriction parameters for the Ga- and Al-substituted samples and a larger variation in the parameters for the Cr- and Mn-substituted samples is reported [138]. Eventhough the magnetostriction strain is measured along the parallel direction, for $x \geq 0.7$ in the Cr-, Al- and Ga-substituted samples, the magnetostriction strain is positive at lower magnetic fields and changes to negative sign as the applied field increases, except for the composition $CoCr_{0.79}Fe_{1.21}O_4$ in which the strain is positive and almost constant even at higher measuring fields [137]. It has been stated that the sign of the anisotropy coefficient changes from positive to negative so that magnetic easy axes changed the magnetostriction from negative to positive at low fields for higher amounts of substitution. Such type of variation is not reported in the case of Mn-substituted samples, even for $x \geq 0.7$ [135].

Lo *et al.* have carried out experimental studies and modeling of the magnetostrictive effect in the Cr- and Mn-substituted cobalt ferrite [139, 140]. The observed increase in the strain sensitivity at lower amount of substitution ($x \leq 0.4$) is correlated to the ratio of the magnetostriction coefficient to anisotropy constant (λ_{max}/K_1). The authors suggested that increase in the strain sensitivity for $x \leq 0.4$ is due to the fast decrease of K_1 than λ_{max} and the

decreased magnetostriction coefficient for x>0.4 in both the cases is attributed to the fast decrease in the value of λ_{max} compared to K_1 [140].

Bhame and Joy have studied the magnetostrictive properties of $Co_{1.2}Fe_{1.8}O_4$ by substituting both Fe and Co by Mn, i.e., $Co_{1.2-x}Mn_xFe_{1.8}O_4$ and $Co_{1.2}Fe_{1.8-x}Mn_xO_4$ ($0 \leq x \leq 0.4$), prepared by the solid state reaction method and sintered at 1400 ^oC for 10 minutes [141]. It has been shown that for the system $Co_{1.2-x}Mn_xFe_{1.8}O_4$ λ_{max} is increased up to x=0.1 and $[d\lambda/dH]_{max}$ up to x=0.3 followed by a decrease for higher values of x, whereas both parameters decreased when more and more Fe being replaced by Mn in $Co_{1.2}Fe_{1.8-x}Mn_xO_4$. The higher values of magnetostriction and strain derivative at lower magnetic fields in the case of $Co_{1.2-x}Mn_xFe_{1.8}O_4$ have been attributed to the substitution of Mn at the octahedral sites as compared to the displacement of Co from the octahedral sites to tetrahedral sites when Mn is substituted for Fe in the $Co_{1.2}Fe_{1.8-x}Mn_xO_4$ system. In other studies [142,143], the substitution of Mn in place of Co in $Co_{1-x}Mn_xFe_2O_4$, prepared by the same synthesis method and sintered at 1450 ^oC for 10 minutes, showed 10% enhancement in the λ_{max} for the composition x=0.1 over x=0 (-138 ppm) and decreased for x>0.1, when the strain is measured along the perpendicular direction. On the other hand, along the parallel direction, although the reported λ_{max} is lower for the Mn-substituted samples compared to the unsubstituted sample, among the substituted samples, higher λ_{max} as well as the the slope at lower magnetic fields are obtained for the composition x=0.3. It has been concluded that 30% Mn-substitution for Co is an optimum composition to have higher magnetostriction coefficient at lower magnetic fields.

Atif *et al*. reported magnetostriction studies on $Co_{1-x}Mn_xFe_2O_4$ ($0 \leq x \leq 0.4$), prepared by the solid state reaction method, sintered at 1350 ^oC for 24 hours [144]. The authors measured the magnetostriction along both the directions and showed a continuous decrease of λ_{max} from -200 ppm for x=0 to -73 ppm for x=0.4 along the parallel direction and higher λ_{max} for $0 < x \leq 0.2$ and lower for x>0.2 along the perpendicular direction. The highest $[d\lambda/dH]_{max}$ is obtained for x=0.3 against other compositions. The changes in the magnitude of the magnetostriction parameters with increasing Mn content were correlated with the changes in the microstructures influenced by Mn concentration in the lattice of cobalt ferrite. Interestingly, the authors did not observe any peculiar behavior for x=0.3 along the parallel direction, as reported by Bhame and Joy in their studies, although Mn is substituted for Co in $CoFe_2O_4$ in both studies. However, both reports are closely consistent with the λ_{max} obtained along the perpendicular direction. The magnitudes of λ_{max} reported in the individual studies

are different, and it is likely to be due to the difference in the processing conditions (compaction pressure, sintering temperature and holding time) despite with same synthesis method.

Magnetostrictive properties of $CoFe_{2-x}Mn_xO_4$ ($0 \leq x \leq 0.6$), prepared by the solid state reaction method and sintered at 1180 ^oC for 4 hours, investigated by Rao *et al.*, showed a decrease in the value of λ_{max} from -167 ppm for x=0 to -73 ppm for x=0.6, with increase in $[d\lambda/dH]_{max}$ for x>0.2 [145]. It has been concluded that the decrease in λ_{max} is due to the increase in the Mn at the octahedral sites and increase in $[d\lambda/dH]_{max}$ after x=0.2 is attributed to the reduction in the anisotropy together with changes in the microstructural parameters.

Khaja and Joy have studied the magnetostrictive characteristics of Mn-substituted cobalt ferrite, $CoMn_xFe_{2-x}O_4$ ($0 \leq x \leq 0.3$), sintered from nanocrystalline powders of average crystallite size of <5 nm [146]. It has been shown that it is possible to achieve higher strain sensitivity with comparable magnetostriction coefficient at lower magnetic fields, at a particular Mn-substitution level. Also, all the Mn-substituted samples are reported to show higher $[d\lambda/dH]_{max}$ at lower magnetic fields than for the parent compound. The λ_{max} of the composition x=0.2 is found to be comparable to that of the unsubstituted composition with the magnitude of ~-232 ppm, but at a lower field, and it is higher than the value, -198 ppm, reported by Paulsen *et al*. [135] for the similar Mn-substituted composition, sintered from the bulk powder. The λ_{max} and $[d\lambda/dH]_{max}$ are further increased to -262 ppm and -3.2×10^{-9} m/A, respectively, after annealing the sample in a magnetic field of ~400 kA/m for 30 minutes. Magnetostriction characteristics of the composition $CoMn_{0.2}Fe_{1.8}O_4$ sintered at different temperatures are also reported, and the changes in the magnetostriction parameters with sintering temperatures are correlated to changes in the microstructural components such as grain size, density, porosity, etc. [146].

Bulai *et al.* studied the effect of substitution of a small amount of rare earth elements for Fe in cobalt ferrite, $CoFe_{1.97}RE_{0.03}O_4$ (RE=La, Ce, Sm, Gd, Dy, Ho, Er, Yb), on the magnetostrictive properties [147]. The compositions have been prepared by the solid state reaction method and sintered at 1250 ^oC for 5 hours. A slight drop in λ_{max} and a marginally higher $[d\lambda/dH]_{max}$ for the RE-substituted samples, at higher magnetic fields, compared to the parent compound, is reported. Although the substitution level is very lower, secondary phases are observed in the XRD patterns of sintered RE-substituted samples due to the larger size of RE. A similar magnetostriction as well as structural features have been reported for RE-

substituted cobalt ferrite, $CoFe_{1.8}RE_{0.2}O_4$ (RE = La, Dy, and Gd), prepared and processed under identical conditions [148]. Recently, Kakade *et al*. reported magnetostrictive properties of Er-substituted cobalt-rich cobalt ferrite compositions, $Co_{1.1}Fe_{1.9-x}Er_xO_4$ ($0 \leq x \leq 0.2$), prepared by the sol-gel autocombustion method and sintered at 700 ^oC for 3 hours [149]. The authors have shown higher λ_{max} (-200 ppm) and the $[d\lambda/dH]_{max}$ ($\sim -4.1 \times 10^{-9}$ m/A) for the substituted composition x=0.05 and at lower magnetic fields over the other compositions.

Most of the studies on the magnetostrictive properties of the metal ion substituted cobalt ferrites were carried out at room temperature. Meanwhile, to understand the influence of thermal effect on the magnetostrictive properties, the temperature dependent magnetostrictive parameters of Ga- and Al-substituted cobalt ferrites has been investigated by Nlebedim *et al*. by measuring the strain curves of the compositions at various temperatures [150,151]. For the unsubstituted cobalt ferrite, the highest λ_{max} of ~-500 ppm has been observed at temperature -223 ^oC, and it is nearly two-fold larger than the value (~-220 ppm) obtained at 27 ^oC. Moreover, the magnetostriction curve showed a higher degree of hysteresis behavior and also high field was required to achieve maximum magnetostriction coefficient. However, with increasing temperature, the magnitudes of λ_{max} reduced to -150 ppm at 77 ^oC, the field at which λ_{max} is obtained, and the magnetostriction hysteresis was also decreased progressively, and it has been attributed to a reduction in the magnetocrystalline anisotropy with an increase in the temperature. For the Ga- and Al-substituted samples, λ_{max} is lower than that for the unsubstituted counterpart over all measured temperatures, except for the composition $Co_{1.03}Al_{0.18}Fe_{1.79}O_4$ at -123 ^oC and -23 ^oC where λ_{max} is larger than that of the parent compound.

1.7.3 Tetravalent metal ion substituted cobalt ferrite

Magnetostriction studies on $CoSi_xFe_{2-x}O_4$ ($0 \leq x \leq 0.5$) compositions, prepared by the solid state reaction method and sintered at 1250 ^oC for 4 hours, by Rao *et al*. [152] showed no significant variation of λ_{max} even after substituting the higher amount of Si^{4+} into the lattice of cobalt ferrite. Even though a monotonic decrease in the T_C and M_s with increasing the Si content was observed, the magnitude of λ_{max} of all the Si-substituted compositions is reported to be nearly comparable to the value of -90 ppm obtained for the parent compound (x=0) [152]. In another study on $Co_{1+x}Si_xFe_{2-2x}O_4$ [153], it has been shown that λ_{max} is almost comparable up to x=0.2 with the magnitude of ~80 ppm and decreased for the higher values of x. It has been suggested that the decrease in the iron content as a result of increased Si

content is responsible for the steep decrease of magnetostriction for x>0.2. The strain sensitivity was observed to increase from -1.13 × 10^{-9} to -2.51× 10^{-9} m/A for x=0.2. The observed variations in the magnetostriction parameters were described based on the strength of the exchange interactions between cations, and anisotropy modifications induced by migration of cobalt ions.

Ranvah *et al.* have investigated the magnetostrictive properties of sintered $CoFe_2O_4$ by substituting both Ge^{4+} and Co^{2+} with equal amounts for Fe^{3+} in $Co_{1+x}Ge_xFe_{2-2x}O_4$, prepared by the solid state reaction method and sintered at 1350 ^oC for 24 hours [154]. The primary purpose of co-substitution of the tetravalent ion together with the excess amount of divalent Co in place of two trivalent Fe is to maintain charge neutrality and also to increase the concentration of Co^{2+} at the octahedral site. Furthermore, Ge^{4+} has a strong preference for the tetrahedral site, and therefore it pushes more amount of Co^{2+} into the octahedral sites. The results showed that the composition with x=0.1exhibits higher amplitude of λ_{max} (-241 ppm) and $[d\lambda/dH]_{max}$ (-2.4 × 10^{-9} m/A) at lower magnetic fields compared to the values -220 ppm and -2.0 × 10^{-9} m/A obtained for the unsubstituted compound and both parameters decreased for higher values of x. In another study by Nlebedim *et al.* on the magnetostriction properties of $Co_{1+x}Ti_xFe_{2-2x}O_4$, a systematic drop in λ_{max} as well as $[d\lambda/dH]_{max}$ with x is reported [155]. It has been stated that the different site preferences of Ge^{4+} and Ti^{4+} in cobalt ferrite lattice are responsible for such variations in the magnetostriction parameters, where Ge^{4+} preferentially occupies the A-sites and pushes Co^{2+} from the A-sites to the B-sites whereas Ti^{4+} occupy the B-sites and displaces Co^{2+} from the B-sites to the A-sites.

Monaji *et al*. have studied the magnetostrictive properties of Zr^{4+}/Co^{2+} co-substitution in cobalt ferrite, $Co_{1+x}Zr_xFe_{2-2x}O_4$, where Zr^{4+} has a strong preference for the tetrahedral site much similar to that of Ge^{4+} [156]. A marginally higher magnitude of λ_{max} (-186 ppm) with large enhancement in $[d\lambda/dH]_{max}$ (-3.32 × 10^{-9} m/A) for the composition with x=0.2 compared to the values -180 ppm and -0.8 × 10^{-9} m/A for the unsubstituted composition has been reported. In those reported studies on tetravalent ion substitution, the maximum values of λ and $d\lambda/dH$ are observed at different levels of substitutions, x=0.1 in the Ge-substituted sample and 0.2 in Zr-substituted sample, despite the fact that both Ge^{4+} and Zr^{4+} are occupied at the tetrahedral sites of the cobalt ferrite lattice. Even though the samples of both systems are prepared by the solid state reaction method, the large variation in the magnetostrictive parameters is likely to be due to the difference in the processing conditions.

1.7.4 Pentavalent metal ion substituted cobalt ferrite

Ramchandra *et al.* have reported comparative studies on the magnetostrictive properties of cobalt ferrite and the effect of co-substitution of Co^{2+}/Nb^{5+} in place of Fe in cobalt ferrite, $Co_{1.1}Fe_{1.85}Nb_{0.05}O_4$, prepared by the solid state method and sintered at 1200 ^oC for 20 hours [157]. Although λ_{max} is lower (-123 ppm) for the Co^{2+}/Nb^{5+}-substituted sample compared to the value -210 ppm for the unsubstituted compound, higher magnetostriction at lower magnetic fields is obtained for the co-substituted sample. The authors have claimed that even though the Co^{2+} concentration at the octahedral site is higher for $Co_{1.1}Fe_{1.85}Nb_{0.05}O_4$, the anisotropy is found to be reduced to 1.4×10^5 J/m^3 compared to that for unsubstituted $CoFe_2O_4$ (2.1×10^5 J/m^3), and the octahedral distortion induced by the partially unquenched spin-orbit coupling is the factor for lower anisotropy in the former case.

1.8 Factors affecting magnetostriction parameters of cobalt ferrite

A comparison of the different reports in the literature shows that the magnetostriction parameters of the sintered polycrystalline cobalt ferrite are affected by multiple factors. The sintering parameters such as sintering temperature, sintering time, rate of heating and cooling, the atmosphere in which sintering has been carried out, etc., are known to strongly affect the microstructural parameters like grain size, shape, grain boundaries, porosity, density and also cations distribution, and hence the magnetostriction parameters are likely to be affected by the changes in the processing conditions. Similarly, the different synthesis methods (solid state and wet chemical methods) used for the preparation of the samples affect the size of the particles in the starting powders which are used for making the compacts for sintering. Thus, the method of synthesis is also one of the factors that affect the microstructure of the sintered products which in turn may affect the magnitude of the magnetostriction parameters. The sintered compacts with smaller and homogeneously sized grains and high sintered density are required to have higher magnetostriction characteristics. The samples sintered from nanosized powders exhibited higher magnetostriction parameters at lower magnetic fields compared to the samples sintered from bulk powders, and this is attributed to the difference in the microstructures. It is easy to control the microstructure of the samples sintered from the nanosized powders whereas hard to control for samples sintered from bulk powders because

there will be more grain growth when bulk powders are used. Compaction pressure is another parameter that affects the microstructure. Higher compaction pressure gives rise to close contact of the particles that lead to higher degree of grain growth during the sintering process. On the other hand, lower compaction pressure may lead to lower sintered density and porous structure. Aligning the particles in the powder by a magnetic field during the compaction leads to textured (grain orientation) microstructures in the final sintered samples. These textured samples exhibit better magnetostriction parameters at low magnetic field compared to the randomly oriented polycrystalline samples. Further, the magnetostriction parameters of the sintered cobalt ferrite compacts are enhanced at lower magnetic fields after annealing the sintered compacts in a magnetic field. The large enhancement of the magnetostriction parameters of the field annealed samples is attributed to uniaxial anisotropy induced along the annealing field direction. Thus, the literature studies suggest that the magnetostriction parameters of sintered polycrystalline cobalt ferrite can be tuned and controlled by controlling the synthesis and processing parameters as well as by suitable substitution of Co and Fe in $CoFe_2O_4$.

1.9 Scope of the present work

Although there are many reports on the magnetostrictive properties of various magnetic and nonmagnetic metal ions substituted for cobalt or iron site in cobalt ferrite, most of the studies are made on the samples prepared by the ceramic process involving the high-temperature solid state reaction. The magnetostriction parameters of the same metal ion substituted compositions are not comparable due to the difference in the processing parameters adopted. For most of the metal ion substituted studied systems, synthesized by the solid state reaction method, it is found that the magnitude of the maximum magnetostriction strain is reduced significantly with large enhancement in the maximum strain sensitivity at low magnetic fields. The enhancement in the strain sensitivity is reported only at lower levels of substitution. Comparison of the results reported in the literature revealed that it is possible to enhance the strain sensitivity without any decrease or with higher values of magnetostriction strain at lower amounts of metal ion substitution in cobalt ferrite samples sintered from nanocrystalline powders. Moreover, systematic studies on the role of valency, size, and site preference of the substituted metal ions in the cobalt ferrite lattice on the magnetostrictive properties have not been reported in the literature.

The prime objective of the present thesis work is to develop metal ion (M) substituted cobalt ferrite compositions in $CoFe_{2-x}M_xO_4$, with high magnetostriction strain and strain sensitivity at low magnetic fields, for applications in sensors and actuators. As part of the study, the other objectives are to,

- Prepare and process different compositions of metal ions substituted cobalt ferrite under identical conditions for a better comparison of the structural, magnetic and magnetostrictive properties,
- To investigate the role of valency, ionic size and crystallographic site preference of the substituted metal ion (divalent nonmagnetic metal ions Zn and Mg, trivalent nonmagnetic metal ions Al, Ga and In) on the structural, magnetic and magnetostrictive properties.
- To understand the effect of co-substitution of different metal ions having different site preferences in the cobalt ferrite lattice on the magnetostrictive properties.
- To enhance the magnetostriction parameters by controlling the microstructures of the metal ion substituted cobalt ferrite samples sintered from compacts made from powders of different initial particle sizes.

Bibliography

[1] M. D. Eddy, *The Language of Mineralogy* (Ashgate Publishing Limited, Burlington, 2008).

[2] J. F. Shackelford, *Introduction to Materials Science for Engineers* (Prentice Hall, New Jersey, 2009).

[3] W. Callister and Jr. D. G Rethwisch, *Materials Science and Engineering – An Introduction* (8th ed. John Wiley and Sons, 2009).

[4] R. M. Jones, *Mechanics of Composite Materials* (2nd ed. Taylor & Francis, New York, 1999).

[5] V. Van and H. Lawrence, *Materials Science for Engineers* (Addison-Wesley, 1970).

[6] M. V. Gandhi and B. S. Thompson, *Smart Materials and Structures* (Chapman & Hall, 1992).

[7] S. L. Kakani and A. Kakani *Materials Science* (New Age International, New Delhi, 2006).

[8] C. Galassi, M. Dinescu, K. Uchino and M. Sayer, *Piezoelectric materials: Advances in science, Technology and Applications* (Kluwer Academic Publishers, New York, 2000).

[9] K. Otsuka and C. M. Wayman, *Shape Memory Materials* (Cambridge University Press, New York, 1999).

[10] G. Bossis, *Electrorheological Fluids and Magnetorheological Suspensions* (World Scientific, 2002).

[11] G. Engdahl, *Handbook of Giant Magnetostrictive Materials* (Academic press, Sandiego, 2000).

[12] W. F. Brown, *IEEE Trans. Magn*. **20**, 112 (1984).

[13] M. Getzlaff, *Fundamentals of Magnetism* (Springer, New York, 2008).

[14] B. D. Cullity and C. D. Graham, *Introduction to Magnetic Materials* (John Wiley & sons, New Jersey, 2009).

[15] N. A. Spladin, *Magnetic Materials Fundamentals and Applications* (2nd ed. Cambridge University Press, New York, 2011).

[16] J. Smit and H. P. J. Wijn, *Ferrites* (Philips Technical Library, Eindhoven, 1959).

[17] S. Chikazumi, Physics of ferromagnetism (2nd ed. Oxford University Press, Oxford, 1997).

[18] C. G. Shull and J. S. Smart, *Phys. Rev*. **76**, 1256 (1949).

[19] A. Hubert and R. Schäfer, *Magnetic Domains: The Analysis of Magnetic Microstructures* (Springer, Heidelberg, 1998).

[20] J. McCord, *J. Phys. D: Appl. Phys*. **48**, 333001 (2015).

[21] B. Betz, P. Rauscher, R. P. Harti, R. Schäfer, A. Irastorza-Landa, H. Van Swygenhoven, A. Kaestner, J. Hovind, E. Pomjakushina, E. Lehmann, and C. Grünzweig, *Phys. Rev. Appl*. **6**, 024023 (2016).

[22] A. Goldman, *Modern Ferrite Technology* (Van Nostrand Reinhold, New York, 1990).

[23] Y. Kitagawa, Y. Hiraoka, T. Honda, T. Ishikura, H. Nakamura, T. Kimura, *Nat. Mater*. **9**, 797 (2010).

[24] S. H. Chen et al. *Phys. Rev. Lett*. **108**, 177201 (2012).

[25] K. Okumura, K. Haruki, T. Ishikura, S. Hirose, and T. Kimura, *Appl. Phys. Lett*. **103**, 032906 (2013).

[26] S. Shen and Y. Chai and Y. Sun, *Sci. Rep*. **5**, 8254 (2015).

[27] V. G. Harris et al. *J. Magn. Magn. Mater*. **321**, 2035 (2009).

[28] B. Viswanathan and V. R. K. Murthy, *Ferrite Materials: Science and Technology* (Narosa Publishing House, New Delhi, 1990).

[29] M. Sugimoto, *J. Am. Ceram. Soc*. **82**, 269 (1999).

[30] S. E. Lyshevski and K. S. Martirosyan, Nanotechnology (IEEE-NANO), 11th IEEE Conference, 2011.

[31] F. S. Galasso, *Structure and Properties of Inorganic Solids* (Pergamon Press, New York, 1970).

[32] E. J. W. Verwey and E. L. Heilman, *J. Chem. Phys*. **15**, 174 (1947).

[33] E. J. W. Verwey, F. De Boer and J. H. V. Santen, *J. Chem. Phys*. **16,** 1091 (1978).

[34] F.C. Romeijn, *Philips Res. Rep*. **8**, 316 (1953).

[35] J.D. Dunitz and L.E. Orgel, *Adv. Inorg. Radiochem*. **2**, 1 (1960).

[36] D. S. McClure, *J. Phys. Chem. Solids* **3**, 311 (1957).

[37] G. Blasse, *Philips Res. Rep*. **3**, 13 (1964).

[38] M. Atif, R. Sato-Turtelli, R. Grössinger, M. Siddique, M. Nadeem, *Ceram. Int*. **40**, 471 (2014).

[39] Z. J. Zhang, Z. L. Wang , B. C. Chakoumakos, and J. S. Yin, *J. Am. Chem. Soc*. **120**, 1800 (1998).

[40] F. Li, J. Liu, D. G. Evans, and X. Duan, *Chem Mater*. **16**, 1597 (2004)

[41] E. Prince, *Phys. Rev*. **102**, 674 (1956).

[42] L. P. Skolnick, S. Kondo and L. R. Lavine, *J. Appl. Phys*. **29**, 198 (1958).

[43] S. W. da Silva, F. Nakagomi, M. S. Silva, A. Franco Jr, V. K. Garg, A. C. Oliveira, and P. C. Morais, *J. Nanopart. Res*. **14**, 798 (2012).

[44] K. B. Modi, P. Y. Raval, S. J. Shah, C. R. Kathad, S. V. Dulera, M. V. Popat, K. B. Zankat, K. G. Saija, T. K. Pathak, N. H. Vasoya, V. K. Lakhani, U. Chandra, and P. K. Jha, *Inorg. Chem*. **54**, 1543 (2015).

[45] S. H. Song, Doctoral dissertation, Department of Materials Science and engineering, State University, Ames, Iowa, 2007.

[46] R. Pandit, K. K. Sharma, P. Kaur and R. Kumar, *Mater. Chem. Phys*. **148**, 988 (2014).

[47] P. N. Anantharamaiah and P. A. Joy, *Phys. Chem. Chem. Phys*. **18**, 10516 (2016).

[48] P. N. Anantharamaiah and P. A. Joy. *J. Mater. Sci*. **50**, 6510 (2015).

[49] S. Singhal, S. K. Barthwal, K. Chandra, *J. Magn. Magn. Mater*. **306**, 233 (2006).

[50] L. Kumar and M. Kar, *J. Magn. Magn. Mater*. **323**, 2042 (2011).

[51] J. P. Joule, *Ann. Electr. Magn. Chem.* **8**, 219 (1842).

[52] C. Heck, *Magnetic Materials and their Applications* (Butterworth & Co. Publishers, London, 1974).

[53] E. Villari, *Ann. Phys. Chem.* **6**, 87 (1865).

[54] G. Wiedemann, *Ann. Phys. Chem.* **117**, 193 (1862).

[55] R. Skorski, *J. Appl. Phys.* **35**, 1213 (1964).

[56] A. G. Olabi and A. Grunwald, *Mater. Design* **29**, 469 (2008).

[57] A. G. Olabi and A. Grunwald, http://citeseerx.ist.psu.edu.

[58] D. C. Jiles, *Introduction to Magnetism and Magnetic Materials* (Chapman & Hall, New York, 1998).

[59] R. M. Bozorth, E. F. Tilden, and A. J. Williams, *Phys. Rev*. **99**, 1788 (1955).

[60] I. C. Nlebedim, N. Ranvah, P. I. Williams, Y. Melikhov, J. E. Snyder, A. J. Moses, and D. C. Jiles, *J. Magn. Magn. Mater*. **322**, 1929 (2010).

[61] P. N. Anantharamaiah and P. A. Joy, *J. Appl. Phys*. **121**, 093904 (2017).

[62] Y. Chen, B. K. Kriegermeier-Sutton, J. E. Snyder, K. W. Dennis, R.W. McCallum, D.C. Jiles, J. Magn. Magn. Mater. **236**, 131 (2001).

[63] R. M. Bozorth, *Ferromagnetism* (Van Nostrand Co., New York, 1951).

[64] N. Ranvah, *Ph D Thesis* "*Investigation of chemical substituted cobalt ferrite for high magnetostrictive based sensors and actuators applications*" (University of Cardiff, Cardiff, 2010).

[65] M. R. J. Gibbs, *Modern Trends in Magnetostriction Study and Application* (Kluwer Academic, Dordrecht, 2001).

[66] H. A. Chowdhury, S. A. Mazlan, and A. G. Olabi, *Solid State Phenomena* **154**, 41 (2009).

[67] S. Datta, www.comsol.com/blogs/modeling-magnetostriction-using-comsol.

[68] R. Grossinger, G. V. Duong and R. Sato-Turtelli, *J. Magn. Magn. Mater*. **320**, 1972 (2008).

[69] F. L. Zabotto, A. J. Gualdi, P. C. de Camargo, A. J. A. de Oliveira, J. A. Eiras and D. Garcia, *J. Alloys Compd*. **676,** 80 (2016).

[70] C. W. Nan, M. I. Bichurin, D. Shuxiang, D. Viehland and G. Srinivasan, *J. Appl. Phys*. **103,** 031101(2008).

[71] B. W. Wang, S.C. Busbridge, Y. X. Li, G. H. Wu, A. R. Piercy, *J. Magn. Magn. Mater*. **218**, 198 (2000).

[72] A. E. Clark, B. F. Disparage and R. Bozorth, *Phys. Rev.* **138** A216 (1965).

[73] R. Abbundi and A. E. Clark, *IEEE Trans. Magn*. **13**, 4510 (1977).

[74] A. E. Clark, K. B. Hathaway, M. W. -Fogle, J. B. Restorff, T. A. Lograsso, V. M. Keppens, G. Petculescu and R. A. Taylor, *J. Appl. Phys*. **93**, 8621 (2003).

[75] A. E. Clark, J. B. Restorff, M. Wun-Fogle, T. A. Lograsso and D. L. Schlagel, *IEEE Tran. Magn*. **36**, 3238 (2000).

[76] R. A. Kellogg, A. M. Russell, T. A. Lograsso, A. F. Flatau, A. E. Clark, and M. Wun-Fogle, *Act. Mater*. **52**, 5043 (2004).

[77] R. A. Kellogg, *PhD Thesis,* Engineering Mechanics, Iowa State University, Iowa, 2003.

[78] J. R. Cullen, A. E. Clark, M. Wun-Fogle, J. B. Restorff and T. A. Lograsso, *J. Magn. Magn. Mater*. **226**, 948 (2002).

[79] A. E. Clark, M. Wun-Fogle, J. B. Restorff, T. A. Lograsso and G. Petculescu, *J. Appl. Phys*. **95**, 6942 (2004).

[80] S. F. Xu, H. P. Zhang, W. Q. Wang, S. H. Guo, W. Zhu, Y. H. Zhang, X. L. Wang, D. L. Zhao, J. L. Chen, and G. H. Wu, *J. Phys. D: Appl. Phys*. **41**, 015002 (2008).

[81] J.-H. Yoo, S.-M. Na, J. B. Restorff, M. Wun-Fogle, and A. B. Flatau, *IEEE Trans. Magn*. **45**, 4145 (2009).

[82] E. C. Estrine, W. P. Robbins, M. M. Maqableh, and B. J. H. Stadler, *J. Appl. Phys*. **113**, 17A937 (2013).

[83] P. J. Grundy, D. G. Lord, and P. I. Williams, *J. Appl. Phys*. **76**, 7003 (1994).

[84] E. Quandt, *J. Appl. Phys*. **75**, 5653 (1994).

[85] H. Uchida, Y. Matsumura, H. Uchida, H. Kaneko, *J. Magn. Magn. Mater*. **239**, 540 (2002).

[86] N. Srisukhumbowornchai and S. Guruswamy, *J. Appl. Phys*. **90**, 5680 (2001).

[87] T. A. Duenas and G. P. Carman, *J. Appl. Phys*. **87**, 4696 (2000).

[88] O. Y. Kwon, H. Y. Kim, and S. H. Hong, *J. Appl. Phys*. **100**, 123905 (2006).

[89] F. Sayetat, *J. Magn. Magn. Mater.* **58**, 334 (1986).

[90] F. Licci and S. Rinaldi, *J. Appl. Phys.* **52**, 2442 (1981).

[91] M. R. Ibarra, P. A. Algarabel, C. Marquina, J. Blasco and J. Garcia, *Phys. Rev. Lett*. **75**, 3541 (1995).

[92] J. M. De Teresa, J. Blasco, M. R. Ibarra, J. Garcia, C. Marquina, P. Algarabel, and A. Del Moral, *J. Appl. Phys.* **79**, 5175 (1996).

[93] B. Dabrowski, L. Gladczuk, A. Wisniewski, Z. Bukowski, R. Dybzinski, A. Szewczyk, M. Gutowska, S. Kolesnik, C. W. Kimball and H. Szymczak, *J. Appl. Phys*. **87**, 3011 (2000).

[94] R. V. Demin, L. I. Koroleva and A. M. Balbashov, *Phys. Lett. A* **231** 229 (1997).

[95] H. Khuwahara, Y. Tomioka, A. Asamitsu, Y. Mortitomo and Y. Tokura, *Science* **270**, 961 (1995).

[96] F. Rivadulla, L. E. Hueso, D. R. Miguens, P. Sande, A. Fondado, J. Rivas, M. A. Lopez-Quintela and C. A. Ramos, *J. Appl. Phys.* **91**, 7412 (2002).

[97] J. S. Gwag, H. Kim and J. W. Kim, *J. Appl. Phys.* **93**, 1142 (2003).

[98] M. R. Ibarra, R. Mahendiran, C. Marquina, B. Garcia-Landa and J. Blasco, *Phys. Rev. B* **54**, R327 (1998).

[99] I. O. Tryonchauk, N. V. Samsonenko, A. Nabialek and H. Szymczak, *J. Magn. Magn. Mater*. **168**, 309 (1997).

[100] A. Muhammad, M. Nadeem, R. Grossinger and R. S. Turtelli, *J. Alloys Compd*. **509**, 5720 (2011).

[101] R. Adhikari, A. Sarkar, M. V. Limaye, S. K. Kulkarni, and A. K. Das, *J. Appl. Phys*. **111**, 073903 (2012).

[102] K. K. Bharathi, G. Markandeyulu and C. V. Ramana, *J. Phys. Chem. C* **115**, 554 (2011).

[103] H. Shenker, *Phys. Rev*. **107**, 1246 (1957).

[104] F. J. Pedrosa, J. Rial, K. M. Golasinski, M. N. Guzik, A. Quesada, J. F. Fernandez, S. Deledda, J. Camarero, and A. Bollero, *Appl. Phys. Lett*. **109**, 223105 (2016).

[105] E. Prince, *Phys. Rev*. **102**, 674 (1956).

[106] G. A. Sawatzky, F. V. D. Woude and A. H. Morrish, *J. Appl. Phys*. **39**, 1204 (1968).

[107] H. L. Yakel, *J. Phys. Chem. Solids* **41**, 1097 (1980).

[108] C. Liu, B. Zou, A. J. Rondinone, and Z. J. Zhang, *J. Am. Chem. Soc*. **122**, 6263 (2000).

[109] J. C. Slonczewski, *J. Appl. Phys*. **32**, S253 (1961).

[110] R. W. McCallum, K. W. Dennis, D. C. Jiles, J. E. Snyder and Y. H. Chen, *Low Temp. Phys*. **27**, 266 (2001).

[111] R. S. Turtelli, M. Kriegisch, M. Atif and R .Grössinger, IOP Conf. Series: Materials Science and Engineering **60**, 012020 (2014).

[112] I. C. Nlebedim , J. E. Snyder , A. J. Moses , and D. C. Jiles, *IEEE Trans. Magn*. **48**, 3084 (2012).

[113] K. K. Mohaideen and P. A. Joy, *Appl. Phys. Lett*. **101**, 072405 (2012).

[114] K. K. Mohaideen and P. A. Joy, *ACS Appl. Mater. Interfaces* **4**, 6421 (2012).

[115] S. D. Bhame and P. A. Joy, *Sens. Actuators A* **137**, 256 (2007).

[116] A. Muhammad, R. Sato-Turtelli, M. Kriegisch, R. Grossinger, F. Kubel and T. Konegger, *J. Appl. Phys*. **111**, 013918 (2012).

[117] S. D. Bhame and P. A. Joy, *J. Am. Ceram. Soc*. **91**, 1976 (2008).

[118] I. C. Nlebedim, J. E. Snyder, A. J. Moses, D. C. Jiles, *J. Magn. Magn. Mater*. **322**, 3938 (2010).

[119] I. C. Nlebedim, N. Ranvah, P. I. Williams, Y. Melikhov, F. Anayi, J. E. Snyder, A. J. Moses, D. C. Jiles, *J. Magn. Magn. Mater*. **321**, 2528 (2009).

[120] J. Wang, X. Gao, C. Yuan, J. Li and X. Bao, *J. Magn. Magn. Mater*. **401**, 662 (2016).

[121] J. -Quan Wang, J. -Heng Li, C. Yuan, X. -Qian Bao and X. -Xu Gao, *Rare Met*. DOI 10.1007/s12598-016-0817-1

[122] A. Aubert, V. Loyau, F. Mazaleyrat and M LoBue, *J. Eur. Ceram. Soc*. **37**, 3101 (2017).

[123] C. C. H. Lo, A. P. Ring, J. E. Snyder, D. C. Jiles, *IEEE Tran. Magn*. **41**, 3676 (2005).

[124] Y. X. Zheng, Q. Q. Cao, C. L. Zhang, H. C. Xuan, L. Y. Wang, D. H. Wang, and Y. W. Du, *J. Appl. Phys*. **110**, 043908 (2011).

[125] K. K. Mohaideen and P. A. Joy, *J. Magn. Magn. Mater*. **346**, 96 (2013).

[126] K. K. Mohaideen and P. A. Joy, J. Eur. Ceram. Soc. **34**, 677 (2014).

[127] K. K. Mohaideen and P. A. Joy, *J. Magn. Magn. Mater*. **371**, 121 (2014).

[128] I. C. Nlebedim, and D. C. Jiles, *J. Appl. Phys*. **115**, 17A928 (2014).

[129] N. Somaiah, T. V. Jayaraman, P. A. Joy, and D. Das, *J. Magn. Magn. Mater*. **324**, 2286 (2012).

[130] I. C. Nlebedim, M. Vinitha, P. J. Praveen, D. Das, and D. C. Jiles, *J. Appl. Phys*. **113**, 193904 (2013).

[131] I. C. Nlebedim, R. L. Hadimani, R. Prozorov, and D. C. Jiles, *J. Appl. Phys*. **113**, 17A928 (2013).

[132] B. C. Sekhar, G. S. N. Rao, O. F. Caltun, B. D. Lakshmi, B. P. Rao, and P. S. V. S. Rao, *J. Magn. Magn. Mater*. **398**, 59 (2016).

[133] V. L. Mathe and A. D. Sheikh, *Physica B* **405**, 3594 (2010).

[134] G. Xi and Y. Xi, *Mater. Lett*. **164**, 444 (2016).

[135] J. A. Paulsen, A. P. Ring, C. C. H. Lo, J. E. Snyder, and D. C. Jiles, *J. Appl. Phys*. **97**, 044502 (2005).

[136] S. H. Song, C. C. H. Lo, S. J. Lee, S. T. Aldini, J. E. Snyder and D. C Jiles, *J. Appl. Phys*. **101,** 09C517 (2007).

[137] S. J. Lee, C. C. H. Lo, P. N. Matlage, S. H. Song, Y. Melikhov, J. E. Snyder and D. C. Jiles, *J. Appl. Phys*. **102,** 073910 (2007).

[138] I. C. Nlebedim, N. Ranvah, Y. Melikhov, P. I. Williams, J. E. Snyder, A. J. Moses and D. C. Jiles, *IEEE Tran. Magn*. **45**, 4120 (2009).

[139] C. C. H. Lo, *J. Appl. Phys*. **107**, 09E706 (2010).

[140] C. C. H. Lo, *IEEE Tran. Magn*. **43**, 2367 (2007).

[141] S. D. Bhame and P. A. Joy, *J. Appl. Phys*. **99**, 073901 (2006).

[142] S. D. Bhame and P. A. Joy, *J. Appl. Phys*. **100,** 113911 (2006).

[143] S. D. Bhame and P. A. Joy, *J. Phys. D: Appl. Phys*. **40,** 3263 (2007).

[144] M. Atif, R. Sato Turtelli, R. Grossinger, and F. Kubel, *J. Appl. Phys*. **113**, 153902 (2013).

[145] G. S. N. Rao, O. F. Caltun, K. H. Rao, P. S. V. S. Rao, and B. P. Rao, *J. Magn. Magn. Mater*. **341**, 60 (2013).

[146] K. K. Mohaideen and P. A. Joy, *Curr. Appl. Phys*. **13**, 1697 (2013).

[147] G. Bulai, L. Diamandescu, I. Dumitru, S. Gurlui, M. Feder, O. F. Caltun, *J. Magn. Magn. Mater*. **390**, 123 (2015).

[148] G. Dascalu, T. Popescu, M. Feder, O. F. Caltun, *J. Magn. Magn. Mater*. **333**, 69 (2013).

[149] S. G. Kakade, R. C. Kambale, C. V. Ramanna and Y. D. Kolekar, *RSC Adv*. **6**, 33308 (2016).

[150] I. C. Nlebedim, N. Ranvah, Y. Melikhov, P. I. Williams, J. E. Snyder, A. J. Moses, and D. C. Jiles, *J. Appl. Phys*. **107**, 09A936 (2010).

[151] I. C. Nlebedim, Y. Melikhov, J. E. Snyder, N. Ranvah, A. J. Moses,1 and D. C. Jiles, *J. Appl. Phys*. **109**, 07A908 (2011).

[152] G. S. N. Rao, O. F. Caltun, K. H. Rao, B. P. Rao, A. Gupta, S. N. R. Rao and A. M. Kumar, *Hyperfine Interact*. **184**, 51 (2008).

[153] G. S. N. Rao, O. F. Caltun, K. H. Rao, B. P. Rao, H. L. Wamocha and H. H. Hamdeh, *Hyperfine Interact*. **184**, 179 (2008).

[154] N. Ranvah, I. C. Nlebedim, Y. Melikhov, J. E. Snyder, D. C. Jiles, A. J. Moses, P. I. Williams, F. Anayi, and S. H. Song, *IEEE Tran. Magn*. **44**, 3013 (2008).

[155] I. C. Nlebedim and D. C. Jiles, *Smart Mater. Struct*. **24**, 025006 (2015).

[156] V. R. Monaji and D. Das, *J. Alloys Compd*. **634**, 99 (2015).

[157] R. K. Ramchandra, R. A. Mandal, S. Dwevedi, G. Markandeyulu, *J. Alloys Compd*. **610**, 517 (2014).

Chapter 2

Experimental methods

and

Characterization techniques

2.1 Introduction

This chapter discusses details of the different synthesis methods used for the preparation of cobalt ferrite and its metal ions substituted compositions as well as the various experimental techniques used for the characterization of the materials. The experimental tools including thermogravimetric analysis (TGA) for determining the thermal decomposition temperature of the precursors, powder X-Ray diffraction (XRD) for structural characterization, transmission electron microscopy (TEM) for the morphological characterization of the nanoparticles, X-Ray photoelectron spectroscopy (XPS) for determination of the oxidation states of metal ions, scanning electron microscopy (SEM) for microstructural analysis, Raman spectroscopy (RS) for the cation distribution, vibrating sample magnetometer (VSM) for the magnetic characterization, density measurements and magnetostriction measurements using strain gauges are elaborated. The experimental details of different techniques employed for the materials characterization and measurements on the properties and performance parameters are discussed.

2.2 Methods of synthesis

The most commonly used synthesis methods for the preparation of ceramic oxides are the ceramic or solid state reaction method and the wet chemical methods such as autocombustion, sol-gel, coprecipitation, citrate/tartrate-gel, etc [1-4]. In the present study, solid state reaction, autocombustion, and citrate/tartrate-gel methods are used for preparing nanocrystalline as well as bulk cobalt ferrite and metal ions substituted cobalt ferrite powders.

2.2.1 Solid state reaction method

This method is also known as the ceramic method or high temperature reaction method and it is commonly used method for the preparation of polycrystalline powder samples [1-2]. Furthermore, the method is very simple and more appropriate when larger quantities of samples are required. The solid state reaction method involves heating the mixed constituent raw materials, mainly in the form of metal oxides, carbonates, nitrates, carboxylic acids, etc, at elevated temperatures with intermediate grindings. When metal carbonates or other corresponding metal salts are exploited as raw materials for the synthesis, a pre-calcination, particularly at lower temperatures, is recommended to mitigate the evolution of the various gaseous products in the final sintering stage. Due to the lack of reactivity between the two or more solids at room temperature, it is always indispensible to heat the raw materials to very

high temperatures, often 1000 to 1500 ^{o}C, in order accelerate the reactivity between the raw materials at an appropriate rate. This is because ions in the solids are firmly trapped on their lattice sites and difficult for them to jump out of their sites and migrate to adjacent sites at lower temperatures. However, at high temperatures, ions will have adequate thermal energy to leave their sites and diffuse through the crystals [5-6]. After an appropriate heat treatment of the mixed reactants, the nucleation will form at the interfaces of the raw materials due to the structural reorganization and that eventually grown in to a product layer with time. As the thickness of the product layer increases, the rate of the reaction decreases exponentially due to hindrance offered by the product layer for ions to diffuse through [6]. Therefore grinding is essential to break the product layer from the reactant interfaces and to expose new layer for further reaction to take place.

In the present study, cobalt ferrite ($CoFe_2O_4$) and metal ion substituted compositions $CoM_xFe_{2-x}O_4$ (M=Ga, In, Al, Mn) were prepared from high purity (> 99 %) Fe_2O_3, Co_3O_4, In_2O_3, Ga_2O_3, MnO_2, Al_2O_3 as starting raw materials. Stoichiometric amounts of these metal oxides, for a particular chemical composition, were weighed and mixed thoroughly using an agate mortar and pestle and acetone as the mixing medium. After thorough grinding, the ground dry powder mixture was transferred to alumina crucibles and calcined at 850 ^{o}C for 10 hours at heating and cooling rates of 5 ^{o}C per minute. After the calcination, the resultant powder was ground again for one hour and further calcined at series of elevated temperatures (1000, 1100 and 1200 ^{o}C) at the same heating and cooling rates, with intermediate grindings, until the desired phase is formed.

2.2.2 Glycine-nitrate autocombustion method

Autocombustion reaction is a low-temperature synthesis method that involves a self-sustained reaction in homogeneous solution of different oxidizers, usually metal nitrates, and fuels such as urea, glycine, hydrazides, citric acid, tartaric acid, etc [7,8]. The term autocombustion is used for the combustion synthesis because combustion reaction will be initiated automatically without any influence of any external sources. The reaction is highly exothermic in nature and liberates vast amount of gaseous products at the event of combustion process and nature of the reaction differs depending on the type of fuel used. The method is highly versatile and has been used for the preparation of wide verities of important metal oxides with interesting properties such as magnetic, optical, dielectric, catalytic, etc [9-12].

Among the amino acids, glycine (CH_2NH_2COOH) has been used extensively as a fuel in the combustion reaction due to its higher combustion efficiency [13,14]. Other amino acids are also used as fuels in the combustion reaction to prepare nanocrystalline ceramic materials [15]. Glycine will function in two different ways in the combustion reaction. Firstly, it is a bi-dentate ligand due to the presence of carboxylic (-COOH) and amino ($-NH_2$) groups and therefore both functional groups bind to the metal ions of different sizes through strong coordination bonds. In general, one mole of amino acid can bind to two moles of metal ions that improves the homogeneous mixing of metal ions in the solution. Secondly, it acts as the fuel during the combustion process. Flame temperature of the combustion reaction strongly depends on the amount of fuel used and also on the fuel to oxidant (or glycine: nitrate ratio) [14]. The flame temperature as high as ~1500 ^oC has been reported in the literature when using glycine as a fuel at a specific glycine to nitrate ratio, for the preparation of perovskite compound $La_{0.76}Sr_{0.24}CrO_3$[14]. Such a high flame temperature will be released at a short span of time that induces high crystallinity in the resultant powder and also the powder will be in the form of sintered state [16].

The complete combustion reaction of divalent (A) and trivalent (B) metal nitrates with glycine for the preparation of spinel compounds can be expressed by the following chemical equation:

$$9A(NO_3)_2 + 18B(NO_3)_3 + 40\ NH_2CH_2COOH \longrightarrow 9AB_2O_4 + 56N_2 + CO_2 + 100H_2O$$

(or)

$$A(NO_3)_2 + 2B(NO_3)_3 + 4.44\ NH_2CH_2COOH \longrightarrow AB_2O_4$$

In the above balanced chemical equation, 4.44 mole of glycine is required for a complete combustion to yield a mole of spinel compound or 1.48 mole of glycine is required per mole of metal ion for the same combustion reaction. In terms of glycine to nitrate ratio, G/N=4.44/(2+3×2)=0.555 is required for the complete combustion. By varying the glycine to nitrate ratio, it is possible to tune the crystallite size of the prepared ferrite powders, as reported [17]. Higher the G/N ratio higher will be the crystallite size of the powder due to increased in the flame temperature.

The main advantages of the glycine-nitrate method are:

- Simple and single step method and also short time required to prepare the samples.
- The method is highly versatile and applicable even for larger scale sample preparation.
- Crystallite size can be tuned depending upon fuel/nitrate ratio and further calcination process can be avoided.
- High purity and homogeneity in the particle size distribution can be obtained.
- High surface area and porous powders can be obtained due to evolution of large volume of gases at the verge of the combustion process.
- The method is applicable for the preparation of almost all metal oxide systems.

In the present work, the glycine-nitrate process, as reported in the literature [18], has been exploited to prepare nanocrystalline powders of various metal substituted cobalt ferrite compositions. Stochiometric amounts of metal nitrates were weighed in to a crystallizing dish and dissolved them in a minimum amount of water. Calculated amount of glycine, corresponding to number of moles per mole of metal ion, was also dissolved separately in minimum amount of water and sonicated for few minutes. Later, the glycine solution was added to the mixed solution of the metal nitrates followed by sonication to achieve better homogeneity of the solution. Then the resultant solution was placed on a pre-heated hot plate of temperature of about 200 ^{o}C. After complete evaporation of water molecules, the resulting viscous liquid ignited automatically giving rise to a fluffy mass of the metal oxide.

2.2.3 Citrate- and tartrate-gel methods

The citrate-gel method is a kind of sol-gel method for the synthesis of nanocrystalline ceramic materials using citric acid as the complexing agent and simple metal salts [19,20]. The method is applicable for the synthesis of a wide range of mixed metal oxides including highly complex crystalline materials at relatively low temperatures. It involves metal salts in the form of carbonates, nitrates, alkoxides, etc., which are complexed in an aqueous solution using the complexing or chelating agent. When the resultant metal complex solution is heated with a polymerizing agent like polyhydroxy alcohol, polyestarifiaction occurs. In the polymer complex matrix, the metal ions are homogeneously distributed. A thick polymer resin resulted after the evaporation of the excess solvent molecules and the resin is then heat treated to decompose the organic moieties [20]. Depending on the controlled calcination of

the gel or resin, it is possible to tune the crystalline size of the material. The citrate-gel method has the advantage of better control over homogeneity of the crystallite size and also stoichiometry of the material [21]. Recently, sol-gel auto-combustion method has drawn much attention among the researchers to synthesize metal oxides including spinel ferrites [22-26]. In this method, metal nitrates are mainly used because the nitrate ion serves as the oxidizer and the organic complex as the reductant. The procedure is almost similar to the citrate-gel method but in the case of sol-gel auto-combustion the gel is allowed to undergo self-combustion on a hot plate.

In the present work, different compositions in $CoM_xFe_{2-x}O_4$ (M = Al, Ga In) are synthesized using the citrate-gel method following the procedure reported in the literature [16]. Other compositions in $CoM_xFe_{2-x}O_4$ (M= Mg, Zn, Ga, Al, Mn) were prepared by the tartrate-gel method [27]. The corresponding metal nitrates, taken in the appropriate molar ratio, were dissolved separately in minimum amount of distilled water and sonicated for 10 minutes. A calculated amount of the chelating agent (citric acid or tartaric acid, 1.5 moles per mole of metal ion) was dissolved in minimum amount of water in a 1000 ml crystallizing dish and stirred constantly on a magnetic stirrer at 50 ^oC for 30 minutes. Later, the resultant metal nitrates solution was added drop wise to the solution of citric/tartaric acid. The stirring was continued for another 2 hours at the same temperature to obtain a homogeneous sol. Later, a known amount of the polymerizing agent, ethylene glycol, (chelating agent: ethylene glycol= 70:30) was added to the sol followed by increase in the temperature of the reaction to 75 ^oC under the same stirring condition. After the evaporation of solvent molecules, a brown thick viscous metal polymer gel was obtained and the resultant gel was dried at 80 ^oC for 20 hours in an oven. The dried gel was calcined at a particular temperature depending up on the decomposition temperature known from the thermo gravimetric analysis.

2.3 Compaction and sintering

Compaction is a process by which the synthesized powder samples obtained by the various synthesis procedures are moulded in to a desired shape and size using a suitable moulding apparatus under the application of pressure. At the time of applying the pressure, the volume of the powder specimen will be reduced due to the rearrangement of the powder particles in to close packing under the extreme conditions. It is hard to make solid compacts from the dried particulate powder samples due to lack of firm connectivity between the particles even at elevated applied pressure. The main condition of the compaction is that the

moulded specimen must have sufficient strength to withstand ejection from the mould tools after releasing the applied pressure and also able to withstand the sintering conditions without leading to cracks or breakage [28]. In order to have better particulate compacts, it is always recommended to wet the powder samples with a small amount of low concentration of a polymer solution. Applied pressure during the compaction defines the density of the compacts and in most cases the amount of binder and the applied pressure are crucial factors. Various methods of compactions are available such as pressure-less shaping technique, isostatic and uniaxial pressings such as cold pressure shaping technique and hot pressure shaping technique, according to the strength of properties required.

Sintering is an important processing condition extensively used in the field of powder metallurgy for the purpose of densification of materials. Sintering is a heat-treatment supplied to the powders (nano/bulk) or powders in the form of compacts in order to enhance it strength by aggregating the particles together. The temperature used for sintering must be lower than the melting point of the major constituent of the specimen [29]. Since it is a processing step mainly used to produce material with controlled microstructure and also involves material transport, i.e., mass diffusion leading to reduction in the porosity and increase in the mechanical strength and density of the compacts. During the sintering process, the rate of crystal growth will be higher and it is proportional to the sintering temperature. Moreover, free energy of the system also reduces subsequently due to contribution from the densification and coarsening mechanisms [29,30]. Sintering usually causes many changes in the properties of the ceramics, metals and composites materials [29]. In the case of polycrystalline ceramic materials, the microstructural parameters such as grain size, grain boundaries, porosity, density and grain orientation are known to be controlled by the sintering parameters such as temperature, time, heating and cooling rates and sintering atmosphere. Therefore by optimizing the sintering processing conditions, it is possible to develop a material with better properties for various applications. Various sintering processes are reported in the literature including liquid phase sintering, spark plasma sintering, microwave sintering and single stage and two stage sintering process [31-33]. Recently, spark plasma sintering technique received more attention from the materials research community due to the various advantages associated with the technique such as fast heating and cooling rates, better control over the microstructures, etc [34,35].

In the present work, cold uniaxial pressing technique was used to make green compacts. The synthesized powder samples were lubricated with 2% solution of polyvinyl alcohol as a

binder and moulded in to a cylindrical shape of dimension 8 mm diameter × 12 mm length under a pressure of 8 MPa, using a steel die. The pressed green compacts were sintered using a high-temperature programmable furnace (Nabertherm, Germany). Sintering was carried out in air at various conditions, and therefore the details about the sintering parameters are given in the respective chapters.

2.4 Characterization techniques

2.4.1 Thermogravimetric analysis (TGA)

In this technique, mass of a substance is precisely monitored while it is heated. The technique helps to probe both physical and chemical properties of wide varieties of materials including ceramics, polymers, biomaterials, organic compounds, composites, petrochemicals, and etc [36]. TGA is widely exploited to examine particular characteristics of materials that exhibit either weight loss or gain accompanied by phase transition, decomposition, oxidation, reduction or loss of volatiles such as gas and solvent molecules. A TGA curve is a plot of change in weight of a substance as a function of temperature and the curve is characterized by the presence of horizontal and vertical lines with respect to the temperature axis, where the horizontal line corresponds to no weight loss and the vertically curved line represents weight loss at a specific temperature range. The TGA experiment can be performed under various atmospheric environments like vacuum, air, inert, reducing, and etc to fetch more information pertaining to the stability and reactivity of the materials in those atmospheres and conditions [36]. A TGA instrument consists of a sample pan that is supported by a precision balance and the pan is located inside a programmable furnace and is heated or cooled while performing the experiment. The furnace is also supported by inlet and outlet channels to purge a gas or to create a vacuum during the experiment. The sample quantity required for the TGA analysis will be around 10 to 20 mg. The corresponding weight change of a specimen at a particular temperature is recorded by a computer.

In the present investigation, the decomposition temperature of the dried metal polymer precursor gel prepared by the citrate-gel and tartrate-gel reaction methods was analyzed on a model SDTQ600 TG-DTA analyzer from room temperature to 800 ^{o}C with a heating rate of 10 ^{o}C per minute under air flow atmosphere.

2.4.2 X-Ray Diffraction (XRD)

X-Ray diffraction is one of the most widely used characterization techniques in the field of materials science [37,38]. Information such as phase purity and crystal structure of crystalline materials could be obtained from the technique using X-Rays as source. Each crystalline material has its own X-Ray diffraction pattern. Hence, an X-Ray diffraction pattern is a finger print of the crystalline materials.

It is well-documented in the literature that diffracted peaks in the XRD patterns develop extra broadening when the crystallite size is below a certain limit (<100 nm) [6,38]. Therefore, the crystallite size can be estimated by measuring the developed width of the peaks in the XRD patterns. In general, there will a contribution to the line broadening from the instrument as well due to various factors and that has to be subtracted from the measured line width. The average crystallite size is calculated from X-Ray line broadening using the Scherrer formula [38],

$$t = \frac{0.9\lambda}{\beta\cos\theta} \tag{2.1}$$

where λ is wavelength of X-Ray beam, β is full width at half maximum intensity of a peak, in radian, and is obtained from the Warren formula, $\beta = \sqrt{(\beta_{Obs})^2 - (\beta_{inst})^2}$, and θ is Bragg's angle. β_{obs} and β_{inst} are the observed and instrumental contribution to line width, respectively.

X-Ray diffraction patterns of the bulk and nanosized powders as well as the sintered samples in the present work were recorded on a PANalytical X'pert pro powder X-Ray diffractometer using Cu-K_α radiation with the wavelength 1.5405 and 1.5443 Å for $K_{\alpha1}$ and $K_{\alpha2}$ components, respectively. The K_β component was eliminated from the X-Ray source using a Ni β-filter. Since the $K_{\alpha2}$ component was not removed, both the components of the K_α lines are present in all the recorded XRD patterns. The current and voltage applied to the X-Ray tube to generate the above mentioned wavelength were 40 kV and 30 mA, respectively. Prior to the XRD experiment, the instrument was calibrated using polycrystalline Si sample, therefore internal standards are not used. The samples were scanned in the 2θ range 10-80 degrees. For the nanosized powder samples, the XRD patterns were recorded at a scanning rate of 2^o per minute whereas for the sintered samples, a slow scan rate 0.72^o per minute was used. To identify the phase purity of the powder samples, the simulated XRD pattern of cobalt ferrite was generated using the Powder Cell for Window

(PCW) software [39] using the space group, lattice parameter(s) and atomic positions, taken from the literature, as in puts. Rietveld refinement analysis was carried out on the slow scanned XRD patterns of the sintered samples to extract detailed structural information.

Rietveld refinement is a technique developed by Hugo Rietveld for the analysis of powder XRD patterns to fetch information on the crystal structure of the crystalline materials [40,41]. For the refinement analysis, well-defined XRD patterns are essential to get accurate information on the crystal structure of the interested compound. However, the technique is not recommended for the refinement of XRD patterns of nanosized powder samples, owing to the poor signal to noise ratio. The intensity, line width and position of the Bragg reflections can be used to obtain all information on the crystal structure because an XRD pattern is the product of the crystal symmetry, atomic positions and interplanar distances of the crystal structures. Rietveld method uses a least-squares approach to obtain a good fit between the observed and calculated XRD patterns. This is done by minimizing the residual S_y given by the equation [42],

$$S_y = \sum_i w_i[y_i(obs) - y_i(cal)]^2 \tag{2.2}$$

where S_y is the Rietveld residual, $y_i(obs)$ and $y_i(cal)$ are the observed and calculated intensities, respectively, at the end of i^{th} step; w_i is the weight factor to y_i.

Rietveld refinement process will adjust the refinable parameters until the residue is minimized. There are many residual factors from which a good fit between the observed and calculated patterns can be monitored during the course of the refinement. They are given by [42],

$$\text{R-weighted pattern, } R_{wp} = \sqrt{\frac{\sum w_i(y_i(obs)-y_i(cal))^2}{\sum w_i(y_i(obs))^2}} \tag{2.3}$$

$$\text{R-pattern, } R_p = \sqrt{\frac{\sum(y_i(obs)-y_i(cal)}{\sum y_i(obs)}} \tag{2.4}$$

$$\text{R} - \text{expected, } R_{exp} = \sqrt{\frac{N-P}{\sum w_i y_i(obs)^2}} \tag{2.5}$$

$$\chi^2 = \frac{R_{wp}}{R_{exp}} \tag{2.6}$$

where N and P are number of observations and refinable parameters, respectively. χ^2 is the goodness of the fit and it is one of the important parameters that indicates best fit. Rietveld refinement is treated as a good fit when the value of χ^2 is closer to 1 but not equal to one or less than one [42].

In the present study, Rietveld refinement analysis of the XRD patterns of the sintered compositions has been carried out using the software General Structure Analysis System (GSAS-EXPGUI) [43]. The raw XRD data, the crystallographic information file (CIF) of the standard pattern of single crystal cobalt ferrite with the ICDD #39131 and the instrumental file were used as inputs. In the first step, scale factor and the suitable background functions were refined until the intensity of the patterns are approximately matched, followed by zero-shift correction. In the second step, lattice parameters were refined. Peak profile and symmetry parameters were then refined using the pseudo-Voight function. During the refinement of profile parameters, the background functions were deactivated. Pseudo-Voight function is a mixture of Gaussian and Lorentzian profiles. In the final step, the atomic positions were refined. The refinement was continued until a good fit is obtained as monitored by the value of χ^2. In the case of the substituted cobalt ferrite samples, the site occupancy of the substituents was refined at different crystallographic sites such as tetrahedral and octahedral sites.

2.4.3 Transmission Electron Microscopy (TEM)

TEM is one of the electron microscopes widely used to examine the structure, morphology and particle sizes of the nanomaterials including ceramics, bio, polymer, metallurgical, and so on [44]. The fundamental principle of electron microscopes is much similar to that of optical microscope but use electron beam as a source to illuminate the sample instead of light. The technique comprises three vital components such as the illumination system, the objective lenses/stage and the imaging unit [6, 45]. The electron gun, which is a source of illumination, produces a stream of electrons under thermionic emission, which are again accelerated to condenser lenses by the application of an accelerating voltage in the range 100-1000 kV. Depending on the choice of the accelerating voltage, the wavelength of the electron beam could be tuned that will enhance the image resolution. The main purpose of the condenser lens, also known as electromagnetic lens in electron microscopes, is to focus the electron beam in to a desired spot on the sample. The objective lenses are the heart of the TEM, because they determine how the sample has to be illuminated

with the electron beam [45]. Since the technique uses high energy accelerating electron beam to illuminate the material, ultrahigh vacuum need to be maintained inside the columnar chamber to avoid the possible collision with the suspensions such as air molecules, dust particles. Images are recorded on a conventional film positioned either below or above the fluorescent screen or digital capture can be utilized using a CCD. The resolution of the TEM is about 0.2 nm, which is the typical separation between two atoms in a solid [45]. The imaging of the materials can be made in two different modes viz bright field (BF) and dark field (DF). In the case of BF mode, the diffraction beam from the specimen is blocked and the direct electron beam penetrated from the specimen is allowed passing through the objective aperture, as a result of which a larger contrast can be seen between the lighter and heavier atoms and also thick areas. For the DF mode, the direct beam is blocked by the aperture while the electron beam diffracted from the crystal planes of the specimen is allowed to pass through the objective aperture and collected on the detector. Information such as lattice defects, stacking faults, planar defects, etc, can be extracted from the dark field imaging mode [45]. High resolution TEM (HRTEM) is an advanced version of TEM that helps direct imaging of the atomic structure of the specimen.

In the present thesis work, the morphology and the particle size of the prepared nanosized powder samples were investigated on a model FEI, TEC-NAI G^2TF30 transmission electron microscopy, operating the at the voltage of 200 kV. A small amount of material under investigation was dispersed in a low boiling solvent such as isopropyl alcohol (Boiling Point 82.6 ^oC) followed by sonication for more than 20 minutes to achieve a homogeneous dispersion of the nanoparticles in the solvent matrix. A drop of the same was placed on a specially designed carbon coated TEM grid using a micropipette. Later, the prepared sample was covered with a watch glass and left for more than 20 hours in the ambient atmosphere to evaporate the solvent molecules from the grid matrix and the images were captured on the thoroughly dried samples.

2.4.4 Scanning Electron Microscopy (SEM)

Similar to TEM, the electron gun, condensing lenses, apertures, scanning system and specimen chamber are the major components of SEM. The working principle of each component is almost similar to that of TEM. Unlike TEM, SEM generally operates at lower accelerating voltage (100 eV to 50 kV). The SEM instrument is highly applicable to extract detailed information on the topography, morphology, chemical composition, and

microstructural information of the materials made up of smaller sized particles as well as the bulk [45]. During the SEM experiment, number of signals such as secondary electrons, backscattered electrons, X-Rays, etc, will be generated when high energy electron beam impinges on the surface of a sample [46]. Among the many signals, the secondary and backscattered electrons are utilized for the visual inspection of a sample surface [45, 46]. Secondary electrons are less energetic (50 eV) and are produced due to the inelastic collision and scattering of incident electrons with the electrons of the specimen. The secondary electrons originate within few nanometers from the surface of the sample and are very sensitive to the surface structure and therefore they have been used to get topographic information with a resolution of ~10 nm or better [45]. Highly energetic backscattered electrons are generated due to elastic collision and scattering between the incident electrons and the specimen nuclei or electrons. Backscattered electrons generally originate from much deeper surface of the specimen (few μm) and help to resolve topographical contrast and atomic number contrast with a resolution of >1 micron. The generated X-Ray signal, due to the recombination of electrons and holes, allows determination of the elemental composition of the sample via EDAX (Energy Dispersive Analysis by X-Rays) [46]. The samples to be investigated by SEM must be conductive that prevent charge accumulation on the surface of the samples. If the sample is non-conducting, then the sample has to be coated with carbon or a thin layer of high conducting materials like gold or platinum [46, 47].

In the present work, the SEM images are captured on the fractured inner surfaces of sintered pellets using the instrument FEI, ESEM Quanta 200-3D, operating at the voltage ~30 kV.

2.4.5 Vibrating Sample magnetometer (VSM)

Vibrating sample magnetometer is a very versatile and sensitive technique used for the characterization of magnetic substances [48]. The technique allows precise magnetization measurements to be made as a function of magnetic field, temperature and different crystallographic orientations. VSM works based on Faraday's law which state that an electromagnetic force (emf) will be generated in a coil when there is a change in a magnetic flux linked with the coil [49]. A vibrating sample magnetometer measures the magnetic moment of a sample when it is vibrated perpendicular to uniform magnetic lines of force [48-50]. If the sample is vibrating periodically, it can induce an electrical signal in a pickup coil. The signal intensity is proportional to the magnetic moment produced in the sample,

amplitude of the vibration and the frequency. Amplitude of the vibration may vary depending on the mass of the sample and its interaction with the magnetic field. Therefore, a small permanent magnetic is attached to the sample rod, outside the magnetic field region, with a second set of sensing pickup coils. The portion of the signal from these coils is balanced against the unknown sample through null method [49,50]. Today's vibrating sample magnetometers are able to detect magnetic moments down to 10^{-5} to 10^{-6} emu range, which corresponds to the magnetic moment of approximately 10^{-9} g of iron [50]. In the VSM, the sample is filled in a vertical nonmagnetic tube and is fitted to a rod. This rod is then vibrated between the poles of a powerful electromagnet. The upper part of the rod is connected to a loudspeaker drive or any mechanical vibrator. The sample is vibrated exactly at the centre of the pickup coils. The rod is vibrated at frequency ~80 to 86 Hz. The change in flux is recorded by the pickup coils and is used for calculation of the magnetic moment of the sample.

Magnetic measurements in the present work were made on an EG&G PAR 4500 vibrating sample magnetometer as well as on a Quantum design SQUID-VSM. Prior to the measurement, the VSM was calibrated using a standard Ni sample. The sample holder used was made up of a nonmagnetic polymer material, Kel-F (poly-chlorotrifluoro-ethylene). Field dependent magnetization measurements were performed up to a maximum field of 1200 kA/m at ambient temperature, using the simple VSM. For high temperature measurements, an electrically heated oven was attached to the VSM to heat the sample from room temperature to 700 ^{o}C. The magnetization was measured by heating the sample at a heating rate of 2 ^{o}C per minute, in the presence of a constant low magnetic field 100 Oe (~8 kA/m). Initial magnetization curves of the sintered samples were measured at room temperature up to maximum field 2400 kA/m (3 T) using the SQUID-VSM.

Calculation of the magnetocrystalline anisotropy from the magnetization data

First order magnetocrystalline anisotropy coefficient (K_1) of polycrystalline cobalt ferrite and its metal ions substituted counterparts is calculated from the magnetization data using law of approach to saturation method [51]. According to the law of approach to saturation, magnetization at high fields ($H \gg H_c$) is described by,

$$M = M_s\left[1 - \frac{8}{105}\frac{K_1^2}{\mu_o^2 H^2}\right] + kH \tag{2.7}$$

where M is the magnetization in kA/m, M_s is the saturation magnetization in kA/m, H is the applied magnetic field in kA/m, K_1 is the first order cubic magnetocrystalline anisotropy coefficient in J/m^3, μ_o is the permeability of free space (1.257×10^{-6} $mkg/s^2.A^2$) and kH is the forced magnetization coefficient that describes the linear increase in the spontaneous magnetization at high fields and at higher temperature regions. The constant 8/105 is specific to cubic anisotropy of randomly oriented polycrystalline materials. The forced magnetization term, kH, is taken as zero (k=0) at room temperature, since it is valid only at high temperatures and high fields. Therefore, M_s and K_1 are the only fitting parameters at room temperature. For fitting purpose, the above equation is further simplified as follows,

$$M = M_s\left[1 - \frac{b}{H^2}\right] \tag{2.8}$$

where the constant $b = \frac{8K_1^2}{105\mu_o^2 M_s^2}$

The initial magnetization curve of sintered polycrystalline cobalt ferrite is fitted from 800 to 2400 kA/m, using the law of approach to saturation, as shown in Figure 2.1. The magnetocrystalline anisotropy constant, K_1, is calculated by substitution of value of 'b' obtained after fitting in the above equation.

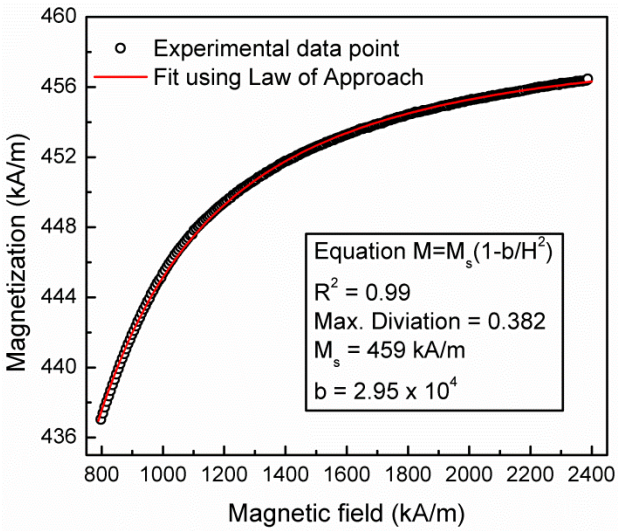

***Figure 2.1**: Initial magnetization curve of sintered polycrystalline cobalt ferrite fitted using the law of approach to saturation. The M-H curve is part of the present thesis work.*

2.3.6 Raman Spectroscopy

Raman spectroscopy is a non-destructive and one of the most widely used characterization tools to investigate the structural features of materials. In most of the cases, it has been used as a 'finger-print' technique to identify the phase formation and purity of the samples [52]. Being a vibrational spectroscopy method, it is highly applicable of extracting information on the local structural symmetry perturbation in materials [53]. When a sample under investigation is irradiated by an intense beam of laser, two distinguishable scattering phenomena will be observed namely the elastic and inelastic scattering effects [54]. Elastic scattering is also called as Rayleigh scattering where the frequency of the scattered photons is exactly the same as that of the frequency of the incident photons. In the inelastic scattering (Raman effect), the frequency of the scattered photons will be either lower or higher than the frequency of the incident photons. The probability of inelastic scattered photon will be one in a million because most of the scattered photons are Rayleigh photons [54,55]. For crystalline materials, the incident photons are likely to be scattered from the phonon i.e., lattice vibration, that will alter the associated energy of the phonon. Energy of the inelastic scattered photon strongly depends on the energy of a vibrational level or phonon level of a system [55]. For example, energy of the scattered photons will be lower than the incident photons when the phonon is created at higher energy level, whereas when the phonon is annihilated, then the energy of the scattered photons is relatively higher than that of the incident photons.

A Raman spectrum is often plotted as intensity of the scattered photons as a function of wavenumber. Wavenumber (cm^{-1}) is number of waves present in one centimetre and it can be calculated by knowing the wave length or frequency of the radiation [54].

$$\text{Wavenumber} = \frac{1}{\lambda} = \frac{\nu}{c}\ (\text{cm}^{-1}) \tag{2.9}$$

Where λ and ν are the wavelength and frequency of the photon, respectively, and c is the speed of light. But in some cases, Raman spectra are expressed as intensity of the scattered photons vs Raman shift ($\bar{\upsilon}$) as [54],

$$\text{Raman shift } (\bar{\upsilon}) = \frac{\Delta\nu}{c} = \frac{\nu_o - \nu_s}{c}\ (\text{cm}^{-1}) \tag{2.10}$$

where ν_o and ν_s are the frequencies of the incident and scattered photons, respectively.

Raman shift is the numerical difference between the wavenumber of Rayleigh-scattered photon and Raman-scattered photon. Unlike other spectroscopic techniques, Raman spectroscopy is instantaneous and prolonged sample preparation is not required to record the Raman spectra of the samples. This technique is extensively used for the analysis of spinel ferrite systems and also as a complimentary tool to other techniques to investigate the cation distribution in the spinel structured systems [56-58].

Group theory analysis predicts the following 42 vibrational modes in the spinel structure, 3 acoustic modes and 39 optical modes.

$$A_{1g}(R)+ E_g(R)+T_{1g} + 3T_{2g}(R) + 2A_{2u} +2E_u+ 5T_{1u}\,(IR) +2T_{2u}$$

where the (R) and (IR) identify Raman-active and infrared-active vibrational components, respectively, The modes A_{1g}, $E_{g,u}$ and $T_{1g,\ 2g,\ 1u,2u,}$ are singly, doubly and triply degenerate, respectively. The three acoustic modes belong to the T_{1u} components. The irreducible representations that describe the normal modes of vibration associated with each atomic species in their Wyckoff positions in the spinel lattice are [52]:

$$8a\ [\text{tetrahedral}] : T_{1u}(IR) + T_{2g}\,(R)$$

$$16d\ [\text{Octahedral}] : A_{2u} + E_u + T_{2u} + 2T_{1u}\,(IR)$$

$$32e\ [\text{Oxygen}] : A_{1g}(R) + A_{2u} + E_u + E_g\,(R) + 2T_{2g}\,(R) + T_{1g} + T_{2u} + 2T_{1u}\,(IR)$$

Hence, in the Raman spectra of spinels, particularly normal spinel such as $ZnFe_2O_4$, $CdFe_2O_4$, etc., only five fundamental modes $A_{1g} + E_g + 3T_{2g}$ should be observed [55]. More than five active modes are reported for inverse and mixed spinels [55]. Appearance of extra modes in the case of inverse and mixed spinels is attributed to random distribution of the di- and trivalent cations in the tetrahedral and octahedral coordination sites of the spinel crystal structure [52,55,58]. The presence of an additional mode at a lower wave number usually observed as a shoulder to the peak due to the A_{1g} active mode in the cubic spinel-type ferrites, designated as $A_{1g}(2)$ mode, is a characteristic mode of inverse as well as mixed spinel compounds [52,55,57,58]. Raman spectrum of cobalt ferrite recoded using a 632.8 nm laser radiation is shown in Figure 2.2. The presence of seven active modes, designated as $A_{1g}(1)$, $A_{1g}(2)$, $E_g(1)$, $E_g(2)$,$T_{2g}(1)$, $T_{2g}(2)$ and $T_{2g}(3)$, indicating that cobalt ferrite is in the

form of inverse or mixed spinel. The peaks due to the $A_{1g}(1)$ mode at ~690 cm^{-1} and the $A_{1g}(2)$ mode at ~610 cm^{-1} correspond to symmetric breathing modes of the FeO_4 and CoO_4 tetrahedra, respectively, in which only oxygen atoms move [58-61]. The $T_{2g}(2)$ mode at ~470 cm^{-1} corresponds to motion of oxygen atoms bonded to Fe^{3+} in the octahedral sites (FeO_6) [57] whereas the $T_{2g}(3)$ mode at ~560 cm^{-1} corresponds to asymmetric bending motion of the oxygens coordinated to Fe^{3+} [52] or Co^{2+} [60] in the tetrahedral sites. E_g modes at 306 and 360 cm^{-1} are related to the symmetric bending motion of the oxygens within the AO_4 units [59]. A weak signal at ~210 cm^{-1}, designated as T_{2g} (1), is related to translational motion of the BO_6 units against the A-site cations [59]. The $A_{1g}(2)$ and $E_g(2)$ are the characteristic modes of inverse as well mixed spinel ferrites [52,58].

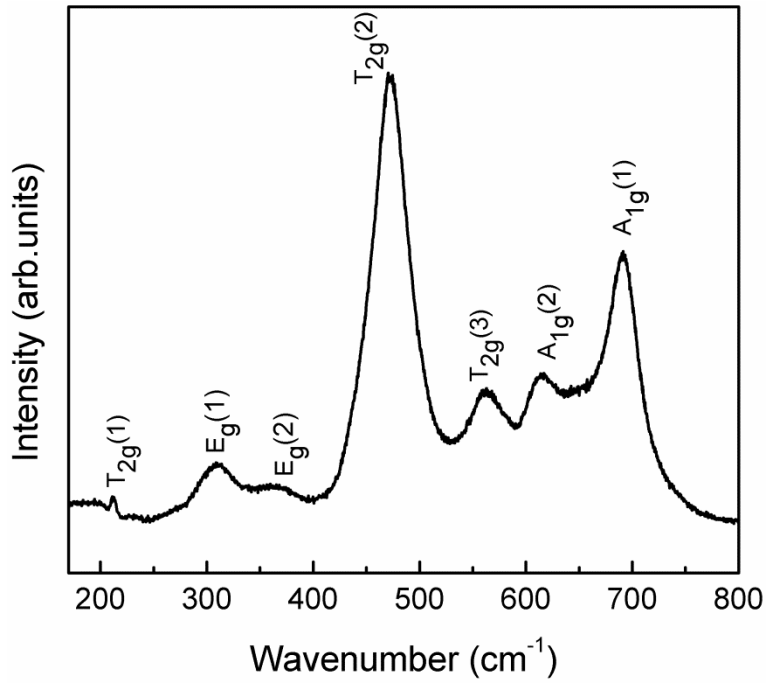

***Figure 2.2**: Raman spectrum of a cobalt ferrite sample, recorded at room temperature by exciting the sample using 632.8 nm radiation. The spectrum is part of the present thesis work.*

In the present work, Raman spectra of all the studied compositions were recorded, at room temperature, on the smooth surface of the sintered pellets using a micro-Raman spectrometer (Horiba JY Labraman HR 800) using 632.8 nm He-Ne laser radiation, with a power of 7 mW on the sample surface.

2.4.7 X-Ray Photoelectron Spectroscopy (XPS)

X-Ray photoelectron spectroscopy (XPS) is also known as ESCA (Electron Spectroscopy for Chemical Analysis) and is intensively used in the field of catalysis, ceramics, metallurgy, polymer materials, corrosion science, etc, to extract qualitative information on the chemical elements and their compositions, bonding and band structure, chemical shift and local structures, surface studies and also the oxidation states of the various metal ions [6, 62]. Since it is a surface-sensitive technique, more information can be obtained only from the surface (2-5 nm depth) of the specimen and not from the interior part [6]. The XPS instrument comprises of a sample chamber, primary X-Ray source and an electron energy analyzer; all the components work in a vacuum chamber which is usually operating in an ultra-high vacuum condition [62]. Soft monochromatic X-Ray radiation from an anodic element, either Al K_α (1486.6 eV) or MgK_α (1253.6 eV), is used as the primary source to illuminate the sample in XPS experiment [62]. When a sample is irradiated using the X-Ray source, an electron from the core shell is knocked out by the incident X-Ray photon of energy $h\gamma$. The energy, usually kinetic energy (KE) of the emitted photo electron, is analyzed by the electron spectrometer and presented as a graph of intensity as a function of binding energy in eV [60]. The KE of the emitted photoelectron depends on the energy of the X-Ray photon and therefore it is not an intrinsic material property. Rather the binding energy of the electron (BE) is the main parameter from which the parent element and the atomic energy level are probed. The relation between the parameters involved in the XPS experiments is [62],

$$\text{Wavenumber} = h\gamma - \text{KE} - \text{W} \tag{2.11}$$

where BE is the binding energy of the electron, $h\gamma$ is the energy of the incident X-ray photon, KE is the kinetic energy of the ejected electron from the specimen and W is the work function. The binding energy is a characteristic feature of the individual element from which one can quantitatively analyze the parent element present in the chemical compositions. Binding energy of an element strongly depends on its oxidation state and chemical environment in which the element is present [62]. The peaks in the XPS spectra are derived from the angular momentum quantum number, j [62]. Two peaks in the XPS spectra are mainly due to the interaction between the spin (s) and orbital (l) momenta. If the electron is ejected from the p-orbital, the corresponding j values are 3/2 and 1/2, whose intensity ratio will be 2:1 because number of degeneracy state (2j+1) is higher for the $np_{3/2}$ compared to $np_{1/2}$. Similarly, for the electron from the d-orbital, the j values are 5/2 and 3/2 and the

corresponding intensity ratio will be 3:2. Moreover, the main peaks in the XPS spectra are also accompanied with shake-up satellite peaks and are originated from the interaction of outgoing photoelectron with the valence electrons [62]. Such shake-up satellite peaks are observable mainly in the 2p spectra of d-band metals like Cu, Co, Fe, Ni, and etc.

In the present work, XPS analysis was carried out on a model VG Microtech multilab ESCA 3000 spectrometer equipped with an Mg K_α source. While performing the experiment, the sintered pellet of particular composition was ground to a fine powder using a mortar and pestle and the powder was made into semi-liquid slurry using a small amount of isopropyl alcohol. The resultant slurry was coated on the XPS sample holder and allowed to dry to remove the solvent molecules. The binding energy shift in the recorded XPS spectra was corrected using the standard binding energy of carbon (284.6 eV). The binding energy of the transition elements is compared with the XPS data base [63].

2.4.8 Density measurements

Density of the sintered compacts in cylindrical form was estimated from their weight and geometrical parameters such as diameter and length. The theoretical density of the sintered samples was calculated from the unit cell parameter obtained from the XRD analysis using the following formula [6],

$$\rho = \frac{ZM}{N_o a^3} \left(\frac{g}{cm^3}\right) \tag{2.12}$$

where 'ρ' is theoretical density, 'Z' is number of molecules present in a unit cell (Z=8, for cubic spinel ferrite systems), 'N_o' is the Avogadro's number (6.023×10^{23} molecules per mole), 'M' is the molecular weight (for cobalt ferrite = 234.63 g/mole), and 'a' is unit cell constant (for cobalt ferrite, a = 8.391 Å, [64]). By substituting all the values in the above equation, the theoretical density (ρ) of cobalt ferrite is obtained as 5.275 g/cm^3. The experimental density of the sintered compacts should be lesser than the theoretical value due to the associated porosity. The percentage sintered density is estimated as the ratio of the experimental density ($\rho_{Expt.}$) to the theoretical density ($\rho_{Theor.}$) multiplied 100.

$$\text{Percentage density} = \frac{\rho_{Expt.}}{\rho_{Theor.}} 100 \tag{2.13}$$

The theoretical density of the different metal ion substituted cobalt ferrite samples would vary depending on the sizes of the substituted ions.

2.4.9 Magnetostriction measurements

Magnetostriction (λ) is the change in dimension (size, length) of a magnetic material under the application of an external magnetic field. Magnetostriction is an important factor determining the domain structure, the magnetization process and the coercivity field of a magnetic material. In general, magnitude of the developed strain in the presence of a magnetic field is very small in the order of 10^{-6} or in ppm [50]. Therefore, accurate measurement of the magnetostriction strain is always indispensible. Various methods are available for the measurement of magnetostriction and continuous investigation in this field is still giving rise to new methods. Magnetostriction can be measured either by direct methods or indirect methods. The direct methods include the use of strain gauge, capacitance transducers, and interferometer whereas Beckner-Kersten method [65] and the small angle magnetization rotation (SAMR) [66] are indirect methods. Other techniques such as capacitance dilatometry and laser deflection are also available for the magnetostriction measurement [67-69].

Among all the methods, the most commonly used method for the magnetostriction measurement is by using a strain gauge. Strain gauge is a semiconductor device whose resistance varies nonlinearly with strain. The strain gauge method was developed by Goldman [70]. Briss et al have found that strain gauge can be successfully exploited for the magnetostriction measurement in the temperature range -196 to 400 ^{o}C [71]. A strain gauge comprises of a thin resistive metallic wire wounded to and fro on a polyamide film as shown in Figure 2.3. The reason for running the wire to and fro is to increase the length thereby enhancing the sensitivity without enlarging the gauge unit [72].

The change in the resistance of strain gauge is measured when a specimen is subjected to an applied magnetic field, and converted into the magnetostrictive strain by using the relation [71],

$$\frac{\Delta L}{L} = \frac{\Delta R/R}{G.F.} \tag{2.14}$$

where L is the initial length of the specimen, ΔL is the change in length in the presence of a magnetic field, R is the gauge resistance in the absence of a magnetic field, ΔR is the change in the gauge resistance at a known applied magnetic field strength and G. F. is the gauge factor. Usually the gauge factor is provided by the manufacturer. The strain gauges are

available commercially with nominal resistance values from 30 to 3000 Ω, with 120, 350 and 1000 Ω being the most common values. It is very important that the strain gauge is properly cemented on the test specimen so that the stain is accurately transferred from the test specimen.

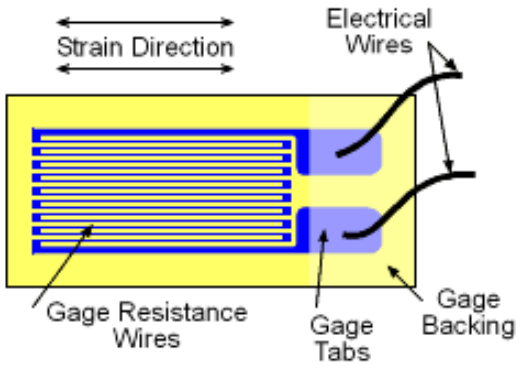

Figure 2.3*: Schematic diagram of a strain gauge.*

Figure 2.4: P*hotograph of a sintered cylindrical shaped pellet with strain gauge cemented on it, used for the magnetostriction measurements.*

In the present study, the magnetostriction measurement was carried out on cylindrical rod shaped specimen. A flat smooth surface is made along the length of the rod using fine emery paper and the smooth surface was cleaned with alkali solution to remove tiny ferrite grains from the surface. The strain gauges used in the present study were purchased from Vishay Micro-Measurements, USA (strain gauge type EK-09-062-AP, matrix size of 6.6 mm × 4.1 mm, gauge size 2.9 mm × 1.57 mm). The strain gauge was cemented on the smooth flat surface made on the specimen using a special binder solution (adhesive M-Bond 610,

supplied by the manufacturer of the strain gauge), as shown in the Figure 2.4. The calibration of the strain gauge was carried out by measuring the magnetostriction of Ni metal. The gauge resistance was measured by the four probe method of resistance measurements using a Keithley 2010 multimeter. The four probe method is one of the most widely used techniques for electrical resistance measurement.

Magnetostriction, $\lambda = \Delta L/L$, the relative change in the length of the sample in an applied magnetic field, was measured at room temperature using 350 Ω resistive strain gauges with a gauge factor 1.96. The magnetostriction measurements were carried out on both parallel and perpendicular directions to the applied magnetic field. A schematic representation of the direction of measurement of the parallel and perpendicular magnetostriction by the application of a magnetic field is shown in Figure 2.5. The parallel magnetostriction (λ_{par}) was measured by applying the field along the cylindrical axis whereas perpendicular magnetostriction (λ_{per}) was recorded by applying the field perpendicular to the cylindrical axis of the pellet. Correction for the shape contribution to magnetostriction is not performed in the present study.

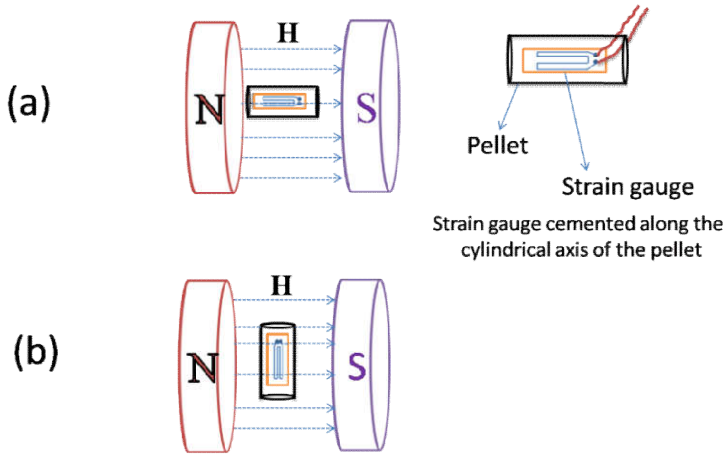

***Figure 2.5**: Schematic representation of the magnetostriction measurement using strain gauge cemented along the cylindrical axis of the pellet along (a) parallel and (b) perpendicular directions to the applied magnetic field.*

2.4.10 Magnetic field annealing

Magnetic field annealing is a process involving heating and cooling of the magnetic materials in a magnetic field. This process has been used effectively to enhance their magnetostriction parameters at lower magnetic fields. The annealing field induces an easy axis along its direction by altering the magnetic domain configurations of the material

because when the magnetic material is cooled from high temperature in the presence of a magnetic field the magnetic moments are frozen along the annealed direction and hence the artificially created easy magnetization axis. In the present work, the magnetic field annealing was carried at a temperature 300 ^{o}C for 30 minutes in the presence of a constant magnetic field. During the annealing process, the magnetic field was applied perpendicular to the cylindrical axis of the sintered pellet, as shown in Figure 2.6. After annealing the sample, the strain gauge was cemented on the smooth flat surface using the adhesive and the magnetostriction measurements were carried out. The parallel magnetostriction, λ_{par}, is measured by applying the field along the cylindrical axis of the pellet (perpendicular to the annealing direction) whereas perpendicular magnetostriction, λ_{per}, was measured by applying the field perpendicular to the cylindrical axis of the sintered pellet (parallel to the annealing direction). A schematic representation of the annealing direction and the λ_{par} and λ_{per} measurements are illustrated in Figure 2.6.

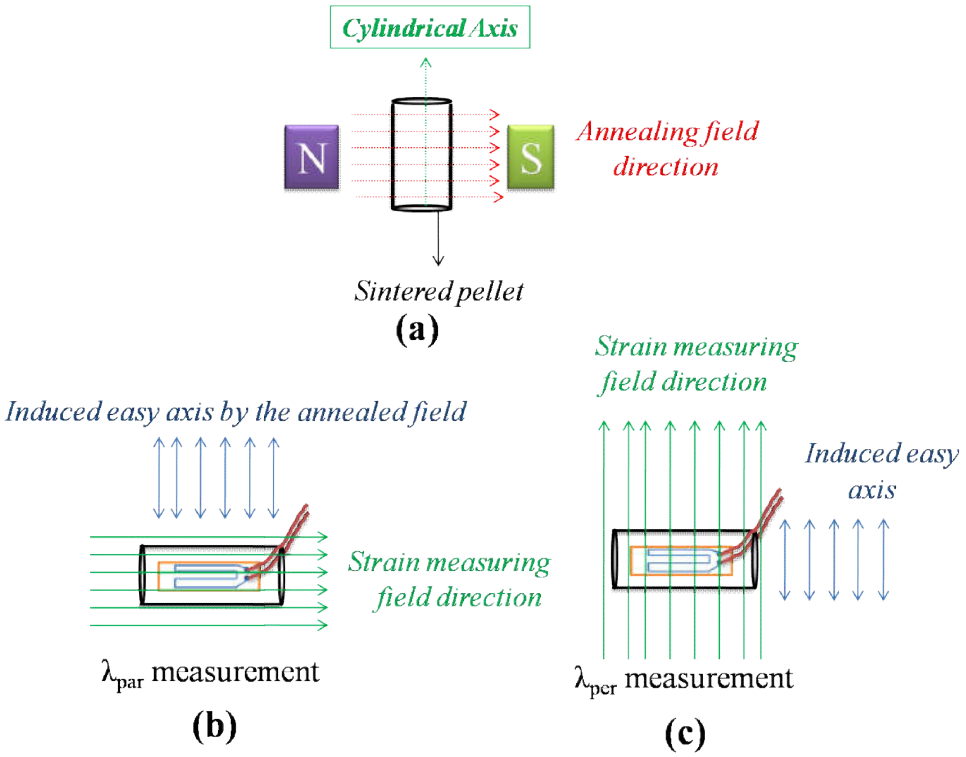

***Figure 2.6**: Schematic representation of (a) magnetic field annealing of the sintered pellet in which the annealing field is applied perpendicular to the cylindrical axis of the pellet, (b) parallel magnetostriction, λ_{par}, measurement in which measuring field is applied perpendicular to the field annealed direction, and (c) perpendicular magnetostriction, λ_{per}, measurement in which measuring field is applied along the field annealed direction.*

Bibliography

[1] O. Masala and R. Seshadri, *Annu. Rev. Mater. Res*. **34,** 41 (2004).

[2] J. M. Honig and C. N. R Rao, *Preparation and Characterization of Materials* (Academic Press, San Diego, 1981).

[3] D. Segal, *Chemical synthesis of Advanced Ceramic materials* (Cambridge University Press, New York, 1991).

[4] J. P. Jolivet, M. Henry and J. Livage, *Metal Oxide Chemistry and Synthesis: From solution to solid state* (Wiley, New York, 2000).

[5] V.V. Boldyrev, M. Bulens and B. Delmon, *The control of the reactivity of solids* (Elsevier-North-Holland, New York, 1979).

[6] A. R West, *Solid State Chemistry and Applications* (John Wiley & Sons, Singapore, 2003).

[7] J. J. Moore and H. J. Feng, *Prog. Mater. Sci*. **36,** 243 (1995).

[8] S. T. Aruna and A. S. Mukasyan, *Curr. Opin. Solid State Mater. Sci*. **12,** 44 (2008).

[9] C. C. Hwang, T. Y. Wu, J. Wan and J. S. Tsai, *Mater. Sci. Eng. B* **111,** 49 (2004).

[10] Y. Xijuan, X. Pingbo and S. Qingde, *Phys. Chem. Chem. Phys.* **3,** 5266 (2001).

[11] G. Zhu, X. Fang, C. Xia and X. Liu, *Ceram. Int*. **31,** 115 (2005).

[12] X. Guo, D. Mao, G. Lu, S. Wang and G. Wu, *J. Catal.* **271,** 178 (2010).

[13] T. Mokkelbost, I. Kaus, T. Grande and M. Einarsrud, *Mater. Chem*. **16,** 5489 (2004).

[14] L. A. Chick, L. R. Pederson, G. D. Maupin, J. L. Bates, L. E. Thomas and G. J. Exarhos, *Mater. Lett*. **6,** 10 (1990).

[15] N. Srinatha, V. D. Kumar, K. G. M. Nair, B. Angadi, *Adv. Powder Technol*. **26**, 1355 (2015).

[16] S. D. Bhame and P A Joy, *Sens. Actuators A* **137,** 256 (2007).

[17] K. K. Mohaideen and P. A. Joy, *J. Magn. Magn. Mater*. **346,** 96 (2013).

[18] K. K. Mohaideen and P. A. Joy, *Appl. Phys. Lett*. **101**, 072405 (2012).

[19] S. Kumar, K. S. Gandhi and R. Kumar, *Ind. Eng. Chem. Res*. **46**, 3128 (2007).

[20] A. Pathak and P. Pramanik, *Proc. Indian Nat. Sci. Acad*. **67**, 47 (2001).

[21] K. Devi, R. Choudhary, A. K. Satsangi, and R. K. Gupta, *Def. Sci. J*. **58**, 545 (2008).

[22] A. Sutka and G. Mezinskis, *Front. Mater. Sci*. **6**, 128 (2012).

[23] M. A. Gabal, A. M. Abdel-Daiem, Y. M. Al Angari, I. M. Ismail, *Polyhedron* **57**, 105 (2013).

[24] H. Bahiraei, M. Z. Shoushtari, K. Gheisari, C. K. Ong, *Mater. Lett*. **122,** 129 (2014).

[25] Z. Yue, J. Zhou, L. Li, H. Zhang, Z. Gui, *J. Magn. Magn. Mater*. **208**, 55 (2000).

[26] B. G. Toksha, S. E. Shirsath, S. M. Patange, K. M. Jadhav, *Solid State Commun*. **147**, 479 (2008).

[27] P. Thakuria and P. A. Joy, *Appl. Phys. Lett*. **97**, 162504 (2010).

[28] G. Y. Onada and L. L. Hench, *Ceramic Processing before Firing* (Plenum, New York, 1978).

[29] S. J. L. Kang, *Sintering: densification, grain growth and microstructure* (Butterworth-Heinemann, Oxford, 2005).

[30] P. Chen and I-Wei Chen, *J. Am. Ceram. Soc*. **80**, 637 (1997).

[31] N. Millot, S. Le Gallet, D. Aymes, F. Bernard, Y. Grin, *J. Eur. Ceram. Soc*. **27**, 921 (2007).

[32] S. G. Chavan, S. M. Mane, S. B. Kulkarni, M. E. Jayasingh, P. B. Joshi and D. J. Salunkhe, *J. Mater. Sci.: Mater. Electron* **27**, 7105 (2016).

[33] I.-Wei Chen & X.-H. Wang, *Nature* **404**, 168 (2000).

[34] S. Song, Q. Song, J. Li, V. R. Mudinepalli and Z. Zhang, *Cerm. Int*. **40**, 6473 (2014).

[35] Z. A. Munir, U. A. Tamburini, M. Ohyanagi, *J. Mater. Sci*. **41**, 763 (2006).

[36] P. Gobbott, *Principles and Applications of Thermal Analysis* (Blackwell, Oxford, 2008).

[37] H. P. Klug and L. E. Alexander, *X-Ray Diffraction Procedures* (Wiley, New York, 1954).

[38] B. D. Cullity and S. R. Stock, *Elements of X-Ray Diffraction* (Prentice Hall, New Jercy, 2001).

[39] W. Kraus and G. Nolze, Powder Cell for Window (PCW), version 2.4 (http://www.cc14.ac.uk)

[40] H. M. Rietveld, *Acta Crystallogr*. **22**, 151 (1967).

[41] H. M. Rietveld, *J. Appl. Crystallogr*. **2**, 65 (1969).

[42] L. B. McCusker, R. B. Von Dreele, D. E. Cox, D. LoueÈrd and P. Scardi, *J. Appl. Crystallogr*. **32**, 36 (1999).

[43] B. Toby, *J. Appl. Crystallogr*. **34**, 210 (2001).

[44] B. D. Williams and C. B. Carter, *Transmission Electron Microscopy: A Text Book for Materials Science* (Plenum Press, New York, 1996).

[45] R. F. Egerton, *Physical Principles of Electron Microscopy, An Introduction to TEM, SEM, and AEM*, (Springer, New York, 2008).

[46] M. T. Postek, K. S. Howard, A. H. Johnson and K. L. McMichael, *Scanning Electron*

Microscopy, A Student's Handbook, (Ladd Research Ind., Inc. Williston, VT., 1980).

[47] FEI. The Quanta 200 *User's Operation Manual 2nd ed.* (2004).

[48] S. Foner, *Rev. Sci. Instrum*. **30**, 548 (1959).

[49] K. H. J. Buschow and F. R. De Boer, *Physics of magnetism and magnetic Materials* (Kluber Academic, New York, 2003).

[50] B. D. Cullity and C. D. Graham, *Introduction to Magnetic Materials* (John Wiley & Sons, New Jersey, 2009).

[51] S. Chikazumi, *Physics of ferromagnetism, (2nd ed.* Oxford University Press, Oxford, 1997).

[52] V. D'Ippolito, G. B. Andreozzi, D. Bersanib, and P. P. Lottici, *J. Raman Spectrosc*. **46**, 1255 (2015).

[53] J. T. Kloprogge and R. L. Frost, *J. Solid State Chem*. **146**, 506 (1999).

[54] J. R. Ferraro and K. Nakamoto. *Introductory Raman Spectroscopy* (Academic press, San Diego, 1994).

[55] B. D. Hosterman, *Raman spectroscopic study of solid solution spinel oxides Ph. D. thesis* (University of Nevada, Los Vegas, 2011).

[56] S. W. da Silva, F. Nakagomi, M. S. Silva, A. Franco Jr, V. K. Garg, A. C. Oliveira, and P. C. Morais, *J. Nanopart. Res*. **14**, 798 (2012).

[57] K. B. Modi, P. Y. Raval, S. J. Shah, C. R. Kathad, S. V. Dulera, M. V. Popat, K. B. Zankat, K. G. Saija, T. K. Pathak, N. H. Vasoya, V. K. Lakhani, U. Chandra, and P. K. Jha, *Inorg. Chem*. **54**, 1543 (2015).

[58] P. Chandramohan, M. P. Srinivasan, S. Velmurugan, and S. V. Narasimha, *J. Solid State Chem*. **184**, 89 (2011).

[59] F. J. Manjon, I. Tiginyanu, and V. Ursaki, *Pressure-Induced Phase Transitions in AB_2X_4 Chalcogenide compounds* (Springer-Verlag, Berlin, Heidelberg, 2014).

[60] G. V. M. Jacintho, A. G. Brolo, P. Corio, P. A. Z. Suarez, and J. C. Rubim, *J. Phys. Chem. C* **113**, 7684 (2009).

[61] G. Shemer, E. Tirosh, T. Livnesh, and G. Markovich, *J. Phys. Chem. C* **111**, 14334 (2007).

[62] J. F. Watt**s** and J. Wolstenholme, *An Introduction to surface Analysis by XPD and AES* (John Wiley & Sons, Chichester, 2003).

[63] NIST X-Ray Photoelectron Spectroscopy Database, https://srdata.nist.gov/xps/

[64] Natl. Bur. Stand. (U.S), **25**, 22 (1971).

[65] R. Beckner and M. Kersten, *Z. Phys*. **64**, 660 (1930).

[66] K. Narita, J. Yamasaki and H. Fukunaga, *IEEE Trans. Magn*. **16**, 435 (1980).

[67] P. T. Squire and M. R. J. Gibbs, *J. Phys. E: Sci. Instrum.* **20**, 499 (2000).

[68] V. T. Cherepin, N. I. Glavatska, I. N. Glavatsky and V. G. Gavriljuk, *Meas. Sci. Technol*. **13**, 174 (2002).

[69] Q. Y. Yan, R. J. Gambino, S. Sampath and Q. Huang, *J. Appl. Phys.* **97**, 033902 (2005).

[70] J. E. Goldman, *Phys. Rev*. **72**, 529 (1947).

[71] R. R. Briss and E. W. Lee, *J. Sci. Instrum*. **37**, 225 (1960).

[72] M. Sullivan, *Rev. Sci. Instrum*. **51**, 382 (1980).

Chapter 3

Studies on divalent metal ion substituted cobalt ferrite, $CoM_xFe_{2-x}O_4$ (M=Mg, Zn)

3.1 Introduction

The effect of substitution of divalent non-magnetic metal ions (Zn and Mg) in place of Fe in $CoFe_2O_4$ on the structural, magnetic and magnetostrictive properties has been investigated. As described in Chapter 1, the magnetostriction in cobalt ferrite is primarily due to the contribution of the Co^{2+} located at the octahedral sites [1,2]. Cobalt is one of the 3d-transition elements and known for its variable oxidation states (Co^{2+}, Co^{3+}). In cobalt ferrite, the cobalt exists in the +2 oxidation state with high-spin electronic configuration [3,4]. Any attempt to change the oxidation state of Co^{2+} cobalt ferrite by chemical substitution will substantially affect the magnitude of the magnetostriction as well as the magnetic parameters [5,6]. Somaiah *et al*. have studied the magnetostrictive properties of $CoZn_xFe_{2-x}O_4$ synthesized by an autocombustion method and reported relatively high values of the strain sensitivity, $[d\lambda/dH]_{max}$, $[d\lambda/dH]_{max}$ for x=0.1 (-1.32×10^{-9} m/A) compared to that for x=0 (-0.71×10^{-9} m/A) with λ_{max}= -148 ppm for x=0.1 and -183 ppm for x=0 [7]. In another study by Nlebedim *et al* [8], a large drop in $[d\lambda/dH]_{max}$ has been reported for $CoMg_xFe_{2-x}O_4$, synthesized by a solid state reaction method. In both studies, a decrease in the value of λ_{max} is observed with increasing x. Although both Zn and Mg are non-magnetic and having nearly comparable sizes and are substituted in place of Fe, the discrepancies in the values of the magnetostriction parameters in the studied systems are most likely to be due to the different synthesis methods and processing conditions adopted to fabricate the samples. It has been reported that the magnetostriction parameters of $CoFe_2O_4$ depend on the synthesis and processing conditions [9-12].

Unlike Co and Fe which have multiple oxidation states, both Zn and Mg have stable +2 oxidation state. Thus, when they are substituted for trivalent Fe in $CoFe_2O_4$, it is expected that some of the metal ions from the parent compound has to be converted to higher oxidation state to maintain charge neutrality that may affect the magnetostriction properties. Zn^{2+} has a strong preference for the tetrahedral sites, whereas Mg^{2+} can occupy both the tetrahedral and octahedral sites, with larger amounts preferably at the octahedral sites in the spinel lattice. Therefore, a significant change in the magnetic and magnetostrictive parameters due to their different site preferences in the cobalt ferrite lattice is envisaged. To make a better comparison and correlation among the structural, magnetic and magnetostrictive parameters, it is always indispensable to prepare and process all the substituted compositions under identical conditions. Since the microstructure of the sintered compacts is one of the factors

affecting the magnetostriction [13-15], the Zn- and Mg-substituted cobalt ferrite compositions in the form of nanosized powders are prepared using a wet chemical method and sintered under identical conditions.

The objective of the present work is:

i) To investigate the role of divalent (Zn^{2+} and Mg^{2+}) ions in place of trivalent Fe on the magnetostriction properties.
ii) To investigate the role of different crystallographic site preferences of Zn and Mg ions in cobalt ferrite on the structural, magnetic and magnetostrictive properties.
iii) To investigate the role of change in the oxidation state of Co^{2+} on the magnetostrictive properties.

3.2 Materials synthesis

Different compositions of $CoMg_xFe_{2-x}O_4$ and $CoZn_xFe_{2-x}O_4$ ($0 \leq x \leq 0.2$) were synthesised by the tartrate-gel method [16]. $Co(NO_3)_2.6H_2O$, $Fe(NO_3)_3.9H_2O$ and $Mg(NO_3)_2.6H_2O$ purchased from Sigma-Aldrich and $Zn(NO_3)_2.6H_2O$ and tartaric acid from Merck chemicals were used for the synthesis without any further purification. Initially, stoichiometric amounts of the metal nitrates were dissolved in 75 ml of distilled water in a 100 ml crystallizing dish and sonicated for 15 minutes to achieve a homogeneous mixture. A calculated amount of tartaric acid (1.5 moles per mole of metal ion) was dissolved in another dish using 75 ml of distilled water followed by 10 minutes of sonication. The tartaric acid solution was stirred continuously on a magnetic stirrer at 50 ^oC for 30 minutes, and the homogeneous metal nitrate solution was addeddropwise to the tartaric acid solution at the same temperature, and continuously stirred for another two hours to obtain a sol. A specific volume of ethylene glycol (tartaric acid: ethylene glycol = 70:30) was added to the reaction mixture, and the temperature was increased to 70 ^oC to obtain a viscous gel. The resultant gel was dried in an oven at 80 ^oC for 24 hours, and during the process of drying, the gel was broken into a porous fluffy mass. The dried gel was pulverized into a fine powder using an agate mortar and pestle, and thermo-gravimetric analysis (TGA) was carried out to ascertain the decompositions temperature.

Thermogravimetric analysis of the dried precursor powder was carried out in an air flow atmosphere from room temperature to 800 ^oC at a heating rate of 10 ^oC per minute, and the TGA curve of the precursor for cobalt ferrite is shown in Figure 3.1. Major weight loss is

observed in the temperature range 200–350 °C. A small weight loss (8%) at ~90 °C is likely to be due to loss of adsorbed water from the metal-polymer network. The decomposition of the precursor starts at temperature ~200 °C and is almost completed at 340 °C, and no significant weight loss is observed at higher temperatures indicating the formation of stable metal oxide. Based on the TGA studies, all the dried precursors of the CMF and CZF series of compositions are calcined at 400 °C for 2 hours.

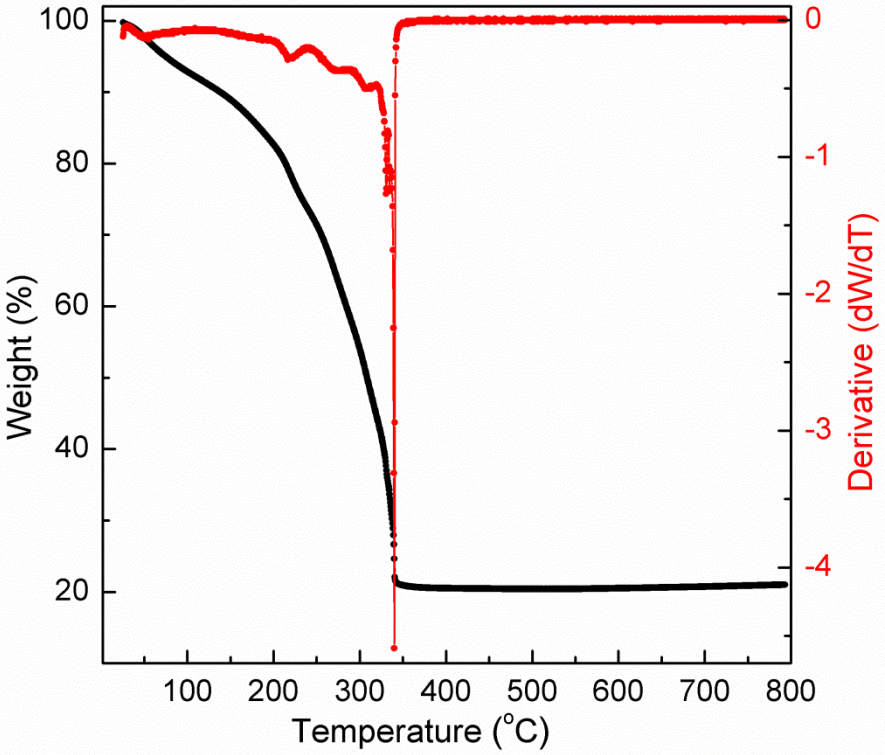

Figure 3.1*: TGA curve of the dried precursor for the system of unsubstituted cobalt ferrite.*

The calcined powders were mixed with 2% polyvinyl alcohol and pressed uniaxially in the form of cylindrical rods (8 mm diameter × 12 mm length) at a pressure of 8 MPa. The pressed green compacts were sintered at 1450 °C for 10 minutes, with heating and cooling rates of 5 °C per min and 20 °C per min, respectively. The density of the sintered compacts was calculated from their measured volume and weight. The percentage sintered density was obtained from the ratio of the experimental density to the theoretical density calculated from the lattice parameter. The sample codes of different compositions of two series are given in Table 3.1.

***Table 3.1**: Different divalent ion substituted compositions and the corresponding sample codes*

x	$CoMg_xFe_{2-x}O_4$ (CMF series)	$CoZn_xFe_{2-x}O_4$ (CZF series)
0	CF	CF
0.025	CMF025	CZF025
0.05	CMF05	CZF05
0.10	CMF10	CZF10
0.15	CMF15	CZF15
0.20	CMF20	CZF20

3.3 Characterization of the calcined powders

3.3.1 Powder X-ray diffraction

The XRD patterns of the calcined powder samples of the CMF and CZF series are shown in Figures 3.2. The simulated pattern of $CoFe_2O_4$ is shown in the figures for comparison. All the reflections in the observed patterns are in agreement with the simulated pattern of cobalt ferrite, generated using the PCW software, indicating the formation of corresponding single-phase cubic spinel ferrite compositions, without any secondary phases. The peaks in the experimental XRD patterns are symmetrically broad signifying nanocrystalline nature of the ferrite particles. Also, the widths of the peaks are found to increase with increasing the degree of substitution in both series revealing a reduction in the crystalline size. The average crystallite size, as estimated from the Scherrer formula, is found to be decreased from ~20 nm for x=0 to ~10-12 nm for x=0.2, in both the series. Such changes in the crystallite size with the degree of substitution for various metal substituted spinel ferrite compositions are reported in the literature [17-19].

Eventhough all samples are synthesized and calcined under identical conditions in the present work, the reduction in the crystallite size with the degree of substitution might be attributed to the lattice strain induced in the crystal structure by the large size mismatch of Zn^{2+}, $Mg^{2+,}$ and Fe^{3+} ions. The ionic radii of Zn^{2+} (0.60 Å for 4-fold coordination) and Mg^{2+} (0.57 Å for 4-fold and 0.72 Å for 6-fold coordination) are larger than that of Fe^{3+} (0.49 Å for 4-fold and 0.645 Å for 6-fold coordination) [20]. When larger sized Zn^{2+} and Mg^{2+} ions

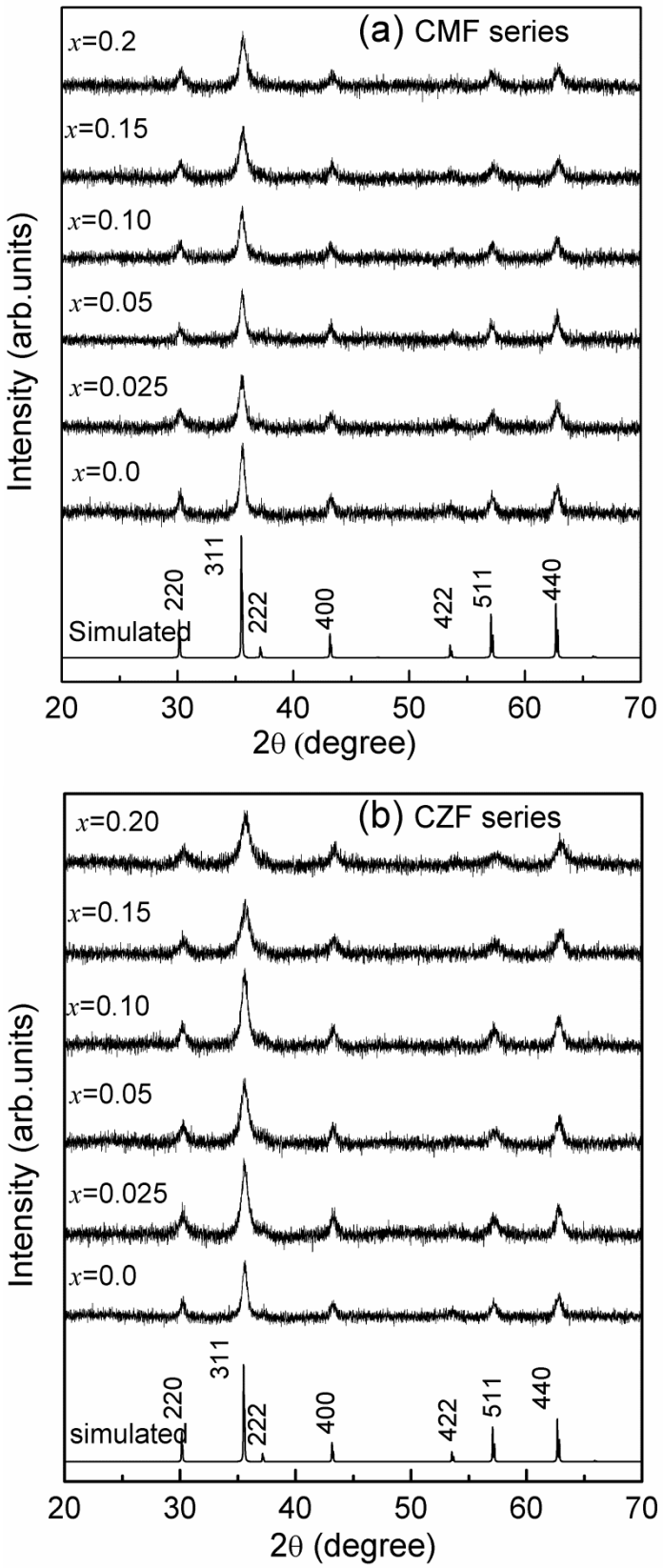

***Figure 3.2**: Powder XRD patterns of calcined powders of (a) CMF and (b) CZF series of compositions. The indexed simulated pattern of cobalt ferrite is shown for comparison.*

are substituted in place of Fe^{3+}, they might induce a crystalline anisotropy and this crystalline anisotropy increases with the degree of substitution. In addition to this, with increasing Mg^{2+} and Zn^{2+} concentration, volume strain inside the material will also increase. Therefore, for a system to remain in a stable equilibrium state, crystal anisotropy and volume strain should balance to each other. To relax the volume strain, the crystallite size decreases with increasing degree of substitution, as reported in the literature [19].

3.3.2 Transmission Electron Microscopy

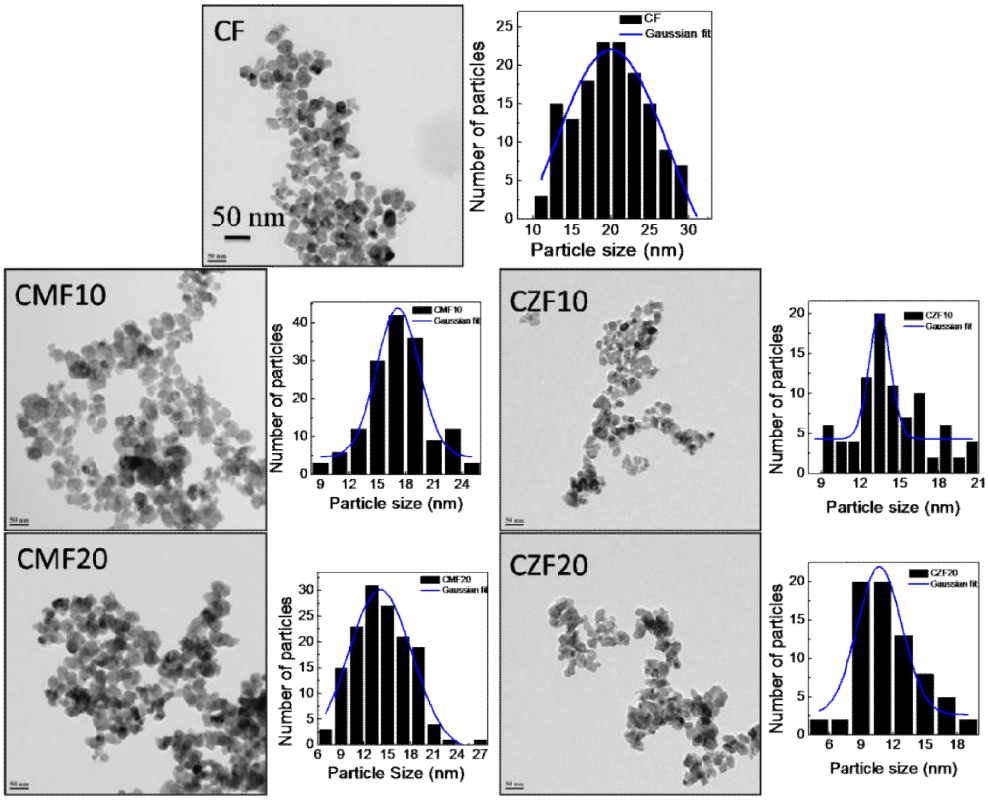

***Figure 3.3**: TEM images (left) and the corresponding particles size distribution histograms (right) of selected calcined compositions of the CMF and CZF series.*

TEM images of the selected compositions of the calcined powders of the two series and the corresponding particle size distribution histograms are shown in Figure 3.3. The TEM images reveal the spherical morphology of the particles. The ferrite nanoparticles are not much agglomerated, and the particle sizes are found to be ranging from 10 to 25 nm. The substituted compositions show the relatively large number of smaller particles than the unsubstituted composition. The average particle size obtained from the TEM images are nearly comparable to the average crystallite size calculated from the X-ray diffraction patterns.

3.4 Characterization of sintered samples

3.4.1 Structure

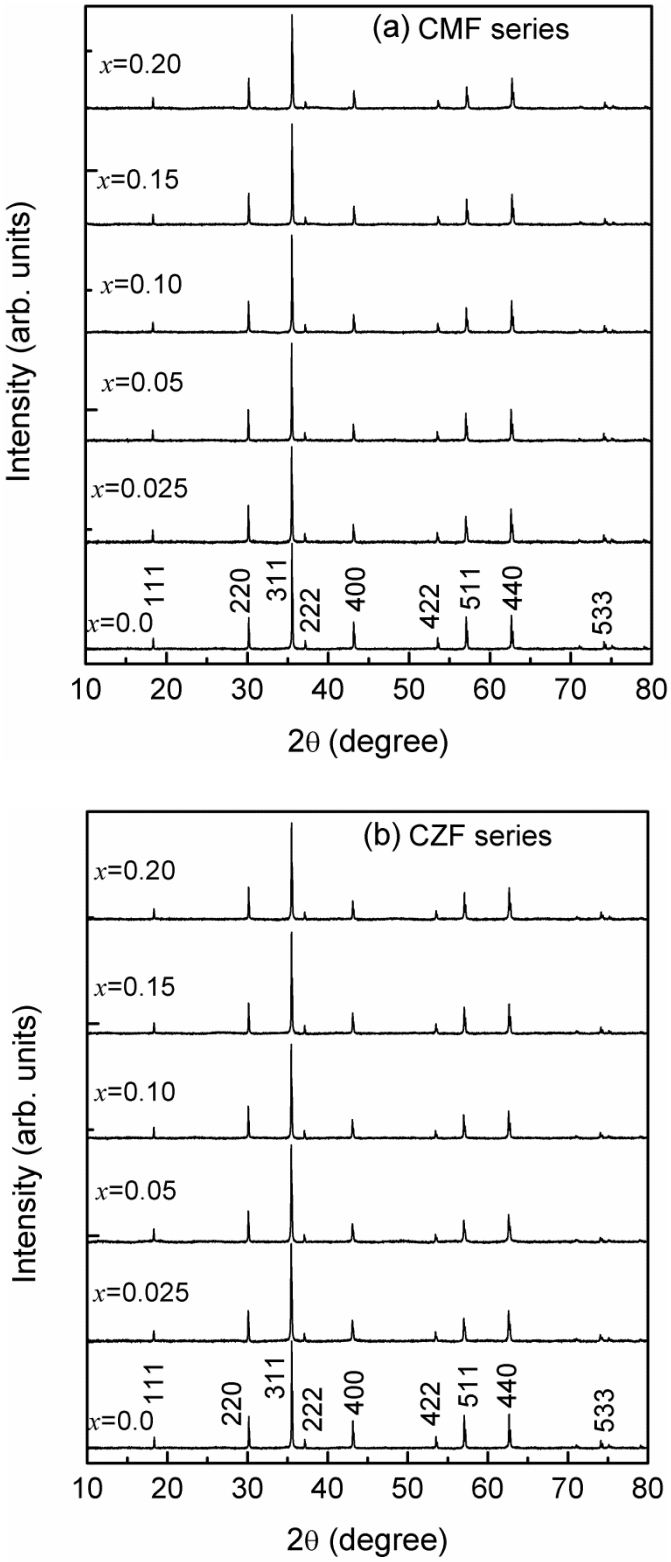

***Figure 3.4**: Powder XRD patterns of sintered (a) CMF series and (b) CZF series.*

The XRD patterns of the sintered compositions of the two series are shown in Figure 3.4. Unlike the broad peaks in the XRD patterns of the calcined powders, the sintered samples exhibit well defined sharp and intense peaks indicating a high degree of crystallinity. To probe the phase purity and to obtain the cubic lattice parameter of the sintered compositions, Rietveld refinement analysis of the XRD patterns has been carried out. The results of the refinement of the unsubstituted and the substituted compositions are presented in Figures 3.5 and 3.6, respectively. In each graph, the experimental pattern, the calculated pattern, the difference between the experimental and the calculated patterns and the peak positions are shown. A good fit is obtained for all the studied compositions, as confirmed by the low values of the fitting parameters given in Table 3.2.

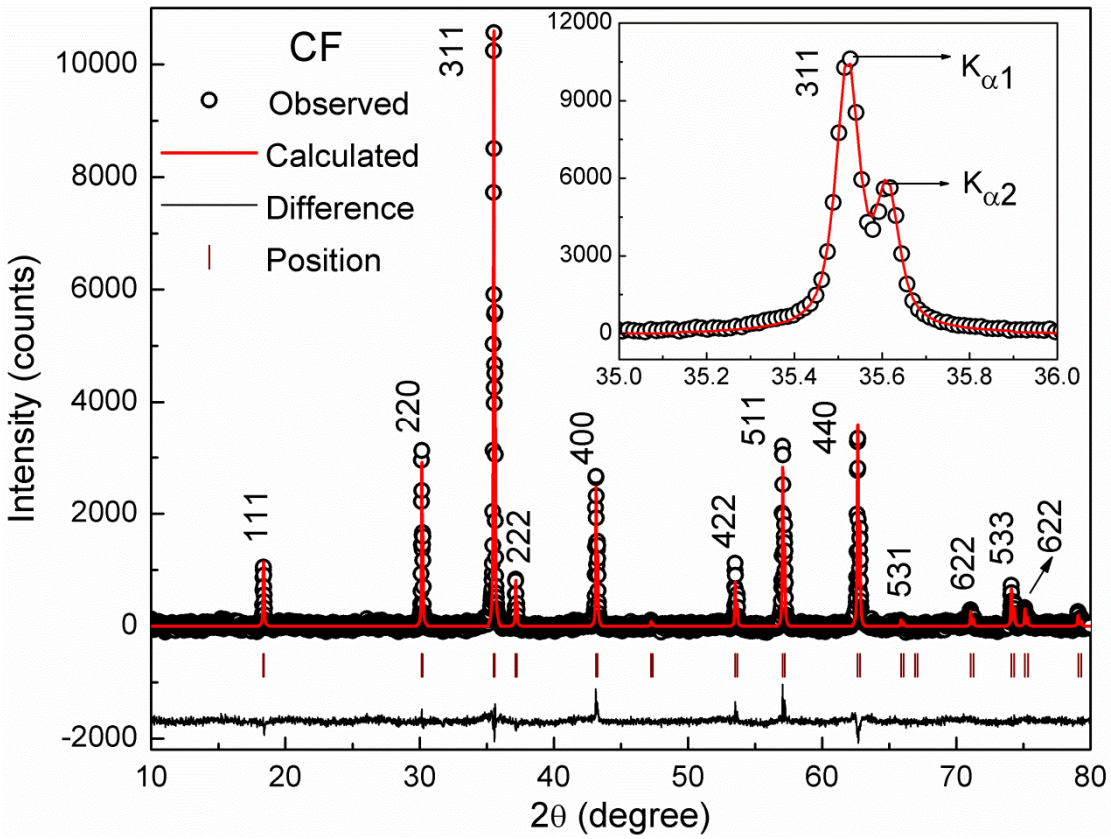

***Figure 3.5**: Rietveld refined XRD pattern of the sintered unsubstituted cobalt ferrite. The inset shows the enlarged view of the (311) peak showing $K_{\alpha 1}$ and $K_{\alpha 2}$ components.*

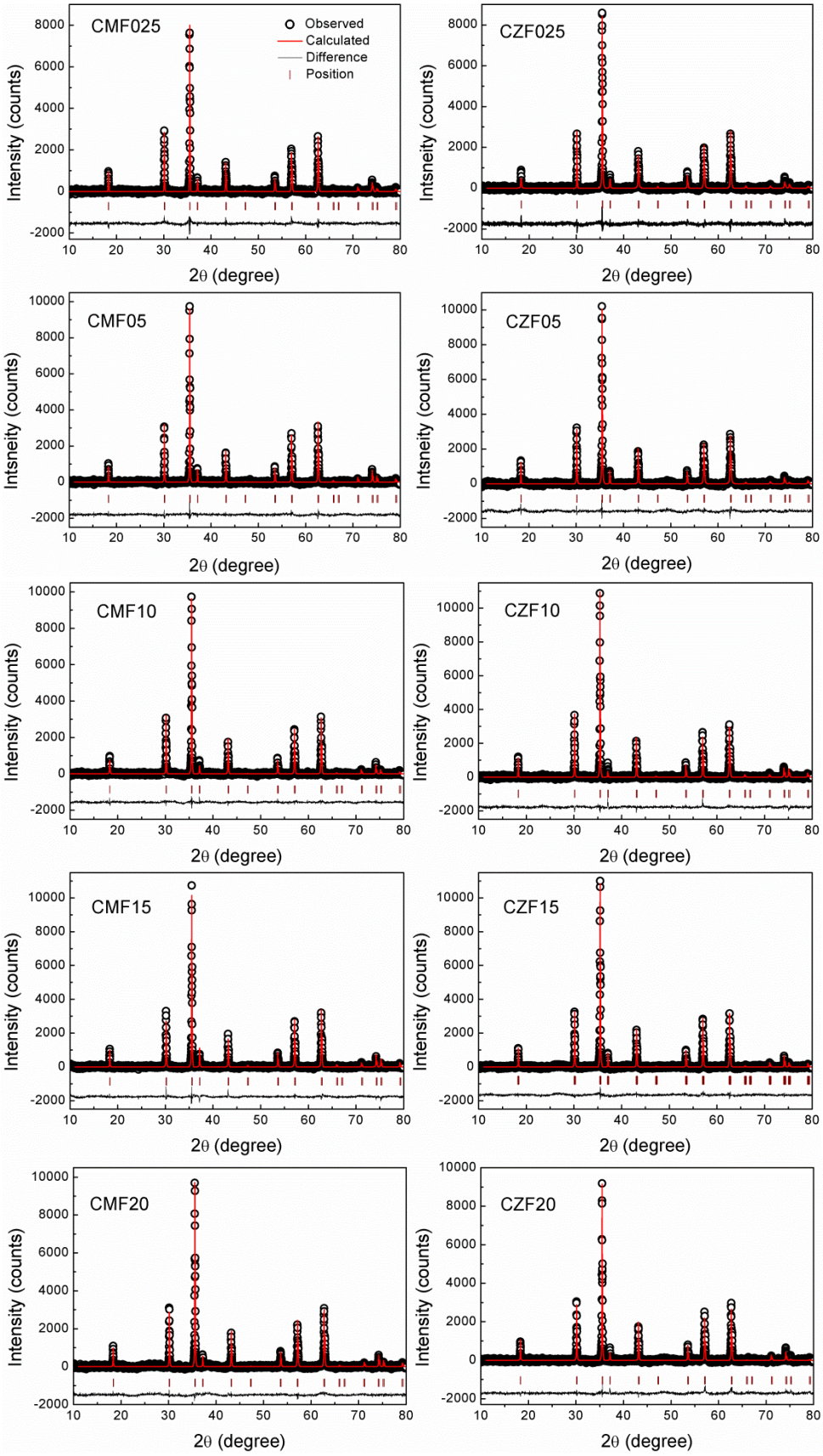

***Figure 3.6**: Results of the Rietveld refinement of the XRD patterns of the sintered substituted compositions of the CMF and CZF series.*

***Table 3.2**: Rietveld fitting parameters for the compositions in the CMF and CZF series.*

Composition	R_{wp}	R_p	$\chi 2$	Composition	R_{wp}	R_p	$\chi 2$
CF	0.033	0.025	1.57	**CF**	0.033	0.025	1.57
CMF025	0.025	0.020	1.19	**CZF025**	0.024	0.018	1.18
CMF05	0.024	0.020	1.07	**CZF05**	0.024	0.019	1.29
CMF10	0.027	0.021	1.05	**CZF10**	0.023	0.018	1.10
CMF15	0.029	0.022	1.34	**CZF15**	0.023	0.019	1.11
CMF20	0.032	0.025	1.54	**CZF20**	0.025	0.020	1.20

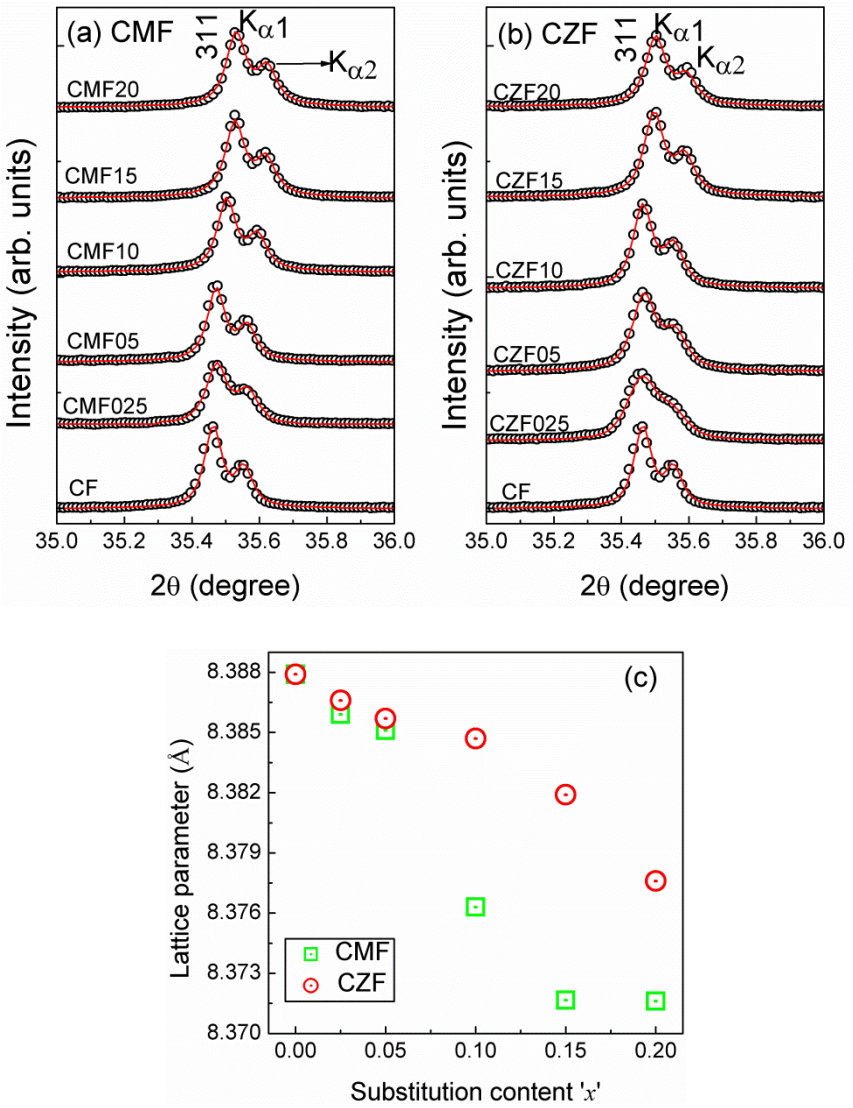

***Figure 3.7**: The enlarged (311) peak of the (a) CMF and (b) CZF series of compositions showing a shift in the peak positions, and (c) variation of the unit cell lattice parameter as a function of substitution content in both series.*

The enlarged view of the refined (311) peak of the CMF and CZF series of samples is shown in the Figures 3.7(a) and 3.7(b), respectively. As the substitution amount *x* increases in both the series, the peaks are shifted towards higher angles indicating a decrease in the lattice parameter. Variation of lattice parameter as a function of *x* in CMF and CZF series is shown in Figure 3.7(c). A nonlinear variation of the cubic lattice parameter is observed. Such a nonlinear variation in the lattice parameter could be expected for the mixed spinel systems which are neither normal nor inverse, due to the high degree of cation distribution [3]. Since the ionic radii of Mg^{2+} and Zn^{2+} are little larger than that of Fe^{3+}, an increase in the lattice parameter is envisaged with substitution. Here, the trivalent Fe^{3+} is being replaced by the divalent Mg^{2+} and Zn^{2+}, and therefore, a corresponding change in the oxidation states of the metal ions would be expected, for maintaining charge neutrality. Thus, the observed decrease in the lattice parameter is likely to be associated with the conversion of equivalent amounts of Co^{2+} to Co^{3+} to maintain the charge neutrality. The Co^{3+} ion is usually present in the low-spin state and prefers the octahedral site in the spinel lattice, as reported for various cobalt-based spinel systems [21,22]. The ionic radius of low-spin Co^{3+} is 0.545 Å, compared to 0.645 Å for Co^{2+}, for 6-fold coordination environment, which is smaller than that of Mg^{2+} and Zn^{2+} in the 4-fold as well as 6-fold coordinations. For $x \leq 0.05$, the compositions in both series show nearly comparable lattice parameter, whereas for $x > 0.05$ relatively large decrease in the lattice parameter is observed for Mg-substituted samples than for the Zn-substituted samples. This suggests a major difference in the cation distributions above and below $x=0.1$. As more and more Co^{2+} is being converted to Co^{3+} to maintain charge neutrality, a larger decrease in the lattice parameter is expected. Therefore, the observed non-linear decrease with substitution is due to the change in the oxidation state of cobalt, as well as the possible re-distribution of Co^{2+} and Fe^{3+} in the two different crystallographic sites of the spinel lattice, for $x \leq 0.05$ and $x > 0.05$. A similar feature of decreasing lattice parameter with increasing substitution has been reported for nanocrystalline $CoZn_xFe_{2-x}O_4$ ($0 \leq x \leq 0.3$) system [19]. The authors have suggested that the decrease is contributed by multiple factors including changes in the oxidation states of Co^{2+} into Co^{3+} and rearrangement of cations between tetrahedral and octahedral sites of the spinel ferrite [19].

3.4.2 Microstructure

SEM images of the sintered compacts captured on the fractured inner surfaces of the CMF and CZF series samples are shown in Figure 3.8. As can see from the images, the microstructures are significantly different for the compositions with $x \leq 0.05$ and $x \geq 0.1$. At a lower degree of substitution, $x \leq 0.05$, the samples comprise of smaller as well as larger sized grains, with a relative increase in the number of irregular shaped smaller grains with inter- and intragranular pores. At higher degrees of substitution, $x \geq 0.1$, the samples exhibit larger and fused grains. There is not much variation in the sintered density of the compositions in the CMF series, whereas a relative increase in density is observed for the compositions in the CZF series. Although all the samples are processed and sintered under identical conditions, the difference in the microstructure is most likely to be associated with the distribution of the cations in the tetrahedral and octahedral sites as well as the effect of initial particle sizes of the nanosized ferrite powders. The microstructure observed for the compositions of the two series in the present study is distinctly different from those microstructures reported for the similar systems [7,8]. The difference in the microstructure could be attributed to different synthesis methods and processing conditions employed.

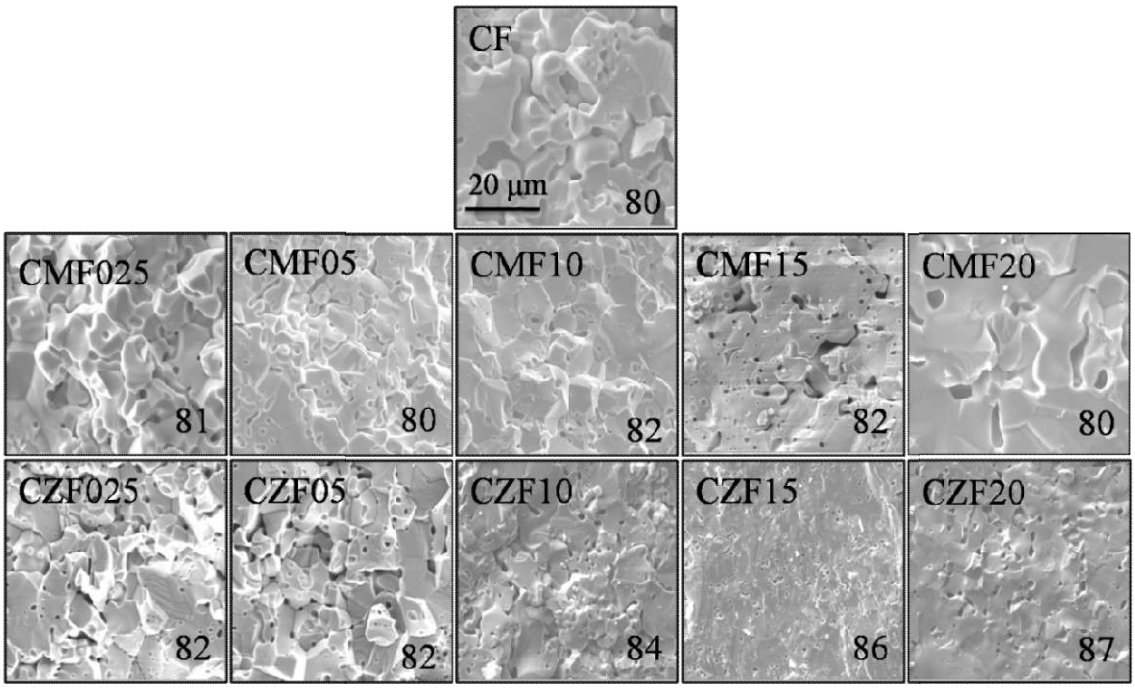

***Figure 3.8**: SEM images of the sintered compositions of the CMF and CZF series. The scale is common for all samples. The number in each image indicates the corresponding percentage sintered density of the sample.*

3.4.3 Magnetic properties

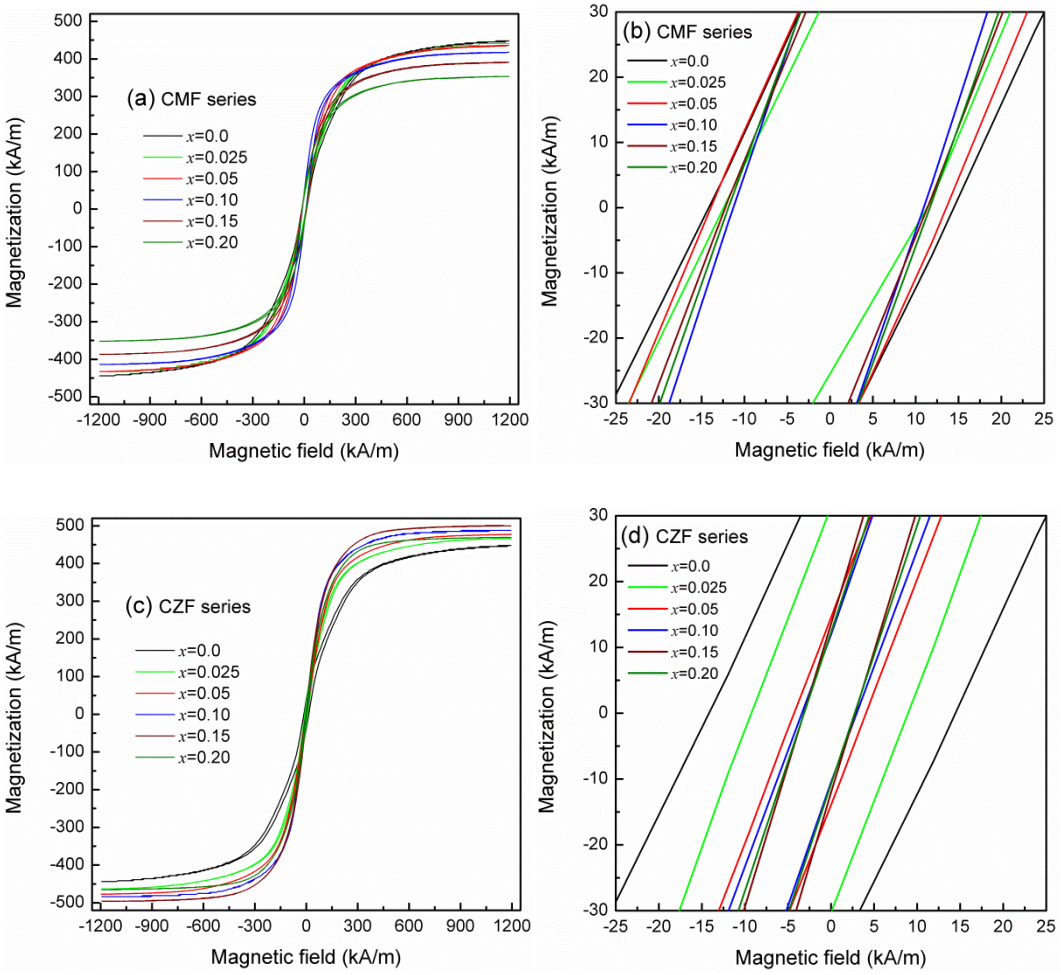

***Figure 3.9**: M-H curves of the sintered (a,b) CMF and (c,d) CZF series of samples, recorded at room temperature.*

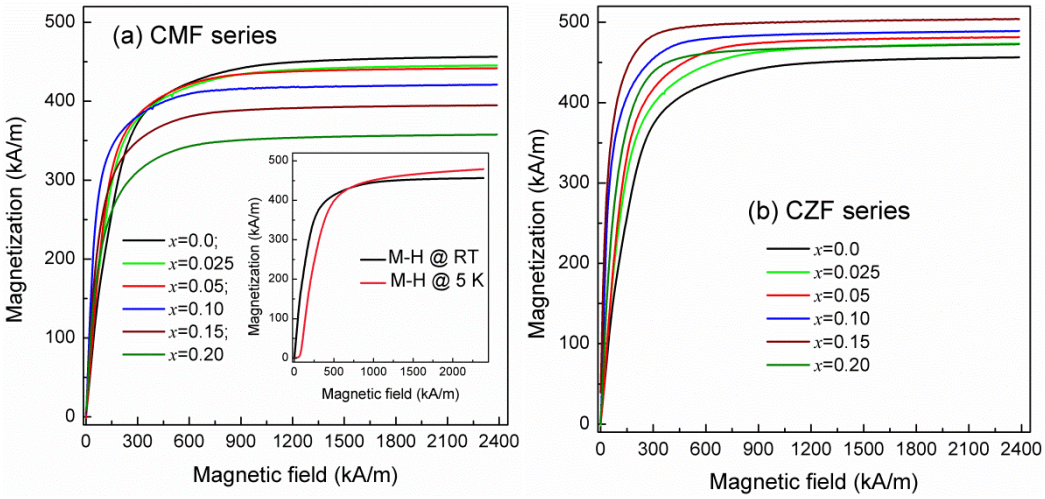

***Figure 3.10**: Initial magnetization curves of the sintered (a) CMF and (b) CZF series of samples, recorded at RT using SQUID. Inset of (a) comparison of the M-H curves of CF at RT and 5 K.*

Substitution of the non-magnetic Mg^{2+} and Zn^{2+} ions in place of Fe^{3+} in cobalt ferrite has a strong impact on the magnetic properties. Figures 3.9(a) and 3.9(c) illustrate the M-H hysteresis loops of the CMF and CZF series of samples, respectively, measured at room temperature, using a VSM, up to maximum field strength of 1200 kA/m. An enlarged view of the hysteresis loops at low field regions is shown in the Figures 3.9(b) and 3.9(d) for the CMF and CZF series, respectively. Initial magnetization curves of all the sintered compositions, recorded at room temperature using a SQUID magnetometer up to a magnetic field of 2400 kA/m (3T) are shown in the Figure 3.10(a) and 3.10(b), respectively. The saturation magnetization (M_s) of all the compositions is extracted by extrapolating the M vs. 1/H curve to 1/H=0. M_s is found to decrease with increasing *x* in the CMF series, whereas it increased up to the composition *x*=0.15 in CZF and decreased for the higher substituted compositions as shown in Figure 3.11(a). Such variation in M_s with the degree of substitution is due to the difference in the site preference of Zn and Mg for the A and B sublattices of the spinel ferrite. The M_s values of both CMF and CZF series are given in the Tables 3.3 and 3.4.

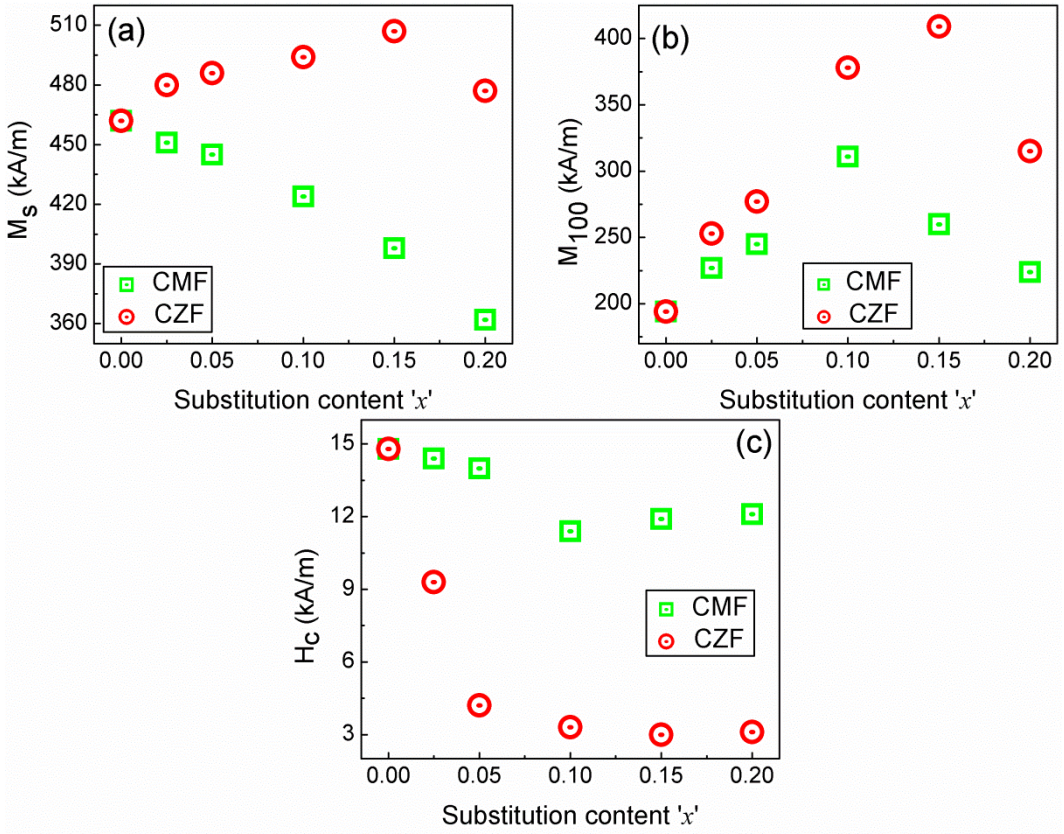

Figure 3.11*: Variation of (a) saturation magnetization, M_s, (b) magnetization at a field 100 kA/m, and (c) coercivity, H_c, as a function of substitution content in the CMF and CZF series.*

The observed variation of M_s in the CMF and the CZF series can be interpreted based on Neel's two sub-lattices magnetization model, as described in chapter 1. In the case of the CZF series, Zn^{2+} is substituted at the A-site (as in $ZnFe_2O_4$), and thereby equivalent amount of Fe^{3+} at the same site is replaced. As a result, the net magnetization of the B-site will be higher than that of the unsubstituted composition due to the magnetically diluted A-site, giving rise to higher M_s for the substituted samples compared to the parent compound. Although more and more Fe^{3+} are being replaced by Zn^{2+} from the A-sites, the decrease in M_s for x=0.2 is likely to be due to the antiparallel magnetic moments within the B sublattice, much similar to the case in $ZnFe_2O_4$ [23,24]. A similar trend, increase in M_s up to a particular substitution content and decline at higher levels of substitution, has been reported for other non-magnetic substituted cobalt ferrite systems [3,25,26]. For the CMF series, the monotonic decrease in M_s is due to the substitution of Fe^{3+} by Mg^{2+} at the B-sites, along with the dilution of the B-site by non-magnetic low-spin Co^{3+} that resulted in the reduction in the net magnetization of the B-site and hence the decrease in M_s with x.

Although a decrease in the value of M_s with x is observed for the CMF series, the measured magnetization is higher at lower measured fields (<200 kA/m). This is evidenced from the initial magnetization curves of the substituted samples compared to that of the unsubstituted sample, shown in Figure 3.10(a). Figure 3.11(b) shows the variation of the magnetization at 100 kA/m (M_{100}), extracted from Figure 3.10, for both series of compositions. Compared to the unsubstituted counterpart, higher magnetization at low fields is found for all the substituted compositions in the both series. The magnetization at 100 kA/m is initially increased up to x=0.1 for the CMF series and x=0.15 for the CZF series and decreased for the higher level of substitution. For the same amount of substitution x, the magnetization is higher for the CZF series compared to the CMF series. The higher magnetization at lower fields, on substitution, is likely to be due to the predominant effect of decreasing magnetocrystalline anisotropy on non-magnetic dilution at the A-site together with the changes in the A-O-B exchange interactions due to the presence of non-magnetic Zn^{2+} ions in the spinel crystal structure.

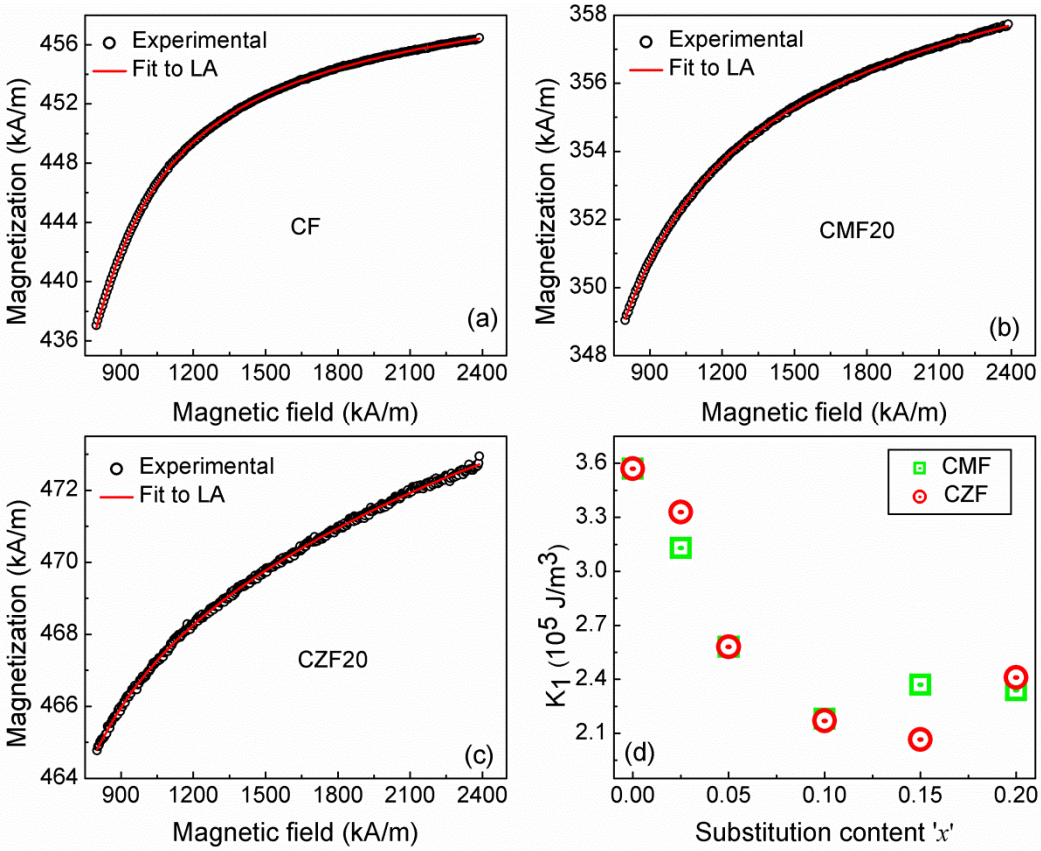

***Figure 3.12**: Room temperature initial magnetization curves of (a) CF, (b) CMF20 and (c) CZF20 fitted using the law of approach (LA) to saturation. The variation of the first order magnetocrystalline anisotropy constant (K_1) with substitution content is shown in (d).*

Magnetocrystalline anisotropy constant (K_1) of the different compositions in the CMF and CZF series is calculated from the room temperature magnetization data using the law of approach (LA) to saturation [27]. The initial magnetization data is fitted from 800 to 2400 kA/m using law of approach to saturation, and the results of the fitted curves for the compositions CF, CMF20 and CZF20 are shown in Figure 3.12(a),(b),(c). The calculated value of K_1 for the unsubstituted compound is comparable to that reported in the literature [28,29]. For the substituted compositions, irrespective of whether the substituted metal ion is located at the A-site or the B-site, the variation of K_1 is found to be similar in both cases, showing a large decrease up to x=0.1 and flattening at higher values of x as shown in Figure 3.12(d). The values of K_1 for both the series are listed in Tables 3.3 and 3.4. The decrease in the value of K_1 with x, in both series, is mainly due to the conversion of Co^{2+} into Co^{3+} at the octahedral site, which is common for both series. Apart from this, the reduction in the A-O-B superexchange interactions, relative changes in the amount of Fe^{3+} at the B-sites and displacement of Co^{2+} from the B-sites to A-sites are also likely to be responsible for the lower

anisotropy of the substituted compositions [30,31]. The decreased anisotropy on substitution explains the relatively larger magnetization of the substituted compositions at low magnetic fields.

***Table 3.3**: Magnetic parameters of the sintered samples in the CMF series.*

Composition	M_s (kA/m)	H_c (kA/m)	T_C (^oC)	K_1 (10^5 J/m^3)
CF	462	14.8	516	3.57
CMF025	451	14.4	498	3.13
CMF05	445	14.0	485	2.58
CMF10	424	11.4	453	2.17
CMF15	398	11.9	438	2.37
CMF20	362	12.1	432	2.34

***Table 3.4**: Magnetic parameters of the sintered samples in the CZF series.*

Composition	M_s (kA/m)	H_c (kA/m)	T_C (^oC)	K_1 (10^5 J/m^3)
CF	462	14.8	516	3.57
CZF025	480	9.3	483	3.33
CZF05	486	4.2	453	2.58
CZF10	493	3.3	405	2.17
CZF15	507	3.0	385	2.06
CZF20	477	3.1	370	2.41

As discussed in Chapter 1, it is possible to estimate the cation distribution in the spinel ferrites using the saturation magnetization obtained at a temperature close to absolute zero. From the M_s of the unsubstituted cobalt ferrite obtained at 5K (see inset of Figure 3.10(a)), the cation distribution has been estimated as $(Co_{0.25}Fe_{0.75})_A[Co_{0.75}Fe_{1.25}]_BO_4$, where the subscripts A and B represent the tetrahedral and the octahedral sites, respectively. This cation distribution is comparable to that reported in the literature, obtained from Mossbauer measurements, which depends on the processing conditions [32]. However, it is hard to estimate the cation distribution for the substituted samples from their M_s values because the substituted Mg ions are present in both the tetrahedral and the octahedral coordination environments.

Unlike the variation of M_s, a decrease of H_c is observed with increasing degree of substitution for $x< 0.1$, and the coercivity becomes nearly constant for higher values of x. The same trend is observed for both CMF and CZF series, as shown in Figure 3.11(c). However, for the same value of x, the rate of decrease of H_c is much faster for the Zn-substituted samples compared to the Mg-substituted samples, as shown in Figure 3.11(c). The values of H_c of both the CMF and CZF series are listed in the Tables 3.3 and 3.4. The variation of H_c is similar to the variation of magnetocrystalline anisotropy constant. It is well documented in the literature that H_c of the ferrite systems is greatly influenced by many factors including K_1, M_s, A-O-B super-exchange interaction, lattice imperfections apart from the microstructural parameters [33]. In the present study, microstructures are nearly comparable for the similar compositions in both series. Therefore, the fast decrease in H_c with x for the Zn-substituted samples over Mg-substituted samples could be ascribed to the dependence on K_1 and M_s via the Brown relation [34,35];

$$H_c = \frac{2K_1}{\mu_o M_s} \tag{3.1}$$

According to the above relation, H_c is directly proportional to anisotropy and inversely proportional to saturation magnetization. Hence, a higher M_s will lower the H_c.

Figures 3.13(a) and 3.13(b) show the temperature dependent magnetization curves of the CMF and CZF series, respectively, measured above room temperature, in a magnetic field of 100 Oe (~8 kA/m). The shapes of the magnetization curves are different for compositions $x<0.1$and $x\geq0.1$ for the CMF series and $x<0.05$ and $x\geq0.05$ for the CZF series. It is known that the M–T measurement on fresh sintered samples can be considered as a true zero field cooled magnetization measurement (M_{ZFC}). The magnitude of the magnetization at a particular temperature as well as the shape of the temperature variation of the magnetization curve, measured in a low magnetic field, suggests the changes in the magnetocrystalline anisotropy with temperature [36]. Thus, the changes in the nature of the M–T curves, and the magnitude of magnetization at lower temperatures, for the two compositional regions mentioned above, suggest a drastic difference in the anisotropy and the domain structure at different substitution levels.

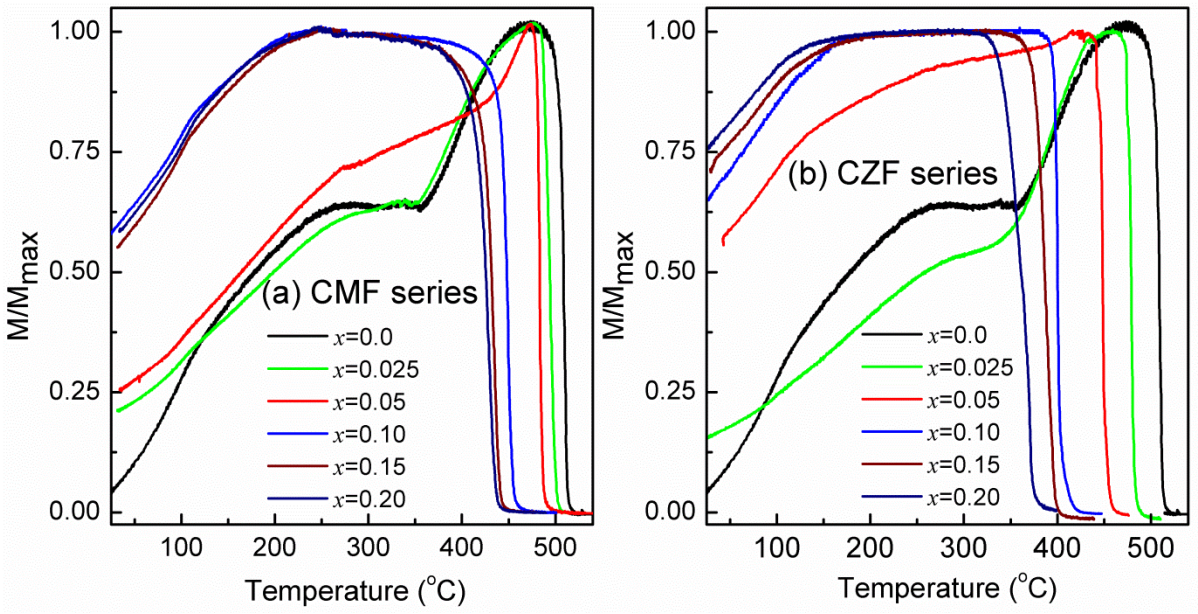

***Figure 3.13**: Magnetization vs. temperature curves of sintered (A) CMF and (b) CZF series samples, measured above room temperature in a magnetic field of 100 Oe (~8 kA/m).*

The Curie temperatures (T_C) of the different compositions are obtained from the M vs. T curves. T_C is obtained by linear extrapolation of the maximum change slope down to the temperature axis. The variation of T_C with the degree of substitution for both the CMF and CZF series is shown in Figure 3.14. The T_C values of both the CMF and CZF series are listed in Tables 3.3 and 3.4. Both the series show decrease in T_C with increasing substitution and this is attributed to the reduction in the A-O-B superexchange interactions triggered by the presence of non-magnetic Zn and Mg in the crystallographic sites of the cobalt ferrite [3,30,37]. The Zn-substituted samples show a larger decrease in T_C compared to the Mg-substituted samples for the same amount of substitution *x*. That is, a larger decrease is observed on substitution at the A-site and smaller decrease on B-site substitution. Such observed trend in T_C could be described by the relation [23,38],

$$T_C = \frac{2zJS(S+1)}{3k_B} \tag{3.2}$$

where, z is the number of nearest neighbors, J is the exchange constant, S is the total spin and k_B is the Boltzmann constant. From the above relation, it is evident that T_C not only depends on the exchange strength but also on the number of nearest neighboringcations and their spin. In cobalt ferrite, each A-site cation (Co or Fe) is magnetically coupled with 12 B-site cations via oxygen as next nearest neighbors whereas each B-site cation (Co or Fe) is coupled to 6 A-site cations via oxygen as next nearest neighbors [39]. In the present case, the magnetization

data revealed that Zn is substituted at the A-sites whereas a large fraction of Mg is substituted at the B-sites. By replacing a magnetic cation at the A-site by a non-magnetic cation like Zn^{2+} in cobalt ferrite lattice, 12 B-site magnetic cations lose their magnetic interactions. This means that the reduction in the exchange strength is considerably stronger. On the other hand, when a B-site magnetic cationis replaced by a non-magnetic cation like Mg^{2+}, only 6 A-site cations lose their magnetic interactions. Hence, the decrease in T_C is larger for the Zn-substituted samples than that for the Mg-substituted samples. A similar feature has been reported for various metal substituted sintered cobalt ferrite systems [3,37].

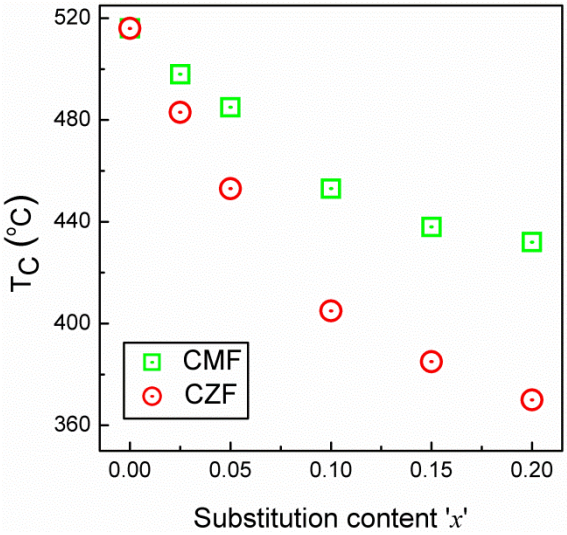

***Figure 3.14**: Variation of the Curie temperature (T_C) as a function of substitution content in the CMF and CZF series.*

3.4.4 Raman spectra

Raman spectra of the different compositions in the CMF and CZF series are shown in Figure 3.15(a) and 3.15(b), respectively. The samples of the both the series show presence of seven active modes, designated as $A_{1g}(1)$, $A_{1g}(2)$, $E_g(1)$, $E_g(2)$, $T_{2g}(1)$, $T_{2g}(2)$ and $T_{2g}(3)$, indicating that the compositions are in the form of inverse or mixed spinel ferrite [40,41]. In cobalt ferrite, the bands due to $A_{1g}(1)$ at ~690 cm^{-1} and $A_{1g}(2)$ at ~610 cm^{-1} correspond to symmetric breathing modes of the FeO_4 and CoO_4 tetrahedra, respectively, in which only oxygen atoms move [42,43]. The high-frequency $T_{2g}(3)$ mode corresponds to asymmetric bending motion of the oxygens co-ordinated to Fe^{3+} [41] or Co^{2+} [44] in the tetrahedral sites. The $T_{2g}(2)$ mode corresponds to the motion of oxygen atoms bonded to Fe^{3+} in the octahedral sites (FeO_6) [45]. E_g mode is related to symmetric bending motion of the oxygens within the AO_4 units. A weak signal at ~210 cm^{-1}, designated as $T_{2g}(1)$, is related to the translational

motion of the BO_6 units against the A-site cations [43]. D'lppolito *et al*. [41] reported eight peaks in the Raman spectra of $MgFe_2O_4$, and it has been concluded that the extra peaks over and above the five expected Raman active modes are caused by the disorder effects of Mg^{2+} and Fe^{3+} over the tetrahedral and octahedral sites. The additional peaks are due to the mixed spinel character, because of the difference in the masses of Mg and Fe in the tetrahedral and octahedral sites of the spinel lattice.

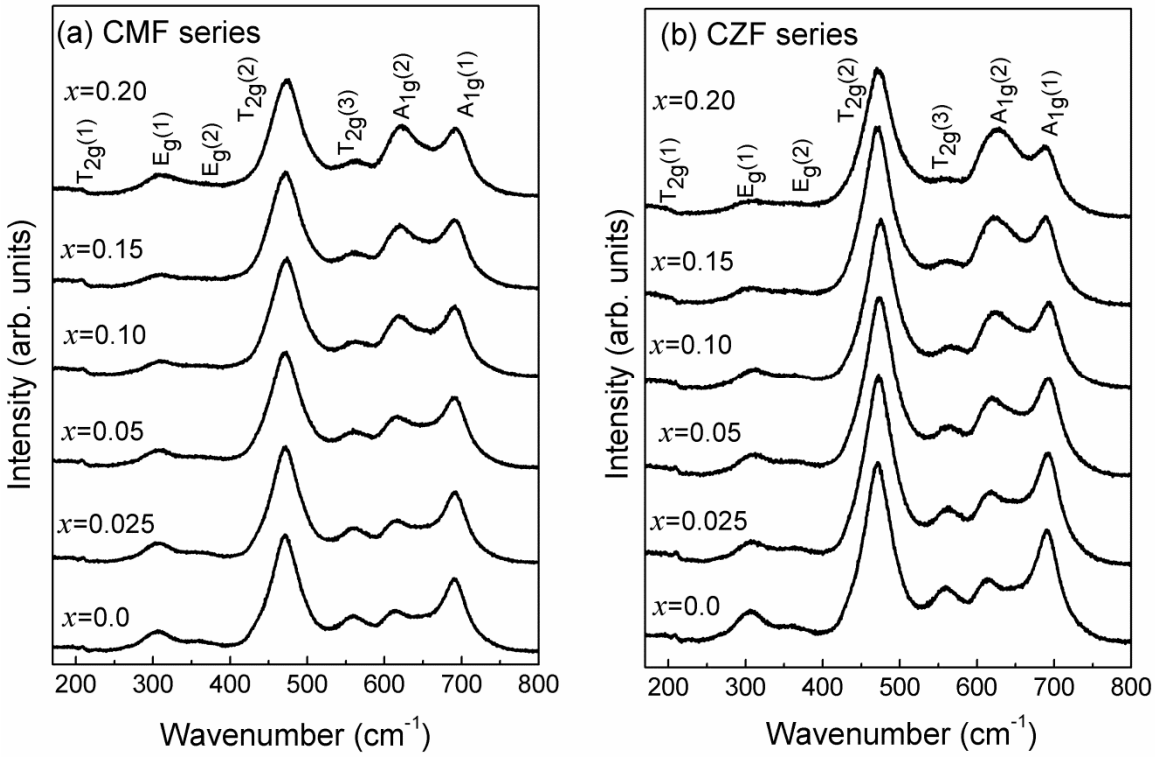

Figure 3.15*: Raman spectra of the sintered (a) CMF and (b) CZF series samples.*

In the Raman spectra shown in Figure 3.15, for both series, it can be seen that the bands belonging to the tetrahedral unit, AO_4, are significantly affected by the degree of substitution. Decrease in the intensities of the $A_{1g}(1)$ and $T_{2g}(3)$ bands and increase in the intensity of the $A_{1g}(2)$ band, with increasing degree of substitution, are observed. The decrease in the intensity of the band due to FeO_4 ($A_{1g}(1)$) and increase in the intensity of the band due to CoO_4 ($A_{1g}(2)$), with increasing the degree of substitution, suggest relative changes in the population of Fe^{3+} and Co^{2+} in the tetrahedral sites of the spinel lattice. However, it may be noted that the variation in the intensities of the peaks is not uniform in the two series. Figure 3.16(a),(b) shows the intensity variation of the A_{1g} band, with respect to the normalized intensity of the $T_{2g}(2)$ band, for different compositions in CMF and CZF. It is clear from the figure that the decrease in the intensity of the $A_{1g}(1)$ band is more pronounced for the CZF series and less pronounced for the CMF series. Also, the $T_{2g}(2)$ band develops a shoulder at

higher wavenumbers, at ~520 cm^{-1}, as shown by the asterisk symbol (*) in Figure 3.16(c) for the composition x=0.2 with reference to x=0. Another important observation is that the $A_{1g}(2)$ mode is more broad at ~650 cm^{-1} as x increases in the CZF when compared to the CMF series and it is shown by the symbol (#) in Figure 3.16(d) for the compositions x=0.2 with reference to x=0.

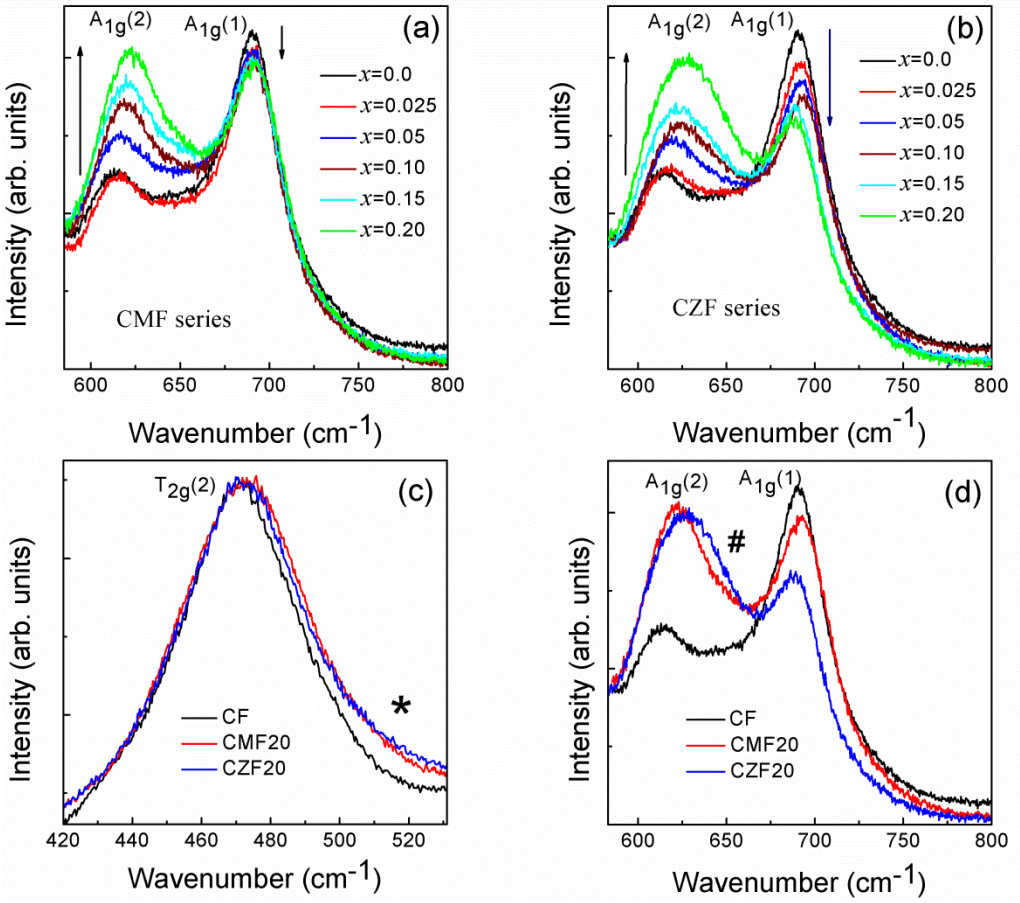

***Figure 3.16**: Variation in the intensities of the A_{1g} bands with respect to the normalized intensity of the $T_{2g}(2)$ band for different compositions in (a) CMF and (b) CZF series. (c) Comparison of the normalized $T_{2g}(2)$ band for x=0 and x=0.2 in the two series showing a shoulder around ~520 cm^{-1} for the substituted compositions, shown by ∗. (d) Comparison of the intensity of the A_{1g} bands for x=0 and x=0.2 in the two series showing a shoulder around ~650 cm^{-1} for the substituted compositions, shown by #. The up and down arrows indicate increasing and decreasing intensities.*

To extract more information, the Raman spectra are deconvoluted after correcting for the baseline. Deconvolution of the spectra of $CoFe_2O_4$ using seven peaks, corresponding to the six Raman bands at 209 ($T_{2g}(1)$), 306 (E_g), 471 ($T_{2g}(2)$), 560 ($T_{2g}(3)$), 613 ($A_{1g}(2)$), and 691 ($A_{1g}(1)$) cm^{-1}, and the weak band at 360 cm^{-1}, did not give a good fit in the 620-670 cm^{-1} region, as shown in Figure 3.17(a). The spectra could be fitted well to eight peaks at 209 cm^{-1}

($T_{2g}(1)$), 306 cm^{-1} ($E_g(1)$), 360 cm^{-1} ($E_g(2)$), 471 cm^{-1} ($T_{2g}(2)$), 560 cm^{-1} ($T_{2g}(3)$), 613 cm^{-1} ($A_{1g}(2)$), 650 cm^{-1} (new peak) and 691cm^{-1} ($A_{1g}(1)$), as shown in Figure 3.17(b).

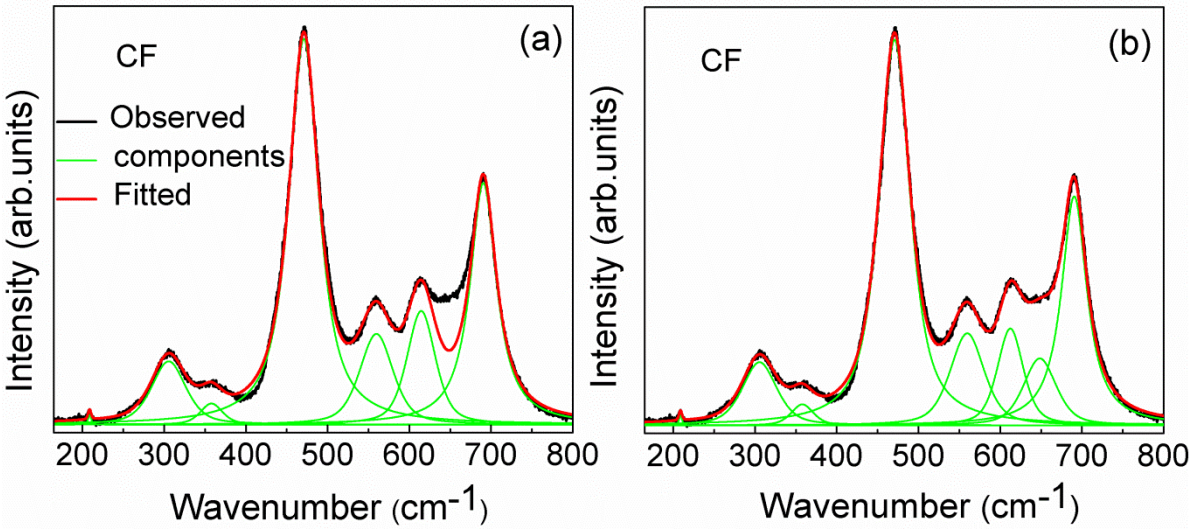

***Figure 3.17**: Deconvoluted Raman spectra of sineterd $CoFe_2O_4$ fitted using (a) seven components and (b) eight componets.*

A peak at 650 cm^{-1} is reported by Shemer et al [46] in the Raman spectra of nanosized powders of cobalt ferrite, where the authors have suggested that the origin of the mode is due to the presence of Co^{2+} in defect sites that are located near the surface of the nanoparticles [46]. However, in the present work, the spectra are recorded on sintered pellets, where the grain size > 1 μm. Hence, it is possible that the peak at 650 cm^{-1} is a feature of cobalt ferrite, irrespective of the particle size and may be originating from the local distortion in the coordination environment due to inhomogeneous distribution of the different ions in the tetrahedral and octahedral coordination environments in the mixed spinel structure. In general, the Raman spectra of the cobalt ferrite samples are almost similar to that reported for magnesium ferrite [41], where additional peaks are observed other than the five Raman modes of vibration and the additional peaks are due to the effect of inhomogeneous distributions of di- and trivalent cations in the A- and B-sites. For $CoFe_2O_4$, the magnetic measurements indicated mixed spinel nature where both Co and Fe are distributed in the tetrahedral and octahedral sites. For the unsubstituted sample, the ratio of the area under the peaks due to $A_{1g}(2)$ (CoO_4) and $A_{1g}(1)$ (FeO_4) is obtained as 0.26 from which the distribution can be assigned as $(Co_{0.26}Fe_{0.74})_A[Co_{0.74}Fe_{1.26}]_BO_4$. This distribution is nearly comparable to that calculated from the magnetization data as $(Co_{0.25}Fe_{0.75})_A[Co_{0.75}Fe_{1.25}]_BO_4$.

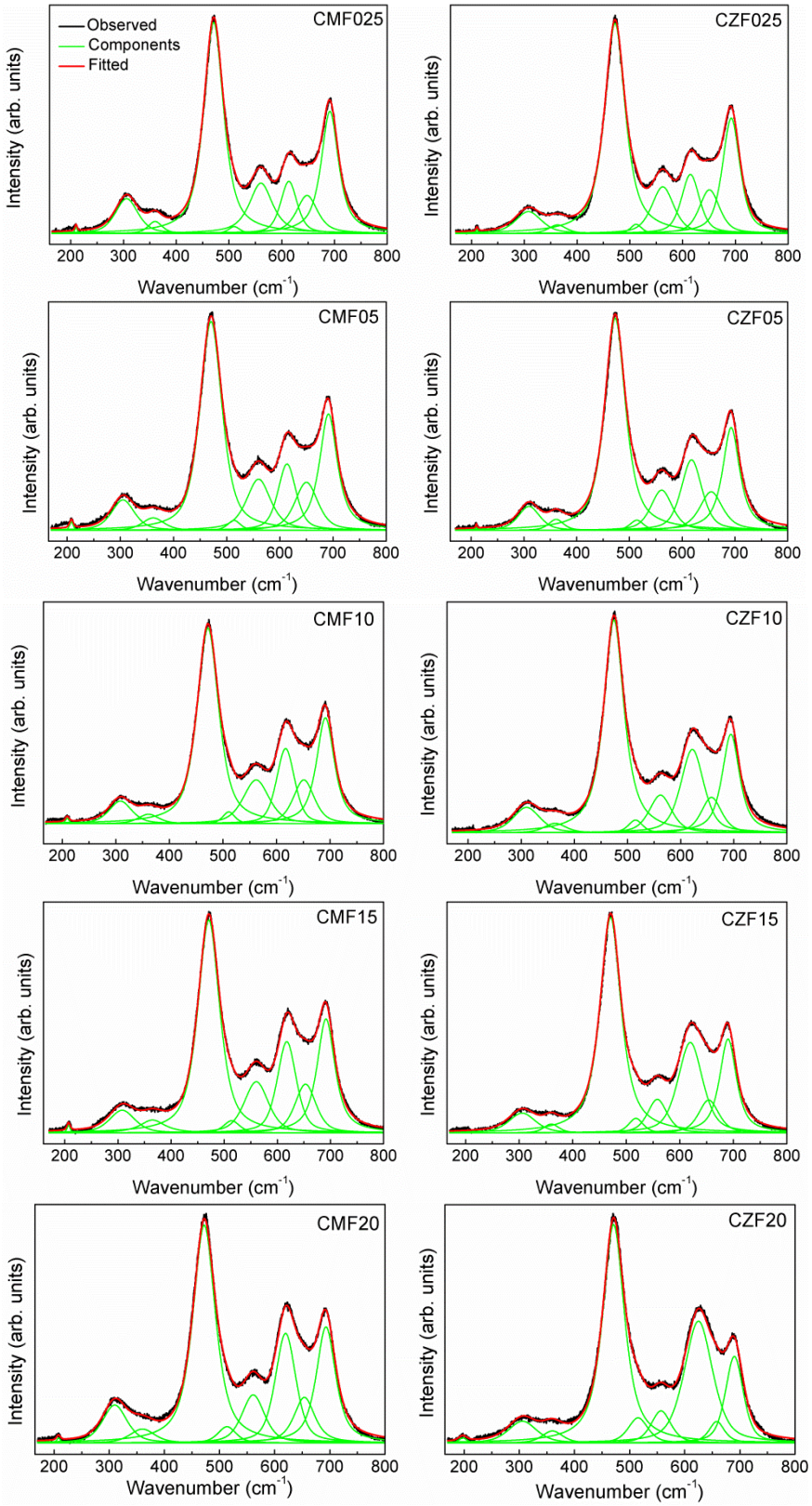

***Figure 3.18**: Deconvoluted Raman spectra of sintered substituted compositions of the CMF and CZF series.*

The results of the deconvoluted spectra of the unsubstituted and the substituted compositions of the CMF and CZF series are shown in Figure 3.18. In the case of the substituted samples, nine peaks are used to deconvolute the spectra, and the 9th peak at ~520 cm^{-1} is likely to be due to Co^{3+} present at the octahedral coordination environment. This assignment has been made based on the reported Raman spectra of bulk as well as nanosized $ZnCo_2O_4$ [47,48], in which Zn^{2+} occupies the tetrahedral sites and Co^{3+} are located at the octahedral sites. The mode observed at ~520 cm^{-1} is consistent with the mode due to CoO_6 in the $ZnCo_2O_4$ systems. Thus, the Raman spectra give information on the presence of Co^{3+} in the substituted compositions which supports the interpretation of the decrease in the lattice parameter with the degree of substitution. The increased broadening of the $A_{1g}(2)$ mode at ~650 cm^{-1} with *x* in CZF is most probably due to the contribution of the ZnO_4 unit at the A-site, and it is in good agreement with the Raman band reported for ZnO_4 at 647 cm^{-1} in $ZnFe_2O_4$ [49,50].

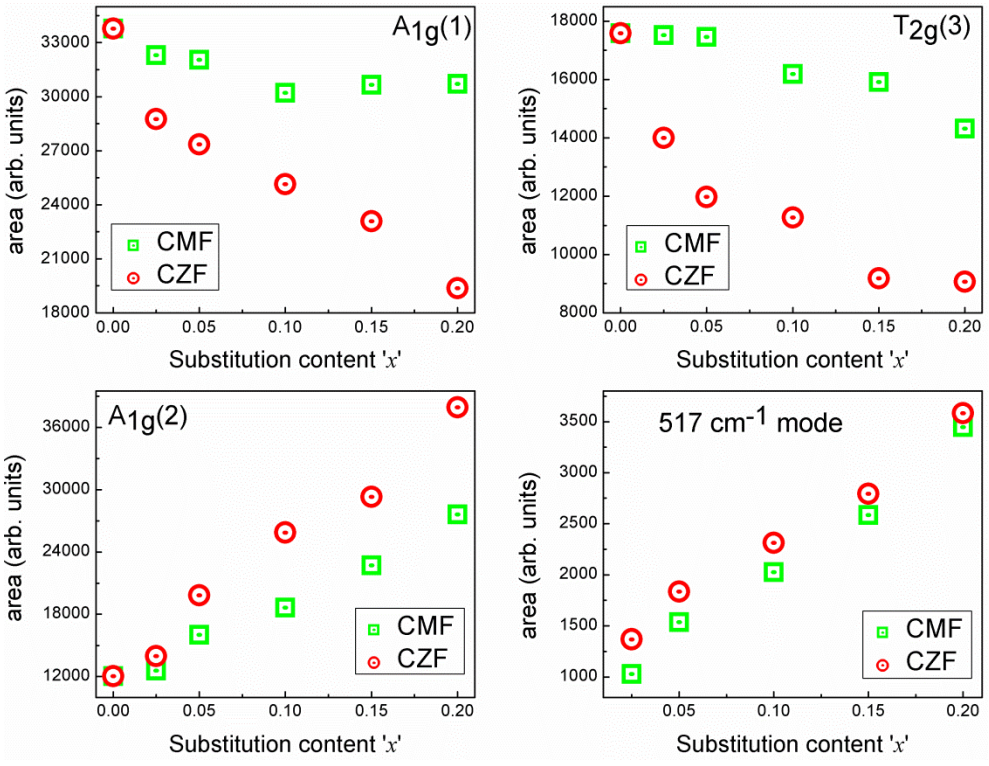

***Figure 3.19**: Variation of the area under different peaks for different Raman active modes as a function of in the CMF and CZF series.*

Figure 3.19 shows a comparison of the variation of the area under the different peaks due to $A_{1g}(1)$ (FeO_4 breathing), $A_{1g}(2)$ (CoO_4 breathing), $T_{2g}(3)$ (FeO_4 bending) modes and the new peak at ~517 cm^{-1} (contribution from $Co^{3+}O_6$) with substitution. The larger decrease in the area of the peak due to the $A_{1g}(1)$ mode with the degree of substitution in the CZF series indicates that Zn is substituted for Fe at the A-sites. For the CMF series, a small decrease in the area of the peak due to $A_{1g}(1)$ is observed up to x=0.1, and the area remains almost constant for the higher substituted compositions. This suggests that a small amount of Mg is substituted for Fe at the A-site. Similar changes are observed in the variation of the area under the $T_{2g}(3)$ band also. A corresponding increase in the area of the $A_{1g}(2)$ band is observed for all compositions due to the additional contributions from ZnO_4 and MgO_4 units. Here again, the increase in the area is larger for the CZF series compared to that for the CMF series, because Zn is fully substituted at the A-sites whereas part of Mg is substituted at the B-sites. Similarly, the variation in the area under the peak at ~517 cm^{-1}, due to $Co^{3+}O_6$ vibrations, is comparable for both the series, which increases linearly with increasing the degree of substitution, as expected. Thus, the Raman spectroscopy studies give a clear indication for the changes in the distribution of the substituted ions in the cobalt ferrite lattice, supporting the conclusions drawn from the magnetic studies.

3.4.5 Summary of Magnetic and Raman Studies

Based on the results of the magnetic and Raman measurements, the following distributions are proposed for the substituted compositions, assuming the distribution calculated for the unsubstituted composition from magnetic measurements.

Zn-substitution at low Zn content ($x \leq 0.05$):

$$(Co_{0.25}Fe_{0.75-x}Zn_x)_A[Co^{2+}_{0.75-x}Co^{3+}_{x}Fe_{1.25}]_BO_4$$

Zn-substitution at higher Zn content ($x > 0.05$):

$$(Co_{0.25+y}Fe_{0.75-x-y}Zn_x)_A[Co^{2+}_{0.75-x-y}Co^{3+}_{x}Fe_{1.25+y}]_BO_4$$

Mg-substitution for all compositions:

$(Co_{0.25+y}Fe_{0.75-xA-y}Mg_{xA})_A[Co^{2+}_{0.75-x-y}Co^{3+}_{x}Fe_{1.25-xB+y}Mg_{xB}]_BO_4$, where $xA + xB = x$, and y is the amount of Co^{2+} displayed from the B-site to the A-site

3.4.6 XPS Spectra

3.4.6.1 CMF series

The oxidation states of the metal ions in the Mg-substituted and the unsubstituted sintered cobalt ferrite samples are examined by X-ray photoelectron spectroscopy. The Co-2p and Fe-2p XPS spectra of the compositions CF, CMF05, CMF10 and CMF20 are shown in Figure 3.20 and Figure 3.21, respectively. In the Co-2p spectra, the $2p_{3/2}$and $2p_{1/2}$ peaks are deconvoluted using two peaks each, corresponding to Co in the octahedral and tetrahedral sites, as reported in the literature [51]. The respective broad shake-up satellite peaks of $2p_{3/2}$ and $2p_{1/2}$ are fitted using only one peak each. The binding energies (BE) of all the peaks along with the respective area under the curves are listed in Table 3.5. The obtained BEs are comparable with the reported values [52,53]. The presence of Co^{2+} and Co^{3+} in Co-based metal oxides can clearly be distinguished by the intensity of the satellite peaks and the energy difference between the $2p_{3/2}$ and $2p_{1/2}$ peaks (ΔE), as suggested [54,55]. Strong and weak satellite intensities of Co-2p indicate the dominant contributions from Co^{2+} and Co^{3+}, respectively. In a similar fashion, the samples with more amounts of Co^{2+} show ΔE ~15.7 to 16.1 eV, whereas ΔE will be 15 to 15.4 eV for the samples with a high content of Co^{3+} [55].

In the present study, the presence of intense $2p_{3/2}$ satellite peak in the XPS spectra of the unsubstituted sample indicates a high content of Co^{2+}. However, a decrease in the intensity of the satellite peak is observed in the substituted samples, revealing the presence of Co^{3+} in small amounts. The intensity ratio of the Co $2p_{3/2}$ satellite to the main peak decreases with increasing Mg content, suggesting the conversion of the equivalent amount of Co^{2+} to Co^{3+}, to preserve charge neutrality when the trivalent Fe^{3+} is substituted by the divalent Mg^{2+} ion. Co^{2+} has a tendency to occupy on either site of the spinel lattice, whereas Co^{3+} has a strong preference for the octahedral B-sites. It has been reported by many authors that the BE of the A-site (tetrahedral) Co^{2+} is larger than the BE of B-site Co^{3+}(octahedral) for the spinel-based metal oxides [56-58]. However, if both Co^{2+} and Co^{3+} are present in the B-sites, where Co^{2+} will be in the high-spin state and Co^{3+} will be in the low-spin state [53], then BE for Co^{2+} might be a little larger than that for Co^{3+}, due to more electronic shielding present in the high-spin Co^{2+} than in the low-spin Co^{3+} located at the B-sites [59]. Because of the small content of Co^{3+} in the substituted samples, it is hard to extract any information by deconvoluting with another peak, since the main $2p_{3/2}$ peak is little wider and the Co^{3+} peak position lies somewhere under the broad peak.

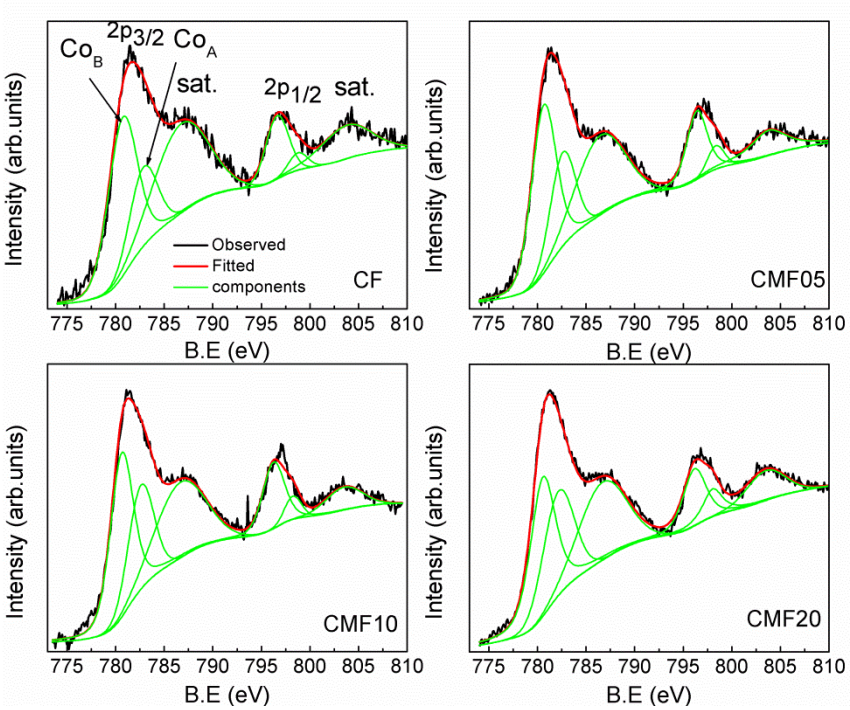

***Figure 3.20**: Co-2p XPS spectra of different compositions in the CMF series.*

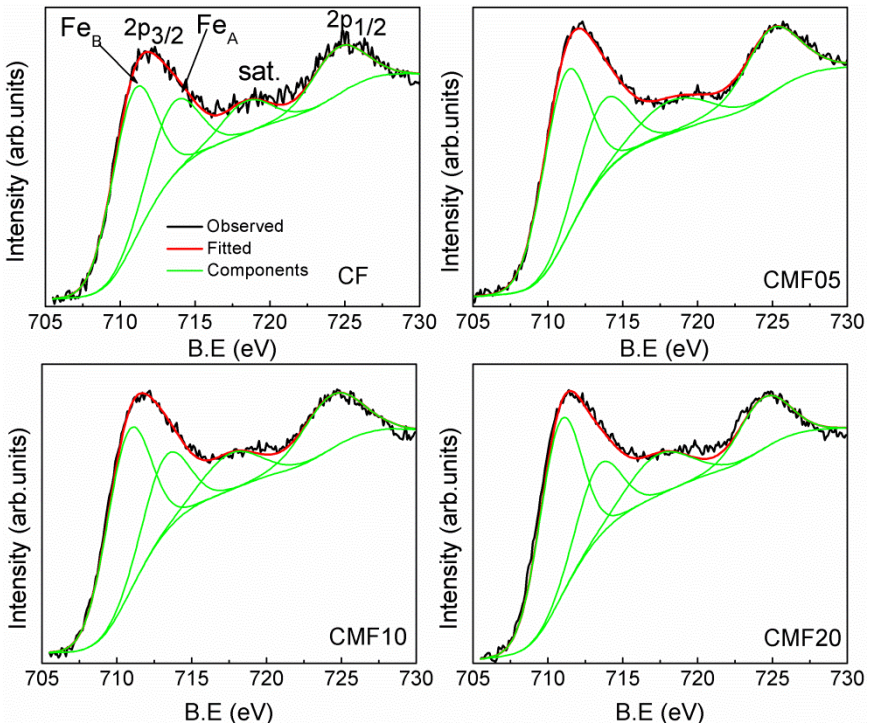

***Figure 3.21**: Fe-2p XPS spectra of different compositions in the CMF series.*

The ratio of the total area of the $2p_{3/2}$ satellite peak to the main $2p_{3/2}$ peak is found to decrease as the Mg content increases in cobalt ferrite (Table 3.5), suggesting that more and more Co^{2+} are converted to Co^{3+} to maintain the charge neutrality, and it is well-supported by the decrease in the lattice parameter. The ΔE between $2p_{3/2}$ and $2p_{1/2}$ is obtainedas 15.9, 15.8, 15.6 and 15.6 eV for the compositionsCF, CMF05, CMF10 and CMF20, respectively. As evident from Table 3.5, the Co-2p peak is slightly shifted towards lower binding energy side, and the area under the curve of B-sites is found to be decreased, whereas the area under the curve of A-sites is found to be increased as more Mg is substituted into the cobalt ferrite lattice.

The Fe-$2p_{3/2}$ XPS spectral peak was also deconvoluted into two peaks, corresponding to Fe^{3+} in two different crystallographic environments. The BEs of Fe^{3+} in the B- and A-sites are obtained in the range of 710.7 to 711.2 eV and 713.2 to 713.6 eV, respectively (Table 3.6). The main $2p_{3/2}$ peak is accompanied by a low-intensity satellite peak around 718.8 eV; means all the samples predominantly comprise of Fe^{3+}. The BE of Fe $2p_{1/2}$ peak is 724.6 eV, and the energy difference between the $2p_{3/2}$ and $2p_{1/2}$ peaks is found to be around 13.6 eV, and these are comparable to the reported values [52]. BEs of Fe^{3+} in the A- and B-sites of themain $2p_{3/2}$ peak is found to be little higher and similar trend has been observed for nanomaterials as reported in the literature [51,60,61]. The possibility of Fe^{2+} content in the sintered CMF series samples is almost negligible as indicated by the absence of a shoulder at lower binding energy. Moreover, BE of the main Fe-$2p_{3/2}$ for Fe^{2+} will be around 709.5 eV and it is accompanied by a satellite peak around 715.5 eV, whereas the BE of Fe-$2p_{1/2}$ for Fe^{2+} will be around 723 eV [62].

The ratio of the area of Co ions in the A-site to the B-site for the unsubstituted compound is obtained as 0.31, and the corresponding ratio of Fe^{3+} in the A-site to B-site is obtained as 0.69 (considering the 1:2 ratio of Co to Fe), in the unsubstituted compound, suggesting a cation distribution of $(Co_{0.31}Fe_{0.69})_A[Co_{0.69}Fe_{1.31}]_BO_4$. This distribution is comparable to that obtained from the magnetic measurements and Raman spectroscopy. There is an increase in the ratio of the area under the curves for the A-site to B-site peaks for $Co2p_{3/2}$, and a corresponding decrease in the ratio of areas of the peaks due to Fe $2p_{3/2}$, suggesting aredistribution of Co^{2+} and Fe^{3+} in the tetrahedral and octahedral sites, as evidenced from the Raman spectroscopy studies.

Table 3.5: *XPS parameters of Co^{2+} for the sintered CMF series samples.*

x	Co-$2p_{3/2}$						Co- $2p_{3/2}$ sat.			Co- $2p_{1/2}$		
	B-site BE (eV)	**Area B-site**	**A-site BE (eV)**	**Area A-site**	**Area 1 (A + B)**	**Area A/B**	**BE of sat. Peak (eV)**	**Area 2 ofsat. peak**	**Area 2/ Area 1**	**BE of B-site (eV)**	**BE of A-site (eV)**	**BE of Sat. (eV)**
0	780.7	2476	782.9	1094	3570	0.44	786.6	2404	0.67	796.6	798.8	803.8
0.05	780.6	2290	782.6	1164	3454	0.50	786.5	1920	0.55	796.4	798.4	803.8
0.1	780.6	2180	782.6	1322	3502	0.51	786.7	1880	0.53	796.3	798.4	803.5
0.2	780.5	2150	782.2	1618	3768	0.75	786.7	1850	0.49	796.2	798.0	803.5

Table 3.6 *: XPS parameters of Fe^{3+} for the sintered CMF series samples.*

x	Fe-$2p_{3/2}$					Fe - $2p_{3/2}$ sat.	Fe - $2p_{1/2}$
	B-site BE (eV)	**Area B- site**	**A-site BE (eV)**	**Area A-site**	**Area A/B**	**BE (eV)**	**BE (eV)**
0	710.8	2207	713.5	1156	0.52	718.4	724.5
0.05	711.1	2260	713.6	1100	0.48	718.3	724.9
0.1	710.7	2280	713.3	1058	0.46	717.6	724.3
0.2	710.8	2350	713.4	991	0.42	717.4	724.4

3.4.6.2 CZF series

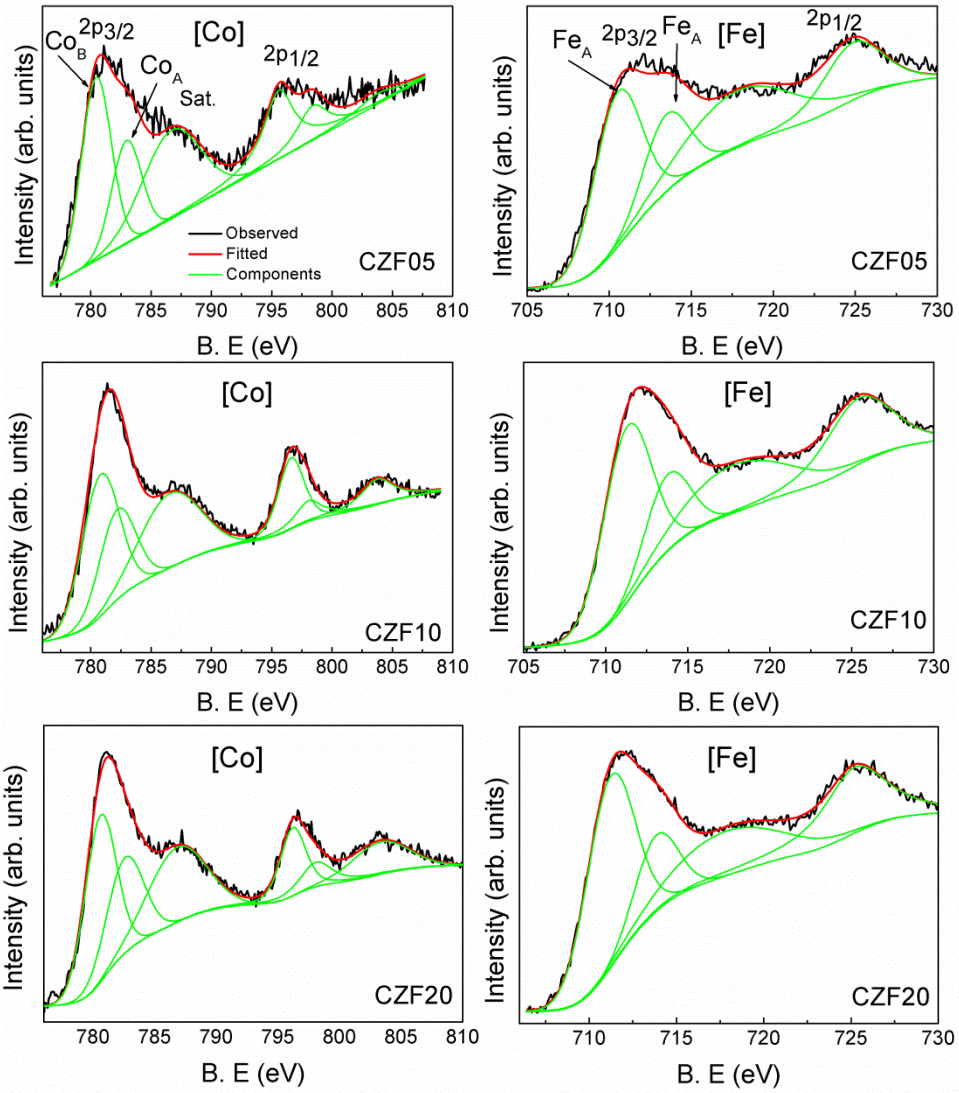

Figure 3.22: *Co-2p and Fe-2p XPS spectra of the CZF series.*

Figure 3.22 shows the deconvoluted Co2p and Fe2p XPS spectra of the sintered compositions CZF05, CZF10 and CZF20 in the CZF series. Similar to the CMF series XPS spectra, the $Co2p_{3/2}$ and $Co2p_{1/2}$ peaks are deconvoluted using two peaks each whereas the corresponding satellite peaks of Co-2p are fitted to a single peak. The areas and binding energies of the peaks corresponding to Co2p spectra are listed in Table 3.7. The intensity of the satellite peak is observed to decrease with increasing Zn content in the lattice of cobalt ferrite signifying convention of Co^{2+} to Co^{3+} to preserve the charge neutrality. As given in Table 3.7, the Co-2p peak is shifted progressively towards lower binding energy side, and the ratio of the area of the peaks for the A to B site is observed to increase with increasing the Zn content in $CoFe_2O_4$ lattice indicating that the Co^{2+} ions are displaced to the A-sites from the

***Table 3.7**: XPS paramters of Co^{2+} for the sintered CZF series samples.*

x	Co-$2p_{3/2}$						Co- $2p_{3/2}$ sat.		Area 2/ Area 1	Co- $2p_{1/2}$		
	B-site BE (eV)	Area B-site	A-site BE (eV)	Area A-site	Area 1 (A + B)	Area A/B	BE of sat. Peak (eV)	Area 2 of sat. peak		BE of B-site (eV)	BE of A-site (eV)	BE of Sat. (eV)
0	780.7	2476	782.9	1094	3570	0.44	786.6	2404	0.67	796.6	798.8	803.8
0.05	780.2	2450	782.9	1363	3813	0.55	786.7	2298	0.60	795.6	798.4	803.8
0.1	780.8	2100	782.2	1300	3400	0.62	786.5	1795	0.53	796.6	798.1	803.7
0.2	780.6	2079	782.6	1389	3468	0.67	786.8	1702	0.49	796.2	798.1	803.3

***Table 3.8**: XPS parameters of Fe^{3+} for the sintered CZF series samples.*

x	Fe-$2p_{3/2}$					Fe - $2p_{3/2}$ sat.	Fe - $2p_{1/2}$
	B-site BE (eV)	Area B- site	A-site BE (eV)	Area A-site	Area A/B	BE (eV)	BE (eV)
0	710.8	2207	713.5	1156	0.52	718.4	724.5
0.05	710.5	2350	713.5	1109	0.47	717.8	724.8
0.1	711.3	2492	713.7	950	0.38	717.8	725.4
0.2	711.2	2548	713.8	870	0.34	717.8	725.2

B-sites. The Fe $2p_{3/2}$ XPS spectral peak was also deconvoluted into two peaks, corresponding to Fe^{3+} in two different crystallographic environments. The BEs and areas of the Fe^{3+} peaks are tabulated in Table 3.8. The area corresponding to the B-site is increased whereas that for the A-site is decreased with increasing the Zn^{2+} concentration indicating more and more Fe^{3+} are displaced from the A-sites to the B-sites. Also, compared to the CMF series samples, the decrease in the ratio of A/B area ratio is more pronounced in the case of the CZF series samples. This again supports the conclusions drawn from the magnetic and Raman spectral analysis.

3.4.7 Magnetostriction studies

Figures 3.23 shows the magnetostriction strain curves of the sintered CMF and CZF series of samples, measured at room temperature, along the parallel [λ_{par}] and perpendicular [λ_{per}] directions to the applied magnetic field. Substitution of Mg^{2+} and Zn^{2+} for Fe^{3+} in the lattice of the cobalt ferrite brought about significant changes in the nature of the magnetostriction curves, measured along both directions. For unsubstituted cobalt ferrite, along the parallel direction, the magnetostriction strain is almost negligible up to an applied magnetic field 100 kA/m. Later, as the field intensity increases, a substantial increment in the strain is observed and reaching a maximum value of -221 ppm at a field 540 kA/m and nearly unchanged at higher applied magnetic field. The maximum magnetostriction value obtained for the $CoFe_2O_4$ in this work is comparable to the values reported for the sintered polycrystalline cobalt ferrite samples [3,8]. However, in the case of the substituted samples in both series, the magnitude of the maximum strain [λ_{max}] is found to be decreased with increasing the substitution content, except for CMF025 and CMF05 in the CMF series where the $[\lambda_{par}]_{max}$ is nearly comparable to that of unsubstituted cobalt ferrite as shown in the Figure 3.24(a). All the substituted compositions exhibit [λ_{max}] values at relatively lower magnetic fields. Unlike for the unsubstituted cobalt ferrite, relatively higher values of magnetostriction strain are observed for all the Zn- and Mg-substituted samples at lower applied field regions (<150 kA/m).

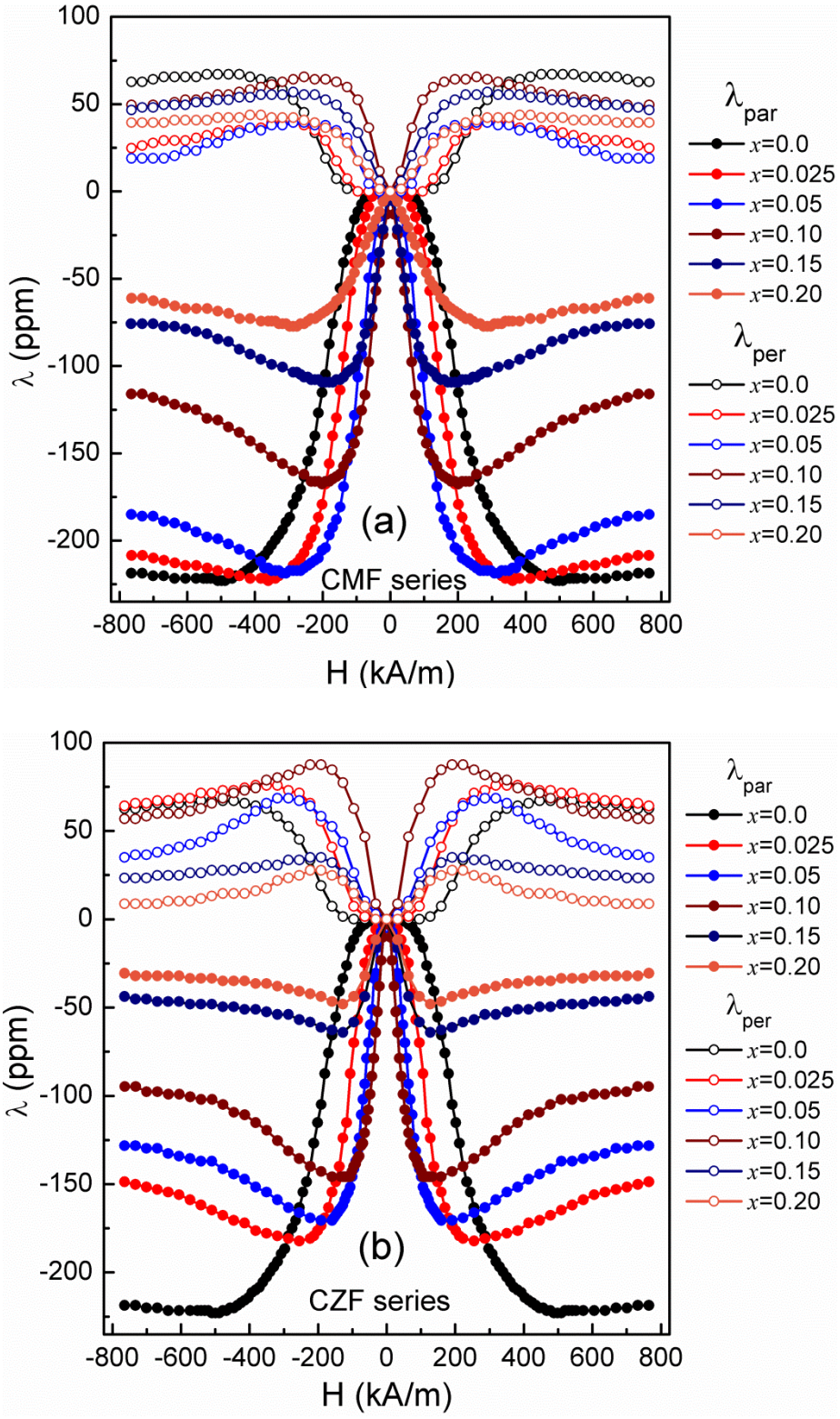

***Figure 3.23**: Magnetostriction strain curves of the sintered (a) CMF and (b) CZF series, measured at room temperature, along the parallel (closed symbol) and perpendicular (open symbol) directions to applied magnetic field.*

Another important observation from the magnetostriction strain curves is that the positive slope is found to increase with increasing the substitution content in both the CMF and CZF series. This is mainly due to the changes in the magnetocrystalline anisotropy of the substituted samples [3,7]. Although $[\lambda_{par}]_{max}$ is lower for the CZF series of samples, the field at which $[\lambda_{par}]_{max}$ is obtained is much lower for the Zn-substituted samples compared to the CMF series. In other words, Zn-substituted samples show higher magnetostriction at low magnetic fields than for the other series. For example, the magnetostriction coefficient has increased from -12 ppm for CF to -106 ppm and -146 ppm, respectively, for CMF05 and CZF05, at a low field of 100 kA/m. Figure 3.24(b) shows a comparison of the variation of magnetostriction at a field of 100 kA/m, as a function of *x*, for both the CMF and CZF series. Higher magnetostriction is obtained for both series for x=0.05 and 0.1. Eventhough anisotropy constant is comparable for the same value of x in both series, the higher magnetostriction associated with Zn-substituted samples at lower magnetic field is mainly due to the strong reduction in the A-O-B superexchange strength induced by the presence of Zn^{2+} at the tetrahedral sites. It is possible that the larger drop in $[\lambda_{par}]_{max}$ above x=0.05 in both the series is due to the migration of Co^{2+} from the octahedral sites to tetrahedral sites with the degree of substitution, as well as the increase in the content of Co^{3+} at the octahedral site with substitution content x, as concluded from the Raman spectral analysis

Table 3.9*: Magnetostriction parameters of the sintered compositions of the CMF series.*

Compositions	**$[\lambda_{par}]_{max}$ (ppm)**	**Field at $[\lambda_{par}]_{max}$ (kA/m)**	**$[\lambda_{per}]_{max}$ (ppm)**	**Field at $[\lambda_{per}]_{max}$ (kA/m)**
CF	-221	541	67	477
CMF025	-222	350	39	286
CMF05	-217	286	39	255
CMF10	-116	191	66	191
CMF15	-109	169	56	223
CMF20	-77	275	44	286

***Table 3.10**: Magnetostriction parameters of the sintered compositions of the CZF series.*

Compositions	$[\lambda_{par}]_{max}$ (ppm)	Field at $[\lambda_{par}]_{max}$ (kA/m)	$[\lambda_{per}]_{max}$ (ppm)	Field at $[\lambda_{per}]_{max}$ (kA/m)
CF	-221	541	67	477
CZF025	-181	182	76	318
CZF05	-170	159	68	286
CZF10	-147	110	87	191
CZF15	-64	127	35	191
CZF20	-46	127	28	191

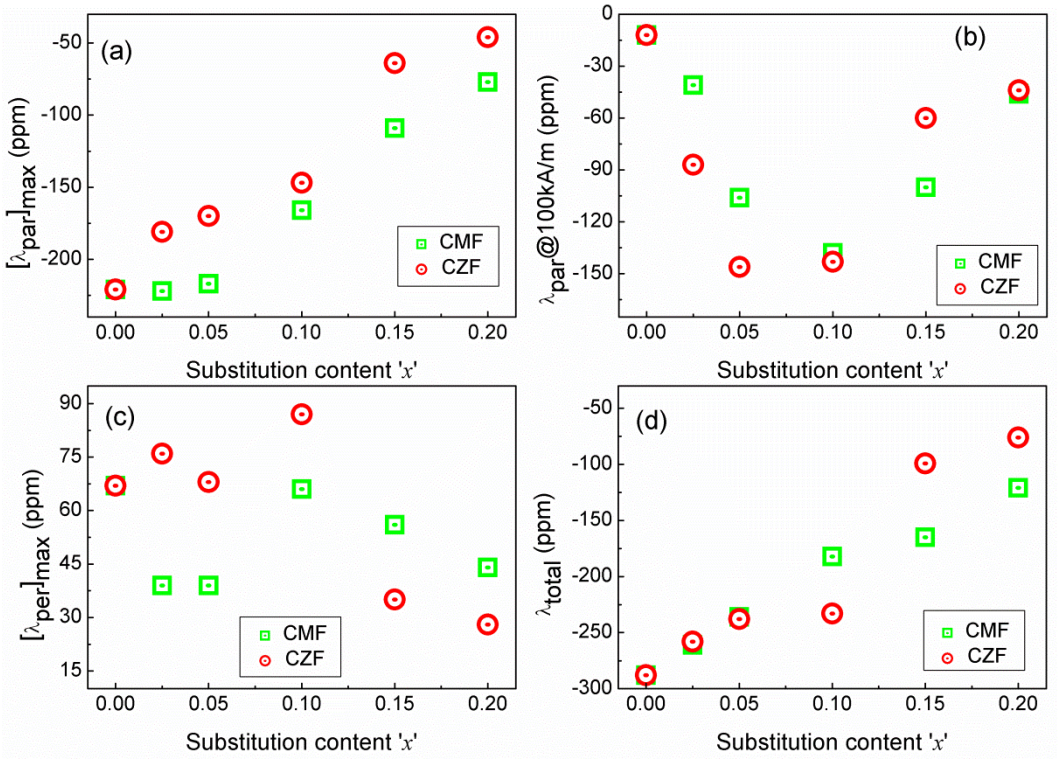

Figure 3.24: Variation of (a) maximum magnetostriction along the parallel direction, $[\lambda_{par}]_{max}$, (b) magnetostriction at 100 kA/m along the parallel direction, (c) the maximum magnetostriction along the perpendicular direction, $[\lambda_{per}]_{max}$, and (d) total magnetostriction, λ_{total}, as a function of x in the CMF and CZF series.

The different magnetostriction parameters are compared in Tables 3.9 and 3.10. Similar to $[\lambda_{par}]_{max}$, all the substituted samples show maximum strain along the perpendicular direction, $[\lambda_{per}]_{max}$, at lower magnetic fields compared to the unsubstituted counterpart. $[\lambda_{per}]_{max}$ is lower for CMF and higher for CZF for $x \leq 0.1$ as shown in Figure 3.24(c). Such

variation in the values of $[\lambda_{par}]_{max}$ and $[\lambda_{per}]_{max}$ with substitution, in particular at lower degrees of substitution, has been reported for other metal-substituted sintered cobalt ferrites [3,25,63,64]. Despite the large variation in the values of $[\lambda_{par}]_{max}$ and $(\lambda_{per})_{max}$ for $x \leq 0.05$ in both series, the total magnetostriction, represented as $\lambda_{total} = [\lambda_{par}]_{max} - [\lambda_{per}]_{max} = 3/2\lambda_S$, where λ_S is the saturation magnetostriction coefficient [3,65], is nearly the same for the compositions $x \leq 0.05$ and decreased with increasing the substitution content x for both series as shown in Figure 3.24(d). This suggests that the substitution affects the orientation of the magnetic moments and hence the domain structure so that the magnetostriction along the different directions are re-distributed and the changes in the magnetostriction coefficient, especially at lower substitution levels, is possibly due to minor local structural distortions.

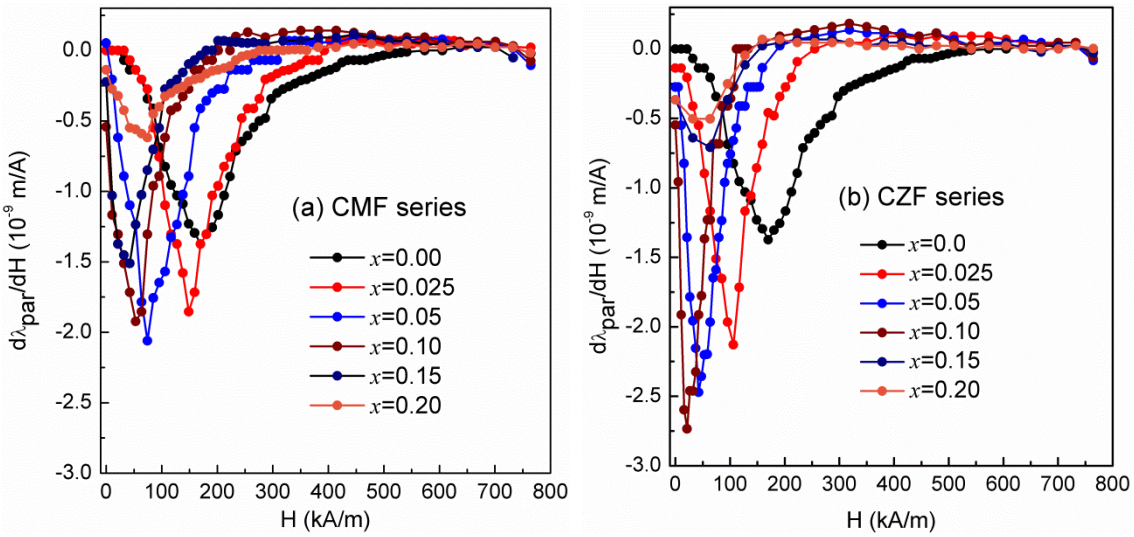

***Figure 3.25**: Field dependance strain sensitivity of (a) CMF and (b) CZF series of samples.*

Figure 3.25 shows the strain sensitivity curves as a function of magnetic field for the CMF and CZF series samples. The variation of the maximum strain sensitivity, $[d\lambda_{par}/dH]_{max}$, for both series, as a function of x is shown in Figure 3.26. The value of $[d\lambda_{par}/dH]_{max}$ of -1.36 $\times$ 10^{-9} m/A for x=0 is comparable to that reported in the literature [30,64]. However, the substituted samples with $x \leq 0.1$ show higher strain sensitivity at much lower magnetic fields than that of the parent compound. Higher magnetostriction strain is obtained at lower magnetic fields, for the similar compositions, as shown in Figure 3.24(b). Higher strain sensitivity of the substituted samples, in particular at a lower degree of substitution, emanates from the combined effect of the reduction in the magnetocrystalline anisotropy as well as the A-O-B superexchange interactions [3,25,30,37]. The lower magnetocrystalline anisotropy of

the substituted samples is evidenced from the magnetic measurements. Thus, lower fields are sufficient to orient the magnetic moments along the applied field direction, leading to higher strain and strain sensitivity at low magnetic fields. For $x \leq 0.1$, the values of $[d\lambda_{par}/dH]_{max}$ for the CZF series are higher than that for similar compositions in the CMF series. For $x>0.1$, $[d\lambda_{par}/dH]_{max}$ decreases dramatically with substitution. A similar trend of decreasing $[d\lambda_{par}/dH]_{max}$ for higher levels of substitution of different metal ions, in cobalt ferrite, is reported in the literature [3,7,66,67]. The decrease in the values of λ_{max} and $[d\lambda_{par}/dH]_{max}$ for $x>0.1$ could be due to the redistribution of Co^{2+} from the octahedral (A) to the tetrahedral (B) sites, combined with the dilution of the octahedral sites by the non-magnetic Co^{3+} ions. This affects the magnetocrystalline anisotropy and the A-O-B superexchange interactions.

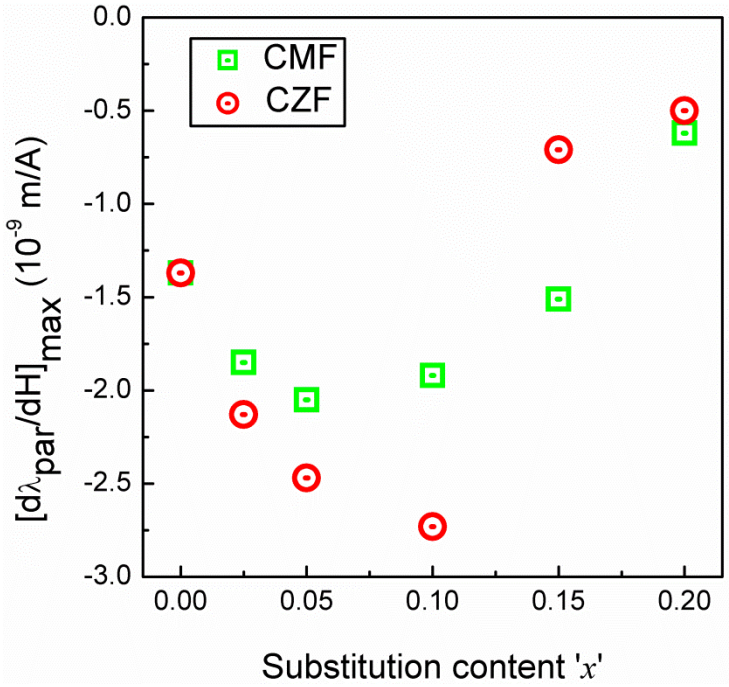

***Figure 3.26**: Variation of the maximum strain sensitivity, $[d\lambda_{par}/dH]_{max}$, as a function of x in the CMF and CZF series.*

Apart from the intrinsic factors associated with the substitution of the divalent metal ions, the microstructure of the sintered compacts is also an important factor that affects the magnitude of $[d\lambda_{par}/dH]_{max}$ [64]. The size, shape, porosity and orientation of the grains affect the magnetic domain structure which is responsible for the magnetostriction effect. However, in the present study, the microstructures are comparable for compositions with the same level of substitution, and therefore the variation in $[d\lambda_{par}/dH]_{max}$ with x is likely to be dominated by the combined effect of magnetic anisotropy and A-O-B superexchange interactions, arising from the distribution of the substituted metal ions. The smaller values of $[\lambda_{par}]_{max}$ and

$[d\lambda_{par}/dH]_{max}$ for similar compositions (Zn- and Mg-substituted) reported in the literature [6,8] are likely to be due to the differences in the cation distribution and microstructure arising from the different preparation and processing conditions, compared to that observed in the present work.

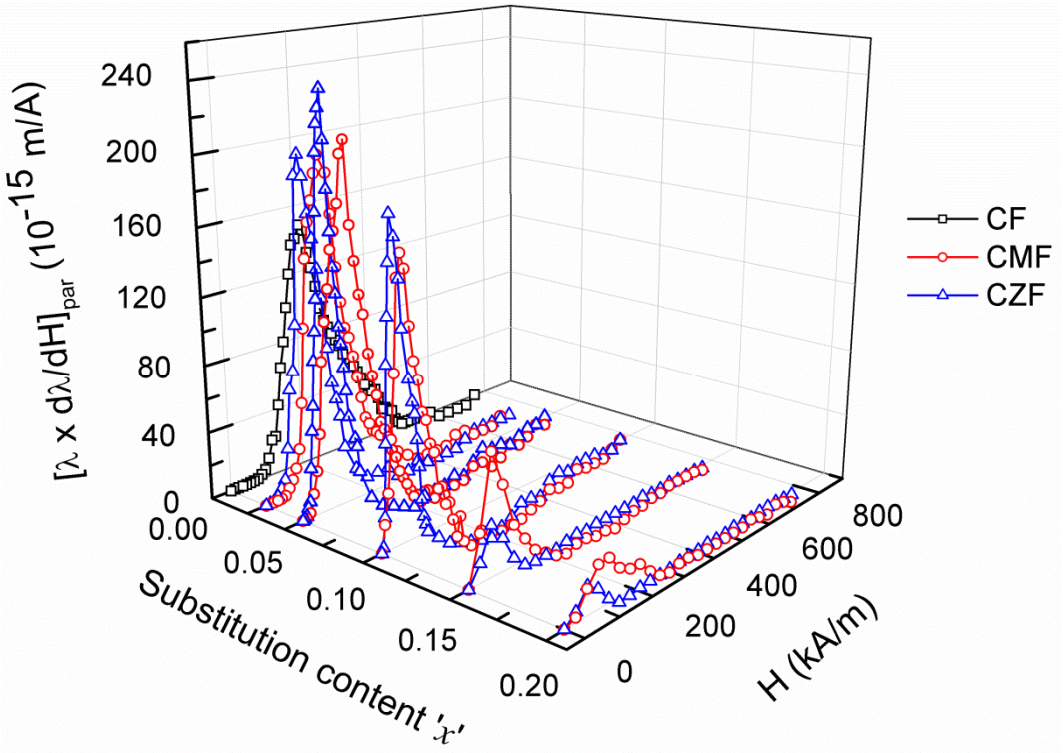

***Figure 3.27**: Variation of $[\lambda \times d\lambda/dH]_{par}$ as a function of substitution content and magnetic field.*

A comparison of the data presented in the Figures 3.23, 3.25 and 3.26 shows that maximum values of λ_{par} and $d\lambda_{par}/dH$ are obtained at different field strengths for different compositions. Hence, a "*Figure of merit*" is defined as $[\lambda \times d\lambda/dH]_{par}$ to identify the compositions giving best performance at a given field strength. Figure 3.27 shows the graph of $[\lambda \times d\lambda/dH]_{par}$ plotted as a function of substitution content *x* and applied magnetic field. As can be seen from Figure 3.27, among all the compositions from the two series, better response to the applied magnetic field is obtained for the compositions CMF05 and CZF05. The maximum value of $[\lambda \times d\lambda/dH]_{max}$ is increased from 150×10^{-15} for CF to 210×10^{-15} m/A for CMF05, and 240×10^{-15} m/A for CZF05. Meanwhile, the field at which the maximum value is obtained is also reduced from 210 kA/m for CF to 140 kA/m for CMF05 and 80 kA/m for CZF05.

3.4.8 Magnetic field annealing

Among the compositions of two studied series in the present work, the compositions CMF025 and CMF05 in the CMF series exhibit $[\lambda_{par}]_{max}$ comparable to that of CF. Therefore, these compositions have been chosen to investigate the effect of magnetic field annealing on the magnetostriction parameters. In this study, magnetic field annealing was carried out in a magnetic field 400 kA/m, at a temperature of 300 ^{o}C for 30 minutes. The magnetostriction strain curves of the annealed composition, measured along the parallel and the perpendicular directions to the applied magnetic field, before and after magnetic field annealing, are presented in Figure 3.28. Along the parallel direction, all the field annealed samples show higher magnitude of $[\lambda_{par}]_{max}$ even at lower magnetic fields compared to that unannealed samples. The values of the magnetostriction parameters and the field at which those parameters are obtained, for the annealed and unannealed samples, are tabulated in Table 3.11.

The enhancement of the magnetostriction strain for the magnetically annealed samples is mainly due to the induced magnetic easy axis (induced uniaxial anisotropy) along the annealing field direction [68-70]. Although the three samples show almost comparable magnetostriction coefficients before field annealing, $[\lambda_{par}]_{max}$ is lower for the substituted samples, after performing magnetic field annealing. This is likely to be due to factors such as the changes in the microstructure where the size and the orientation of the grains are affected and hence the domain structure, changes in the magnetocrystalline anisotropy due to the variations in the cation distribution on substitution, which affects the easy axes, and the magnetization along the easy and hard directions. It is possible that most of the magnetic domains are oriented along the annealing field direction for the substituted samples so that the field annealing effect decreases due to the decreased magnetic anisotropy. Another possible reason is likely to be associated with changes in the domain wall configurations and different magnitudes of uniaxial anisotropy induced in the substituted samples by the annealing temperature and field because T_C, K_1, and M_s of the Mg-substituted compositions are different.

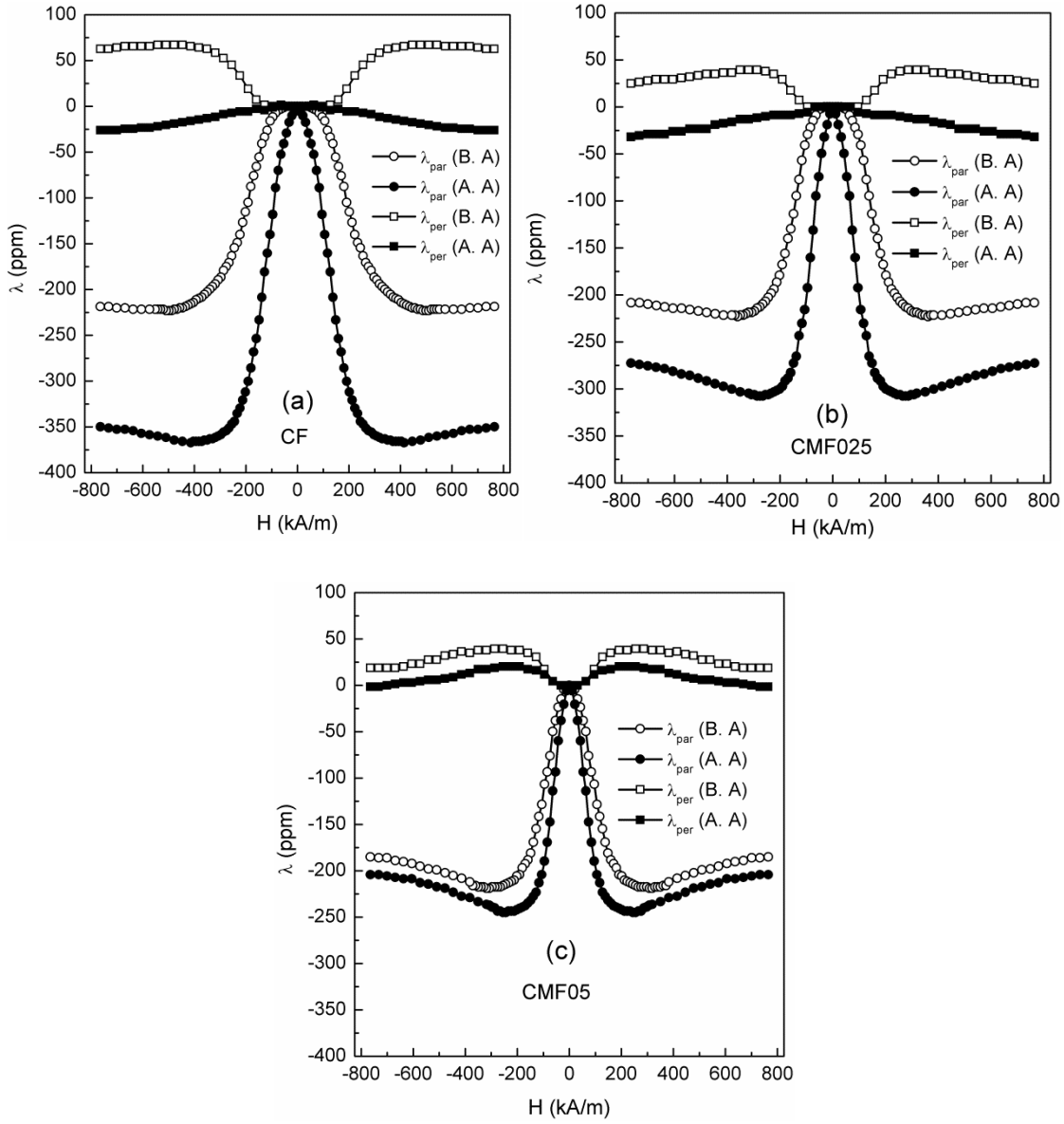

***Figure 3.28**: Comparison of the magnetostriction strain curves of (a) CF, (b) CMF025 and (c) CMF05,measured along parallel (circles) and perpendicular (squares) directions to the applied magnetic field, before annealing (B.A, open symbol) and after annealing (A.A, closed symbol) in field.*

Along the perpendicular direction, compared to the magnetostriction curves of the unannealed samples, significant changes in nature of the magnetostriction curves are observed for the annealed samples. Before field annealing, all the compositions show positive magnetostriction and after the field annealing, the compositions with x=0 and 0.025 manifest negative magnetostriction and do not attain saturation point even at the maximum applied magnetic field. However, in the case of CMF05, the magnetostriction coefficient has the same sign (positive) as that of the unannealed sample. Such variation in the nature of the magnetostriction curves in the substituted and unsubstituted samples, after performing

magnetic field annealing, is attributed to changes in the contribution of the different magnetostriction coefficients, λ_{100}, λ_{111} and λ_{110} [69,70].

***Table 3.11**: Comparison of the magnetostriction parameters of CMF series samples before and after magnetic field annealing.*

Compo--sition	Before annealing		After annealing			
	$[\lambda_{par}]_{max}$ (ppm)	$[d\lambda_{par}/dH]_{max}$ (10^{-9} m/A)	$[\lambda_{par}]_{max}$ (ppm)	H @ λ_{max} (kA/m)	$[d\lambda_{par}/dH]_{max}$ (10^{-9} m/A)	H @ $[d\lambda_{par}/dH]_{max}$ (kA/m)
CF	-221	-1.37	-364	375	-2.66	108
CMF025	-222	-1.85	-310	267	-3.02	94
CMF05	-217	-2.05	-245	215	-2.88	62

3.5 Conclusions

A comparative study has been made on two different series of compositions, $CoMg_xFe_{2-x}O_4$ (CMF) and $CoZn_xFe_{2-x}O_4$ (CZF) for $0 \leq x \leq 0.2$, to understand the role of distribution of the substituted ions on the magnetostriction properties of cobalt ferrite. The impact of the substitution of divalent Zn^{2+} and Mg^{2+} ions for trivalent Fe^{3+}ions in the lattice of cobalt ferrite on the structural, microstructural, magnetic, and magnetostriction parameters is evaluated. The lattice parameter is found to decrease non-linearly with a small drop for $x \leq 0.05$ and large decline for higher values of x, due to the conversion of Co^{2+} to Co^{3+} to maintain charge neutrality. The saturation magnetization, M_s, is found to decrease with x in the CMF series, whereas it increased up to the composition $x=0.15$ in the CZF series and then decreased for the higher values of x indicating substitution of Zn for Fe at the A-sites whereas Mg for Fe at the B-sites. The coercivity, H_c, is found to decrease up to the composition $x=0.1$ and remains constant for $x \geq 0.1$. The microstructures of the sintered compacts also showed the significant variation for compositions with $x \leq 0.05$ and $x \geq 0.1$. A decrease in the Curie temperature, T_C, is observed, in the order of CZF>CMF, revealing a strong reduction in the A-O-B exchange strength for the Zn-substituted samples. A fast decrease in the magnetocrystalline anisotropy constant, K_1, has been observed up to $x=0.1$ with comparable

K_1 for the similar values of x, and remains constant for the higher values of x. Raman spectra analysis revealed that Zn is substituted for Fe at the A-sites whereas a small amount of Mg is also substituted for Fe at A-sites (for $x \leq 0.1$) but a large amount of Mg is substituted for Fe at the B-sites. This supported the conclusions drawn from the magnetic measurements. The careful spectra analysis also revealed the presence of Co^{3+} at the B-sites in the substituted samples. Anomalies in the variation of the structural, magnetic and magnetostriction parameters are observed for $x \leq 0.05$ and $x > 0.05$, for both studied series of compositions. The differences in the variations of the different parameters are explained in terms of i) site preference and distribution of the substituted cations as well as re-distribution of the divalent cobalt ions in the tetrahedral and octahedral sites of the spinel lattice, ii) conversion of Co^{2+} into Co^{3+} to maintain the charge neutrality, due to the substitution of Fe^{3+} by the divalent metal ions, and iii) associated changes in the magnetocrystalline anisotropy, and iv) changes in the A-O-B superexchange interactions. It is found that magnetostriction parameters can be enhanced at smaller levels of substitution. The substituted ion (Zn) at the tetrahedral site enhances the strain derivative with large reduction in the magnetostriction coefficient whereas substitution at the octahedral sites (Mg substitution) decreases the strain sensitivity without much affecting the magnetostriction coefficient. It is proposed that the changes in the magnetostriction parameters at low substitution levels is likely to be due to an inhomogeneous distribution of the substituted metal ions in the unit cells which affect the local structure which in turn affect the magnetocrystalline anisotropy and magnetization. In conclusion, Zn-substituted samples ($x \leq 0.1$) show better magnetostriction parameters at lower magnetic fields compared to the similar compositions of Mg-substituted series. This is mainly due to the strong reduction in the A-O-B superexchange interactions accompanied by the presence of Zn ions at the tetrahedral sites.

Bibliography

[1] J. C. Slonczewski, *J. Appl. Phys*. **32**, S253 (1961).

[2] R. M. Bozorth, E. F. Tilden, and A. J. Williams, *Phys. Rev*. **99**, 1788 (1955).

[3] S. H. Song, *Doctoral Dissertation* (Dept. of Materials Science and Engineering, Iowa State University, Ames, Iowa, 2007).

[4] E. du Tremolet de la Cheisserie, D. Gignoux, and M. Schlenker, *Magnetism I-Fundamentals*, (Kluwer Academic Publishers Group, 2002).

[5] S. D. Bhame and P. A. Joy, *J. Appl. Phys*. **99**, 073901 (2006).

[6] S. D. Bhame and P. A. Joy, *J. Phys. D: Appl. Phys*. **40**, 3263 (2007).

[7] N. Somaiah, T. V. Jayaraman, P. A. Joy, and D. Das, *J. Magn. Magn. Mater*. **324**, 2286 (2012).

[8] I. C. Nlebedim, R. L. Hadimani, R. Prozorov, and D. C. Jiles, *J. Appl. Phys*. **113**, 17A928 (2013).

[9] S. D. Bhame and P. A. Joy, *Sens. Actuators A* **137**, 256 (2007).

[10] S. D. Bhame and P. A. Joy, *J. Am. Ceram. Soc*. **91**, 1976 (2008).

[11] K. K. Mohaideen and P. A. Joy, *J. Eur. Ceram. Soc*. **34**, 677 (2014).

[12] I. C. Nlebedim, J. E. Snyder, A. J. Moses, D. C. Jiles, *J. Magn. Magn. Mater*. **322**, 3938 (2010).

[13] K. K. Mohaideen and P. A. Joy, *J. Magn. Magn. Mater*. **346**, 96 (2013).

[14] K. K. Mohaideen and P. A. Joy, *ACS Appl. Mater. Interfaces* **4**, 6421 (2012).

[15] K. K. Mohaideen and P. A. Joy, *Curr. Appl. Phys*. **13**, 1697 (2013).

[16] P. Thakuria and P. A. Joy, *Appl. Phys. Lett*. **97**, 162504 (2010).

[17] L. Kumar and M. Kar, *J. Magn. Magn. Mater*. **323**, 2042 (2011).

[18] A. A. Birajdar, S. E. Shirsath, R. H. Kadam, M. L. Mane, D. R. Mane and A. R. Shitre, *J. Appl. Phys*. **112**, 053908 (2012).

[19] L. Kumar, P. Kumar, and M. Kar, *J. Alloys compd*. **551**, 72 (2013).

[20] R. D. Shannon, *Acta Crystallogr. A* **32**, 751 (1976).

[21] H. L. Trong, L. Presmanes, E. D. Grave, A. Barnabe, C. Bonningue, and P. Tailhades, *J. Magn. Magn. Mater*. **334**, 66 (2013).

[22] O. Knop, K. I. G. Reid, Sutarno, and Y. Nakagawa, *Can. J. Chem*. **46**, 3463 (1968).

[23] J. Smith and H. P. J. Wijin, *Ferrites*, (Philips Technical Library, Eindhoven, the Netherland 1965).

[24] B. D. Cullity and C. D. Graham, *Introduction to Magnetic Materials* (John Wiley & Sons New Jersey, 2009).

[25] P. N. Anantharamaiah and P. A. Joy, *Mater. Lett*. **192**, 169 (2017).

[26] R. Pandit, K. K. Sharma, P. Kaur and R. Kumar, *Mater. Chem. Phys*. **148**, 988 (2014).

[27] S. Chikazumi, *Physics of Ferromagnetism*, (Oxford university press, Oxford, 1997).

[28] I. C. Nlebedim, N. Ranvah, P. I. Williams, Y. Melikhov, J. E. Snyder, A. J. Moses, and D. C. Jiles, *J. Magn. Magn. Mater*. **322**, 1929 (2010).

[29] A. Muhammad, R. Sato-Turtelli, M. Kriegisch, R. Grossinger, F. Kubel, and T. Konegger, *J. Appl. Phys*. **111**, 013918 (2012).

[30] P. N. Anantharamaiah and P. A. Joy, *J. Mater. Sci*. **50**, 6510 (2015).

[31] Y. Melikhov, J. E. Snyder, C. C. H. Lo, P. N. Matlage, S. H. Song, K. W. Dennis, and D. C. Jiles *IEEE Trans. Magn*. **42**, 2861 (2006).

[32] G. A. Sawatsky, F. van Der Woude and A. H. Morrish, *Phys. Rev*. **187**, 747 (1969).

[33] G. S. N. Rao, O. F. Caltun, K. H. Rao, P. S. V. S. Rao, and B. P. Rao, *J. Magn. Magn. Mater*. 334, 66 (2013).

[34] A. Goldman, *Modern Ferrite Technology* (Van Nostrand Reinhold, New York, 1990).

[35] R. Nongjai, S. Khan, K. Asokan, H. Ahmed, and I. Khan, *J. Appl. Phys*. 112, 084321 (2012).

[36] P. A. Joy and S. K. Date, *J. Magn. Magn. Mater*. **222**, 33 (2000).

[37] I. C. Nlebedim and D. C. Jiles, *Smart Mater. Struct*. **24**, 025006 (2015).

[38] S. E. Shirsath, B. G. Toksha and K. M. Jadhav, *Mater. Chem. Phys*. **117**, 163 (2009).

[39] B. Vishwanathan and V. R. K. Murthy, *Ferrite Materials Science and Technology* (Narosa Publishing House, New Delhi, 1990).

[40] B. D. Hosterman, *PhD thesis*, (University of Nevada, Los Vegas, 2011).

[41] V. D'lppolito, G. B. Andreozzi, D. Bersani and P. P. Lottici, *J. Raman Spectrosc*. **46**, 1255 (2015).

[42] P. Chandramohan, M. P. Srinivasan, S. Velmurugan and S. V. Narasimha, *J. Solid State Chem*. **184**, 89 (2011).

[43] F. J. Manjon, I. Tiginyanu and V. Ursaki, *Pressure-Induced Phase Transitions in AB2X4 Chalcogenide Compounds*, (Springer-Verlag, Berlin, Heidelberg, 2014).

[44] G. V. M. Jacintho, A. G. Brolo, P. Corio, P. A. Z. Suarez, and J. C. Rubim, *J. Phys. Chem. C* **113**, 7684 (2009).

[45] K. B. Modi, P. Y. Raval, S. J. Shah, C. R. Kathad, S. V. Dulera, M. V. Popat, K. B. Zankat, K. G. Saija, T. K. Pathak, N. H. Vasoya, V. K. Lakhani, U. Chandra, and P. K. Jha, *Inorg. Chem*. **54**, 1543 (2015).

[46] G. Shemer, E. Tirosh, T. Livnesh, and G. Markovich, *J. Phys. Chem. C* **111**, 14334 (2007).

[47] K. Samanta, P. Bhattacharya and R. S. Katiyar, *Phys. Rev. B* **73**, 245213 (2006).

[48] S. Ratha, R. T. Khare, M. A. More, R. Thapa, D. J. Late, and C. S. Rout, *RSC Adv*. **5**, 5372 (2015).

[49] Z. Wang, D. Schiferl, Y. Zhao, and H. St. C. O'Neill, *J. Phys. Chem. Solids* **64**, 2517 (2003).

[50] S. W. da Silva, F. Nakagomi, M. S. Silva, A. Franco, V. K. Garg, A. C. Oliveira, and P. C. Morais, *J. Appl. Phys*. **107**, 09B503 (2010).

[51] A. B. Nawale, N. S. Kanhe, K. R. Patil, V. R Reddy, A. Gupta, B. B. Kale, S. V. Bhoraskar, V. L. Mathe, and A. K. Das, *Mater. Chem. Phys*. **137**, 586 (2012).

[52] G. C. Allen and K. R. Hallam, *Appl. Surf. Sci*. **93**, 25 (1996).

[53] M. Oku and K. Hirokawa, *J. Electron Spectrosc. Relat. Phenom*. **8**, 475 (1976).

[54] H. A. E. Hagelin-Weaver, G. B. Hoflund, D. M. Minahan, and G. N. Salaita, *Appl. Surf. Sci*. **235**, 420 (2004).

[55] T. Mathew, N. R. Shiju, K. Sreekumar, B. S. Rao, and C. S. Gopinath, *J. Catal*. **210**, 405 (2002).

[56] H. Wu, G. Wu, Y. Ren, L. Yang, L. Wang, and X. Lid, *J. Mater. Chem. C* **3**, 7677 (2015).

[57] X. F. Lu, D. Wu, R. Li, Q. Li, S. Ye, Y. Tong and G. Li, *J. Mater. Chem. A* **2**, 4706 (2014).

[58] Y. Ding, L. Zhu, A. Huang, X. Zhao, X. Zhang and H. Tang, *Catal. Sci. Technol*. **2**, 1977 (2012).

[59] H. Taguchi, H. Kido and K. Tabata, *Physica B* **344**, 271 (2004).

[60] Z. Gu, X. Xiang, G. Fan, and F. Li, *J. Phys. Chem. C* **112**, 18459 (2008).

[61] W. P. Wang, H. Yang, T. Xian and J. L. Jiang, *Mater. Trans. JIM* **53**, 1586 (2012).

[62] T. Yamashita and P. Hayes, *Appl. Surf. Sci*. **254**, 2441 (2008).

[63] S. D. Bhame and P. A. Joy, *J. Appl. Phys*. **100**, 113911 (2006).

[64] M. Atif, R. Sato-Turtelli, R. Grossinger, and F. Kubel, *J. Appl. Phys*. **113**, 153902 (2013).

[65] S. F. Xu, H. P. Zhang, W. Q. Wang, S. H. Guo, W. Zhu, Y. H. Zhang, X. L. Wang, D. L. Zhao, J. L. Chen, and H. H. Wu, *J. Phys. D: Appl. Phys*. **41**, 015002 (2008).

[66] N. Ranvah, I. C. Nlebedim, Y. Melikhov, J. E. Snyder, P. I. Williams, A. J. Moses, and D. C. Jiles, *IEEE Trans. Magn*. **45**, 4261 (2009).

[67] S. J. Lee, C. C. H. Lo, P. N. Matlage, S. H. Song, Y. Melikhov, J. E. Snyder, and D. C. Jiles, *J. Appl. Phys*. **102**, 073910 (2007).

[68] C. C. H. Lo, A. P. Ring, J. E. Snyder, and D. C. Jiles, *IEEE Trans. Magn*. **41**, 3676 (2005).

[69] A. Muhammad, R. Sato-Turtelli, M. Kriegisch, R. Grossinger, F. Kubel, and T. Konegger, *J. Appl. Phys*. **111**, 013918 (2012).

[70] Y. X. Zheng, Q. Q. Cao, C. L. Zhang, H. C. Xuan, L. Y. Wang, D. H. Wang, and Y. W. Du, *J. Appl. Phys*. **110**, 043908 (2011).

Chapter 4

Studies on trivalent metal ion substituted cobalt ferrite, $CoM_xFe_{2-x}O_4$ (M=Al, Ga, In)

4.1 Introduction

In the previous chapter, it is found that substitution of Fe^{3+} in cobalt ferrite by the divalent nonmagnetic cations (Zn^{2+} and Mg^{2+}), having almost comparable sizes, has brought about a substantial decrease in the magnetostriction parameters (λ_{max} and $[d\lambda/dH]_{max}$) for the compositions x>0.1. When divalent nonmagnetic cations are substituted for the trivalent Fe ions, an equivalent amount of Co^{2+} is converted to Co^{3+} to keep the system electrically neutral. To preserve the oxidation state of Co^{2+}, trivalent nonmagnetic spinel forming cations can be substituted for Fe^{3+} in the cobalt ferrite. Studies on the effect of substitution of Fe^{3+} by trivalent nonmagnetic ions are reported in this chapter. In the present study, three nonmagnetic trivalent metal ions (In^{3+}, $Ga^{3+,}$ and Al^{3+}), having different ionic radii with different crystallographic site preferences, are selected for substitution in place of Fe in $CoFe_2O_4$. The ionic radius of In^{3+} is much larger, Al^{3+} is much smaller, and Ga^{3+} is nearly comparable when comparable to the size of Fe^{3+}, as shown in Table 4.1. In^{3+} and Ga^{3+} have a tendency to occupy the tetrahedral sites [1-4] whereas Al^{3+} has a tendency to occupy both the tetrahedral and octahedral sites, with larger amounts preferably at the octahedral sites of the spinel lattice [5-7]. For a better comparison and correlation, different compositions in $CoIn_xFe_{2-x}O_4$, $CoGa_xFe_{2-x}O_4$ and $CoAl_xFe_{2-x}O_4$ ($0 \leq x \leq 0.3$) are prepared by the same wet chemical method and processed under identical conditions. The roles of size effect and site preference of In^{3+}, Ga^{3+} and Al^{3+} in the cobalt ferrite lattice on the structural, magnetic and magnetostrictive properties are investigated. It is expected that apart from the valency effect and amount of substitution, the size of the substituted ion may influence the magnetostriction properties of cobalt ferrite.

***Table 4.1**: Ionic radii of the different metal ions, taken from the ref. [8]*

Ion	**Ionic radii (Å)**	
	4-coordination	**6-coordination**
Al^{3+}	0.39	0.53
Fe^{3+}	0.49	0.645
Ga^{3+}	0.47	0.62
In^{3+}	0.62	0.80

4.2 Materials synthesis

Different compositions in the series $CoM_xFe_{2-x}O_4$ (M= In, Ga, Al) for $0 \leq x \leq 0.3$ have been synthesized using a citrate-gel method [9]. Stoichiometric amounts of the corresponding metal nitrates ($Co(NO_3)_2.6H_2O$, $Fe(NO_3)_3.9H_2O$, $In(NO_3)_3.9H_2O$, $Ga(NO_3)_3.H_2O$ and $Al(NO_3)_3.9H_2O$ (all Aldrich, [99 %)) were dissolved separately in 75 ml of distilled water and then mixed. The mixed solution was added drop wise to citric acid (1.5 moles per mole of metal ion) solution dissolved in 75 ml of distilled water in a 1000 ml crystallizing dish, with constant stirring at 50 ^oC. The stirring was continued for two h at the same temperature to obtain a sol. Ethylene glycol (citric acid:ethylene glycol ratio of 70:30) was added to the metal citrate sol with constant stirring at 75 ^oC. The stirring was continued until a thick, viscous gel was formed and the gel was dried in an oven at 80 ^oC for 24 h. During the process of drying, the gel swelled into a fluffy mass and eventually broken down into black flakes. The resultant black flakes were pulverized using an agate mortar and pestle and calcined at 500 ^oC for 2 h in a muffle furnace. The powder samples obtained were pressed into the form of cylindrical pellets (8 mm diameter × 12 mm length) using 2 % polyvinyl alcohol as a binder at a pressure of 8 MPa. The pressed compacts were sintered following the two-stage sintering process. For the two-stage sintering, pressed compacts were initially heated to 1350 ^oC at a heating rate of 10 ^oC/min and rapidly cooled to 1200 ^oC at a cooling rate of 30 ^oC/min, held at 1200 ^oC for 2 h and then cooled to room temperature at a cooling rate of 20 ^oC/min. The density of all the sintered compacts was calculated from their measured volume and weight. The percentage sintered density was obtained from the ratio of the experimental density to the theoretical density calculated from the lattice parameter. The different substituted compositions in $CoIn_xFe_{2-x}O_4$, $CoGa_xFe_{2-x}O_4$, and $CoAl_xFe_{2-x}O_4$ are labeled as CIF series, CGF series, and CAF series, respectively. The sample codes are given in Table 4.2.

Table 4.2*: Different trivalent ion substituted compositions and the corresponding sample codes.*

x	**$CoIn_xFe_{2-x}O_4$ (CIF series)**	**$CoGa_xFe_{2-x}O_4$ (CGF series)**	**$CoAl_xFe_{2-x}O_4$ (CAF series)**
0	CF	CF	CF
0.10	CIF10	CGF10	CAF10
0.20	CIF20	CGF20	CAF20
0.30	CIF30	CGF30	CAF30

4.3 Characterization of the calcined powders

4.3.1 Powder X-Ray diffraction

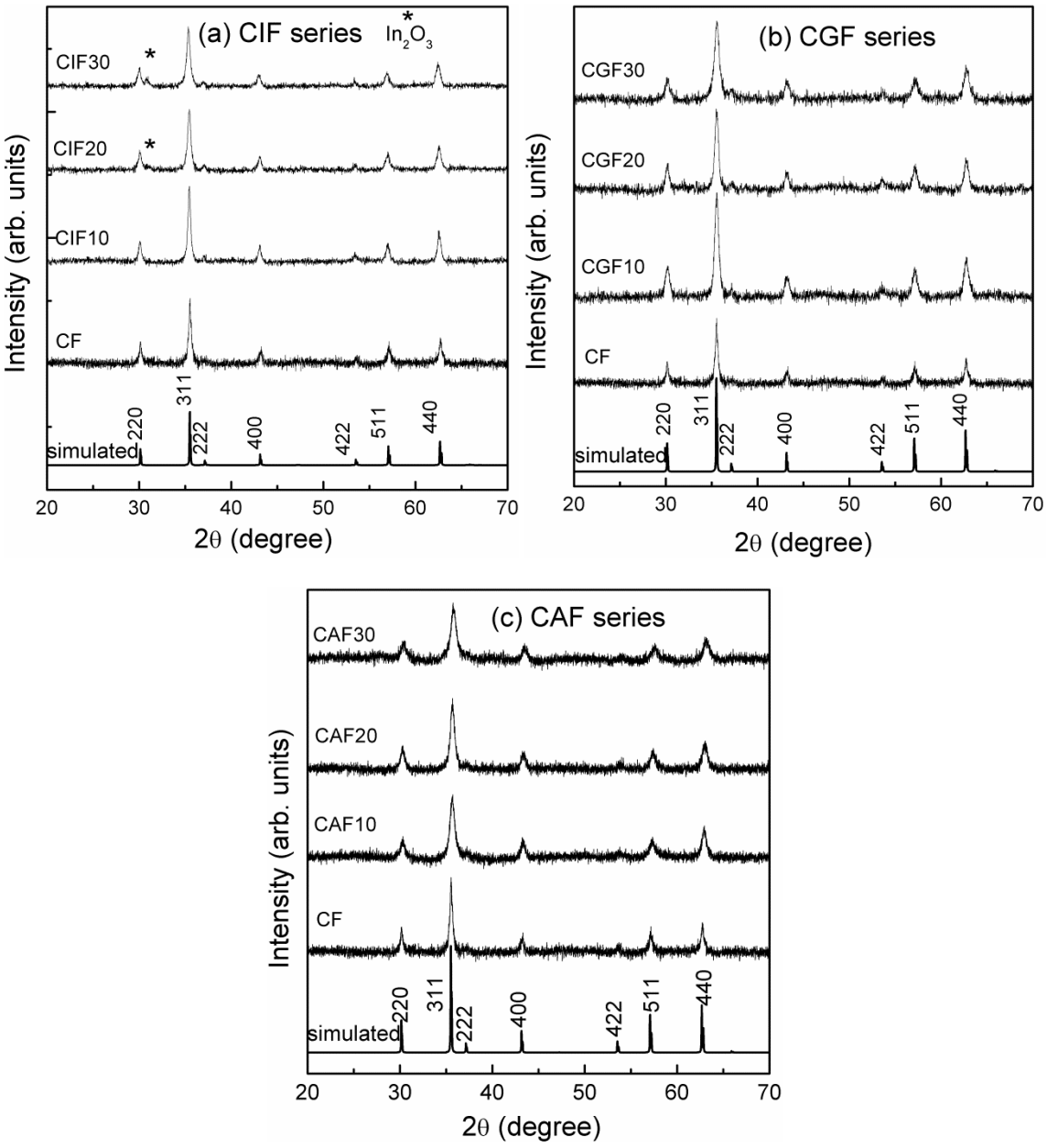

***Figure 4.1**: XRD patterns of the calcined powder samples of (a) CIF (b) CGF and (c) CAF series of samples. Simulated XRD pattern of $CoFe_2O_4$ is shown in each graph for comparison.*

The XRD patterns of the calcined CIF, CGF and CAF series of samples are presented in Figure 4.1. In all three series, the diffraction peaks in the observed XRD patterns are symmetrically broad, indicating the nanocrystalline nature of the particles. In the case of CIF series, on comparison with the simulated XRD pattern of $CoFe_2O_4$, the CF and CIF10

samples are found to form single phase compositions. On the other hand, an extra peak, other than the peaks of spinel phase, has been noticed in the patterns of CIF20 and CIF30 at a diffraction angle $2\theta \approx 30.8^{o}$ (Figure 4.1(a)), and this peak corresponds to that of In_2O_3 (JCPDS 71-2194). Appearance of In_2O_3, as a secondary phase, in the CIF20 and CIF30 compositions is primarily attributed to size effect of In^{3+} ion. The ionic radius of In^{3+} (0.80 for octahedral and 0.62 Å for tetrahedral geometries) is much larger than that of Fe^{3+} (0.645 for octahedral and 0.49 Å for tetrahedral geometries) [8]. The appearance of In_2O_3 as a secondary phase in the nanocrystalline powders of the In-substituted cobalt ferrite, particularly at higher levels of substitution, has been reported in the literature [10]. Several studies on the In-substituted spinel ferrites including cobalt ferrite, prepared by conventional solid state reaction method, have been reported in the literature [1,2,11,12]. In those reported studies, even at a higher amount of In-substitution in the spinel ferrite lattice, the ferrite samples are found to form a single phase solid solutions, without any traceable In_2O_3 phase. Thus, it is apparent that the appearance of In_2O_3 in the nanocrystalline In-substituted spinel ferrites is most likely to be due to the insufficient heat treatments. The calcination temperature used in the present study may not be sufficient to insert all the large size In^{3+} ions into the lattice of the cobalt ferrite and hence the presence of In_2O_3 in the CIF20 and CIF30 compositions.

In the case of CGF and CAF, all the substituted compositions are found to form single phase spinel ferrites without any secondary phases (Figures 4.1(b) and 4.1(c)). In all three cases, with increasing the degree of substitution, the width of the peaks is observed to increase suggesting reduction of crystallite size, as discussed in the chapter 3 (section 3.3.1). The average crystallite size of all the compositions is calculated using the Scherrer's formula from the width of the most intense 311 peak after subtracting the instrumental contribution to the line broadening. In all three cases, the average crystallite size decreased from ~20 nm for x=0 to ~12 nm for x=0.3.

4.3.2 Transmission Electron Microscopy

Figure 4.2 shows the TEM images of selected calcined powders in the three different series. The ferrite particles have nearly spherical shaped morphology with inhomogeneity in the size distributions. Compared to the unsubstituted composition, relatively large number of smaller sized particles can be seen in the TEM images of the substituted compositions. The particle size measured from the TEM images (shown as a histogram) is comparable to that of the crystallite size calculated from the powder XRD patterns. The reduction in the

particle/crystallite size after the substitution by different metal ions into the lattice of the parent compound is likely to be due to the lattice strain induced in the substituted compositions, as discussed in Chapter 3 (section 3.3.1).

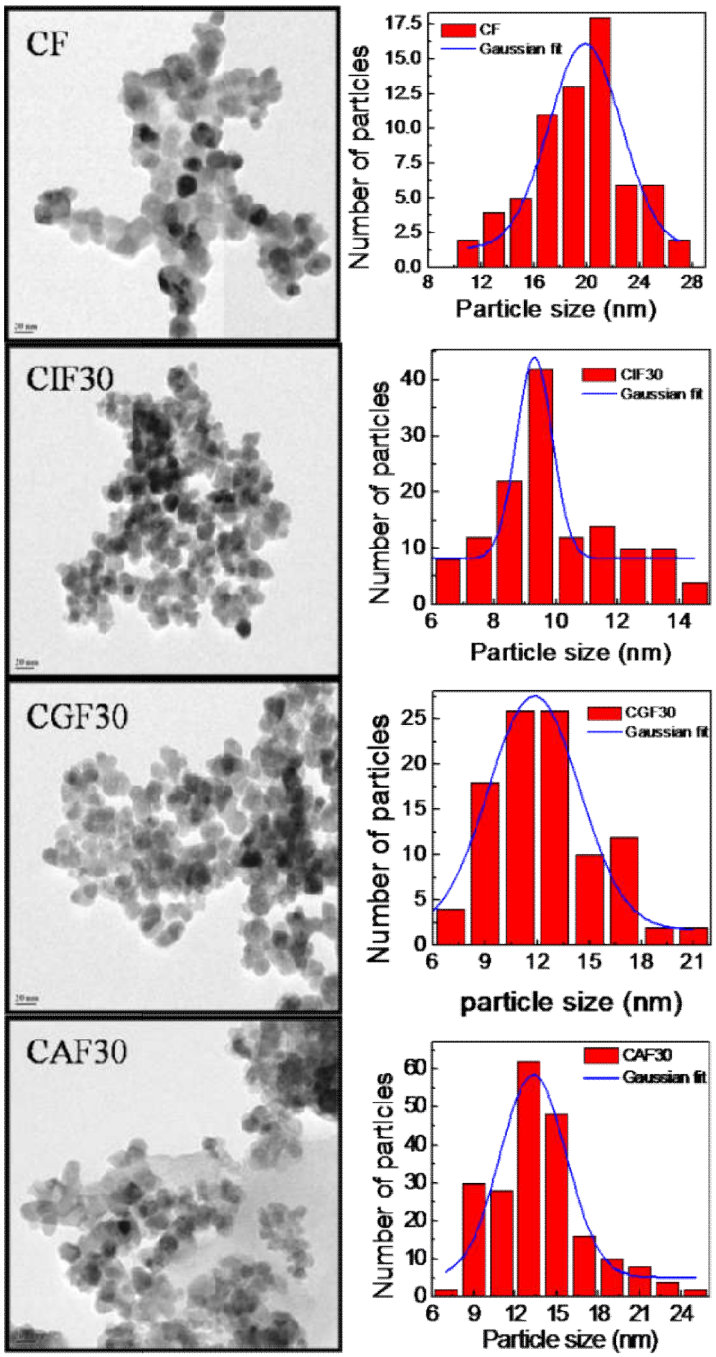

***Figure 4.2**: TEM images of the calcined powders of selected compositions and the corresponding particle size distribution histograms.*

4.4 Characterization of the sintered samples

4.4.1 Structure

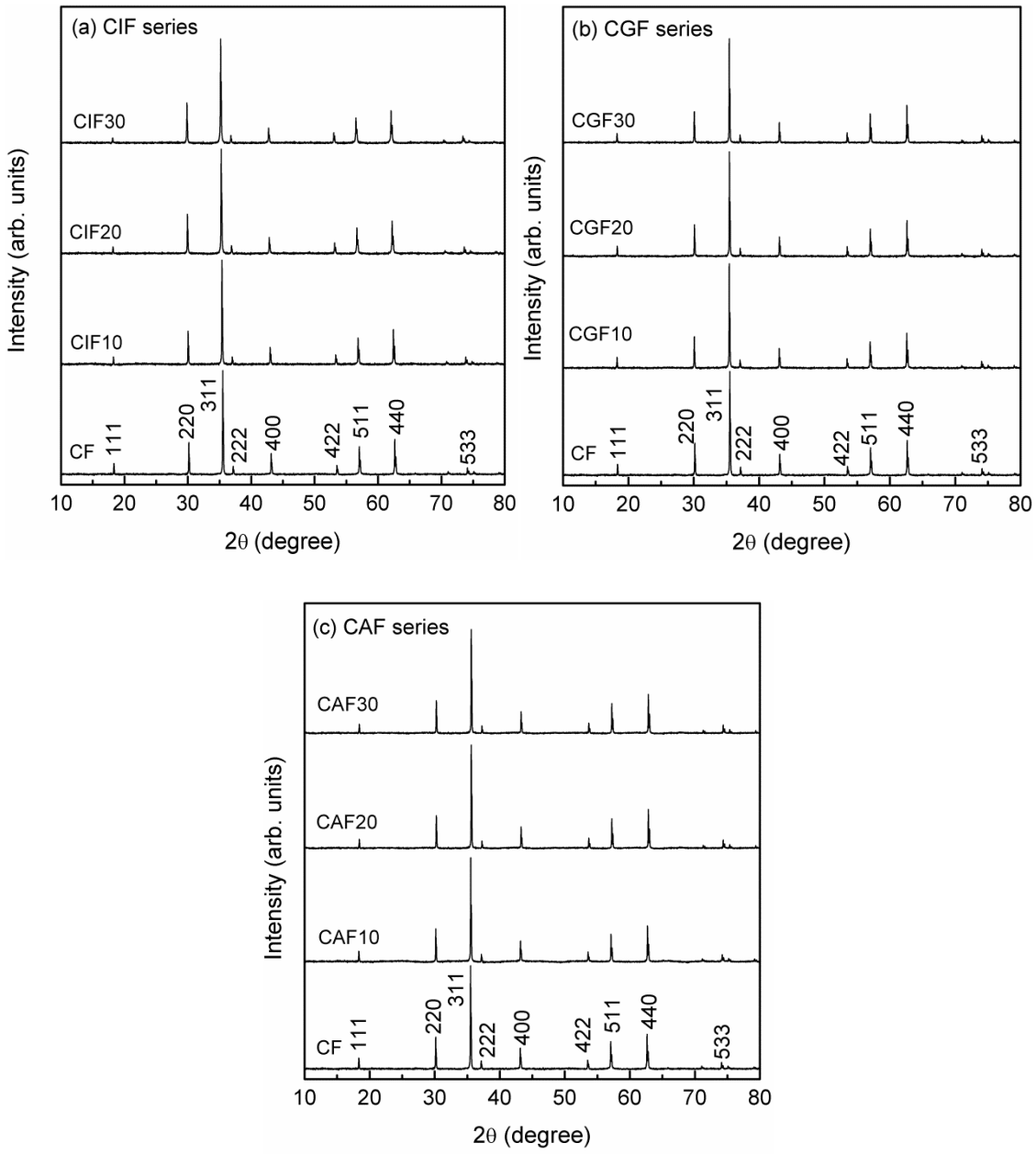

***Figure 4.3**: XRD patterns of the sintered samples of (a) CIF, (b) CGF, and (c) CAF series.*

XRD patterns of the sintered samples of all the three series are presented in Figure 4.3. Unlike calcined powders, all the sintered compositions in the CIF series are found to form single phase cubic spinel compounds without any impurities. This indicates that, at very high temperatures, thermal energy is sufficient for the reaction of the In_2O_3 impurity phase to form the ferrite phase. The sintered compositions of CAF and CGF series are also found to form

single phase spinel ferrite. The phase purity and structural parameters of the sintered compositions of all the three series are ascertained by Rietveld refinement studies, and the results of the Rietveld refinement analysis of all the compositions are given in Figure 4.4.

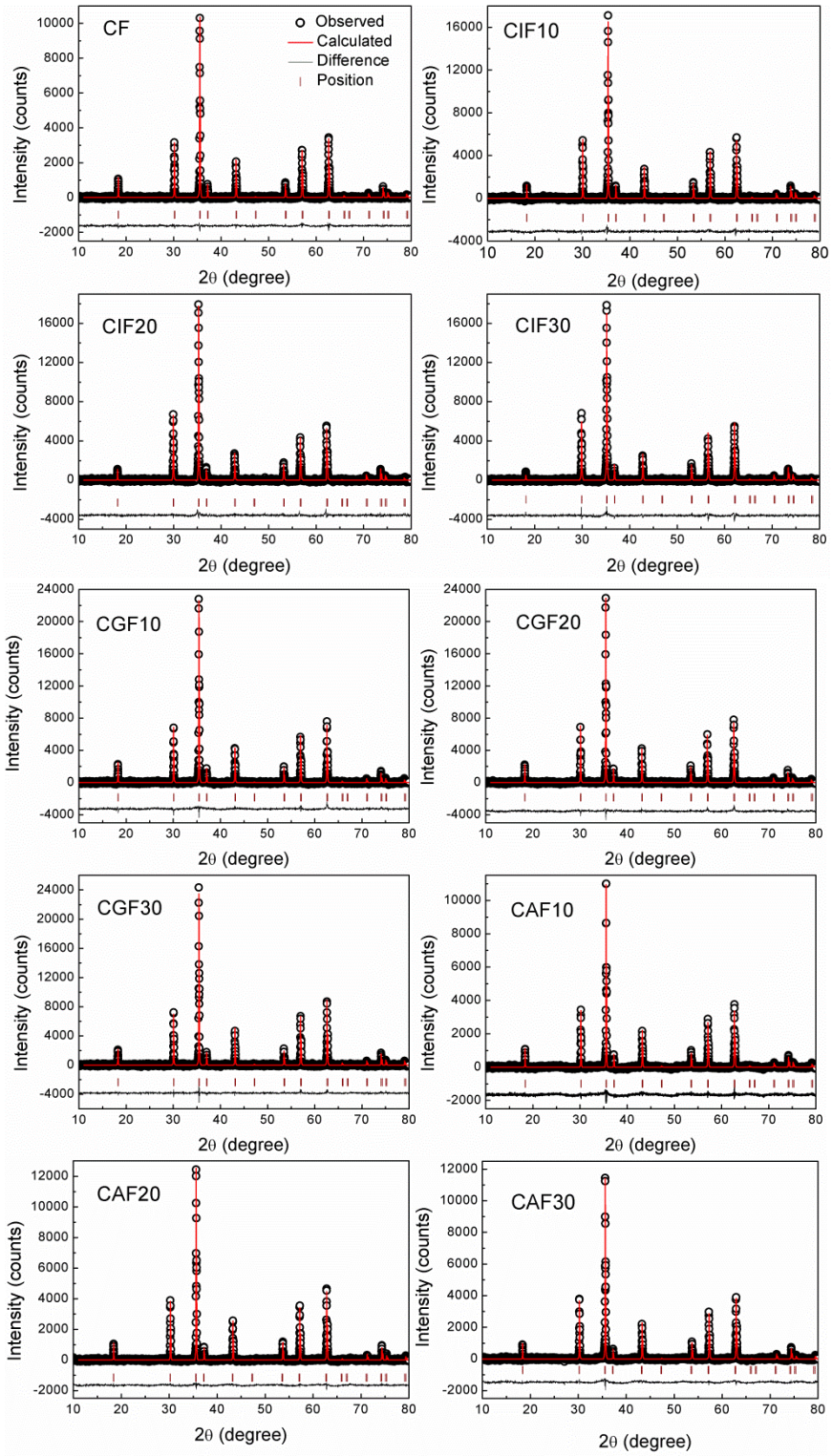

***Figure 4.4**: Results of the Rietveld refinement analysis of the XRD patterns of the sintered compositions of the three series of compositions.*

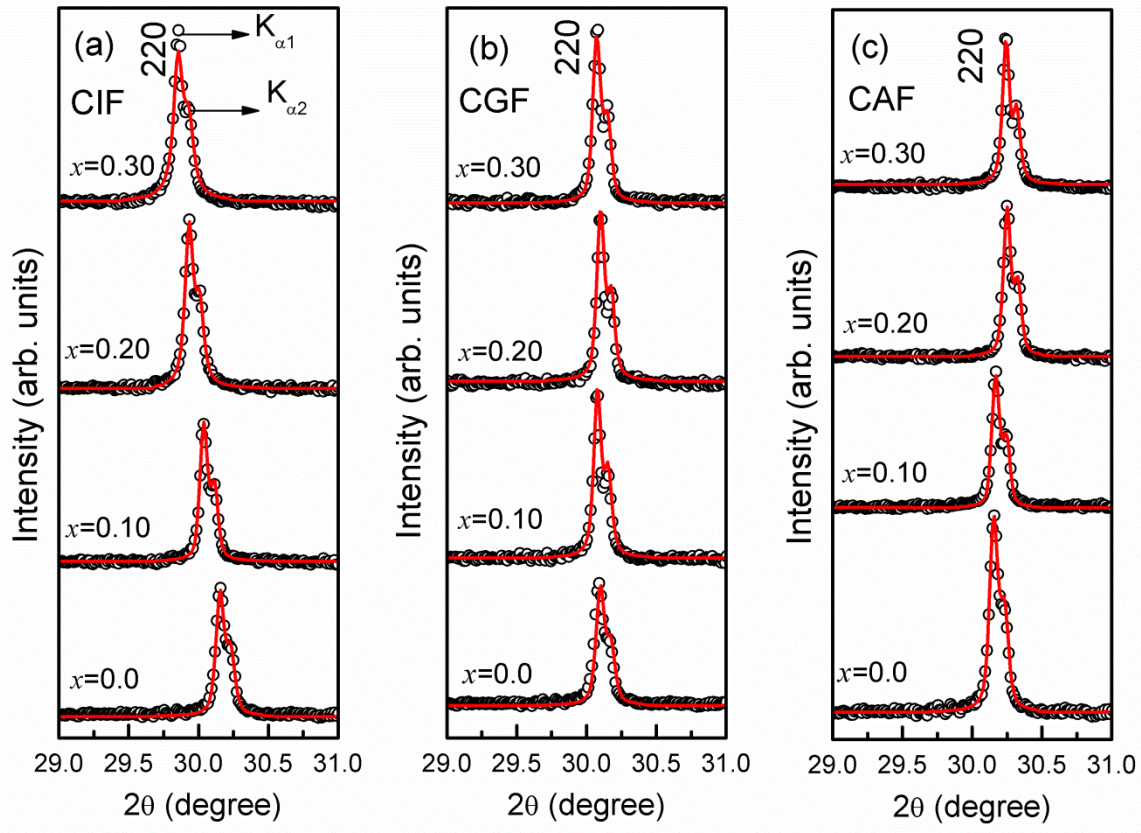

***Figure 4.5**: Zoomed XRD patterns showing the fit to the (220) peak in the XRD pattern of (a) CIF, (b) CGF and (c) CAF series.*

***Table 4.3**: Rietveld fitting parameters for the CIF, CGF, and CAF series of compositions.*

Composition	R_p	R_{wp}	χ^2
CF	0.024	0.031	1.20
CIF10	0.012	0.017	1.54
CIF20	0.011	0.014	1.08
CIF30	0.011	0.015	1.16
CGF10	0.011	0.013	1.20
CGF20	0.011	0.013	1.01
CGF30	0.011	0.012	1.01
CAF10	0.029	0.039	1.80
CAF20	0.022	0.027	1.12
CAF30	0.025	0.037	1.44

Rietveld refinement parameters of the different compositions of the three different series are given in Table 4.3. As shown in Figure 5, the diffraction peaks are shifted progressively towards lower angles for the CIF series and higher angles for the CAF series, whereas only a slight shift is observed for the CGF series, with increasing the degree of substitution. This suggests changes in the lattice parameter of CIF and CAF, due to the larger size of In^{3+}, the smaller size of Al^{3+} and comparable size of Ga^{3+} when compared to the ionic size of Fe^{3+}. The calculated lattice parameter varies almost linearly with increasing the amount of substitution, for the CIF and CAF series, as shown in Figure 4.6. All the three studied series obey Vegard's law, i.e., linear change in the unit cell parameter with the degree of substitution [13], that clearly indicates that the substituents are effectively incorporated into the lattice of $CoFe_2O_4$. The ionic radii of the substituted metal ions and that of Fe^{3+} corresponding to the 4-fold (tetrahedral) and 6-fold (octahedral) coordination environments are listed in Table 4.1. A monotonic increase in the lattice parameter with *x* is observed in the case of the CIF series, due to the replacement of the smaller ion Fe^{3+} by the larger ion In^{3+}. Similarly, for the CAF series, the decrease in the lattice parameter with increasing *x* is due to the replacement of the larger Fe^{3+} by the smaller ion Al^{3+}. For the CGF series, there is only a slight decrease in the lattice parameter due to the comparable sizes of Ga^{3+} and Fe^{3+}, where the size of Ga^{3+} is slightly smaller.

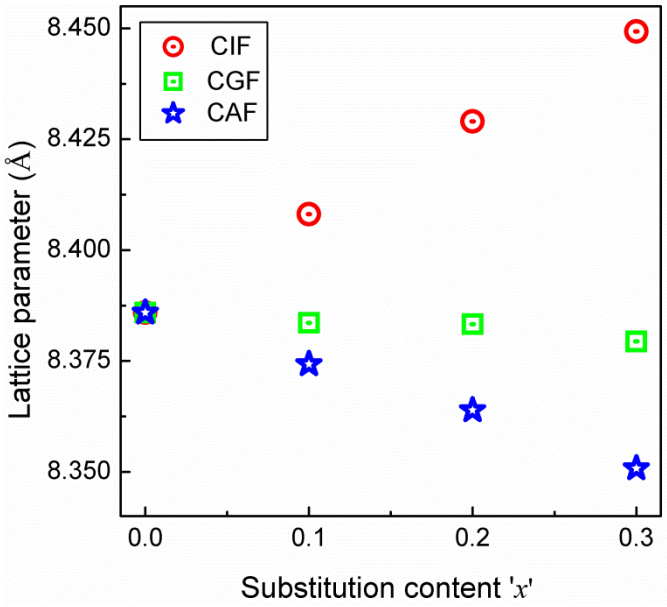

Figure 4.6*: Variation of the unit cell lattice parameter as a function of x in CIF, CGF and CAF.*

4.4.2 Microstructure

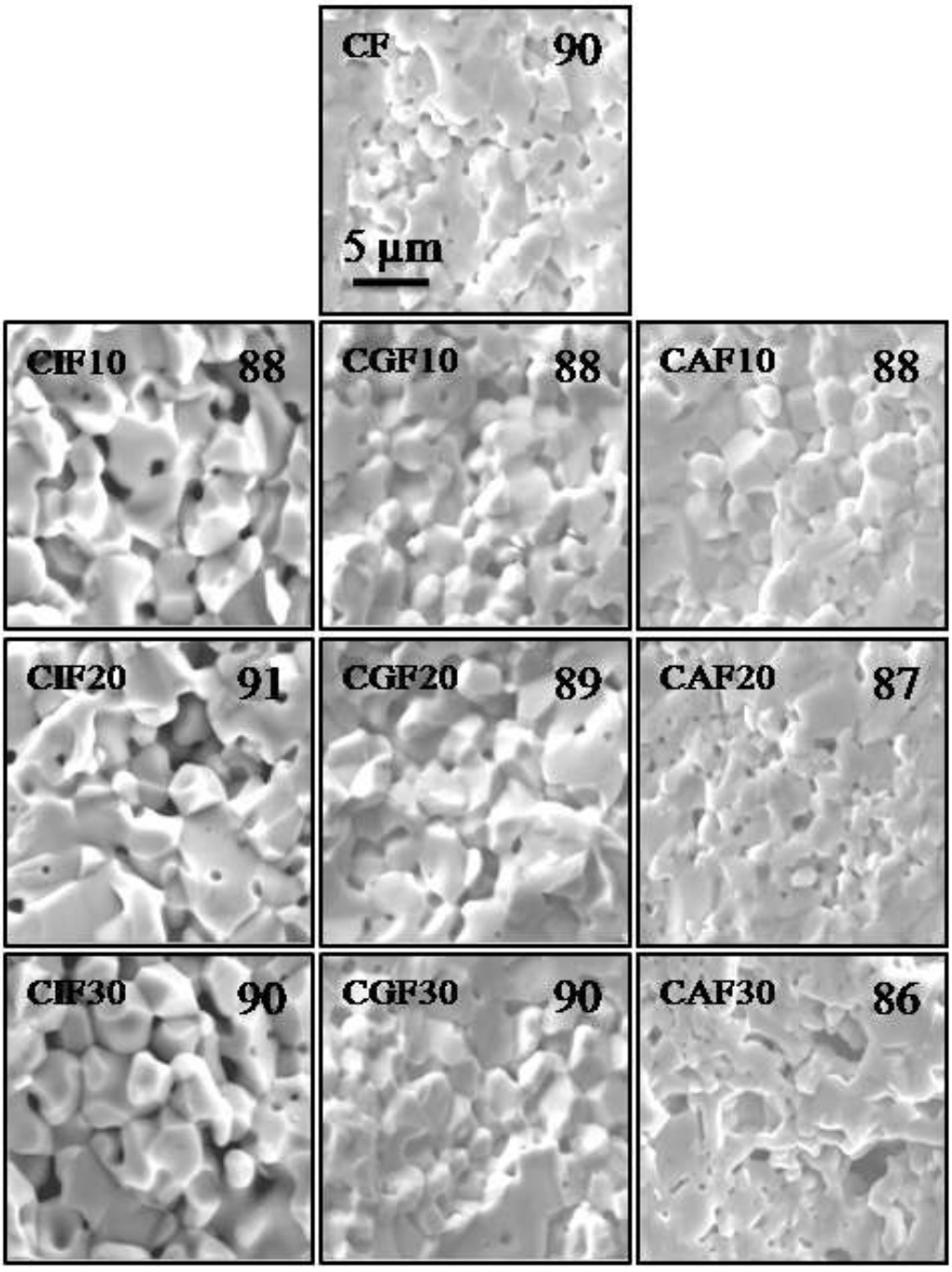

Figure 4.7*: SEM images of the sintered compositions of the three different series. The numbers in the images indicate the sintered density. All images are in the same scale and magnification.*

The SEM micrographs of the fractured inner surfaces of the sintered compositions are shown in Figure 4.7. A noticeable variation in the microstructural parameters including grain size, shape, porosity, and grain orientation, with the degree of substitution, can be seen for all three series. Both CIF and CGF compositions show the relatively large number of larger sized grains with irregular shape whereas smaller sized as well as larger fused grains are observed in the samples of the CAF series. These differences are likely to be due to the contributions of size effect of the substituents as well as the crystallite size of the nanopowders used for making the compacts. The compositions with x=0.1 in all three series show comparable sintered density (88% of theoretical density). However, at higher values of x, the density is observed to decrease in the case of CAF series and for the CIF and CGF series, it is nearly comparable to that of the unsubstituted composition. The decrease in the density with x in the case of CAF series is most probably due to the presence of smaller grains and associated intergranular porosity.

4.4.3 Magnetic properties

Field-dependent magnetization curves of the sintered compositions of the CIF, CGF and CAF series, measured at room temperature, up to a maximum field 1200 kA/m are shown in Figure 4.8(a),(c),(e), respectively. The enlarged magnetization curves showing the magnetic hysteresis loops, for the respective series, are also shown in Figure 4.8(b),(d),(f). Initial magnetization vs. field curves measured up to a field of 2400 kA/m using a SQUID magnetometer for all the sintered compositions of three series are shown in Figure 4.9(a),(b)(c). The variation of saturation magnetization (M_s) and coercivity (H_c) with the degree of substitution for the three different series is shown in Figure 4.10. The saturation magnetization (M_s) is found to decrease almost linearly in the case of the CAF series, whereas it is increased up to x=0.2 and decreased for x>0.2, with nearly comparable values of M_s for the same value of x, for both the CIF and CGF series (Figure 4.10(a)). Based on the value of saturation magnetization obtained at 5 K (shown in figure 4.9(c)), the distribution of Co and Fe in $CoFe_2O_4$ is calculated as $(Co_{0.21}Fe_{0.79})_A[Co_{0.79}Fe_{1.21}]_BO_4$, where the subscripts A and B represent the tetrahedral (A-sites) and octahedral (B-sites) sites, respectively, in the AB_2O_4 spinel structure. The changes in the value of M_s with the degree of substitution can be attributed to different crystallographic site preferences of the substituted ions. Mössbauer spectroscopic studies have indicated that Al in the Al-substituted spinel ferrites [6,14,15] has a tendency to occupy both the tetrahedral and octahedral sites.

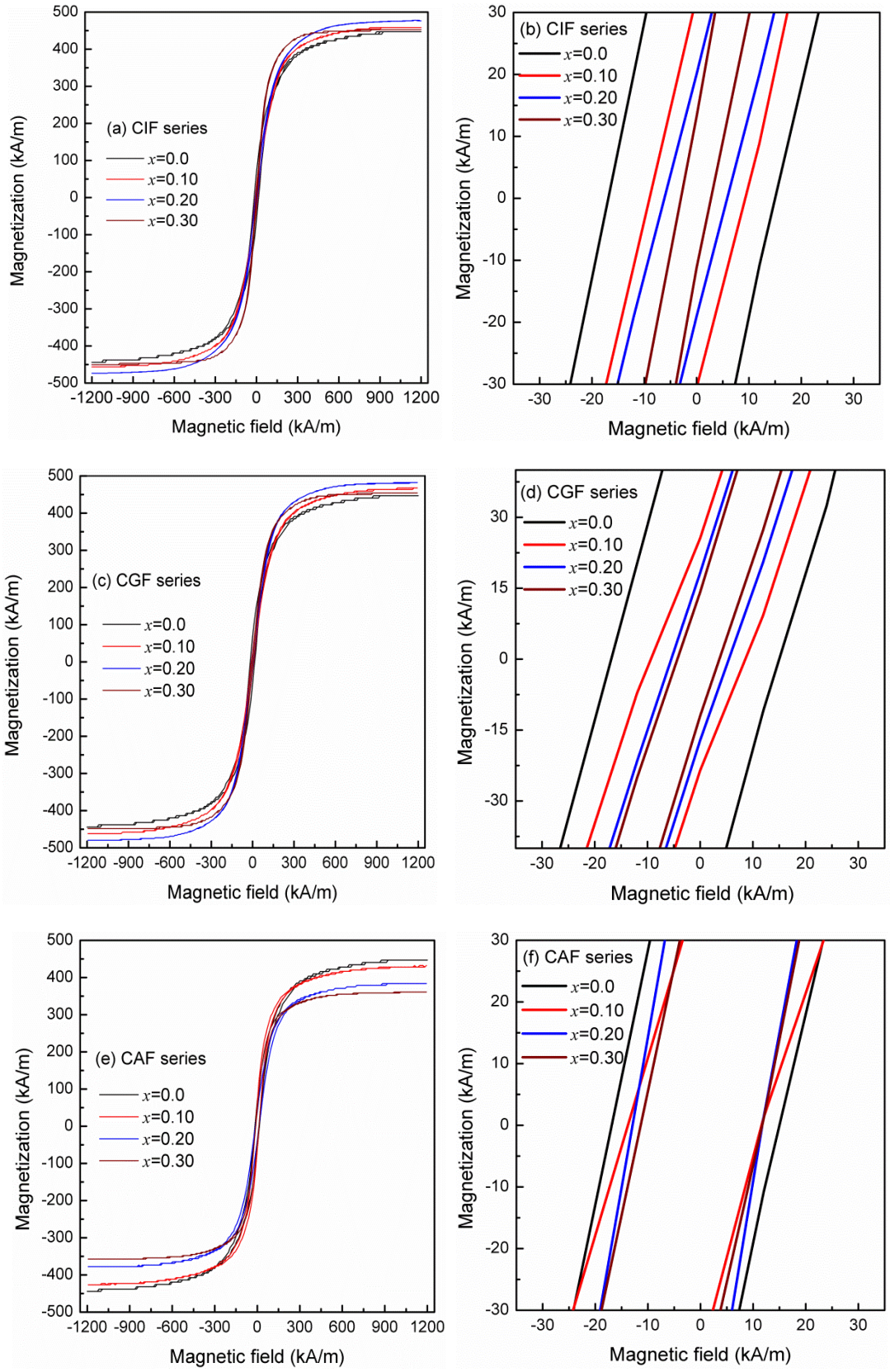

***Figure 4.8**: M vs. H curves and the corresponding zoomed loops at low field regions for (a,b) CIF, (c,d) CGF, and (e,f) CAF, recorded at room temperature.*

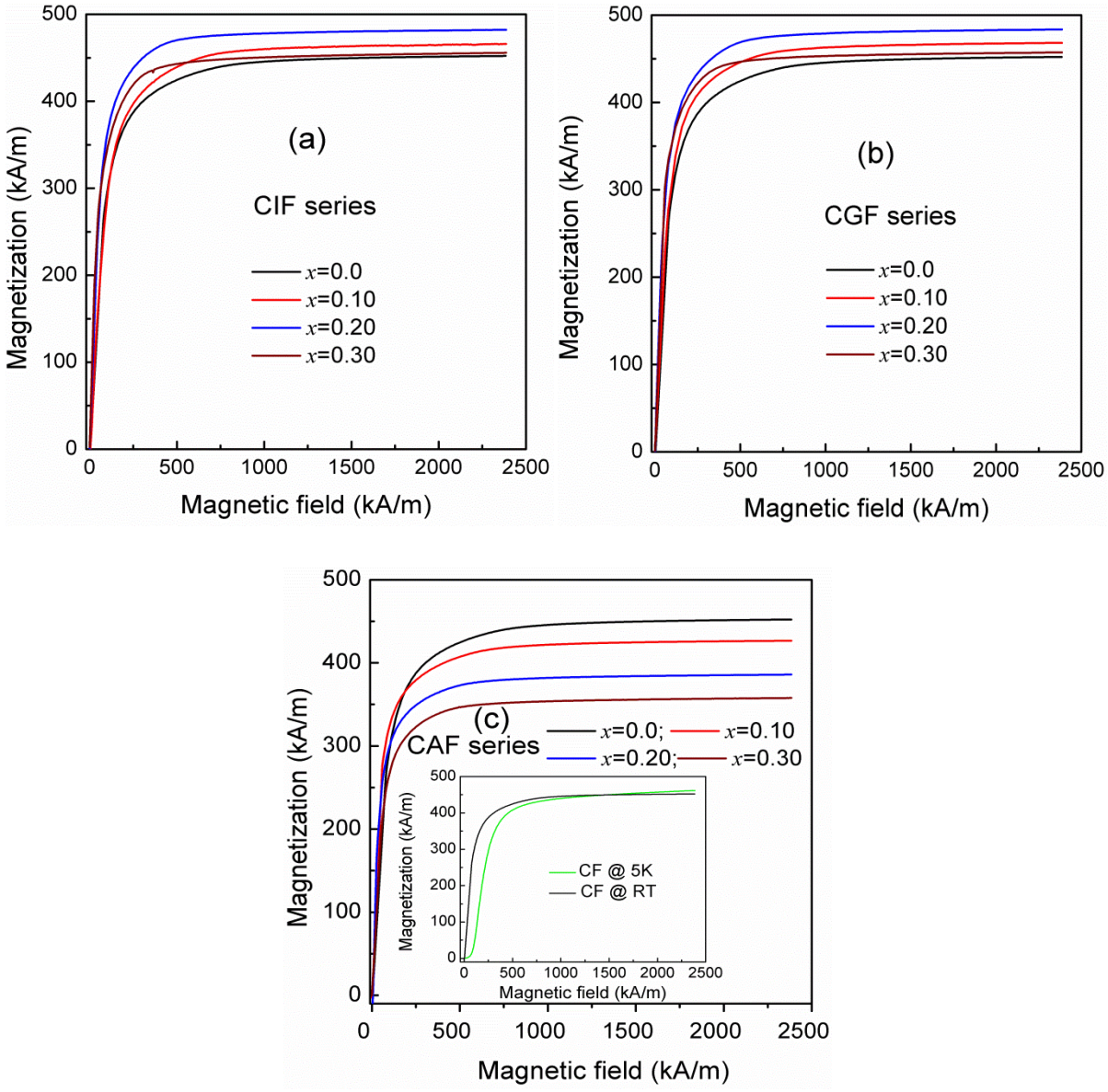

***Figure 4.9**: Initial magnetization curves of sintered (a) CIF, (b) CGF, and (c) CAF series of samples, using a SQUID magnetometer. The inset of (c) shows a comparison of the inital M-H curves of CF recorded at 5K and room temperature.*

Thus, in the case of the CAF series, the systematic decrease in the value of M_s with x is due to the progressive substitution of Fe^{3+} by Al^{3+}, preferably at the octahedral sites. In the case of the CIF and CGF series, the increase of M_s for $x \leq 0.2$ is due to replacement of Fe^{3+} by In^{3+} and Ga^{3+} at the A-sites. This leads to A-site magnetic dilution yielding higher saturation magnetization compared to the parent counterpart. The decrease in the value of M_s for $x>0.2$ in both the CIF and CGF series is most probably due to partial substitution of In^{3+} and Ga^{3+} for Fe^{3+} at the B-sites because both In^{3+} and Ga^{3+} have a tendency to occupy even the octahedral coordination environment [1,2,16]. Despite a large difference in the ionic radii of

Ga^{3+} and In^{3+}, the magnitude of M_s for the same value of *x* in both the CIF and CGF series are nearly equal indicating equal amounts of In^{3+} and Ga^{3+} are substituted for Fe^{3+} at the respective sites.

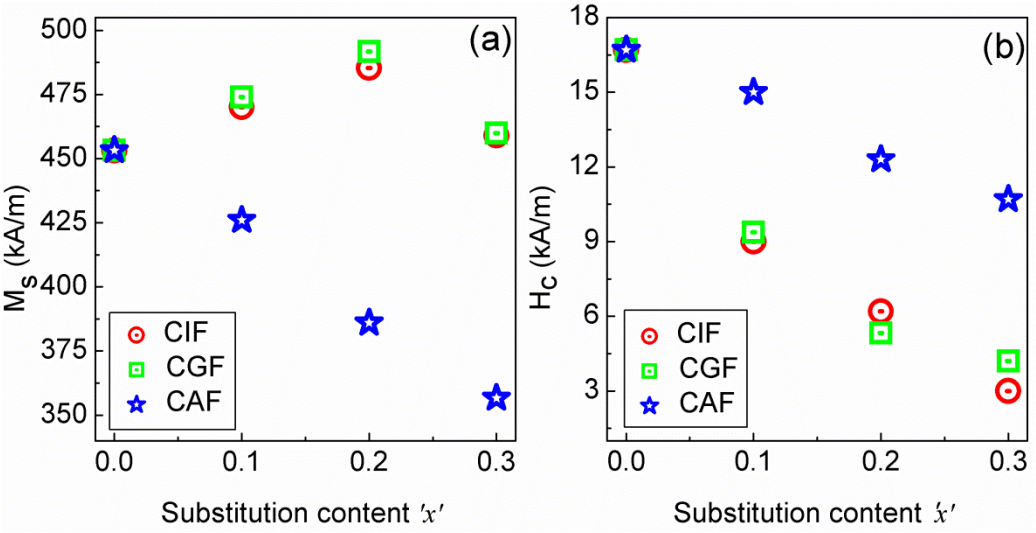

***Figure 4.10**: Variation of (a) saturation magnetization, M_s, and (b) coercivity, H_c, as a function of x in the CIF, CGF and CAF series.*

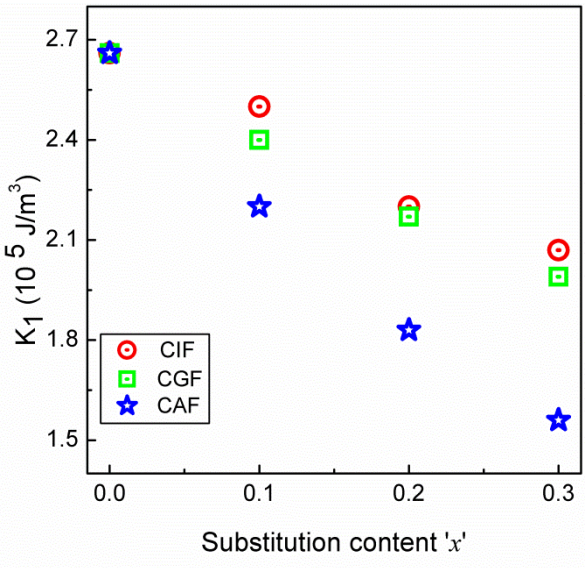

***Figure 4.11**: Variation of the magnetocrystalline anisotropy constant (K_1) as a function of x in CIF, CGF, and CAF.*

Variation of coercivity, H_c, is shown in Figure 4.10(b). The decrease in H_c is mostly due to the reduction in the magnetocrystalline anisotropy [17,18]. However, for the same amount of substitution *x*, the decrease is stronger for CIF and CGF series compared to that of the CAF series (Figure 4.10(b)). Interestingly, much similar to M_s, the values of H_c are also nearly comparable for the same value of *x* in both the CIF and CGF series. CIF and CGF series samples have higher values of M_s than that for the CAF series for the same amount of *x*. Based on the Brown relation (see section 3.4.3, chapter 3), higher the M_s lower will be the H_c. A similar trend of fast decrease in the H_c for the A-site substituted cobalt ferrite compared to the B-site substituted sample is reported in the literature [17,19].

The variation in anisotropy coefficient (K_1), calculated from the law of approach to saturation, as a function of substitution content *x* in three series is presented in Figure 4.11. The decrease in the value of K_1 is more pronounced for the CAF series over the other two series. It could be described based on the strong dependence of K_1 on the amount of Co^{2+} at the octahedral site and the A-O-B exchange interactions in the metal substituted and unsubstituted cobalt ferrites [20-23]. Any changes in the concentration of Co^{2+} at the octahedral site as well as A-O-B exchange interactions eventually affect the magnitude of K_1 of cobalt ferrite and its derivatives.

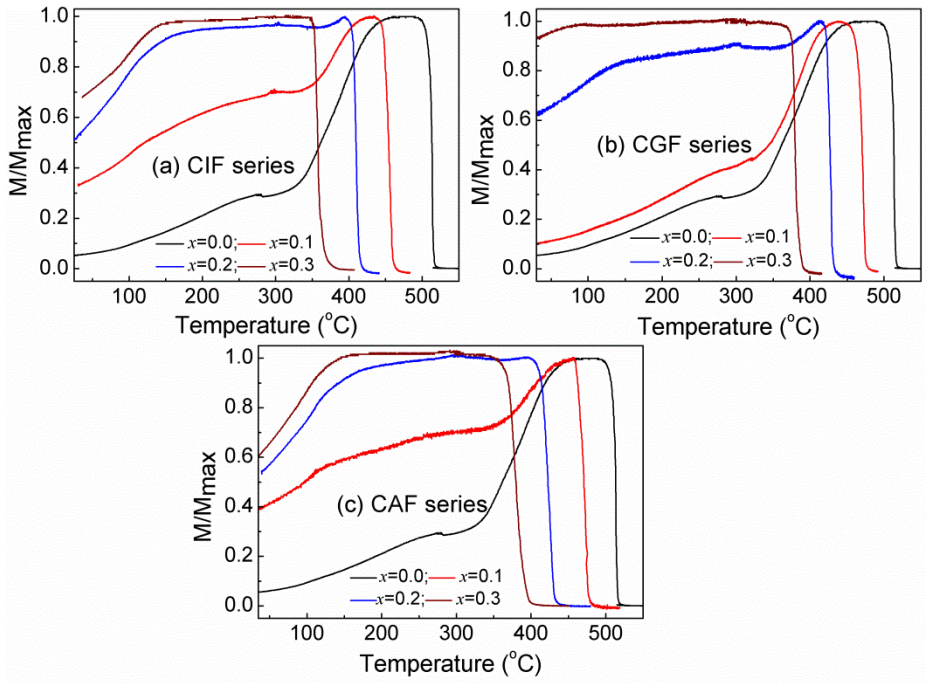

***Figure 4.12**: Magnetization curves of sinetered (a) CIF, (b) CGF and (c) CAF series, measured as a fuction of temperature in a field 100 Oe (~8 kA/m).*

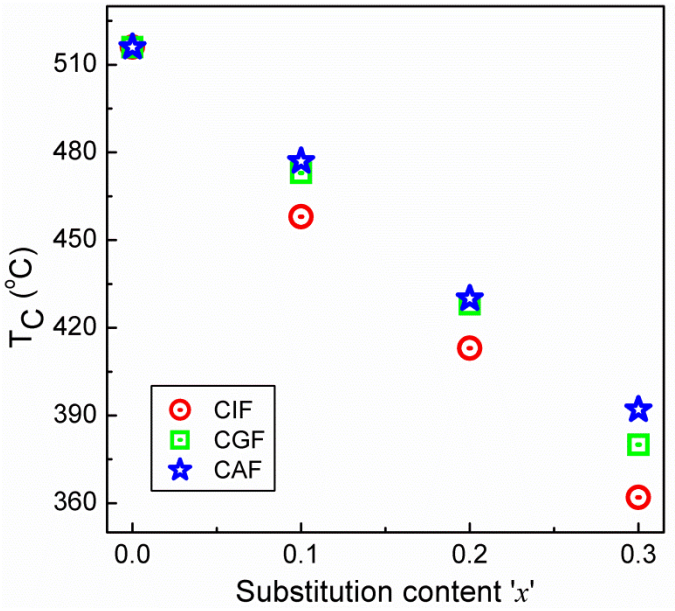

***Figure 4.13**: Variation of the Curie temperature as a function of substitution content in CIF, CGF, and CAF.*

Temperature dependence of magnetization of the sintered compositions measured in a magnetic field of 100 Oe (~8 kA/m) is illustrated in Figure 4.12, and the variation of Curie temperature (T_C) is shown in Figure 4.13. T_C is decreased for all three series, signifying the weakening of the A-O-B superexchange strength caused by the absence of magnetic interactions between magnetic and nonmagnetic cations [24,25]. In fact, T_C is decreased at a faster rate in the case of the CIF series over the CGF and CAF series in the order CIF>CGF>CAF (Figure 4.13). As discussed in the previous chapter (section 3.4.3), that nonmagnetic substitution at the A-sites reduces the T_C at a greater rate compared to the substitution at the B-sites. In the present case, the magnetization measurement revealed that more fraction of Al^{3+} are substituted at the B-sites by replacing Fe^{3+}, and therefore the decrease in T_C for the CAF series is slower compared to the other two series. However, in the case of the CIF and CGF series, even though both In^{3+} and Ga^{3+} are substituted at A-sites with almost equal magnitude of M_s for the same amount of substitution x, the fast decrease in T_C for the CIF series over the CGF series is likely to be emanating from the size effect because the strength of the A-O-B interaction not only depends on the type of cations located at the sublattices but also on the bond lengths and bond angles and that are altered by the size mismatch between the crystallographic sites and the substituent ions. The order of T_C

variation for all the three series resembles the order observed in the lattice parameter variation. Based on the reduction in the strength of the A-O-B exchange interactions, a faster decrease in K_1 is expected for the CIF series compared to the CAF series. However, the observed reverse trend is most likely to be due to the higher concentration of Co^{2+} at the octahedral sites in both the CIF and CGF series compared to the CAF series of samples.

4.4.4 Raman spectra

The magnetic studies revealed that In^{3+} and Ga^{3+} are substituted for Fe^{3+} at the tetrahedral sites, whereas Al^{3+} for Fe^{3+} at the octahedral sites. Raman spectroscopy is used as a complimentary tool to get information on the cation distribution in the substituted compositions of the three series. Raman spectra of the sintered samples of CIF, CGF and CAF series, recorded at room temperature using same data acquisition parameters are shown in the Figures 4.14. Seven active modes, designated as $A_{1g}(1)$, $A_{1g}(2)$, $E_g(1)$, $E_g(2)$, $T_{2g}(1)$, $T_{2g}(2)$ and $T_{2g}(3)$, can be seen in the spectra of all the compositions, suggesting that the compositions are in the form of inverse or mixed spinel ferrite. In the case of the substituted compositions, several changes in the spectral features are observed with the degree of substitution in all the three series. For CIF and CGF, with increasing *x*, the intensity of the $A_{1g}(1)$ mode due to FeO_4 decreases whereas the intensity of the $A_{1g}(2)$ mode due to CoO_4 increases and also the $A_{1g}(1)$ band shows a red shift with more asymmetrical broadening. A broad shoulder, at low wavenumber region, is observed as shown by the symbol '∗' (see Figure 4.15, indicating that Fe^{3+} is replaced by In^{3+} or Ga^{3+} at the tetrahedral coordination environment which strongly supports the conclusions drawn from the magnetic measurements. The shift of the $A_{1g}(1)$ band to lower frequencies, along with the additional broadening of the band, is mainly attributed to the large mass differences between Fe (55.84 amu), In (114.81 amu) and Ga (69.73 amu). Higher the atomic mass, lower will be the stretching frequency [26,27]. On the other hand, no substantial change in the position as well as broadening of the $T_{2g}(2)$ band has been observed, except an increase in the width of the peaks, by increasing the degree of substitution *x,* in both the CIF and CGF series, suggesting that the FeO_6 octahedral sites are not affected.

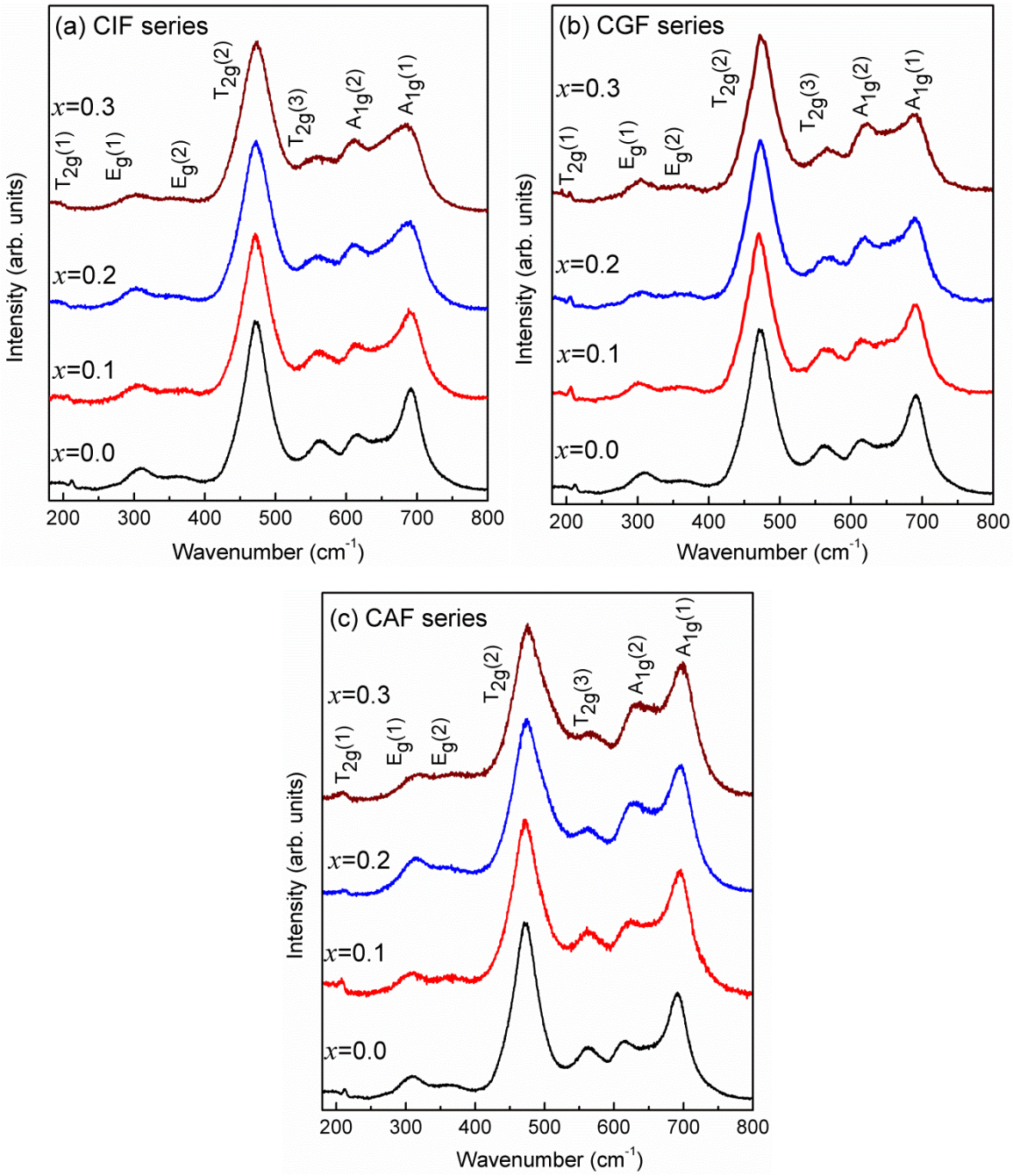

***Figure 4.14**: Raman spectra (a) CIF, (b) CGF and (c) CAF series of samples.*

In the case of the CAF series, with increasing Al^{3+} content, both the $T_{2g}(2)$ band due to FeO_6 and the $A_{1g}(1)$ band due to FeO_4 exhibit blue shift with additional broadening at higher wavenumbers (~720 cm^{-1} for $A_{1g}(1)$ and ~517 cm^{-1} for $T_{2g}(2)$) designated by the symbol '#' in Figure 15(c) and 15(d), revealing that Fe^{3+} is substituted by Al^{3+} at both the crystallographic sites. The blue shifts associated with the $T_{2g}(2)$ and the $A_{1g}(1)$ bands are attributed to the lower atomic mass of Al (26.98 amu) compared to that of Fe and also due to the consequences of the shorter bond length of Al-O compared to Fe-O in both

crystallographic sites. Thus, the Raman spectral analysis provides strong evidence for the presence of Al in both the crystallographic sites.

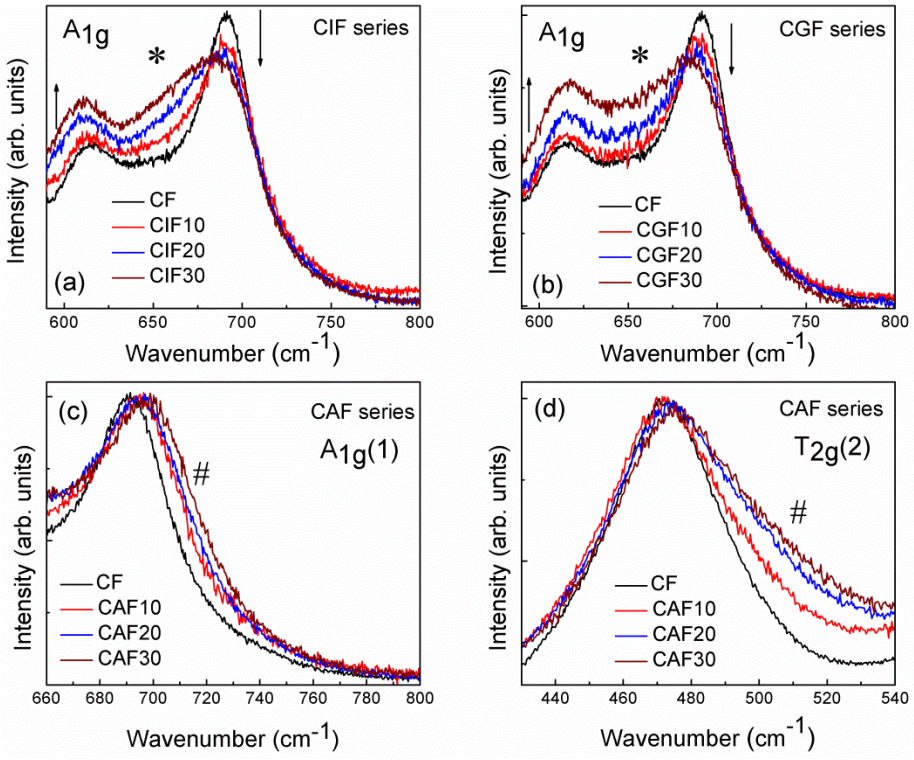

***Figure 4.15**: Variation in the intensity of A_{1g} band with respect to the normalized intensity of the $T_{2g}(2)$ band of the different compositions in (a) CIF and (b) CGF series. Extra broadening at lower wavenumber regions in both the series is shown by the symbol ∗. The up and down arrows indicate increasing and decreasing intensity. Comparison of the normalized intensity of (c) $A_{1g}(1)$ and (d) $T_{2g}(2)$ bands in the CAF series showing extra shoulders for the substituted compositions, shown by the symbol #.*

To gain further information from the Raman spectra, all the spectra were deconvoluted after normalizing with respect to the intense $T_{2g}(2)$ band after correcting for the background contribution. The deconvoluted spectra of selected compositions are shown in Figure 16. A good fit is obtained for the unsubstituted cobalt ferrite using 8 peaks at 209 cm^{-1} ($T_{2g}(1)$), 306 cm^{-1} ($E_g(1)$), 360 cm^{-1} ($E_g(2)$), 471 cm^{-1} ($T_{2g}(2)$), 560 cm^{-1} ($T_{2g}(3)$), 613 cm^{-1} ($A_{1g}(2)$), 650 cm^{-1} and 691 cm^{-1} ($A_{1g}(1)$). Nine peaks were required to fit the Raman spectra of In- and Ga-substituted samples where the 9th peak are at ~660 cm^{-1} for the CIF series and ~670 cm^{-1} for the CGF series. The peak at ~670 cm^{-1} is close to the reported band due to GaO_4 at 676 cm^{-1} for single crystal $ZnGa_2O_4$ [28]. Raman spectra of nanosized In-substituted cobalt ferrite ($CoIn_{0.15}Fe_{1.85}O_4$) have been reported by Nongjai *et al.* [29]. Despite having a large shift in the A_{1g} band positions in the substituted samples, the authors have suggested that the

shift originates from the lattice strain induced in the nanocrystalline structure by the larger sized In^{3+}. Raman spectra of bulk indium based spinel ferrites are not reported in the literature, and therefore, compared to the peak due to GaO_4, the peak obtained at ~660 cm^{-1} is assigned to the vibration of InO_4 tetrahedral unit. The lower wavenumber associated with InO_4 (~660 cm^{-1}) compared to that for GaO_4 (~670 cm^{-1}) is due to the larger atomic mass of In compared to that of Ga. Although the magnetization data revealed that at higher level of substitution (x>0.2) some fraction of In^{3+} and Ga^{3+} are substituted for Fe^{3+} at the B-sites, it is hard to extract the information from the Raman spectra since the $T_{2g}(2)$ band due to FeO_6 is significantly broader and the weak peak due to the contribution from InO_6/GaO_6 is buried under the broad $T_{2g}(2)$ band.

For the Al-substituted compositions, the extra peaks at ~517 and ~720 cm^{-1} are attributed to the presence of Al^{3+} in the octahedral (AlO_6) and tetrahedral (AlO_4) coordination environments, respectively. This assignment has been made based on the reported Raman spectra of spinel based aluminates such as $CoAl_2O_4$, $MnAl_2O_4$ and $MgAl_2O_4$ [27,30]. The obtained peaks at ~720 cm^{-1} due to AlO_4 and ~517 cm^{-1} due to AlO_6 in the present study, are consistent with the bands reported for AlO_4 due to A_{1g} (~700-720 cm^{-1}) and AlO_6 due to $T_{2g}(2)$ (~510-516 cm^{-1}) in the studied aluminate systems [27,30].

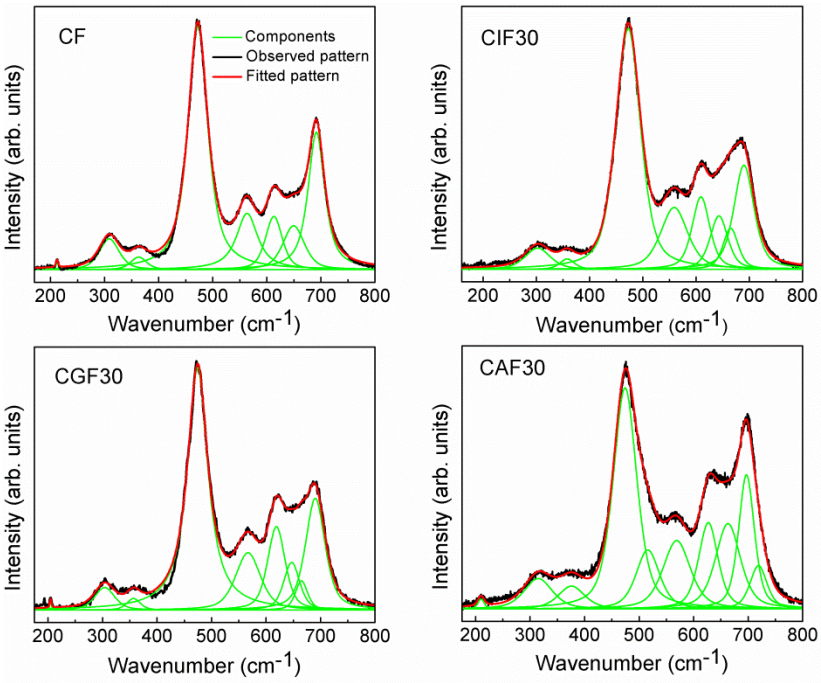

***Figure 4.16**: Deconvoluted Raman spectra of some of the selected compositions of the three series.*

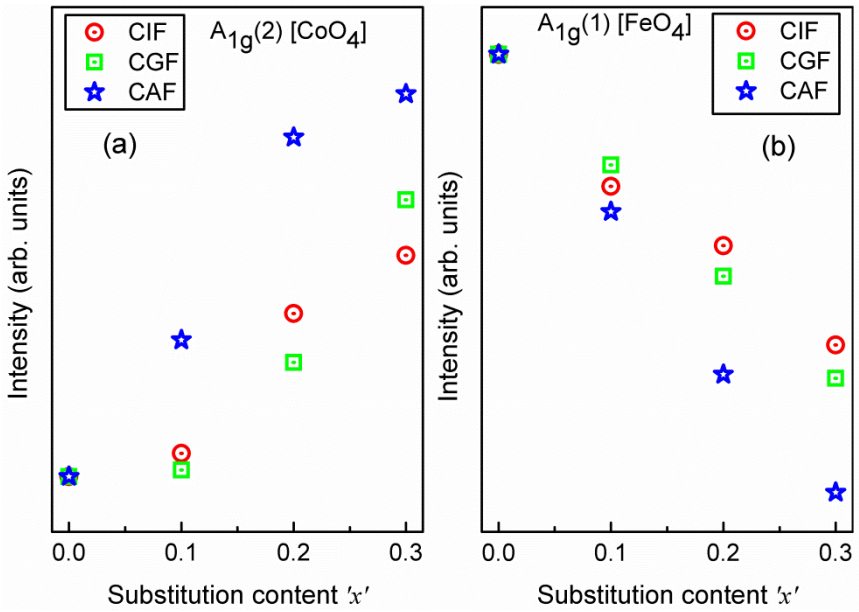

***Figure 4.17**: Variation in the relative area under the peaks due to A_{1g} bands of CoO_4 and FeO_4 as a function of x in CIF, CGF and CAF.*

A comparison of the variation of the area under the peaks due to $A_{1g}(1)$ mode (FeO_4) and $A_{1g}(2)$ mode (CoO_4) with the substitution content in the three series is shown in Figure 4.17. As can be seen from the figure, the area of the $A_{1g}(1)$ peak decreases whereas that of $A_{1g}(2)$ peak increases with increasing x in all three series. However, the rate of increase in the area of $A_{1g}(2)$ peak with x is larger in the case of the CAF series compared to that of other two series. This means that relatively larger amount of Co^{2+} is displaced from the B-sites to the A-sites. It is worth to note here that the areas of the $A_{1g}(2)$ peak for the compositions x=0.1 in both the CIF and CGF series are almost comparable to that of CF (x=0). For x>0.1 also, the areas increase but nearly comparable for the same values of x in both the CIF and CGF series. This is very much similar to the trend observed in the variation of M_s, H_c, and K_1. Similarly, the decrease in the area of $A_{1g}(1)$ peak is faster for the CAF series compared to the samples of CIF and CGF series (Figure 4.17). Also, the areas of the peaks at ~517 cm^{-1} due to AlO_6, at 660 cm^{-1} due to InO_4, at 670 cm^{-1} due to GaO_4 and at 720 cm^{-1} due to AlO_4 are observed to increase with increasing the degree of substitution. The ratio of the relative area of the peaks due to AlO_6 to AlO_4 is obtained as 1.58, 1.73, and 1.87 for the compositions CAF10, CAF20, and CAF30, respectively, indicating that more fraction of Al^{3+} is substituted for Fe^{3+} at the octahedral sites. The overall results from the Raman spectral studies support the conclusions drawn from the interpretation of the magnetic data.

4.4.5 Magnetostriction studies

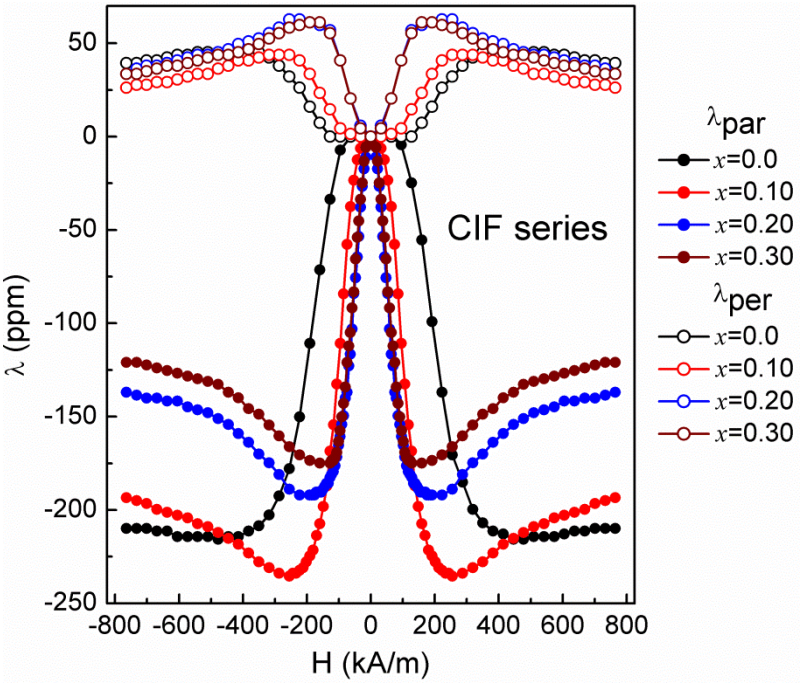

***Figure 4.18**: Magnetostriction strain curves of the CIF series of samples, measured along the parallel (closed symbols) and perpendicular (open symbols) directions to the applied magnetic field.*

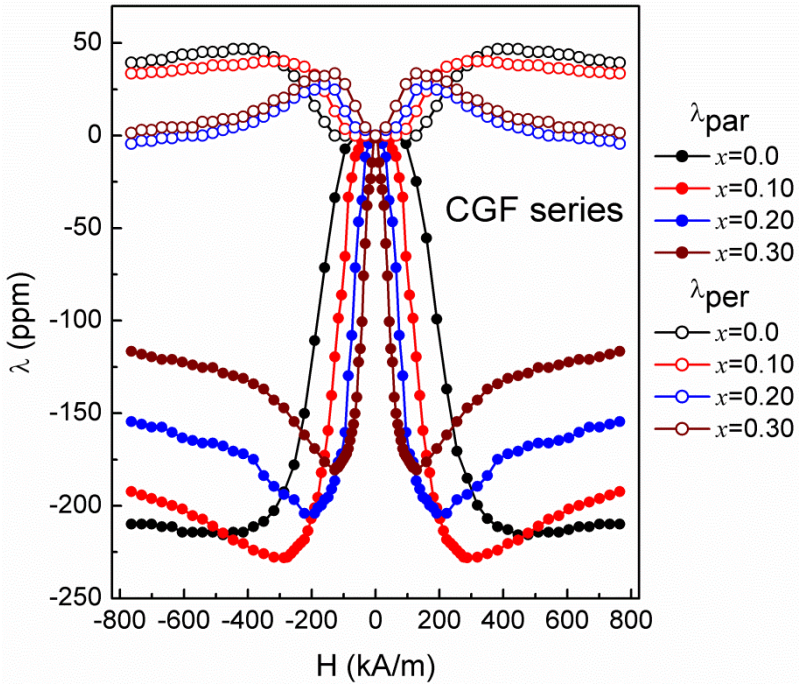

***Figure 4.19**: Magnetostriction strain curves of the CGF series of samples measured along the parallel (closed symbols) and perpendicular (open symbols) directions to the applied magnetic field.*

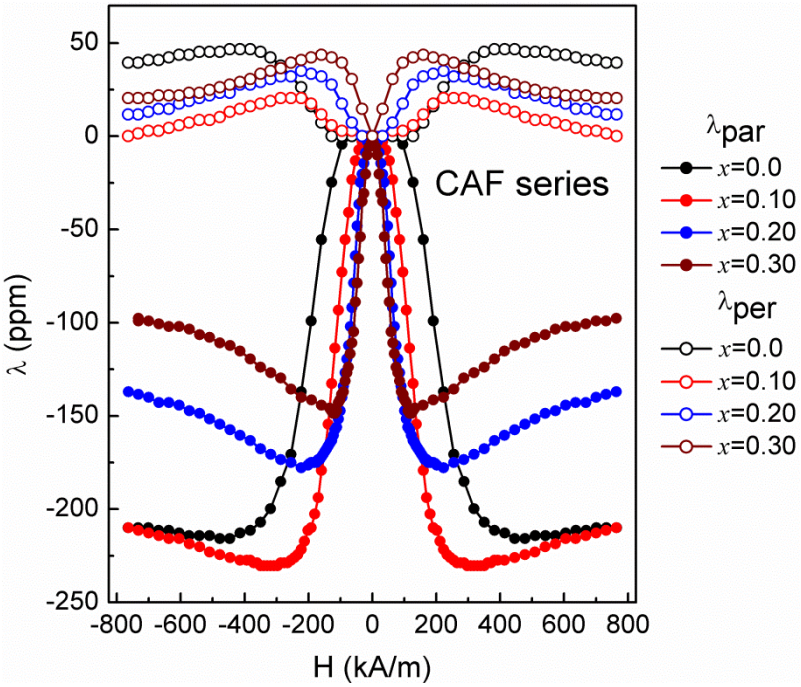

***Figure 4.20**: Magnetostriction strain curves of the CAF series of samples measured along the parallel (closed symbols) and perpendicular (open symbols) directions to the applied magnetic field.*

Figures 4.18, 4.19 and 4.20 compare the field-dependent magnetostriction strain curves of the sintered CIF, CGF, and CAF, respectively, measured along the parallel (λ_{par}) and perpendicular (λ_{per}) directions to the applied magnetic field. All the compositions exhibit negative magnetostriction along the parallel direction and positive magnetostriction along the perpendicular direction. In the present study, with increasing the degree of substitution in the cobalt ferrite crystal structure, significant changes in the amplitude of magnetostriction and slope change have been noticed for all the compositions of the three series. Interestingly, on compared to the magnetostriction of the divalent ion substituted samples i.e. CMF and CZF series of samples discussed in the previous chapter, the trivalent ion substituted samples show better magnetostriction properties. No significant drop in the magnetostriction coefficient has been observed even after substitution of Fe^{3+} up to x=0.3 (by Al^{3+}, Ga^{3+} and In^{3+}) in the cobalt ferrite lattice. However in the case of divalent ion substituted samples, even at the substitution level of x=0.2 the magnetostriction coefficient is substantially reduced. This is because Al^{3+}, Ga^{3+} and In^{3+} are isovalent to that of Fe^{3+} as a result of which the oxidation state of Co^{2+} is conserved in all the trivalent ion substituted compositions whereas, in the case of Zn and Mg-substituted samples, an equal amount of Co^{2+} would be converted into Co^{3+} to maintain the charge neutrality that affects the magnetostriction.

The highest value of the maximum magnetostriction along the parallel direction $[\lambda_{par}]_{max}$ is obtained for the composition x=0.1 in all the three series. All these compositions show comparable magnitude of ~-230 ppm at low magnetic fields (<300 kA/m), against the value of -217 ppm at a higher field of ~450 kA/m for the unsubstituted composition. The magnetostriction coefficient is lower than that of the unsubstituted composition for x=0.2, and the value is decreased further for x=0.3. Thus, larger and comparable value of $[\lambda_{par}]_{max}$ is obtained for x=0.1, irrespective of the size of the substituted ion and the difference in the cation distribution. However, for $x \geq 0.2$, the $[\lambda_{par}]_{max}$ values are observed to decrease in all three series, but the decrease is faster for the CAF series over the other two series (Figure 4.21(a)). Moreover, the field at which the value of $[\lambda_{par}]_{max}$ is obtained is also shifted significantly towards lower magnetic fields with the degree of substitution. This clearly indicates that higher magnetostriction can be achieved at a lower magnetic field by suitable metal ion substitution in $CoFe_2O_4$. The variation of magnetostriction obtained along the parallel direction at a field of 100 kA/m, as a function of substitution content x, is shown in Figure 4.21(b). As can see from the Figure 4.21(b), the magnitude of the magnetostriction has been increased almost linearly from -8 ppm for x=0 to ~-160 ppm for x=0.2 and becomes nearly constant for higher values of x. The strong reduction in the magnetocrystalline anisotropy and A-O-B superexchange interactions, upon increasing degree of substitution, are responsible for attaining higher values of magnetostriction at low magnetic fields [24].

On the other hand, along the perpendicular direction, the substituted compositions exhibit λ_{max} at much lower magnetic fields compared to that of the parent compound, but variation in the maximum value with x does not follow the trend observed for $[\lambda_{par}]_{max}$. $[\lambda_{per}]_{max}$ decreased initially up to x=0.1 in the CIF and CAF series and x=0.2 in the CGF series and slightly increased for higher values of x, as shown in Figure 4.21(c). Despite having large changes in the values of $[\lambda_{par}]_{max}$ and $[\lambda_{per}]_{max}$, a systematic variation in the maximum total magnetostriction, $[\lambda_{total}]_{max}=[\lambda_{par}]_{max}-[\lambda_{per}]_{max}$, with x has been obtained for all the three series (Figure 4.21(d)). The values of $[\lambda_{total}]_{max}$ decreased almost linearly for $x \geq 0.1$, and for CIF10 and CGF10 the values are slightly larger than that of the unsubstituted composition. The values of the maximum magnetostriction coefficients and the field at which these values are obtained along both the directions for the CIF, CGF and CAF series are tabulated in Tables 4.4, 4.5 and 4.6, respectively.

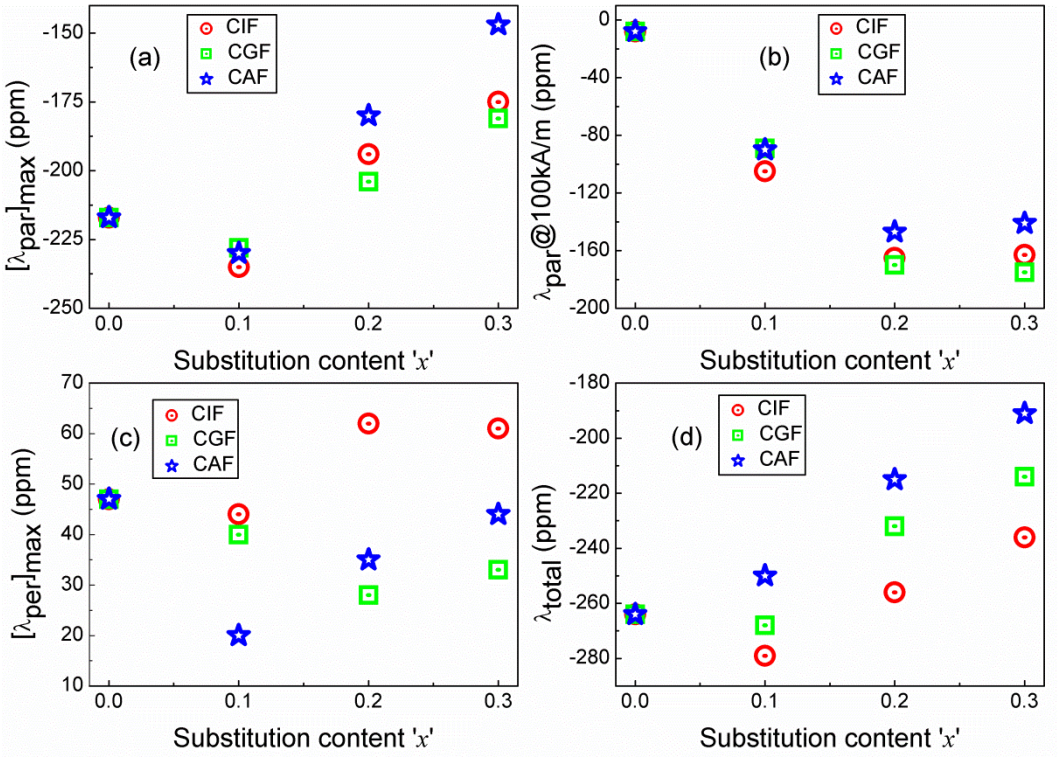

***Figure 4.21**: Variation of (a) maximum magnetostriction obtained along the parallel direction, $[\lambda_{par}]_{max}$, (b) Magnetostriction at 100 kA/m along the parallel direction, (c) maximum magnetostriction obtained along the perpendicular direction, $[\lambda_{per}]_{max}$, and (d) total magnetostriction, $[\lambda_{total}]$, as a function of x in CIF, CGF and CAF.*

***Table 4.4**: Maximum magnetostriction coefficient and the field at which the values are obtained for the CIF series.*

Composition	$[\lambda_{par}]_{max}$ (ppm)	H @ $[\lambda_{par}]_{max}$ (kA/m)	$[\lambda_{per}]_{max}$ (ppm)	H @ $[\lambda_{per}]_{max}$ (kA/m)
CF	-217	446	47	382
CIF10	-235	254	43	254
CIF20	-192	176	63	191
CIF30	-175	127	61	159

***Table 4.5**: Maximum magnetostriction coefficient and the field at which the values are obtained for the CGF series.*

Composition	$[\lambda_{par}]_{max}$ (ppm)	H @ $[\lambda_{par}]_{max}$ (kA/m)	$[\lambda_{per}]_{max}$ (ppm)	H @ $[\lambda_{per}]_{max}$ (kA/m)
CF	-217	446	47	382
CGF10	-228	286	40	286
CGF20	-204	191	27	159
CGF30	-181	127	33	127

***Table 4.6**: Maximum magnetostriction coefficient and the field at which the values are obtained for the CAF series.*

Composition	$[\lambda_{par}]_{max}$ (ppm)	H @ $[\lambda_{par}]_{max}$ (kA/m)	$[\lambda_{per}]_{max}$ (ppm)	H @ $[\lambda_{per}]_{max}$ (kA/m)
CF	-217	446	47	382
CAF10	-230	286	20	254
CAF20	-180	191	35	223
CAF30	-147	115	44	159

In spite of the larger differences in the structural and magnetic parameters, the compositions CIF10, CGF10 and CAF10 show almost comparable magnitudes of maximum magnetostriction along the parallel as well as the perpendicular directions, larger than that for the unsubstituted composition. Similar feature of λ_{max} marginally higher or comparable to that of unsubstituted cobalt ferrite along the parallel direction has been reported in the literature for different metal ions substituted for Fe in cobalt ferrite, such as, Cu^{2+} [31], Zr^{4+} [32], Er^{3+}, [33], Ge^{4+} [25], and Mn^{3+} [34], at lower substitution levels, particularly in the compositional range $0<x\leq0.2$. Thus, at lower substitution levels, it appears that the magnetostriction parameters are not affected by the size and nature of the substituted cation, cation distribution or the magnetic parameters. Thus, the changes in the magnetostriction coefficient, at lower levels of substitution, can be probably attributed to local structural changes due to the inhomogeneous distribution of the substituted metal ions in the unit cells of the cobalt ferrite

lattice that affects the nearest neighbor unit cells. In the substituted samples, at lower levels of substitution, the distribution of the substituted ions is likely to be inhomogeneous. For example, each unit cell of spinel ferrite has eight occupied tetrahedral (A) sites and sixteen occupied octahedral (B) sites by the cations. Also, each A-site is surrounded by 12 B-site cations, and each B-site is surrounded by only six A-site cations [35]. The A-site ions are located at the corner and the face centers of the spinel unit cell. If one Fe atom at the corner (or A-site cation) is replaced by another metal ion, it affects eight nearest unit cells, and the corresponding composition is x= 0.125 (x=1/8). Similarly, if one B-site cation is replaced by the substituted metal ion, it affects the neighboring 6 A-site cations, and this corresponds to x=0.0625 (x=1/16). Thus, $x\approx$ 0.1 is the compositional region where a minimum level of substitution which affects the neighboring octahedral and/or tetrahedral sites leading to local structural distortions.

Secondly, due to incompatibility in the sizes of the crystal lattice sites and the substituted ions, the bond lengths (A-O, B-O) and bond angles (A-O-B, A-O-A, B-O-B) are affected that eventually leads to a slight orientation of the magnetization vector away from the <100> easy direction which in turn affects the magnitude of λ_{max} along the parallel and perpendicular directions. In cobalt ferrite, the positive magnetocrystalline anisotropy is due to <100> easy magnetization axes, and there are reports in the literature that the sign of the anisotropy coefficient changes to negative when higher amounts of magnetic or nonmagnetic metal ions are incorporated into the lattice of cobalt ferrite [18,36]. Thirdly, microstructural parameters such as shape (irregularity), size (inhomogeneity) and orientation (random) of the grains and density of the sintered material have a strong influence on the magnitude of the magnetostriction along both the directions. This is because, most of these parameters influence the magnetization process and the magnetic domain configurations, which ultimately changes the contribution of the easy and hard magnetization directions towards the net magnetization of the polycrystalline sample. Hence, due to relative changes in the easy and hard magnetization directions persuaded by the microstructures affects the magnitude of magnetostriction along the parallel and perpendicular directions.

It is well understood that higher magnetostriction in cobalt ferrite is contributed mainly from the higher concentration of Co^{2+} at the octahedral sites. The strong decrease in the value of $[\lambda_{par}]_{max}$ in the case of the CAF series compared to the CIF and CGF series for $x\geq$0.2 is due to the displacement of more amount of Co^{2+} from the octahedral sites to the tetrahedral sites. Thisis supported by the results of the Raman spectral analysis where an increase in the area of

$A_{1g}(2)$ is higher for the CAF series compared to the samples of the other two series. Also, the results suggest that the higher amplitude of $[\lambda_{total}]_{max}$ associated with the CIF and CGF series are due to the higher content of Co^{2+} at the octahedral sites. It is worth to mention here that the variation of $[\lambda_{total}]_{max}$ with x shows a size-dependent trend, similar to the variation of the unit cell parameter with x and also nearly matches with the variation of the magnetocrystalline anisotropy with x.

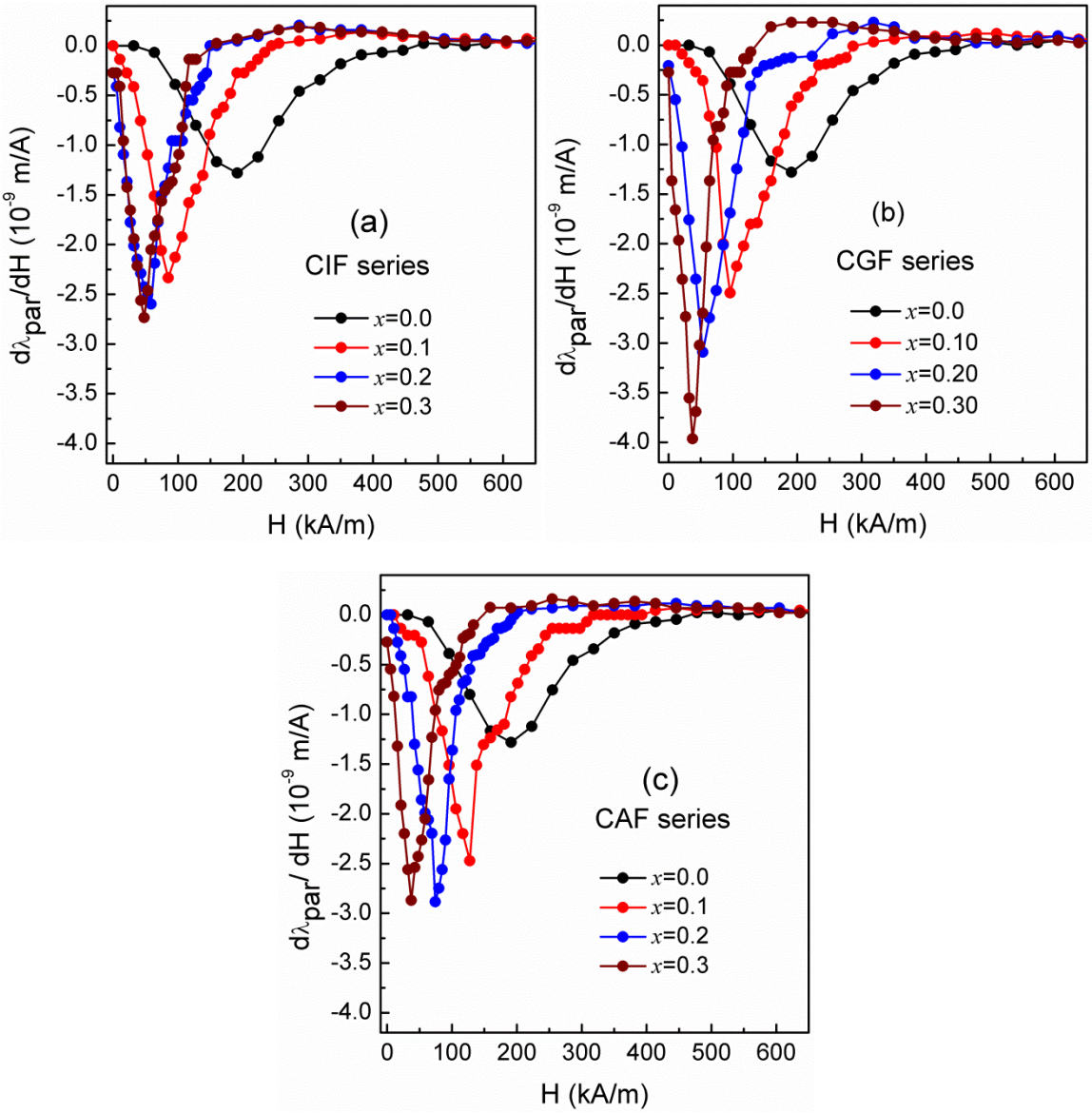

***Figure 4.22**: Strain sensitivity curves as a function of magnetic field for (a) CIF, (b) CGF, and (c) CAF series.*

Figure 4.22 shows the strain sensitivity curves of the three different series as a function magnetic field. The strain sensitivity is almost doubled for x=0.1 compositions compared to that of CF, with higher strain at lower fields. The variation of $[d\lambda_{par}/dH]_{max}$ with the amount

of substitution x is shown in the Figure 4.23. All the substituted compositions show high strain sensitivity (more than double) at relatively lower magnetic fields compared to the unsubstituted composition. For all the three series, the values of the strain sensitivity are comparable up to x=0.2. In the case of the CGF series, the magnitude of $[d\lambda_{par}/dH]_{max}$ increases approximately linearly from -1.28×10^{-9} m/A for x=0 to -3.9×10^{-9} m/A for x=0.3 (209% enhancement). However, for the CIF and CAF series, it increased up to x=0.2, and remains constant for x=0.3. Among the three series, at a lower amount of substitution ($x \leq 0.2$), the field at which $[d\lambda_{par}/dH]_{max}$ obtained is marginally lower for the CIF and CGF series compared to the CAF series.

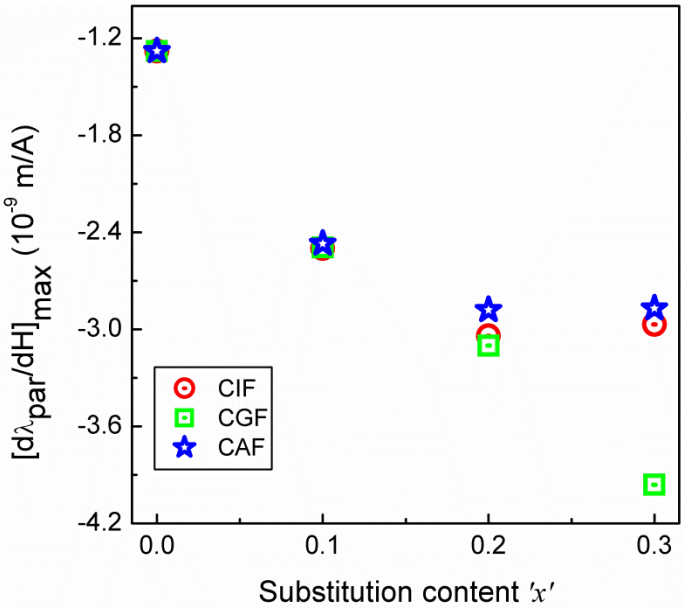

***Figure 4.23**: Variation of the maximum strain sensitivity values as a function of substitution content in the CIF, CGF and CAF series.*

Enhancement of the strain sensitivity at lower magnetic fields after incorporating the nonmagnetic isovalent metal ions into the lattice of cobalt ferrite is attributed to the combined effect of reduction in the magnetocrystalline anisotropy and the strength of the superexchange interactions [24,25,32,37]. Reduction in the strength of the superexchange interactions is primarily attributed to the absence of the magnetic interactions between the magnetic and nonmagnetic cations located at the A and B-sites. Apart from nonmagnetic nature of the substituted metal ions, the strength of the superexchange interactions would also vary with the size of the substituted ion due to the changes in the bond lengths and bond angles. This is because, the A-O-B exchange interaction energy is greatest when the angle A-O-B is closer to 180^{o} and shorter bond lengths of A-O and B-O, and the energy decreases rapidly with

lowering the bond angle and increasing the bond lengths [38]. Therefore, in the present study, substitution of different sizes of metal ions in the cobalt ferrite lattice is expected to alter the bond lengths and angles substantially that leading to a strong reduction in the A-O-B superexchange interactions which ultimately affects the magnetostriction properties.

The $[\lambda_{par}]_{max}$ obtained for the compositions in the CGF and CAF series, in the present work, is larger than the reported values with nearly comparable $[d\lambda_{par}/dH]_{max}$ for the similar systems prepared by the conventional ceramic method [18,37]. The values of the maximum magnetostriction parameters in the present work and the reported systems are compared in Figure 4.24.

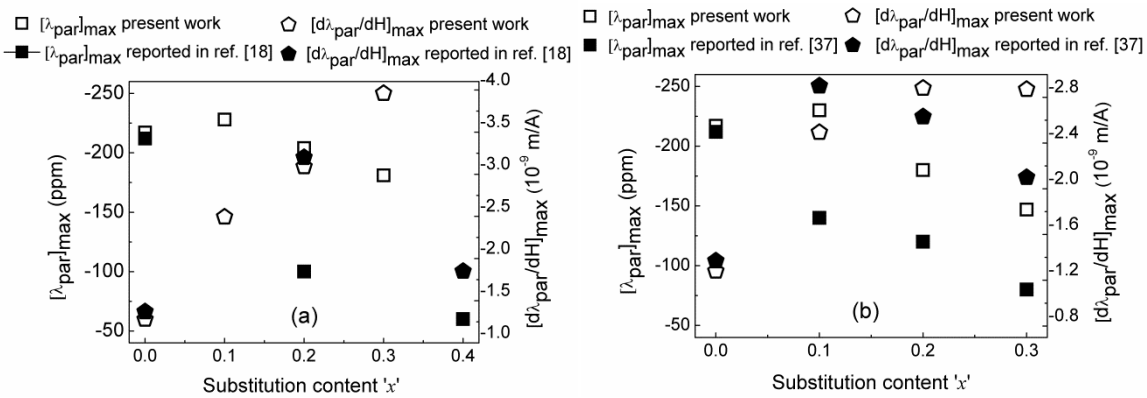

***Figure 4.24**: Comparison of the magnetostriction parameters obtained in the present study and the reported values for (a) CGF series and (b) CAF series.*

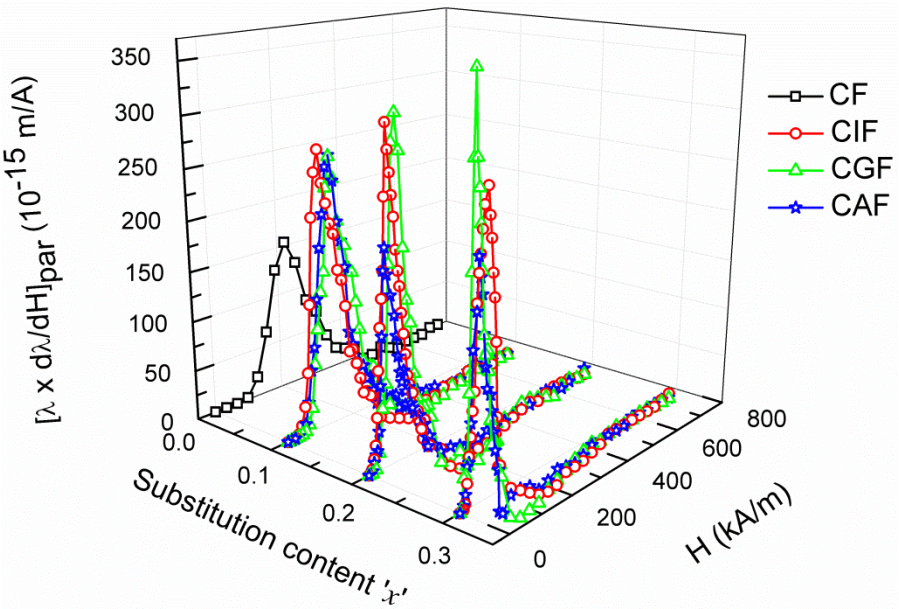

***Figure 4.25**: Variation of $[\lambda \times d\lambda/dH]_{par}$ as a function of substitution content and magnetic field.*

Figure 4.25 shows the three-dimensional graph of $[\lambda \times d\lambda/dH]_{par}$ (defined in chapter 3, section 3.4.7) plotted as a function of substitution content *x* and the applied magnetic field. All the substituted compositions exhibit higher magnitude of $[\lambda \times d\lambda/dH]_{par}$ at lower magnetic fields compared to the unsubstituted composition. Among three series, the CGF series of samples show a better response to the applied magnetic field. The maximum value of $[\lambda \times d\lambda/dH]_{par}$ is almost constant for the compositions x=0.1 with the magnitude of ~260 × 10^{-15} m/A against the value 153 × 10^{-15} m/A for x=0 and increased further upto 370 × 10^{-15} m/A for x=0.3 in the CGF series, 314 × 10^{-15} m/A for x=0.2 in the CIF series and decreased in the case ofthe CAF series.

4.4.6 Magnetic field annealing

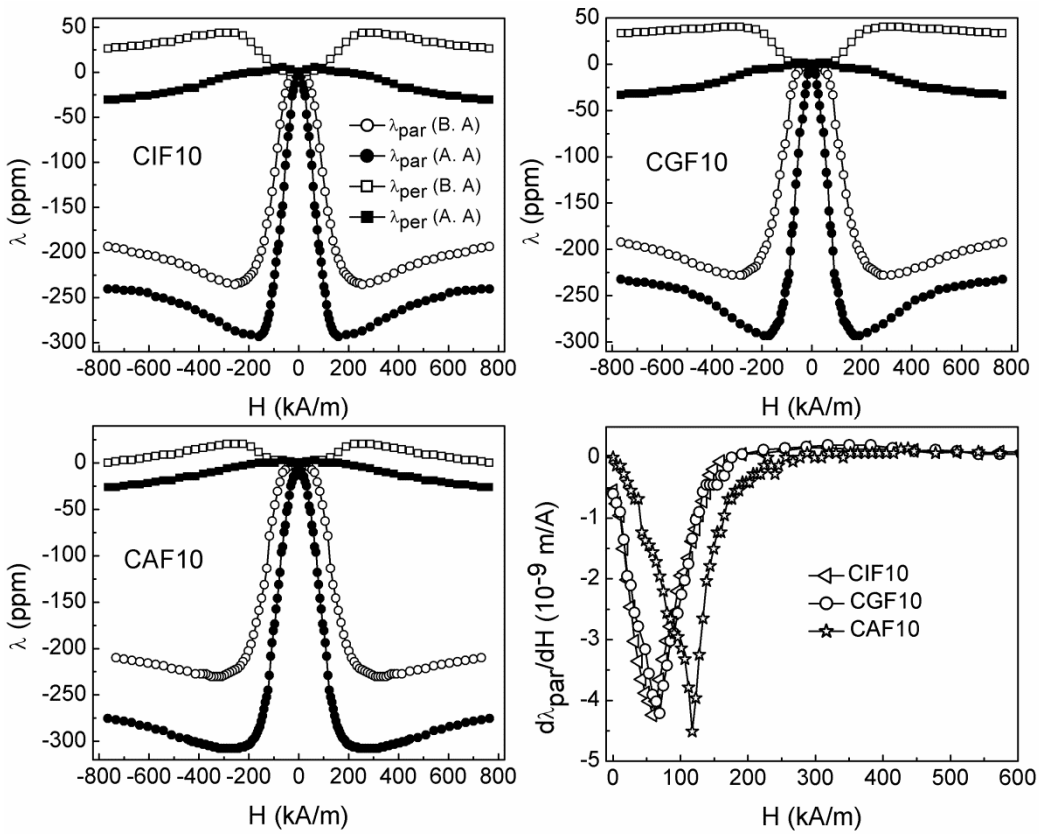

Figure 4.26*: Magnetostriction strain curves of the compositions CIF10, CIGF10 and CAF10, as a function of magnetic field, measured parallel (circles) and perpendicular (squares) to the applied magnetic field, before (open symbols) and after (closed symbols) annealing in a field and strain sensitivity curves along the parallel direction for the field annealed samples.*

Among the various compositions in three different series, CIF10, CGF10, and CAF10 samples exhibit higher amplitude of magnetostriction, higher than that of CF, with almost equal magnitudes. Therefore, these compositions have been investigated to study the effect of magnetic field annealing on the magnetostriction parameters. Figure 4.26 shows a comparison of the magnetostriction strain curves of the compositions CIF10, CGF10 and CAF10, before and after the magnetic field annealing together with strain sensitivity curves of the field annealed compositions.

On comparing with the unannealed samples, the field annealed samples exhibit higher magnitude of magnetostriction parameters at lower magnetic fields. Such a remarkable enhancement in the magnetostriction parameters at lower magnetic fields for the field annealed compositions is primarily attributed to uniaxial anisotropy induced in the samples by the annealing field, as discussed in chapter 3 (section 3.4.8). Similar to the unannealed compositions, the magnetostriction parameters of the annealed compositions are almost comparable, but the fields at which $[\lambda_{par}]_{max}$ and $[d\lambda_{par}/dH]_{max}$ are obtained for CIF10 and CGF10 are lower than that for CAF10, and the values are summarized in Table 4.7. Before magnetic field annealing, λ_{per} has a positive sign for all three compositions but changes to negative sign after annealing the samples in the magnetic field.

The present magnetostriction parameters are the highest values so far reported in the literature for the sintered metal substituted polycrystalline cobalt ferrite. Also, the observed parameters are nearly comparable to that reported of single crystal Galfenol-based magnetostrictive materials [39] and much higher than that for polycrystalline Galfenol and Terfenol-D based composite magnetostrictive materials [40-42]. Hence, the present trivalent metal ion substituted sintered cobalt ferrites are highly suitable candidates for both sensors and actuators.

Table 4.7*: Magnetostriction parameters of the compositions CIF10, CGF10, and CAF10, before and after magnetic field annealing.*

Compo-sitions	Before annealing				After annealing			
	$[\lambda_{par}]_{max}$ (ppm)	H @ $[\lambda_{par}]_{max}$ (kA/m)	$[d\lambda_{par}/dH]_{max}$ (10^{-9} m/A)	H @ $[d\lambda_{par}/dH]_{max}$ (kA/m)	$[\lambda_{par}]_{max}$ (ppm)	H @ λ_{max} (kA/m)	$[d\lambda_{par}/dH]_{max}$ (10^{-9} m/A)	H @ $[d\lambda/dH]_{max}$ (kA/m)
CIF10	-235	255	-2.33	85	-293	160	-4.24	58
CGF10	-228	286	-2.49	95	-290	170	-4.21	69
CAF10	-230	286	-2.47	127	-306	220	-4.51	117

4.5 Conclusions

From the present study, it is concluded that the structural, magnetic and magnetostrictive parameters can be effectively tuned by incorporation of small amounts of nonmagnetic trivalent metal ions substituted for Fe^{3+} in $CoFe_2O_4$. Irrespective of the sizes and crystallographic site preferences of the substituted ions in the cobalt ferrite lattice, enhanced magnetostriction parameters can be attained. It is concluded that the comparable values of magnetostriction parameters for similar substituted compositions, irrespective of the size of the substituted ion, is due to local structural distortions. All the substituted compositions show maximum magnetostriction coefficient at lower magnetic fields along both parallel and perpendicular directions compared to the unsubstituted composition. It is found that $[\lambda_{par}]_{max}$ is highest for x=0.1 in all cases with thealmost equal magnitude and decreased for x>0.1. Similar to $[\lambda_{par}]_{max}$, the substituted compositions exhibit higher magnitude of $[d\lambda_{par}/dH]_{max}$ at much lower magnetic fields compared to the parent compound. The magnetostriction parameters can be further enhanced by annealing the samples in a magnetic field. The present studies show the importance of substitution of nonmagnetic metal ions in the cobalt ferrite lattice to achieve higher magnetostriction coefficient and strain sensitivity suitable for various applications.

Bibliography

[1] S. E. Shirsath, B. G. Toksha, and K. M. Jadhav, *Mater. Chem. Phys*. **117**, 163 (2007).

[2] R. Pandit, K. K. Sharma, P. Kaur and R. Kumar, *Mater. Chem. Phys*. **148**, 988 (2014).

[3] K. Krieble, M. Devlin, S. J. Lee, S. T. Aldini, and J. E. Snyder, *J. Appl. Phys*. **103**, 07E508 (2008).

[4] M. B. Mohamed and M. Yehia, *J. Alloys Compd*. **615**, 181 (2014).

[5] A. Sattar, H. El-Sayed, K. El-Shokrofy, and M. El-Tabey, *J. Appl. Sci*. **5**, 162 (2005).

[6] S. Singhala, S. K. Barthwalb, and K. Chandra, *J. Magn. Magn. Mater*. **306**, 233 (2006).

[7] N. Ranvah, I. C. Nlebedim, Y. Melikhov, J. E. Snyder, P. I. Williams, A. J. Moses, and D. C. Jiles, *IEEE Trans. Magn*. **45**, 4261 (2009).

[8] R. D. Shannon, *Acta Crystallogr. A* **32**, 751 (1976).

[9] S. D. Bhame and P. A. Joy, *Sens. Actuator A* **137**, 256 (2007).

[10] P. Vlazan, S. F. Rus, I. Grozescu, and E. Vasile, *Phys. Scr*. **T157**, 014047 (2013).

[11] C.-Y. Tsay, S.-C. Liang, C.-M. Lei, C.-C. Chang, *Cerm. Int*. **42**, 4748 (2016).

[12] A. Lakshman, P. S. V. S. Rao, B. P. Rao, and K H Rao, *J. Phys. D: Appl. Phys*, **38**, 673 (2005).

[13] A. R. West, *Solid State Chemistry and its Applications*, (J. Wiley & Sons, Chichester, 1984).

[14] R. Pandit, P. Kaur, K. K. Sharma, and R. Kumar, *AIP Conference Proceedings* **1512**, 1130 (2013).

[15] S. K. Kulshreshtha and G. Ritter, *J. Mater. Sci.* **20**, 821 (1985).

[16] N. Ranvah, Y. Melikhov, D. C. Jiles, J. E. Snyder, A. J. Moses, P. I. Williams, and S. H. Song, *J. Appl. Phys*. **103**, 07E506 (2008).

[17] S. H. Song, *Doctoral Dissertation* (Dept. of Materials Science and Engineering, Iowa State University, Ames, Iowa, 2007).

[18] S. H. Song, C. C. H. Lo, S. J. Lee, S. T. Aldini, J. E. Snyder, D. C. Jiles, *J. Appl. Phys*. **101**, 09C517 (2007).

[19] V. R. Monaji, S. Indla, S. Rayprol, S. Sowmya, A. Srinivas, and D. Das, *J. Alloys Compd*. **700**, 92 (2017).

[20] P. N. Anantharamaiah and P. A. Joy, *Phys. Chem. Chem. Phys*. **18**, 10516 (2016).

[21] Y. Melikhov, J. E. Snyder, D. C. Jiles, A. P. Ring, J. A. Paulsen, C. C. H. Lo, and K. W. Dennis, *J. Appl. Phys*. **99**, 08R102 (2006).

[22] P. N. Anantharamaiah and P. A. Joy, *Mater. Lett*. **192**, 169 (2017).

[23] A. Muhammad, R. Sato-Turtelli, M. Kriegisch, R. Grossinger, F. Kubel, and T. Konegger, *J. Appl. Phys*. **111**, 013918 (2012).

[24] P. N. Anantharamaiah and P. A. Joy, *J. Appl. Phys*. **121**, 093904 (2017).

[25] I. C. Nlebedim and D. C. Jiles, *Smart Mater. Struct*. **24**, 025006 (2015).

[26] K. B. Modi, P. Y. Raval, S. J. Shah, C. R. Kathad, S. V. Dulera, M. V. Popat, K. B. Zankat, K. G. Saija, T. K. Pathak, N. H. Vasoya, V. K. Lakhani, U. Chandra, and P. K. Jha, *Inorg. Chem*. **54**, 1543 (2015).

[27] V. D'lppolito, G. B. Andreozzi, D. Bersani and P. P. Lottici, *J. Raman Spectrosc*. **46,** 1255 (2015).

[28] G. G. P. Van Gorkom, J. H. Haanstra, and H. V. D. Boom, *J. Raman Spectrosc*. **1**, 513 (1973).

[29] R. Nongjai, S. Khan, K. Asokan, H. Ahmed, and I. Khan, *J. Appl. Phys*. **112**, 084321 (2012).

[30] H. Cynn, S. K. Sharma, T. F. Cooney, and M. Nicol, *Phys. Rev. B* **45**, 500 (1992).

[31] B. C. Sekhar, G. S. N. Rao, O. F. Caltun, B. D. Lakshmi, B. P. Rao and P. S. V. S. Rao, *J. Magn. Magn. Mater*. **398**, 59 (2016).

[32] V. R. Monaji and D. Das, *J. Alloys Compd*. **634**, 99 (2015).

[33] S. G. Kakade, R. C. Kambale, C. V. Ramanna and Y. D. Kolekar, *RSC Adv*. **6** 33308 (2016).

[34] K. K. Mohaideen and P. A. Joy, *Curr. Appl. Phys.* **13** 1697 (2013).

[35] B. Viswanathan and V. R. K. Murthy, *Ferrite Materials: Science and Technology* (Narosa Publishing House, New Delhi, 1990).

[36] S. J. Lee, C. C. H. Lo, P. N. Matlage, S. H. Song, Y. Melikhov, J. E. Snyder, and, D. C. Jiles, *J. Appl. Phys*. **102**, 073910 (2007).

[37] I. C. Nlebedim , N. Ranvah, Y. Melikhov, J. E. Snyder, P. I. Williams, A. J. Moses, and D. C. Jiles, *IEEE Trans. Magn*. **45**, 4120 (2009).

[38] Smith J and Wijin H P J 1965 *Ferrites* (Philips Technical Library, Eindhoven, The Netherland).

[39] A. E. Clark, K. B. Hathaway, M. Wun-Fogle, J. B. Restorff, T. A. Lograsso, V. M. Keppens, G. Petculescu, R. A. Taylor, *J. Appl. Phys*. **93**, 8621 (2003).

[40] S. F. Xu, H. P. Zhang, W. Q. Wang, S. H. Guo, W. Zhu, Y. H. Zhang, X. L. Wang, D. L. Zhao, J. L. Chen and G. H. Wu, *J. Phys. D: Appl. Phys*. **41**, 015002 (2008).

[41] J. -H. Yoo, S. -M. Na, J. B. Restorff, M. Wun-Fogle, and A. B. Flatau, *IEEE Trans. Magn*. **45**, 4145 (2009).

[42] E. M. Summers, T. A. Lograsso, J. D. Snodgrass, and J. C. Slaughter, http://lib.dr.iastate.edu/ameslab_conf/59.

Chapter 5

Studies on co-substituted cobalt ferrite

$CoM_{x/2}M'_{x/2}Fe_{2-x}O_4$ (M,M' = Ga,Mn; Ga,Al; Mg,Zn)

5.1 Introduction

The studies on divalent and trivalent ions substituted cobalt ferrite, as discussed in the previous chapters, provided information on the distribution of the substituted ions at the tetrahedral (A-site) or the octahedral (B-site) sites of the AB_2O_4 spinel lattice, and the associated changes in the magnetostriction parameters. It is found that the Co^{2+} at the B-sites is displaced to the A-sites with increasing the degree of substitution. This means that it is hard to get control over the cation distribution when the metal ion are substituted for Fe. It may be possible to get control over the site distribution by co-substitution of different metal ions having different site preferences for Fe in the cobalt ferrite. Studies on the magnetostrictive properties of co-substitution of tetravalent and divalent metal ions in place of trivalent Fe in the cobalt ferrite lattice have been reported in the literature [1-3]. In the reported studies, the tetravalent nonmagnetic ions (Ge, Ti, and Zr) along with equal amount of Co have been substituted to achieve better magnetostriction parameters at lower magnetic fields. The advantage of substituting the tetravalent metal ions along with Co^{2+} for Fe^{3+} is that the charge neutrality is maintained in the substituted compositions along with an increase in the Co^{2+} content at the octahedral site where it is expected to give higher magnetostriction parameters at low fields.

Ranvah *et al.* have investigated the magnetostrictive properties of the Ge^{4+}/Co^{2+} co-substituted cobalt ferrite, $Co_{1+x}Ge_xFe_{2-2x}O_4$ [1]. The authors have shown that the composition with x=0.1 exhibits relatively larger values of λ_{max} (-241 ppm) and strain sensitivity (-2.4 × 10^{-9} m/A) at lower magnetic fields against the values -220 ppm and -2 × 10^{-9} m/A for the unsubstituted composition and both parameters decreased at higher values 'x'. In another study by Nlebedim *et al*., on the magnetostriction properties of $Co_{1+x}Ti_xFe_{2-2x}O_4$, a systematic drop in the values of λ_{max} as well as $[d\lambda/dH]_{max}$ with 'x' is reported [2]. In the reported studies, the authors have commented that the different site preferences of Ge^{4+} and Ti^{4+} in the cobalt ferrite lattice are responsible for such variations in the magnetostriction parameters. Ge^{4+} preferentially occupy the A-sites and pushes Co^{2+} from the A-sites to the B-sites, whereas Ti^{4+} occupies the B-sites and displaces Co^{2+} from the B-sites to the A-sites. Manoji *et al*. [3], have studied the magnetostrictive properties of Zr^{4+}/Co^{2+} co-substituted cobalt ferrite, $Co_{1+x}Zr_xFe_{2-2x}O_4$, where Zr^{4+} has a strong preference for the tetrahedral site much similar to that of Ge^{4+}. A marginally higher magnitude of λ_{max} (-186 ppm) with large

enhancement in the $[d\lambda/dH]_{max}$ (-3.32×10^{-9} m/A) for the composition with x=0.2 against the values -180 ppm and -0.8×10^{-9} m/A for the unsubstituted composition.

The studies on the co-substitution of different metal ions for Fe^{3+} in the cobalt ferrite, where one metal ion will have a strong preference for the A-site and another for the B-site, on the structural, magnetic and magnetostrictive properties, have not been reported in the literature. Therefore in this study, the effect of co-substitution of three different pairs of metal ions is investigated. The compositions $CoGa_{x/2}Mn_{x/2}Fe_{2-x}O_4$, $CoAl_{x/2}Ga_{x/2}Fe_{2-x}O_4$ and $CoMg_{x/2}Zn_{x/2}Fe_{2-x}O_4$, prepared by a wet chemical method and processed under identical conditions, are studied. Zn^{2+} and Ga^{3+} have a strong preference for the A-site whereas Mg^{2+} and Al^{3+} have the ability to occupy both the A and B-sites, with larger amounts preferably at the B-sites and Mn^{3+} will have a strong preference for the B-sites.

5.2 Materials synthesis

Compositions in the three different series, $CoGa_{x/2}Mn_{x/2}Fe_{2-x}O_4$, $CoAl_{x/2}Ga_{x/2}Fe_{2-x}O_4$ and $CoMg_{x/2}Zn_{x/2}Fe_{2-x}O_4$ are prepared using the tartrate-gel method and processed under identical conditions by following the procedures described in Chapter 3. The sample codes for the different compositions of the three series are givenin Table 1.

***Table 1**: Different co-substituted compositions and the corresponding sample codes.*

x	**$CoGa_{x/2}Mn_{x/2}Fe_{2-x}O_4$ (CGMF series)**	**$CoAl_{x/2}Ga_{x/2}Fe_{2-x}O_4$ (CAGF series)**	**$CoMg_{x/2}Zn_{x/2}Fe_{2-x}O_4$ (CMZF series)**
0	CF	CF	CF
0.02	--	--	CMZF02
0.05	CGMF05	CAGF05	CMZF05
0.10	CGMF10	CAGF10	CMZF10
0.20	CGMF20	CAGF20	CMZF20
0.30	CGMF30	CAGF30	--

5.3. Characterization of the calcined powders

5.3.1 Powder X-Ray diffraction

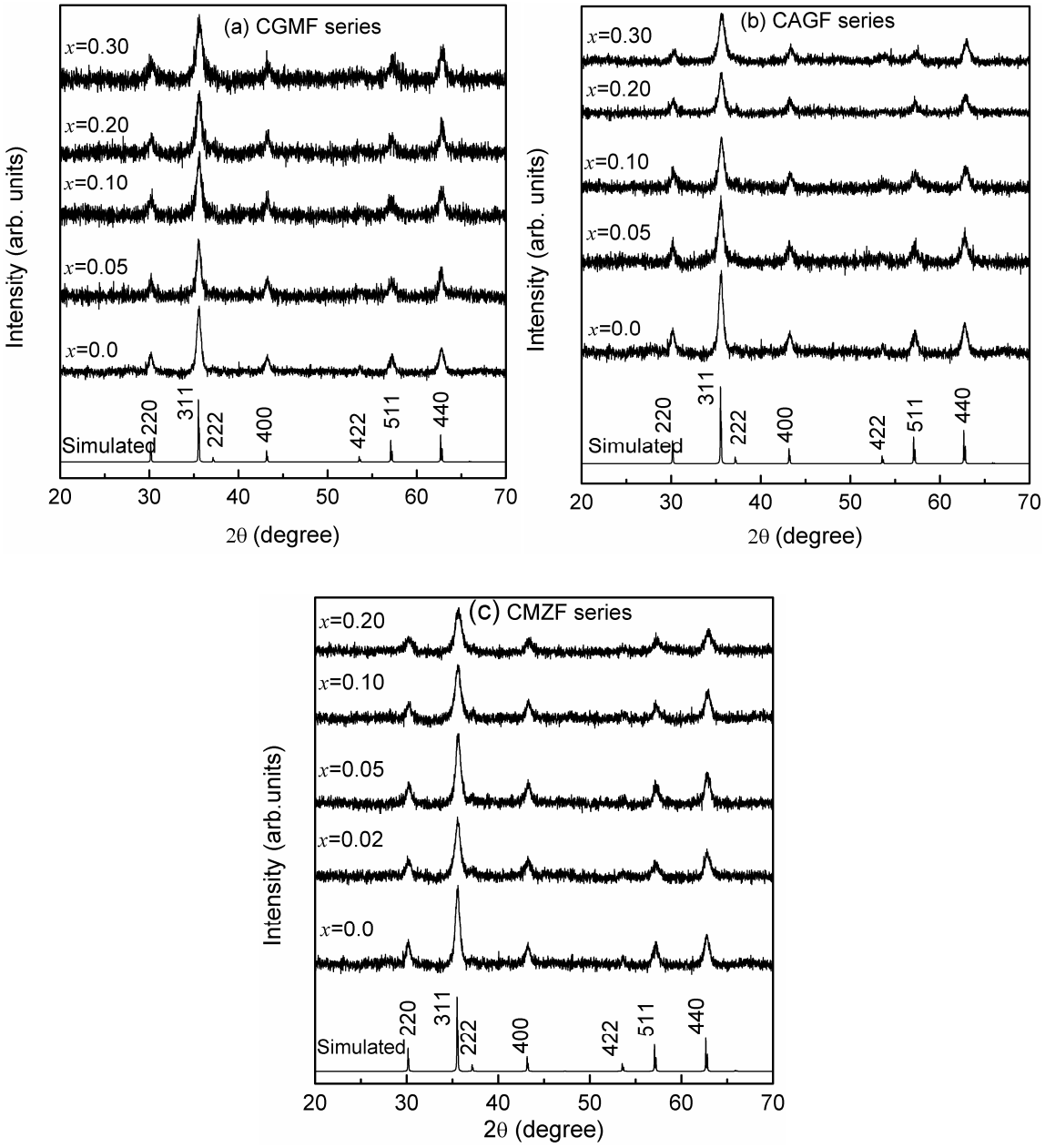

***Figure 5.1**: XRD patterns of the calcined powders of the co-substituted cobalt ferrite compositions (a) CGMF, (b) CAGF, and (c) CMZF series.*

Figure 5.1 shows the powder XRD patterns of the calcined powder samples of all the three series along with the simulated pattern of cobalt ferrite. The peaks in the observed XRD patterns are in agreement with the simulated pattern of cobalt ferrite, indicating the formation of the corresponding single-phasespinel ferrite powders, without any secondary phases. It is

observed that irrespective of size, site preferences and valency of the substituents, the crystallite size decreased with increasing the amount of substitution. The calculated average crystallite sizes are 14 nm, 12 nm and 10 nm for the compositions CGMF30, CAGF30 and CMZF20, respectively, against the value 18 nm for the unsubstituted composition (CF). Among the three studied series, the decrease in the crystallite is more pronounced in the case of the CMZF series, over the other two series. This is probably due to more lattice strain induced in the crystal structure due to the difference in the valencies and size effects.

5.3.2 Transmission electron microscopy

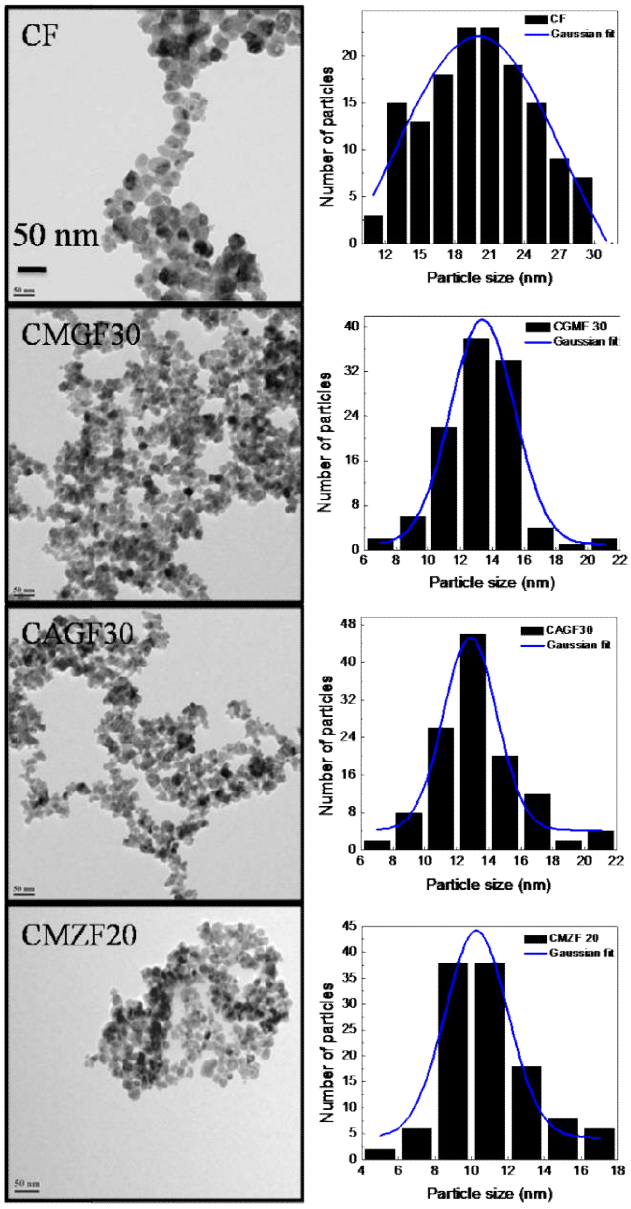

***Figure 5.2**: TEM images of selected compositions of the three series, and the corresponding particle size histograms. The scale shown is the same for all images.*

TEM images of selected compositions (CF, CGMF30, CAGF30 and CMZF20) from the three series are shown in Figure 5.2. As can be seen from the images, the particles are smaller in size in the substituted compositions compared to the unsubstituted composition. The histogram of the particle size distribution, fitted using the Gaussian peak profile function, is shown along with each image. The center of the peak is taken as the average particle size. The particle size distribution is very wide in the case of the unsubstituted composition whereas nearly narrow size distribution is obtained for the substituted compositions. The obtained average particle sizes are ~20 nm, ~11 nm, ~13 nm and ~10 nm for the compositions CF, CGMF30, CAGF30, and CMZF20, respectively. The average particles size obtained from the TEM analysis is comparable with the average crystallite size calculated from the XRD patterns.

5.4 Characterization of the sintered samples

5.4.1 Structure

XRD patterns of the sintered compositions of all the three series are shown in Figure 5.3. All the XRD patterns correspond to cubic spinel phase structure suggesting that all compositions are formed as single phase spinel ferrites. Rietveld refinement analysis of the XRD patterns was carried out to confirm the phase purity and extract the unit cell parameters. The Rietveld refinement analysis confirmed that all the sintered compositions of the three series formed single-phase solid solutions of cubic spinel ferrites, indicating that the co-substituted ions are effectively incorporatedinto the crystallographic sites of the spinel ferrite. The results of the Rietveld fit for the selected compositions (CGMF30, CAGF30, and CMZF20) of the three series are illustrated in Figure 5.4. The variation of the unit cell lattice parameter is shown in Figure 5.4(d) as a function the substitution content x. A non-linear variation of the lattice parameter for the CGMF and the CMZF series and almost a linear variation for the CAGF series with increasing the substitution amount have been observed. The nonlinearity in the lattice parameter can be envisaged when the co-substituted metal ions have the ability to occupy both the tetrahedral and octahedral coordination environments. It is worth to mention here that all three series show two different slopes below and above the composition x=0.1, suggesting some changes in the local structure and/or cation distribution around this composition.

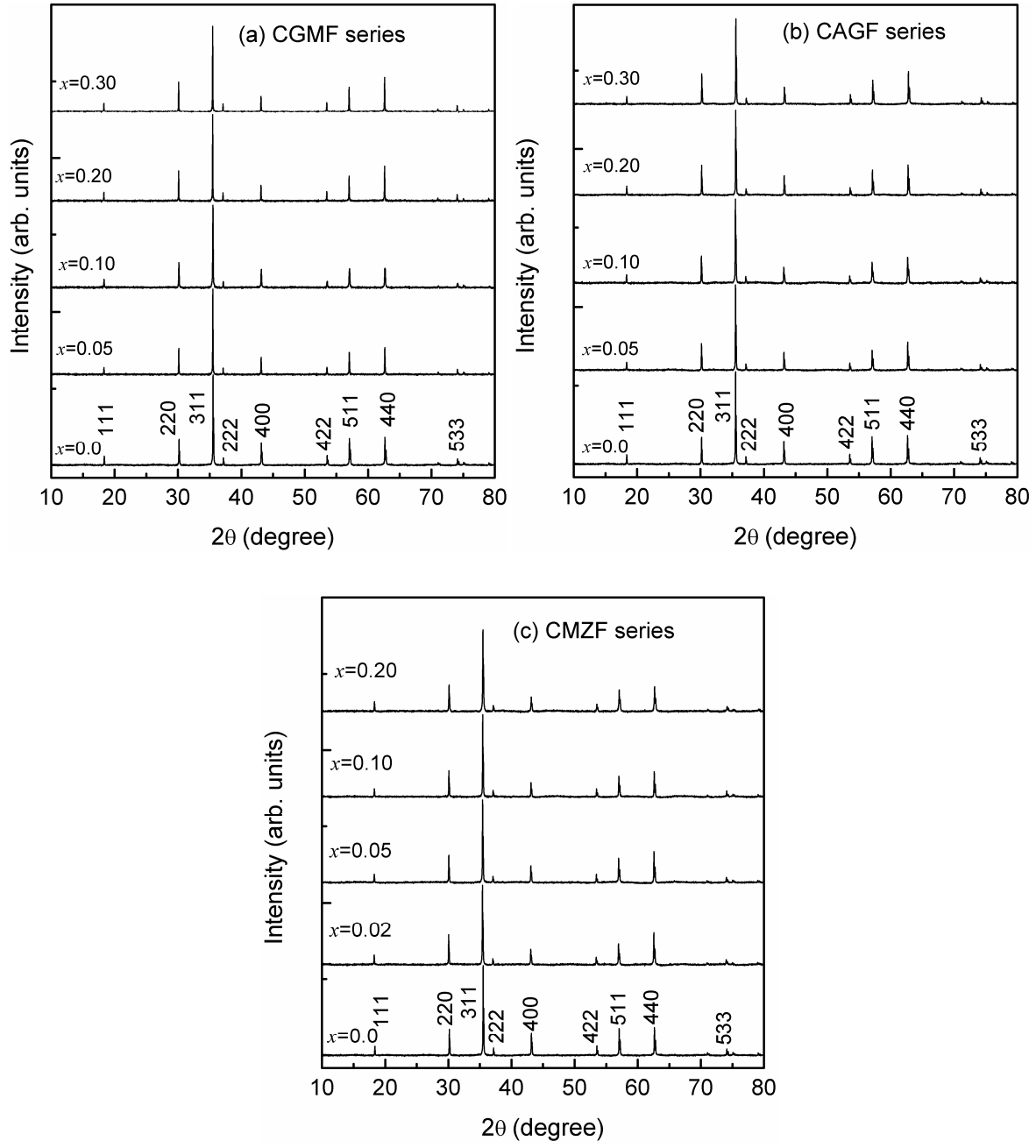

***Figure 5.3**: XRD patterns of the sintered compositions of (a) CGMF, (b) CAGF, and (c) CMZF series.*

For the same amount of substitution *x*, the rate of decrease in the lattice parameter is more pronounced with the CAGF series followed by the CGMF and less pronounced in the case of CMZF series. As described in Chapter 3, the decrease in the lattice parameter in the case of CMZF series with *x* is attributed to the conversion of a high-spin Co^{2+} into low-spin Co^{3+} to maintain the charge neutrality. However, the fast decrease in the lattice parameter in the CAGF series is due to replacement of the larger Fe^{3+} ions by the smaller sized Al^{3+} and nearly comparable sized Ga^{3+} ions. Although the size of Mn^{3+} (0.645 Å for high-spin

electronic configuration) is equal to that of Fe^{3+} (0.645 Å for high-spin configuration) [4] at the octahedral site, the decrease in the lattice parameter in the CGMF series with *x* is most probably due to the contribution from the slightly lower size of Ga^{3+}, compared to that of Fe^{3+}, and also the distribution of Co^{2+} and Fe^{3+} in the two crystallographic sites. Although Mn^{3+} and Fe^{3+} have the same ionic radius at the B-sites, there are inconsistencies in the variation of lattice parameters reported for the Mn-substituted cobalt ferrite samples where Mn has been substituted in place of Fe [5-7]. Some authors have reported a decrease whereas others reported an increase in the lattice parameter with increasing the Mn content. Such discrepancies in the lattice parameter with Mn content have been interpreted based on the competing tendency of the Mn for the site occupation either at the A-sites or the B-sites. In the present case, the decrease in the lattice parameter at higher substitution level is likely to be due to the displacement of Co^{2+} from the B-sites to the A-sites.

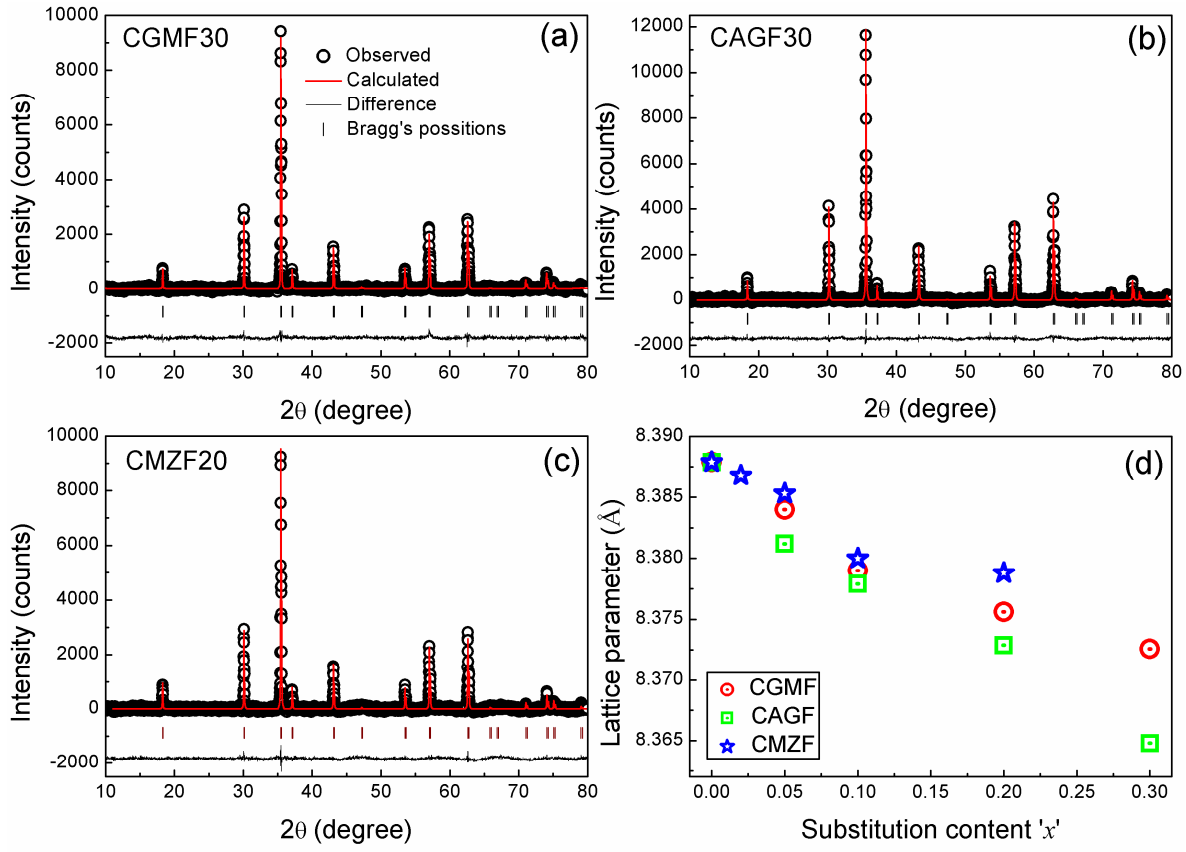

***Figure 5.4**: Results of the Rietveld refinement analysis for (a) CGMF30, (b) CAGF30, and (c) CMZF20 and (d) variation of the cubic unit cell lattice parameter as a function of substitution content in all the three series.*

***Table 5.2**: Rietveld fitting parameters for the CGMF, CGAF, and CMZF series of compositions.*

Composition	R_p	R_{wp}	χ^2
CF	0.025	0.033	1.5
CGMF05	0.022	0.020	1.4
CGMF10	0.022	0.021	1.2
CGMF20	0.021	0.024	1.1
CGMF30	0.020	0.026	1.1
CAGF05	0.021	0.055	1.5
CAGF10	0.023	0.031	1.5
CAGF20	0.020	0.025	1.1
CAGF30	0.020	0.025	1.1
CMZF02	0.021	0.026	1.2
CMZF05	0.022	0.028	1.4
CMZF10	0.021	0.027	1.1
CMZF20	0.019	0.024	1.1

5.4.2 Microstructure

Microstructures of the sintered compositions of the three different series are studied, and the SEM images of different compositionsare shown in Figure 5.5. The sintered densities of the corresponding compositions are marked in the images. A distinguishable variation in the microstructure and sintered densities between the substituted and unsubstituted compositions can be seen from the images. All the substituted compositions have a relatively higher percentage of sintered densities compared to that for the parent compound. Also, the substituted compositions show inter- and intra-granular pores with irregular shapes. This is likely to be originating from the fusion of two or more grains into larger grains. Apparently, no significant variation in the microstructures is observed for the samples of both the CAGF and CGMF series. However, in the case of the CMZF series, a substantial increase in the grain size, together with sintered density, is observed when the substitution content is increased from x=0.02 to x=0.2.

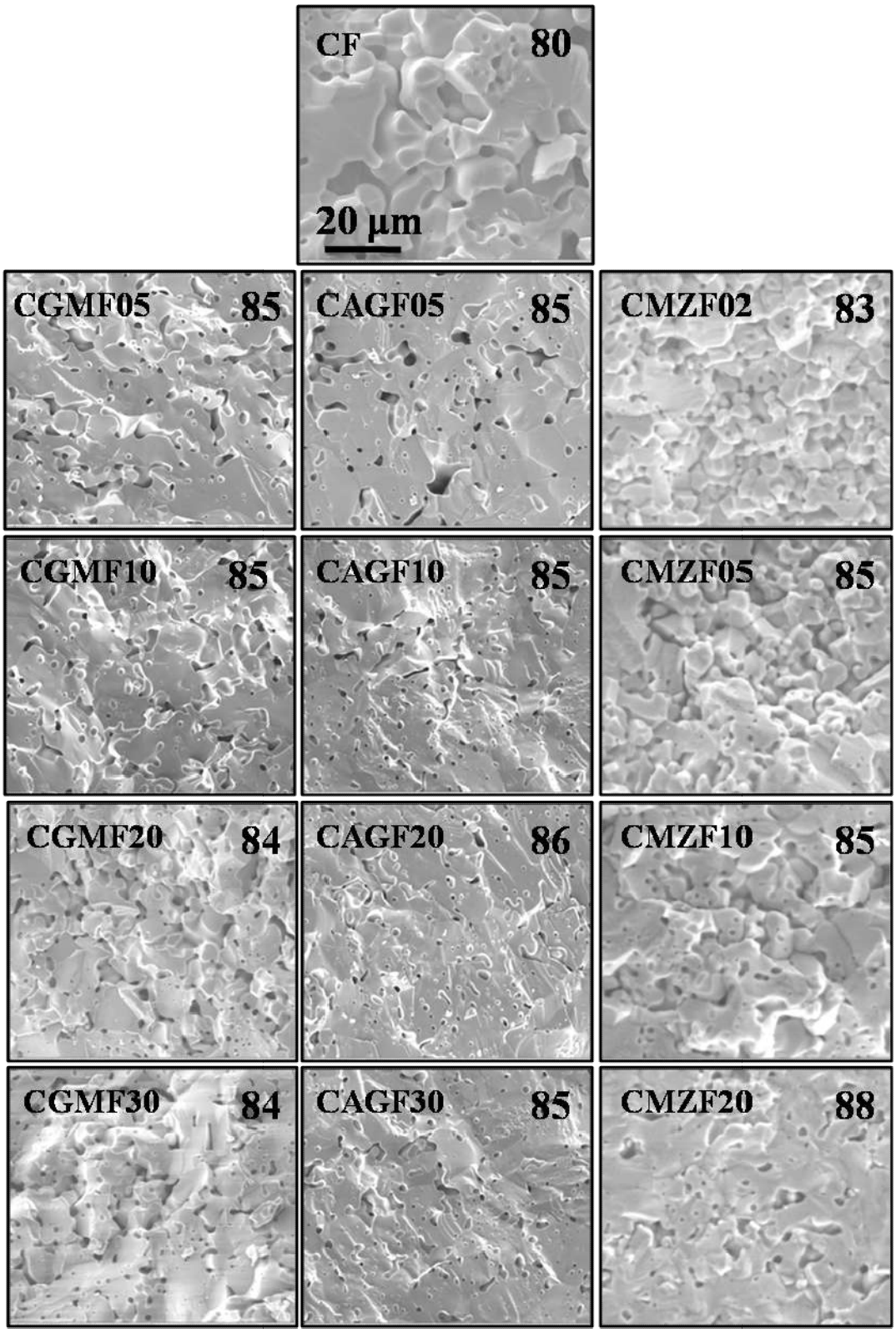

Figure 5.5*: SEM images of the sintered compositions of the three series. The numbers in the images indicate percentage sintered densitys. All images are in same scale and magnification.*

5.4.3 Magnetic properties

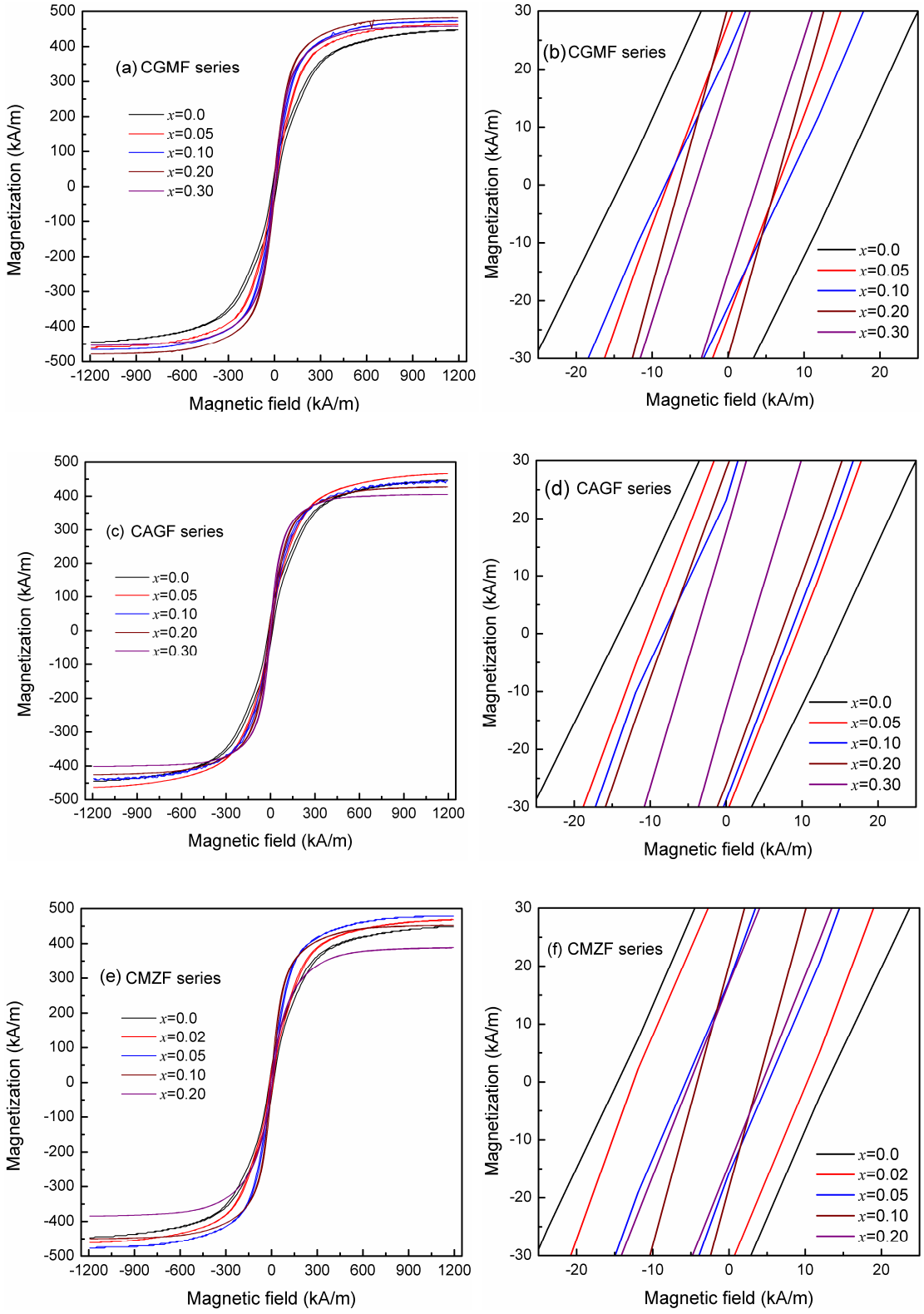

***Figure 5.6**: Magnetization vs field curves and the zoomed M-H loops at low field regions for (a,b) CGMF, (c,d) CAGF, and (e,f) CMZF series.*

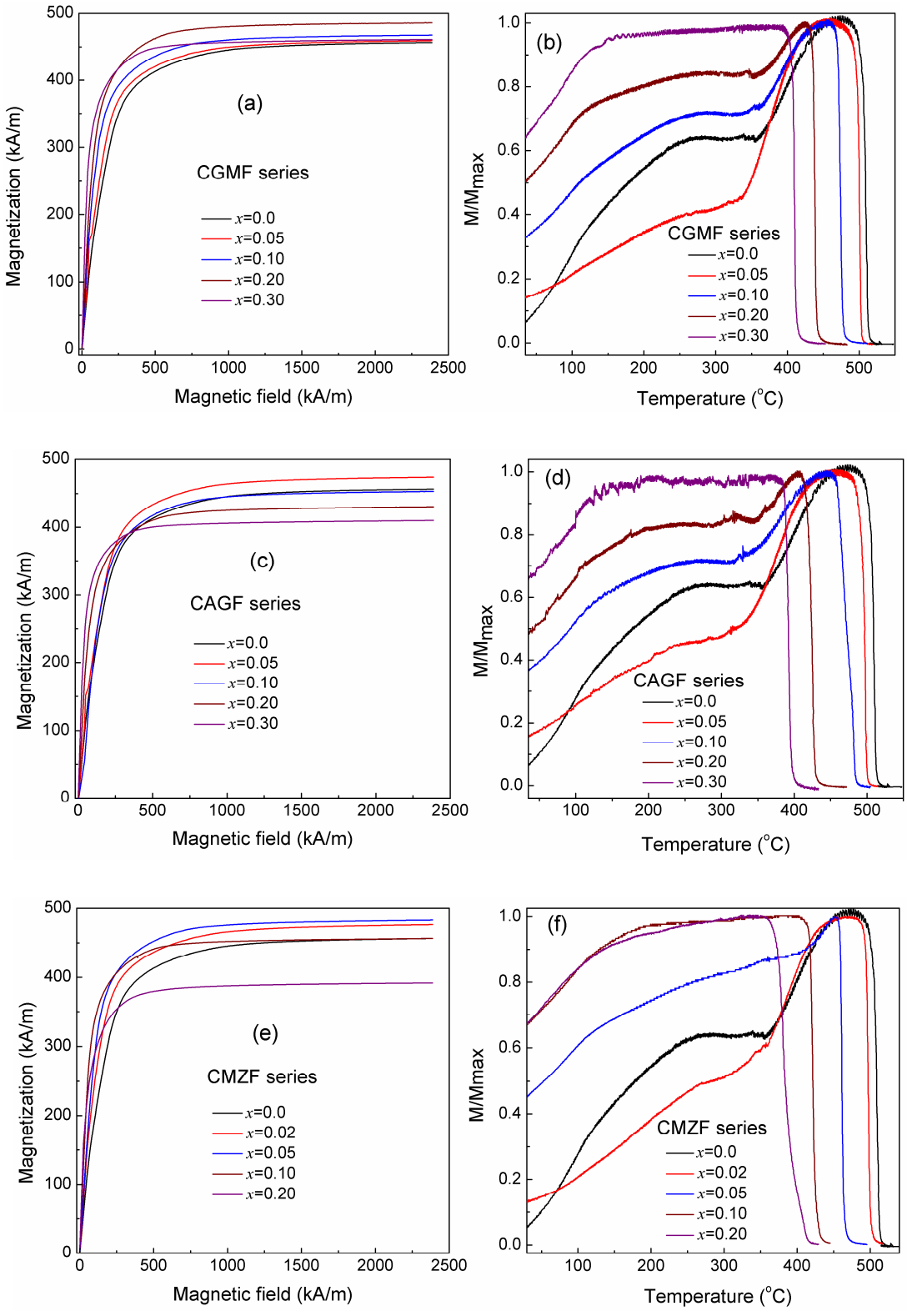

Figure 5.7: *Initial magnetization curves measured at room temperature, using a SQUID magnetometer and the temperature dependent magnetization curves, measured @ 100 Oe (~8 kA/m), using a VSM, for (a,b) CMGF, (c,d) CAGF, and (e,f) CMZF series.*

Figure 5.6 shows the field dependence of the magnetization of sintered compositions measured using a VSM up to a maximum field strength 1200 kA/m. Initial magnetization curves measured up to a maximum field 2400 kA/m using a SQUID magnetometer, and the temperature dependence of magnetization of the different compositions measured in a field 100 Oe (~8 kA/m) using a VSM are shown in Figure 5.7. The variation of the different magnetic parameters with the substitution content *x* for the three series is presented in Figure 5.8. The values of the magnetic parameters of the different compositions in the CGMF, CAGF and the CMZF series are listed in Tables 5.3, 5.4, and 5.5, respectively. It is found that the saturation magnetization (M_s) is increased from 462 kA/m for x=0 to 488 kA/m for x=0.05 in the CMZF series, to 480 kA/m for x=0.05 in the CAGF series, and to 490 kA/m for x=0.2 in the CGMF series and decreased for the higher values of x, as shown in Figure 5.8(a). Such changes in the M_s values above and below the composition x=0.1 in the CMZF and CAGF series and x=0.2 in the CGMF series can be interpreted based on the cation distribution between the tetrahedral and the octahedral sites. In the case of the CMZF series, the initial increase of M_s up to x=0.05 is most likely to be due to the substitution of both Mg and Zn for Fe at the A-site. If Mg is substituted at the B-site and Zn at the A-site, then the M_s of the substituted compositions, x=0.02 and 0.05, should have been almost equal to that of x=0. This argument is valid because the M_s is (483 kA/m for x=0.02 and 488 kA/m for x=0.05 in the present study) almost comparable for the same value up to x=0.05 in Zn-substituted cobalt ferrite, $CoZn_xFe_{2-x}O_4$, (480 kA/m for x=0.025 and 486 kA/m for x=0.05), as discussed in Chapter 3 (section 3.4.3). At the higher amount of substitution, Mg prefers the B-site and hence the magnetization decreases, as in the case of Mg-substituted samples discussed in Chapter 3. For x=0.1 (463 kA/m) in the CMZF series, the M_s is comparable to that for x=0, due to Zn in the A-site which increases the net magnetization and Mg in the B-site which reduces the magnetization.

The variation of M_s above and below x=0.1 in the CAGF series can be explained based on the same arguments as above. The higher M_s for the composition x=0.05 (480 kA/m) over the x=0, is due to the substitution of Ga and large fractions of Al for Fe at the A-site. The marginally lower value of M_s compared to the similar composition of x in the CMZF series (x=0.05) could be attributed to the partial magnetic dilution of the B-site by small amounts of Al. Although Al has more tendency to occupy the B-site, more fraction of Al might have been substituted at the A-site, at alower level of substitution, as reported [8,9]. Surprisingly, the M_s of x=0.1 in the CAGF series (461 kA/m) is comparable to that of x=0.1 in the CMZF

series which is nearly equal to that for x=0, indicating B-site magnetic dilution by Al and magnetic dilution of the A-site by Ga to equal extents. However, at higher values of x, both Al and Ga are diluting the B-site and hence the decrease in the M_s.

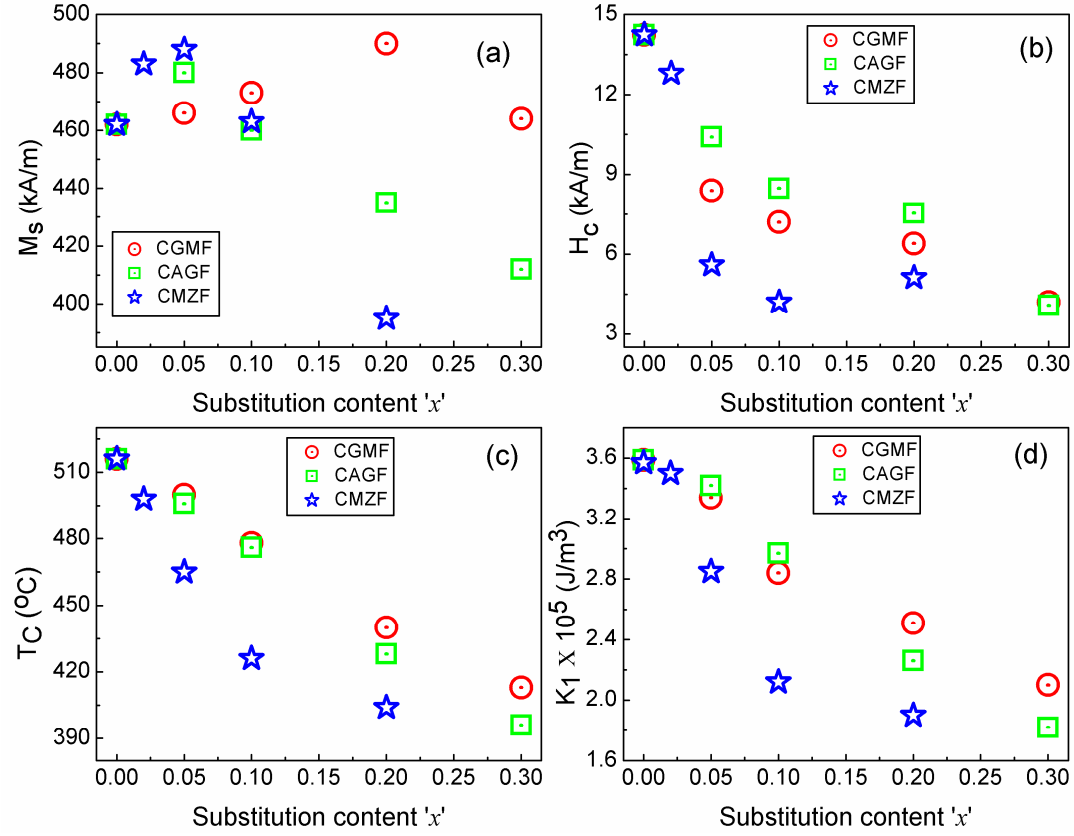

***Figure 5.8**: Variation of the magnetic parameters (M_s, H_c, T_C and K_1) as a function of substitution content in the CGMF, CAGF, and CMZF series.*

In the case of the CGMF series, Mn will be substituted in cobalt ferrite lattice in the form of $Mn^{3+,}$ and it has a strong preference for the octahedral coordination environment based on the crystal field stabilizing energy [10,11]. As more and more of Mn^{3+} are being substituted for Fe^{3+} in cobalt ferrite lattice, a decrease in the value of M_s is expected due to the decrease in the magnetic moment from $5\mu_B$ for Fe^{3+} to $4\mu_B$ for Mn^{3+} as reported in the literature [12,13]. In the present case, the M_s of the composition for x=0.05 in the CGMF series (466 kA/m) is nearly comparable to that for x=0 but considerably lower than the values obtained for x=0.05 in the CMZF and CAGF series. This could be interpreted in terms of the substitution Ga at the A-sites and displacement of Fe from the A-sites to the B-sites, whereas Mn will be substituted for Fe at the B-sites and may displace some fraction of Fe from the B-sites to the A-sites. Thus Ga-substitution increases the magnetization and Mn-substitution reduce the magnetization. Due to this kind of cations redistribution, some fraction of Co^{2+}

might be displaced from the A-sites to B-sites. However, the increase in the M_s up to x =0.2 is likely to be due to the migration of more Fe^{3+} from the A-sites to the B-sites and displacement of the low magnetic moment Co^{2+} from the B-sites to the A-sites, as reported [6,14,15]. The slight decrease in the value of M_s for the composition x=0.3 is likely to be due to the dilution of the B-sites by the nonmagnetic ion Ga^{3+}, as discussed in the previous chapter. Overall, the variation of M_s with x in the case of the CGMF series closely matches with that observed in the case of Ga-substituted cobalt ferrite, as discussed in Chapter 4.

A non-linear decrease in the coercivity is observed with increasing x for all three series as shown in Figure 5.8(b). In the case of the CMZF series, H_c is decreased at a faster rate up to x=0.1 and do not vary much for x=0.2. Similarly, for the CAGF and CGMF series, H_c is decreased for $x\leq0.1$ at a faster rate, even though not that sharp as in the case of the CMZF series, followed by slow decrease up to x=0.2 and a larger decrease for the higher values of x. As expected, T_C is found to decrease with increasing substitution content in all three series where the value is decreased from 515 ^oC for x=0 to 404 ^oC for x=0.2 in the CMZF series, to 396 ^oC for x=0.3 in the CAGF series and to 413 ^oC for x=0.3 in the CGMF series, as shown in Figure 5.8(c). For the same amount of substitution, the rate of decrease of T_C is more pronounced for the CMZF series over the other two series. The T_C values of all the compositions of the three series are listed in Tables 5.3, 5.4 and 5.5. A similar observation, a faster reduction of T_C for the Zn-substituted cobalt ferrite over the other different metal ions substituted cobalt ferrite is reported in the literature [2]. Upto $x\leq0.1$ in both the CAGF and CGMF series, T_C decreases at almost the equal rate for the same value of x but for $x>0.1$ the decrease is much faster in the case of the CAGF series compared to the CGMF series. Although the content of Ga is same in both the series, the slower decrease of T_C for $x>0.1$ for the CGMF series over the CAGF series is most likely to be due the participation of the magnetic ions Mn^{3+}, located at the octahedral sites, in the superexchange interaction with the magnetic ions located at the tetrahedral sites whereas such interaction is absent with the nonmagnetic ions (Mn-O-Fe>>Mn-O-Co, Al-O-Fe = Al-O-Co =0). This interpretation has been made based on the reported T_C variation with x in the Ga, Al and Mn-substituted cobalt ferrite systems [2,16] where the rate of decrease of T_C is more for the Ga, Al-substituted samples over the Mn-substituted samples.

First order magnetocrystalline anisotropy (K_1) is also found to vary in a similar way to the variation T_C with x in all three series as shown in Figure 5.8(d). The faster decrease in the value of K_1 for the CMZF series over other two series is likely to be contributing from

multiple factors such as strong reduction in the the A-O-B superexchange interactions (as confirmed from the T_C measurements), increasing the low-spin diamagnetic Co^{3+} content at the B-site and displacement of more amount of Co^{2+} from the B-sites to the A-sites.

It is worth to mention here, from the magnetic parameters of the studied compositions, that divalent metal ions co-substituted samples (Zn and Mg) have a more pronounced effect on the magnetic parameters over the trivalent ions substituted samples, probably due to the conversion of Co^{2+} to Co^{3+} in the former case.

***Table 5.3**: Magnetic parameters for the CGMF series.*

Composition	M_s (kA/m)	H_c (kA/m)	T_C (^oC)	K_1 (10^5 J/m^3)
CF	462	14.2	516	3.58
CGMF05	466	8.4	500	3.34
CGMF10	473	7.2	478	2.84
CGMF20	490	6.4	440	2.51
CGMF30	464	4.1	413	2.10

***Table 5.4**: Magnetic parameters for the CAGF series.*

Composition	M_s (kA/m)	H_c (kA/m)	T_C (^oC)	K_1 (10^5 J/m^3)
CF	462	14.2	516	3.58
CAGF05	480	10.4	496	3.42
CAGF10	460	8.5	476	2.97
CAGF20	435	7.5	428	2.26
CAGF30	412	4.1	394	1.82

***Table 5.5**: Magnetic parameters for the CMZF series.*

Composition	M_s (kA/m)	H_c (kA/m)	T_C (^oC)	K_1 (10^5 J/m^3)
CF	462	14.2	516	3.58
CMZF02	483	12.8	498	3.50
CMZF05	488	5.6	465	2.85
CMZF10	463	4.2	426	2.12
CMZF20	395	5.1	404	1.90

5.4.4 Raman spectra

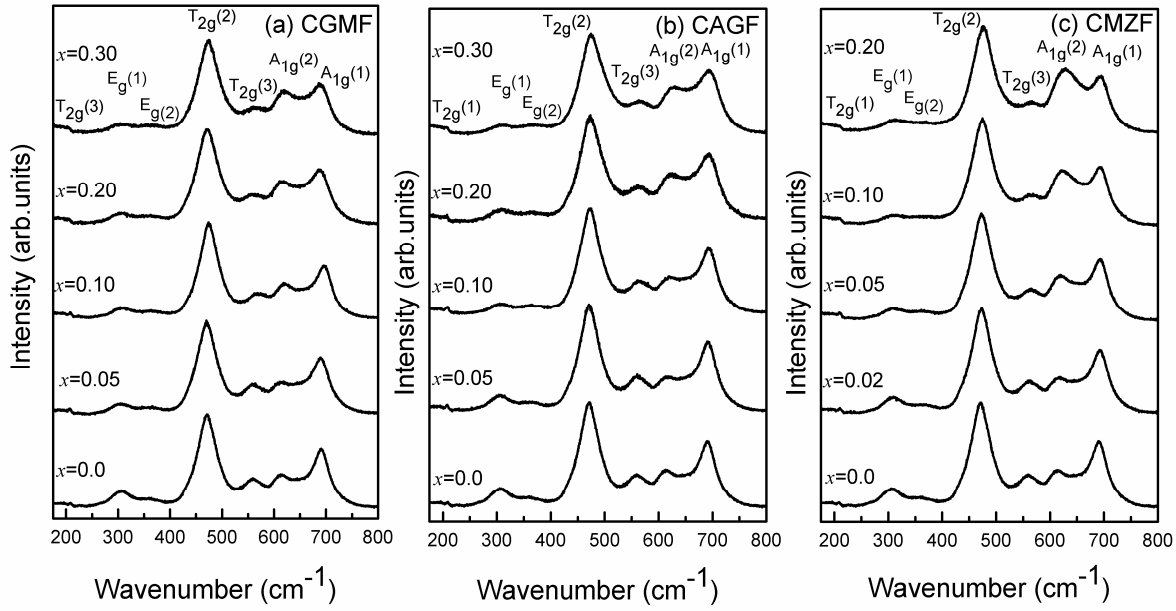

***Figure 5.9**: Raman spectra of the sintered compositions of (a) CGMF (b) CAGF, and (c) CZMF series.*

Figure 5.9 shows the Raman spectra of all the compositions in the three series. The presence of seven active modes in the spectra indicates that the compositions are in mixed spinel form. Among the three series, the bands belonging to the tetrahedral site are found greatly affected in the CMZF series compared to the other two series. It is worth to mention that a significant variation in the spectral features of the A_{1g} band is noticed for x=0.2 in the case of the CMZF series compared to x=0.3 in the CAGF and the CGMF series. Figure 5.10 shows the intensity variation of the A_{1g} bands with respect to the normalized intensity of the $T_{2g}(2)$ band. A large decrease in the intensity of the $A_{1g}(1)$ band due to the FeO_4 tetrahedra, with a red shift, is observed for the CMZF series (Figure 5.10(c)) compared to a moderate decrease in the intensity of the band, with blue shift, with increasing x in the CGMF and the CAGF series (Figure 5.10(a),(b)). The red shift in the case of the CGMF series and the blue shift in the case of the CAGF series are due to the presence of Ga and Al at the tetrahedral sites. As discussed in Chapter 4 (section 4.4.4), the stretching frequencies are lower for GaO_4 and higher for AlO_4 compared to that for the FeO_4 unit. On the other hand, the intensity of $A_{1g}(2)$ band due to CoO_4 tetrahedra shows distinguishable variation at different compositional regions in both cases. The compositions x=0.05 and 0.1 show lower intensities and 0.2 and 0.3 show higher intensities compared to that of CF (x=0). Also, both CMGF and CAGF series show a blue shift with x. In the case of the CMZF series, a large increase in the intensity of

the $A_{1g}(2)$ band is observed with increasing x, except for x=0.02 where it is lower than that for x=0. On the other hand, the intensity of the $A_{1g}(1)$ band is decreased monotonically with x as shown in Figure 5.10(c), indicating changes in the population of Fe and Co in the tetrahedral coordination environment. As can be seen from the Figure 5.10(c), the $A_{1g}(2)$ band develops a shoulder in the wavenumber region around 645 cm^{-1} that corresponds to the ZnO_4 unit, as described in Chapter 3 for the Zn-substituted cobalt ferrite.

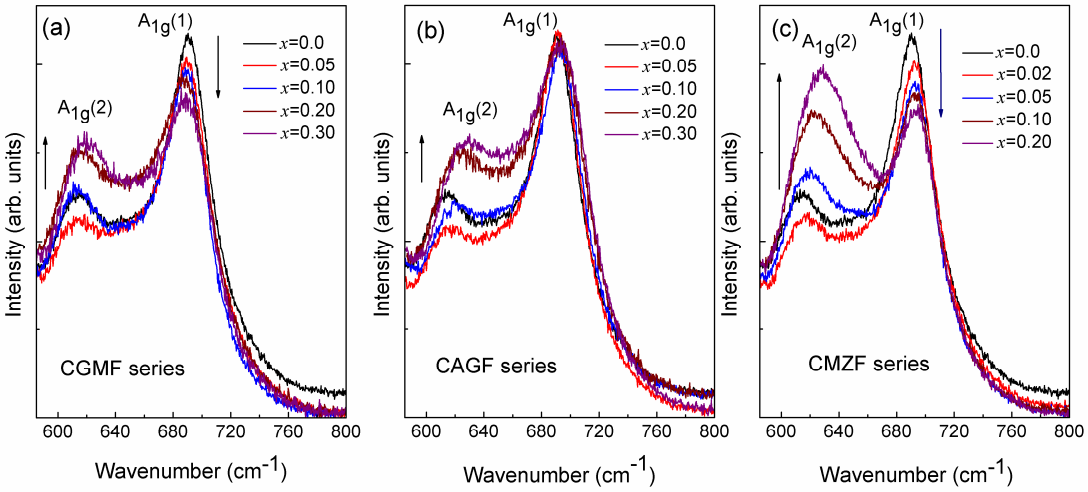

***Figure 5.10**: Variation in the intensity of A_{1g} bandswith respect to the normalized intensity of the $T_{2g}(2)$ band for (a) CGMF, (b) CAGF, and (c) CMZF series.*

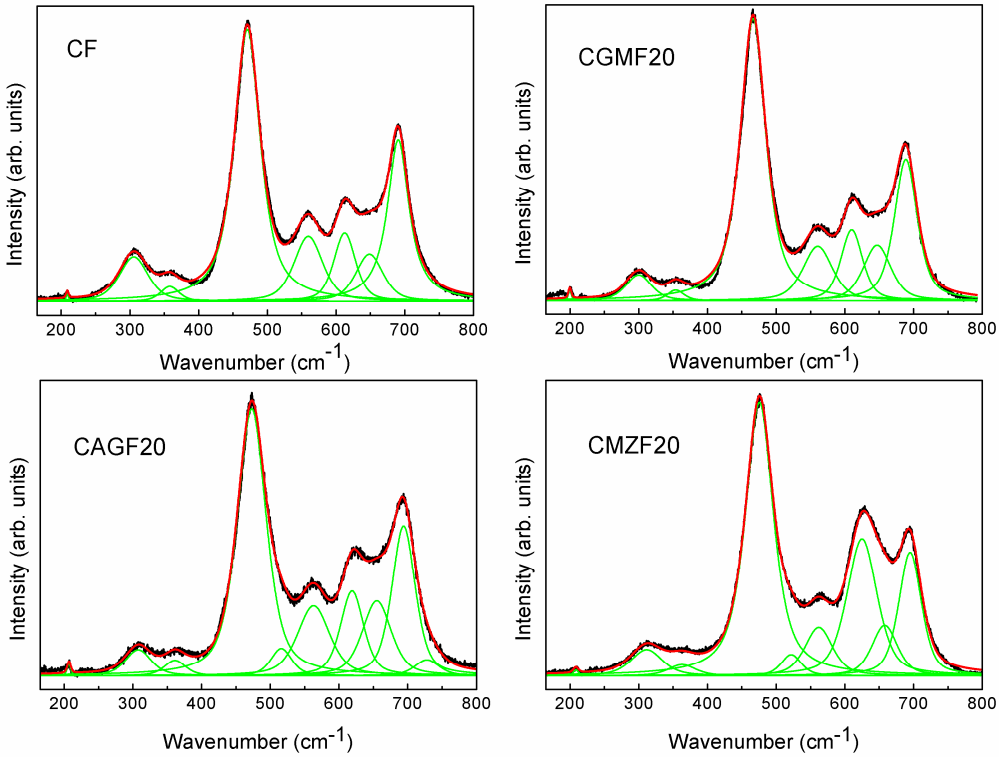

***Figure 5.11**: Deconvoluted Raman spectra of selected compositions in the three series.*

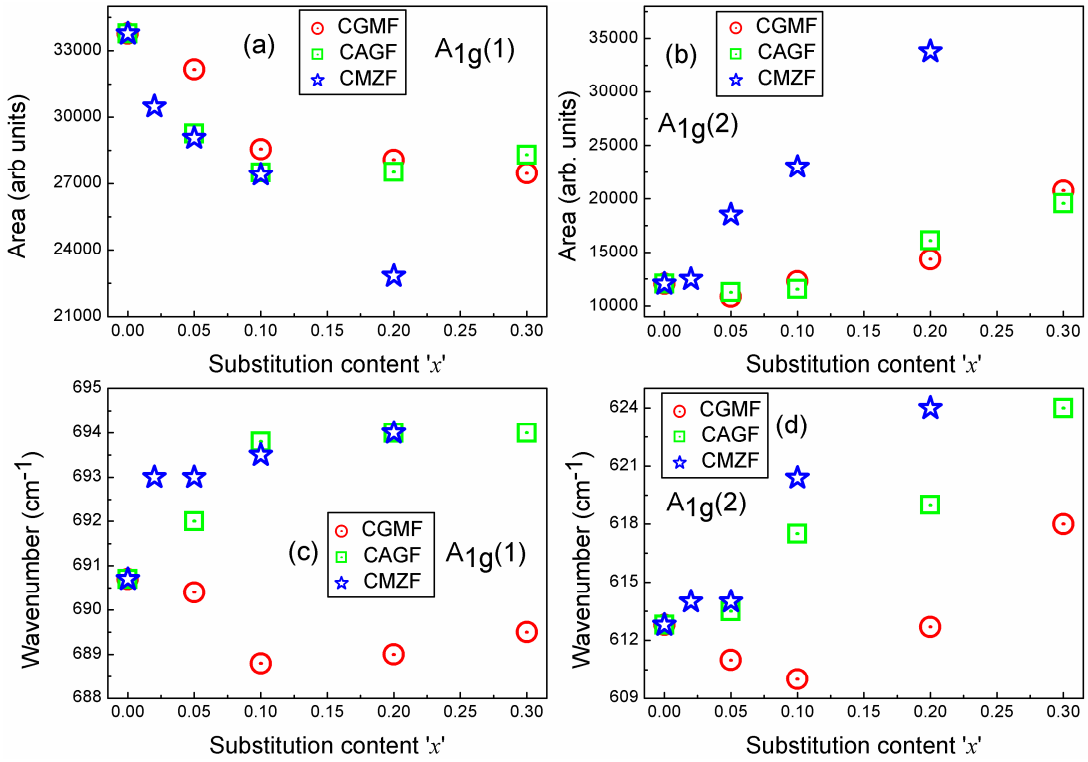

***Figure 5.12**: Variation of the area under the peaks for (a) $A_{1g}(1)$ and (b) $A_{1g}(2)$ bands and changes in the peak position of (c) $A_{1g}(1)$ and (d) $A_{1g}(2)$ bands as a function of substitution content in all three series.*

Raman spectra of all the compositions of the three series are deconvoluted, and the results of selected compositions (CF, CGMF20, CAGF20, and CMZF20) are presented in Figure 5.11. For the CAGF series, ten peaks are required to deconvolute the spectra, and the peaks at ~517 and ~720 cm^{-1} correspond to the AlO_6 and AlO_4 units, respectively, similar to the discussed in Chapter 4 (section 4.4.4) for the Al-substituted compositions. For the CMZF series, the 9th peak at ~517 cm^{-1} is likely to be due to the CoO_6 unit, as observed for the Zn and Mg-substituted compositions, as described in Chapter 3. Variation of the relative areas and the peak positions of the A_{1g} bands of as a function of x is shown in Figure 5.12. A fast decrease in the area of the $A_{1g}(1)$ band is observed for $x \leq 0.1$, and no significant variation is noticed for higher values of x in both the CGMF and CAGF series (Figure 5.12(a)). On the other hand, the area of the $A_{1g}(2)$ band is slightly lower for the compositions $x \leq 0.1$ and increased, with almost equal magnitude, for higher values of x in the CGMF and the CAGF series (Figure 5.12(b)). However, in the case of the CMZF series, a continuous decrease in the area of the $A_{1g}(1)$ band and an increase in the area of the $A_{1g}(2)$ band are observed with increasing x. The rate of increase in the area of the $A_{1g}(2)$ band with x is faster for the CMZF series compared to that for the CGMF and the CAGF series, revealing more amount of Co^{2+}

ions have been displaced from the B-sites to the A-sites in the CMZF series. The peak position of $A_{1g}(1)$ is decreased slightly up to x=0.1 in the CGMF series and increased up to x=0.1 in the CAGF, and the CMZF series and not much changes are observed at higher values of x in all three series (Figure 5.12(c)). For the CGMF series, position of the $A_{1g}(2)$ band is slightly decreased up to x=0.1, and a larger increase is observed for higher values of x. However, for the CAGF and the CMZF series, a larger increase in the peak positions is observed for the compositions x>0.05 (Figure 5.12(d)). It is worth to note here that for the CGMF and the CAGF series, a large variation (both in the areas as well as positions of the peaks) is observed above and below the composition x=0.1, indicating a possible local structural variation around this particular composition.

5.4.5 Magnetostriction studies

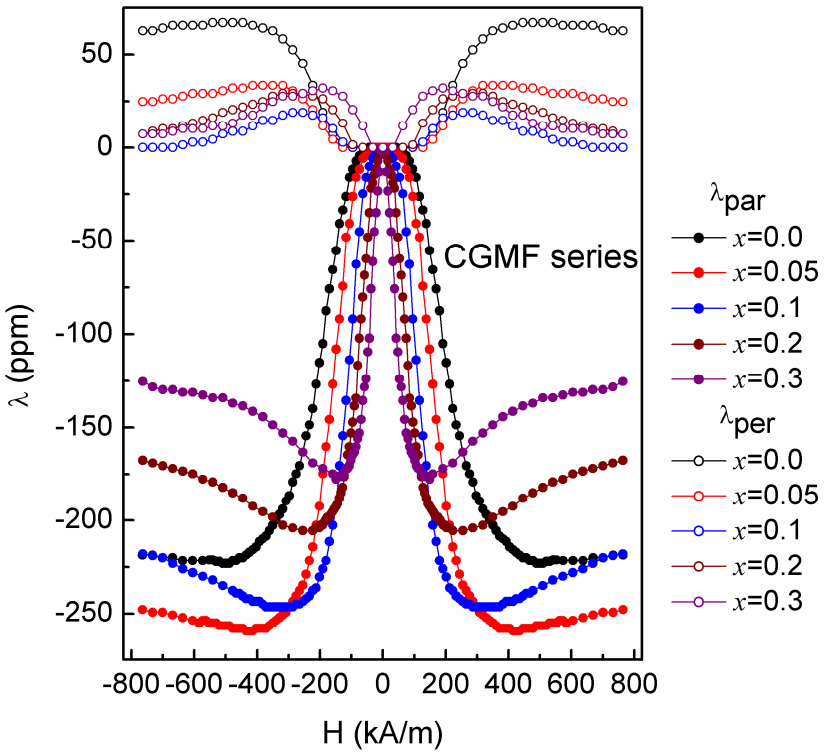

***Figure 5.13**: Magnetostriction strain curves of the CGMF series as a function of field, measured along the parallel (closed symbols) and perpendicular (open symbols) directions.*

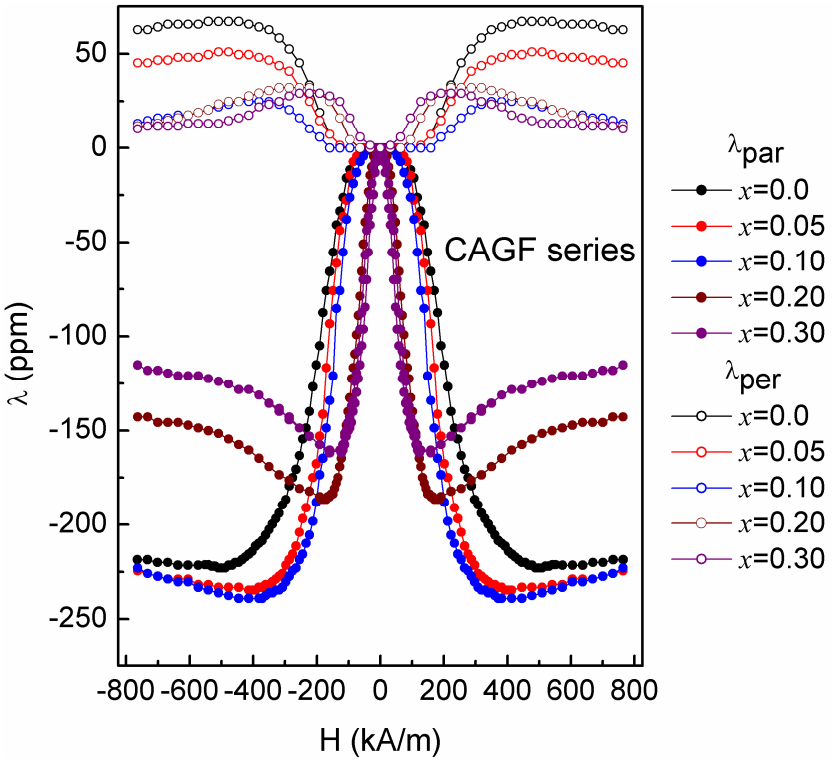

***Figure 5.14**: Magnetostriction strain curves of the CAGF series as a function of field, measured along the parallel (closed symbols) and perpendicular (open symbols) directions.*

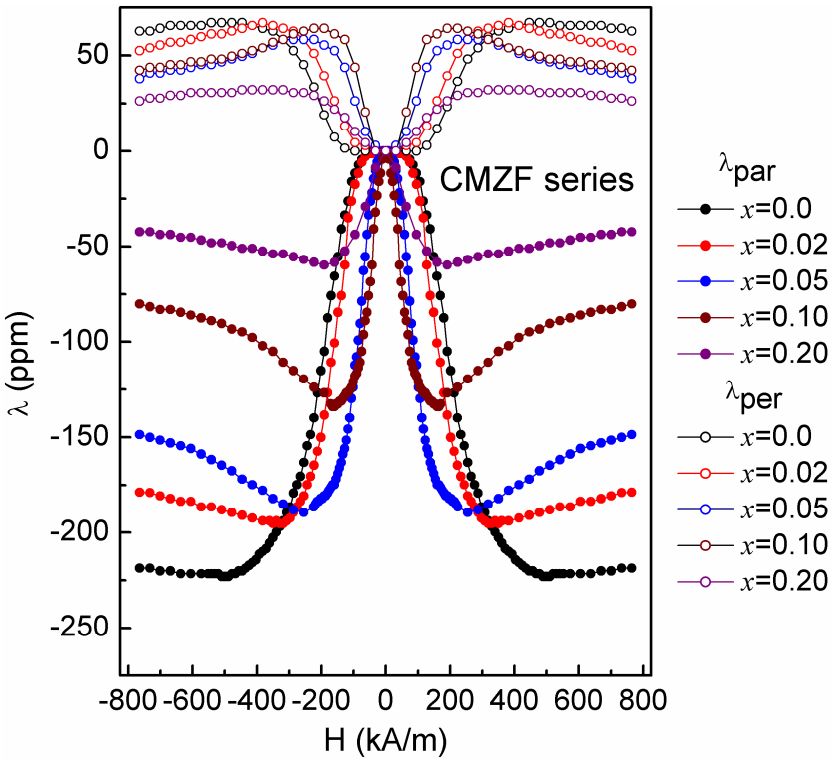

***Figure 5.15**: Magnetostriction strain curves of the CMZF series as a function of field, measured along the parallel (closed symbols) and perpendicular (open symbols) directions.*

Magnetostriction strain curves measured along the parallel and perpendicular directions to the applied magnetic field for the sintered compositions of the CGMF, CAGF, and CMZF series are shown in Figure 5.13, Figure 5.14, and Figure 5.15, respectively. Larger changes in the amplitudes and slopes of the magnetostriction curves, on substitution, along both directions can be seen in the case of the CMZF series over other two series.The CGMF and the CAGF seriesof compositions exhibit higher magnetostriction along the parallel direction even at higher amounts of substitution compared to the CMZF series. This indicates that trivalent metal ion substitution for Fe in cobalt ferrite is much more efficient to achieve higher magnetostriction at lower magnetic fields, compared to the divalent metal ion substitution.

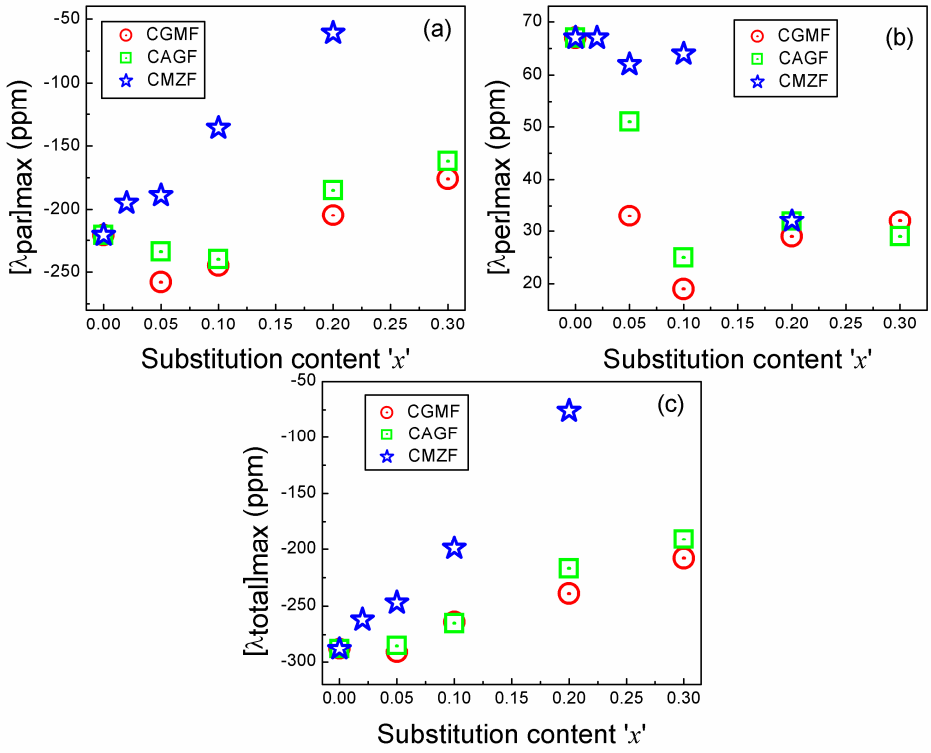

***Figure 5.16**: Variation of maximum magnetostriction obtained (a) along the parallel direction, $[\lambda_{par}]_{max}$, (b) along the perpendicular direction, $[\lambda_{per}]_{max}$, and (c) maximum total magnetostriction $[\lambda_{total}]_{max}$, as a function of x in all three series.*

The composition dependence of maximum magnetostriction along the parallel direction, $[\lambda_{par}]_{max}$, is shown in Figure 5.16(a). The $[\lambda_{par}]_{max}$ is highest with a value of -258 ppm for the composition x=0.05 in the CGMF series and -240 ppm for the composition x=0.1 in the CAGF series and these values are larger than that of the unsubstituted composition (-221 ppm) even at lower magnetic fields. With further increase in the substitution content x in both the CGMF and CAGF series, $[\lambda_{par}]_{max}$ is decreased. Similar to the $[\lambda_{par}]_{max}$ observed for x=0.1 in the CAF, CGF and CIF series, as discussed in Chapter 4 (section 4.4.5), the higher values of $[\lambda_{par}]_{max}$ for $x \leq 0.1$ in the CAGF and CGMF series against the unsubstituted composition in the present case is likely to be due to inhomogeneous distribution of the substituted cations in the unit cells of the cobalt ferrite lattice. However, in the case of the CMZF series, a small decrease in the value of $[\lambda_{par}]_{max}$ up to x=0.05 and a faster decrease at higher values of x are observed. The relatively faster decrease of $[\lambda_{par}]_{max}$ with increasing amount of substitution in the case of CMZF over the other two series is mainly due to the conversion of Co^{2+} to Co^{3+} and also due to the displacement of Co^{2+} from the B-sites to the A-sites, as evident from the Raman spectral analysis.

Along the perpendicular direction, the maximum value of magnetostriction, $[\lambda_{per}]_{max}$, is decreased up to x=0.1 in the CGMF and CAGF series and slightly increased for x=0.2 and 0.3 with almost equal magnitudes. However, in the case of the CMZF series, no significant change in $[\lambda_{per}]_{max}$ is observed up to the composition x=0.1, and a larger drop is noticed for the composition x=0.2 (Figure 5.16(b)). These observed changes in the the values of $[\lambda_{per}]_{max}$, in particular at lower amounts of substitution, in all the three series, indicate slight change in the orientation of the magnetic moments away from the respective easy and hard axes due to the presence of the substituted ions in the cobalt ferrite lattice that gives rise to distribution of the magnetostriction coefficients along the parallel and perpendicular directions. The values of the maximum magnetostriction obtained along both directions and the fields at which these maxima attained for all the three series are listed in Table 5.6, Table 5.7, and Table 5.8. Similar to $[\lambda_{par}]_{max}$, the maximum value of λ_{total} also varies with x in all the three series. $[\lambda_{total}]_{max}$ decreases continuously for the CMZF series and for the compositions x=0.05 in the CGMF and CAGF series $[\lambda_{total}]_{max}$ is equal to that of x=0.0 (-289 ppm) and decreased for higher values of x, as shown in Figure 5.16(c).

***Table 5.6**: Magnetostriction parameters of the CGMF series.*

Compo--sition	$[\lambda_{par}]_{max}$ (ppm)	H@ $[\lambda_{par}]_{max}$ (kA/m)	$[\lambda_{per}]_{max}$ (ppm)	H@ $[\lambda_{per}]_{max}$ (kA/m)	$[\lambda_{total}]_{max}$ (ppm)
CF	-221	541	67	413	-288
CGMF05	-258	371	33	318	-291
CGMF10	-245	318	19	254	-264
CGMF20	-205	286	29	254	-239
CGMF30	-176	133	32	190	-208

***Table 5.7**: Magnetostriction parameters of the CAGF series.*

Compo--sition	$[\lambda_{par}]_{max}$ (ppm)	H@ $[\lambda_{par}]_{max}$ (kA/m)	$[\lambda_{per}]_{max}$ (ppm)	H@ $[\lambda_{per}]_{max}$ (kA/m)	$[\lambda_{total}]_{max}$ (ppm)
CF	-221	541	67	413	-288
CAGF05	-234	413	51	477	-285
CAGF10	-240	371	25	350	-265
CAGF20	-185	185	32	222	-217
CAGF30	-162	122	29	190	-191

***Table 5.8**: Magnetostriction parameters of the CMZF series.*

Compo--sition	$[\lambda_{par}]_{max}$ (ppm)	H@ $[\lambda_{par}]_{max}$ (kA/m)	$[\lambda_{per}]_{max}$ (ppm)	H@ $[\lambda_{per}]_{max}$ (kA/m)	$[\lambda_{total}]_{max}$ (ppm)
CF	-221	541	67	413	-288
CMZF02	-195	329	67	382	-262
CMZF05	-189	254	62	255	-247
CMZF10	-135	165	64	191	-199
CMZF20	-61	191	32	328	-76

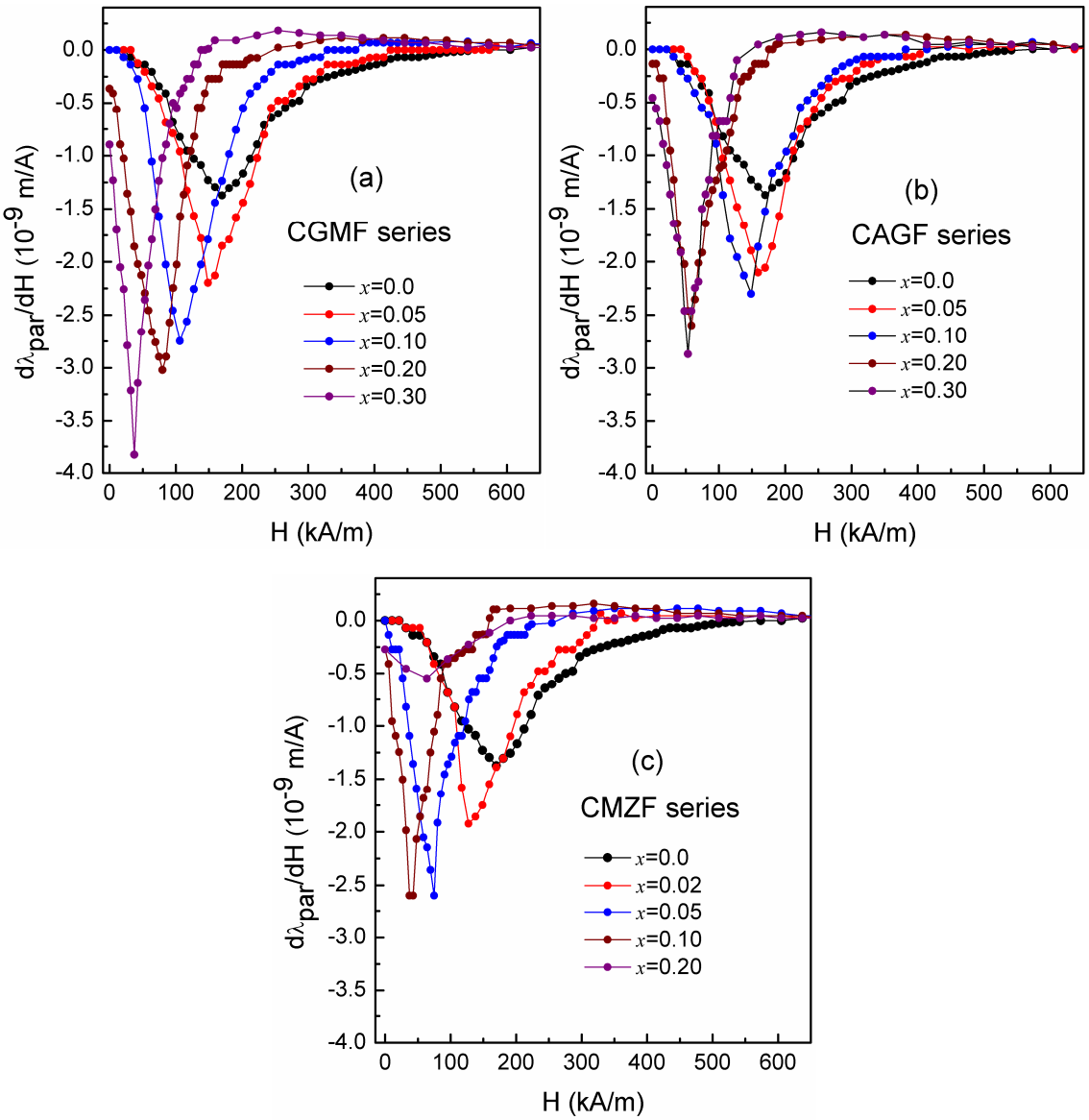

***Figure 5.17**: Field dependent strain sensitivity curves of (a) CGMF, (b) CAGF, and (C) CMZF series.*

Figure 5.17 shows the field dependence of strain sensitivity for all the three series. All the substituted compositions, except for x=0.2 in the CMZF series, show the higher amplitude of the strain sensitivity at lower magnetic fields compared to that of the unsubstituted composition. As discussed in the previous chapters, this is due to a reduction in the A-O-B superexchange interactions. The variation of the maximum strain sensitivity, $[d\lambda_{par}/dH]_{max}$, as a function of substitution content x in the three series, is shown in Figure 5.18(a). As can be seen from the figure, at a lower level of substitution, $x \leq 0.05$, a higher value of $[d\lambda_{par}/dH]_{max}$ is obtained for the CMZF series compared to the similar compositions in the other two series. However, with further increasing the amount of substitution, $[d\lambda_{par}/dH]_{max}$ is decreased in the case of the CMZF series and a steady increase in the same is observed for the CGMF and CAGF series. For x>0.05 in the CGMF and CAGF series, the rate of increase in the value of

$[d\lambda_{par}/dH]_{max}$ is larger for the CGMF series compared to that for the CAGF series for the identical values of *x*. The higher values of $[d\lambda_{par}/dH]_{max}$ are due to the combined factors including strong reduction in the A-O-B superexchange interactions as evidenced from the T_C measurements, anisotropy constant as calculated from the magnetic data, and higher value of the magnetostriction at lower magnetic field (as shown in Figure 5.18(b)).

The value of $[d\lambda_{par}/dH]_{max}$ not only depends on the values of anisotropy constant and A-O-B superexchange interactions but also on the magnitude of λ_{max} [17,18]. Therefore, the fast decrease in the value of $[d\lambda_{par}/dH]_{max}$ for the compositions $x>0.1$ in the CMZF series is due to the lower value of the $[\lambda_{par}]_{max}$. Similarly, higher values of $[d\lambda_{par}/dH]_{max}$ for the compositions $x>0.05$ in the CGMF series over the CAGF series, for the similar compositions, is likely to be due to the marginally higher values of $[\lambda_{par}]_{max}$ as well as λ_{par} at lower magnetic fields.

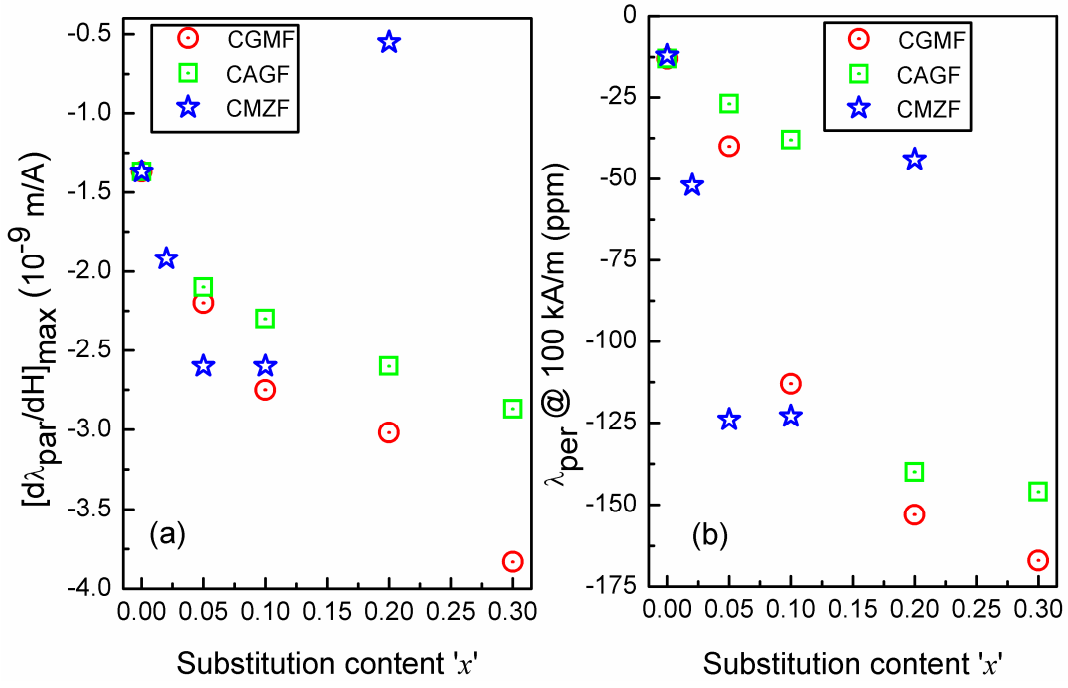

***Figure 5.18**: (a) Variation of the maximum strain sensitivity, $[d\lambda/dH]_{max}$, and (b) magnetostriction obtained along the parallel direction at a field of 100 kA/m, as a function of substitution content in the three series.*

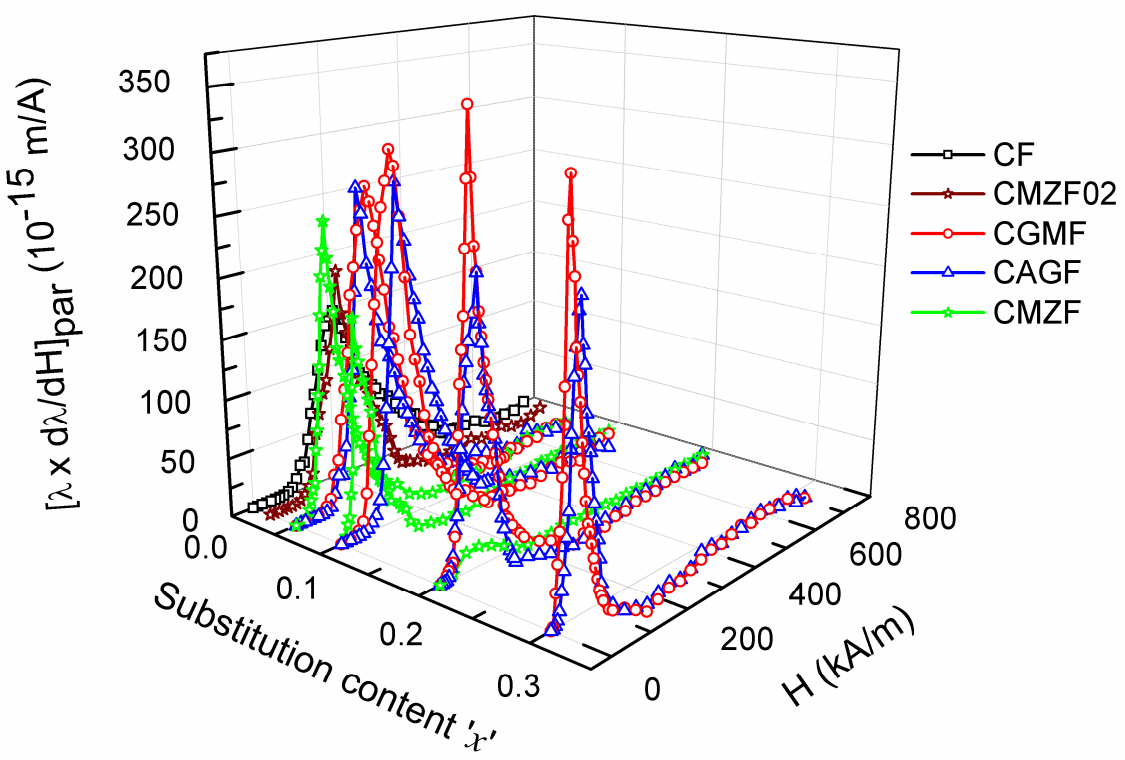

***Figure 5.19**: Variation of $[\lambda \times d\lambda/dH]_{par}$ as a function of substitution content and magnetic field.*

Figure 5.19 illustrates the variation of $[\lambda \times d\lambda/dH]_{par}$ as functions of the substitution content *x* and the applied magnetic field for the three series. As can be seen from the Figure, among all the three series, better response to the applied magnetic field is obtained for the compositions in the CGMF series even at higher substitution content. The maximum values of $[\lambda \times d\lambda/dH]$ for the three series are obtained for the compositions CMZF05 (245×10^{-15} m/A at 90 kA/m), CGMF20 (350×10^{-15} m/A at 80 kA/m), and CAGF10 (275×10^{-15} m/A at 148 kA/m) against the value of 150×10^{-15} m/A at 210 kA/m for CF (x=0). Although the maximum values of $[\lambda \times d\lambda/dH]_{par}$ are decreased at a faster rate at higher substitution levels in the case of the CMZF series, at lower substitution levels ($x \leq 0.05$), a better response is obtained at lower magnetic fields compared that for the CGMF and CAGF series for similar compositions. For example, for the composition x=0.05 in all the three series, $[\lambda \times d\lambda/dH]_{max}$ is nearly comparable but the field at which the maximum value is obtained for CMZF05 (245×10^{-15} m/A at 90 kA/m) is nearly one-half of that for CGMF05 (264×10^{-15} m/A at 193 kAm) and CAGF05 (264×10^{-15} m/A at 170 kA/m). This is mainly due to the associated higher magnetostriction and strain sensitivity for CMZF05 at lower magnetic fields.

5.4.6 Magnetic field annealing

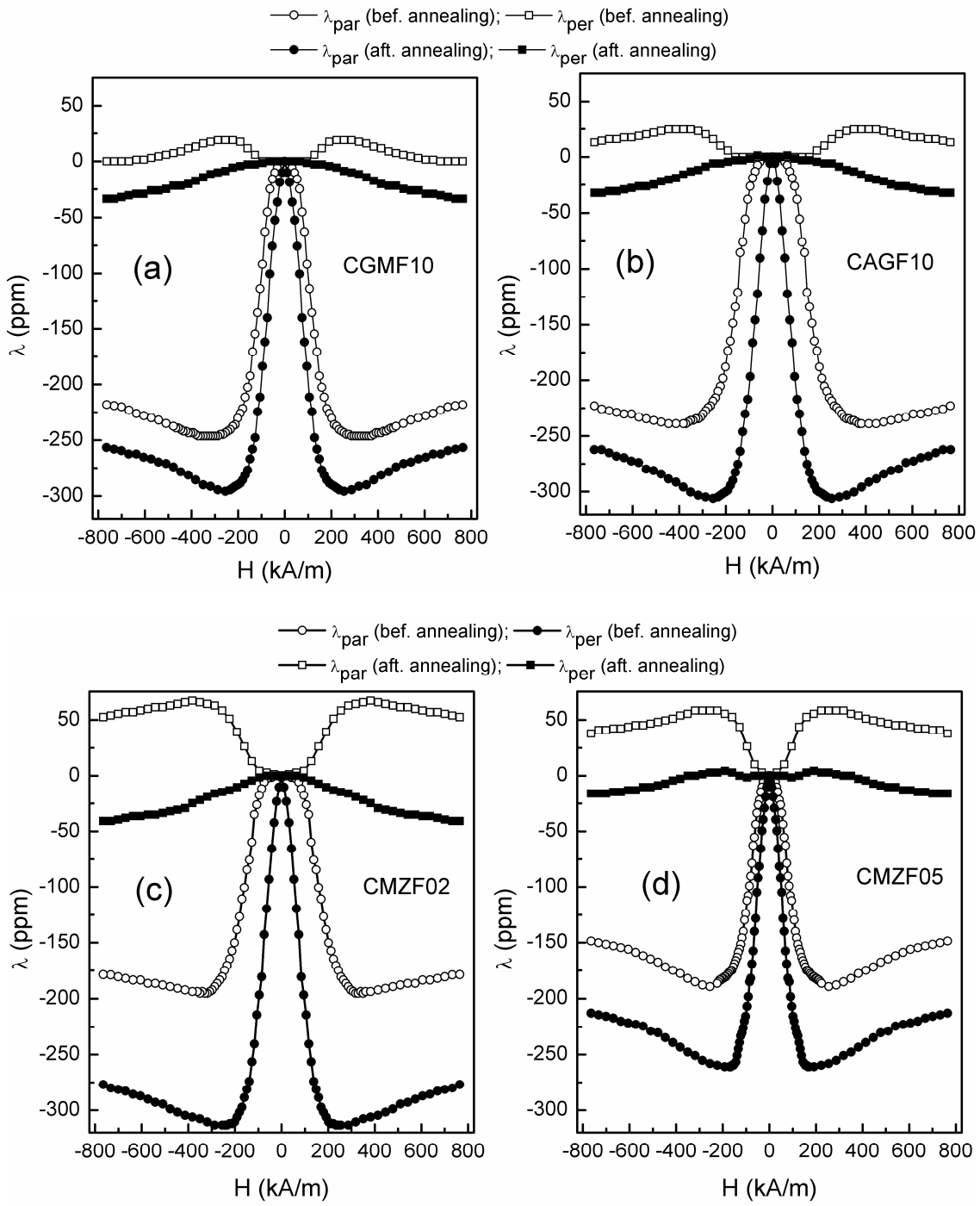

Figure 5.20*: Magnetostriction strain curves of the compositions (a) CGMF10, (b) CAGF10, (c) CMZF02,and (d) CMZF05 as a function of magnetic field, measured parallel (circles) and perpendicular (squares) directions to the applied magnetic field before (open symbols) and after (closed symbols) annealing in a field.*

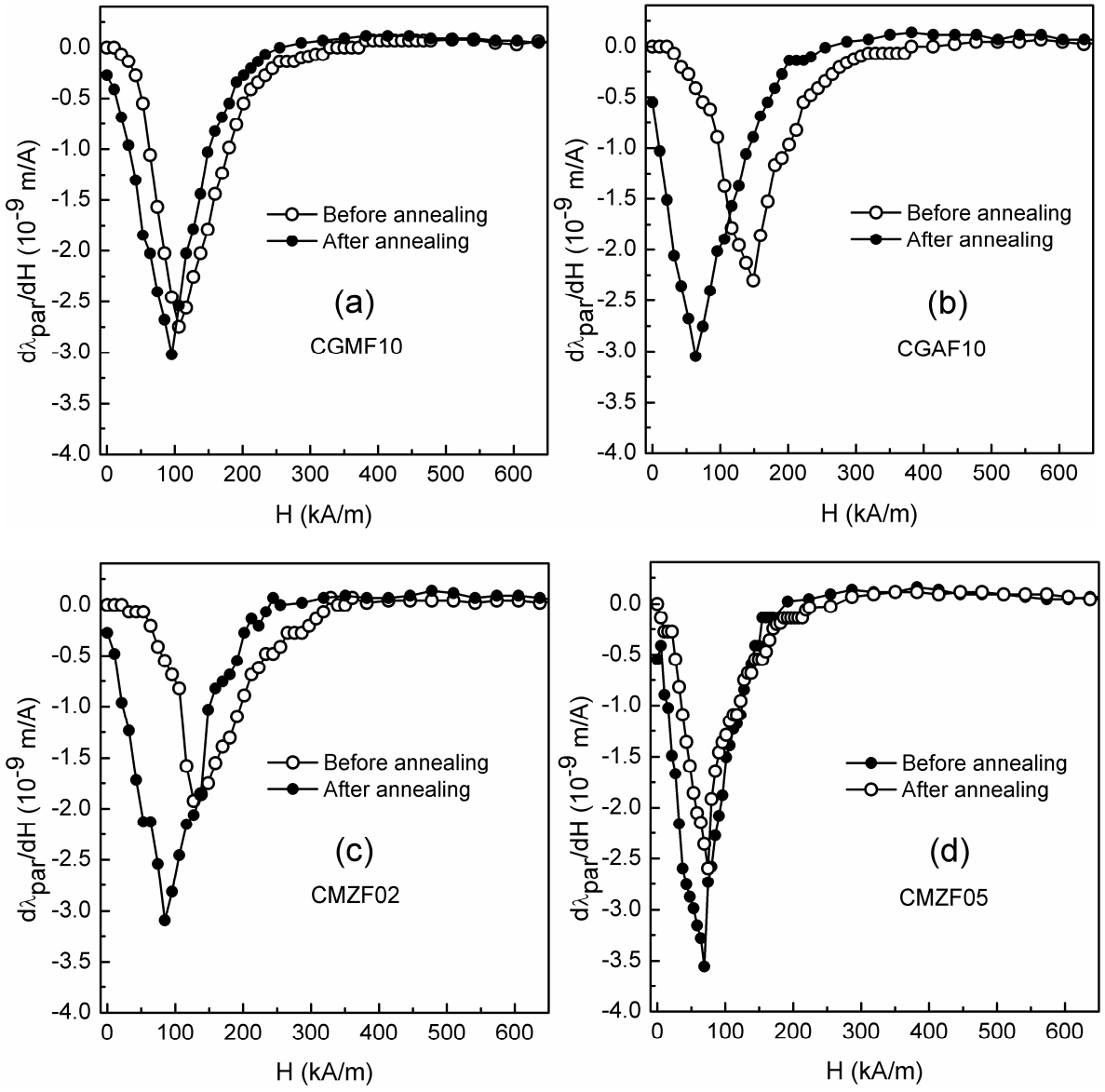

***Figure 5.21**: Comparison of the strain sensitivity curves of (a) CGMF10, (b) CAGF10, (c), CMZF02, and (d) CMZF05 before and after annealing in a magnetic field.*

***Table 5.9**: Magnetostriction parameters of the different compositions obtained before and after the field annealing.*

Compo--sitions	Before annealing				After annealing			
	$[\lambda_{par}]_{max}$ (ppm)	H @ λ_{max} (kA/m)	$[d\lambda_{par}/dH]_{max}$ (10^{-9} m/A)	H @ $[d\lambda_{par}/dH]_{max}$ (kA/m)	$[\lambda_{par}]_{max}$ (ppm)	H @ λ_{max} (kA/m)	$[d\lambda_{par}/dH]_{max}$ (10^{-9} m/A)	H @ $[d\lambda_{par}/dH]_{max}$ (kA/m)
CF	-221	541	-1.37	170	-364	375	-2.66	108
CMGF10	-245	318	-2.75	106	-290	254	-3.02	95
CAGF10	-240	371	-2.30	148	-306	254	-3.05	64
CMZF02	-195	329	-1.92	127	-313	233	-3.10	85
CMZF05	-189	254	-2.60	74	-261	165	-3.55	69

A comparison the magnetostriction strain curves of the selected compositions (CGMF10, CAGF10, CMZF02 and CMZF05) before and after annealing in a field 400 kA/m for 30 minutes, measured along the parallel and perpendicular directions is shown in Figure 5.20. The values of $[\lambda_{par}]_{max}$ and field at which the maximum value is obtained, before and after the field annealing, are listed in Table 5.9. All the field annealed compositions show higher amplitudes of maximum magnetostriction at lower magnetic fields compared to the unannealed compositions, due to induced uniaxial anisotropy along the direction of the annealing field. Before the magnetic field annealing, λ_{per} has a positive sign for all the studied compositions and the sign changes to negative after performing the magnetic field annealing indicating changes in the contribution of different magnetostriction coefficients, λ_{100}, λ_{111}, λ_{110}, as discussed in the previous chapters. Although $[\lambda_{par}]_{max}$ values for the compositions CGMF10 and CAGF10 are larger than that of the unsubstituted composition, before annealing, the $[\lambda_{par}]_{max}$ values are lower for both the compositions after the annealing in a field. Interestingly, $[\lambda_{par}]_{max}$ of CMZF02, after field annealing, is nearly comparable to that for CGMF10 and CAGF10. Much lower $[\lambda_{par}]_{max}$ is observed for the annealed sample of CMZF05, even though the level of substitution in CMZF05 is half of that in CGMF10 and CAGF10. This reduction is mainly due to the presence of Co^{3+} at the octahedral sites and the relatively lower amount of Co^{2+} at the same site. Similarly, higher strain sensitivity at lower magnetic fields is obtained for all the annealed compositions as shown in Figure 5.21, where the strain sensitivity curves of the different samples before and after annealing the samples are compared. Despite having a lower value of $[\lambda_{par}]_{max}$ for the field annealed sample of CMZF05 compared to the other field annealed compositions, highest $[d\lambda_{par}/dH]_{max}$ is observed for this composition, among all the field annealed compositions.

5.5 Conclusions

Studies on three different co-substituted compositions, where two different metal ions in equal amounts are substituted for Fe in $CoFe_2O_4$ have been performed to tune the magnetostrictive properties of the parent compound. The divalent nonmagnetic metal ions combination Zn^{2+}/Mg^{2+}, the trivalent nonmagnetic metal ions combination Al^{3+}/Ga^{3+}, and the magnetic-nonmagnetic metal ions combination Mn^{3+}/Ga^{3+} are substituted for Fe^{3+} in $CoFe_2O_4$. The different metal ions are selected based on their site preference in the spinel lattice. It is found that co-substitution of different metal ions in place of Fe in cobalt ferrite can effectively tune the structural, magnetic and magnetostrictive parameters. The study also confirmed that trivalent metal ions for the co-substitution are suitable over the divalent metal ions regarding the enhanced properties. Irrespective of the site preference and valency of the co-substituted metal ions, higher magnetic and magnetostrictive parameters are obtained at a lower amount of substitution at relatively lower magnetic fields, compared to the unsubstituted composition. In the case of divalent ions co-substitution, the magnetostriction parameters are greatly affected due to the conversion of Co^{2+} to Co^{3+} to maintain the charge neutrality and also due to the migration of Co^{2+} from the octahedral sites to the tetrahedral sites. At lower amounts of trivalent ions co-substitution ($x \leq 0.1$), a higher magnitude of λ_{max} at lower magnetic fields, compared to the parent compound, has been obtained. A very high strain sensitivity without much drop in the magnetostriction coefficient, compared to the parent compound counterpart, has been achieved even with a higher amount of co-substitution of Ga and Mn. The magnetostriction parameters of all three different series could be further enhanced to higher values at lower magnetic fields after annealing the samples in a magnetic field.

Bibliograpy

[1] N. Ranvah, I. C. Nlebedim, Y. Melikhov, J. E. Snyder, D. C. Jiles, A. J. Moses, P. I. Williams, F. Anayi, and S. H. Song, *IEEE Tran. Magn*. **44**, 3013 (2008).

[2] I. C. Nlebedim and D. C. Jiles, *Smart Mater. Struct*. **24**, 025006 (2015).

[3] V. R. Monaji and D. Das, *J. Alloys Compd*. **634**, 99 (2015).

[4] R. D. Shannon, *Acta Crystallogr. A* **32**, 751 (1976).

[5] S. Supriya, S. Kumar, and M. Kar, *J. Appl. Phys*. **120**, 215106 (2015).

[6] C. V. Ramana, Y. D. Kolekar, K. K. Bharathi, B. Sinha, and K. Ghosh, *J. Appl. Phys*. **114**, 183907 (2013).

[7] S. H. Song, Doctoral dissertation, Department of Materials Science and engineering, State University, Ames, Iowa, 2007.

[8] L. Kumar and M. Kar, *J. Magn. Magn. Mater*. **323**, 2042 (2011).

[9] N. Ranvah, I. C. Nlebedim, Y. Melikhov, J. E. Snyder, P. I. Williams, A. J. Moses, and D. C. Jiles, *IEEE Tran. Magn*. **45**, 4261 (2009).

[10] D. S. McClure, *J. Phys. Chem. Solids* **3**, 311 (1957).

[11] R. G. Burns, *Mineralogical Applications of Crystal Field Theory* (2nd ed. Cambridge University press, Cambridge, 1993).

[12] J. A. Paulsen, A. P. Ring, C. C. H. Lo, J. E. Snyder, and D. C. Jiles, *J. Appl. Phys*. **97**, 044502 (2005).

[13] S. D. Bhame and P. A. Joy, *J. Appl. Phys*. **99**, 073901 (2006).

[14] G. S. N. Rao, O. F. Caltun, K. H. Rao, P. S. V. S. Rao, B. P. Rao, *J. Magn. Magn. Mater*. **341**, 60 (2013).

[15] K. Krieble, T. Schaeffer, J. A. Paulsen, A. P. Ring, C. C. H. Lo, J. E. Snyder, *J. Appl. Phys*. **97**, 10F101 (2005).

[16] S. H. Song, C. C. Lo, S. J. Lee, S. T. Aldini, J. E. Snyder and D. C. Jiles, *J. Appl. Phys*. **101**, 09C517 (2007).

[17] C. C. H. Lo, *J. Appl. Phys*. **107**, 09E706 (2010).

[18] S. J. Lee, C. C. Lo, P. N. Matlage, S. H. Song, Y. Melikhov, J. E. Snyder and D. C. Jiles, *J. Appl. Phys*. **102**, 073910 (2007).

Chapter 6

Magnetostrictive properties of self-composites of $CoM_xFe_{2-x}O_4$ (M=Al, Ga, In, Mn)

6.1 Introduction

It is found that the magnetostriction parameters of the sintered polycrystalline metal ion substituted cobalt ferrites are significantly influenced by the oxidation state, amount of substitution, site preference (tetrahedral or octahedral) and sizes of the metal ions that are substituted for Fe in $CoFe_2O_4$. Among the studied di- and trivalent nonmagnetic metal ions for substitution, the trivalent metal ions In^{3+}, $Ga^{3+,}$ and Al^{3+} are found to be more suitable candidates to achieve better magnetostriction parameters because of their isovalent nature with that of Fe^{3+}. Similarly, among the different trivalent metal ions substituted cobalt ferrite compositions studied, the compositions with x=0.1 in $CoFe_{2-x}M_xO_4$ showed better magnetostriction parameters at lower magnetic fields compared to the unsubstituted cobalt ferrite. Apart from the dependence of the magnetostriction parameters on the cation distribution, magnetic exchange interactions, and magnetocrystalline anisotropy in the metal ions substituted compositions, the microstructure of the sintered compacts is also one of the crucial factors that strongly affect the magnetostriction strain and strain sensitivity [1-3]. It has been shown in the literature for the sintered unsubstituted polycrystalline cobalt ferrite that microstructure of the sintered compacts can be effectively controlled by various approaches including sintering temperature, quenching process, compaction made from the nanosized powders of different sizes, use of sintering aids [4-7].

Making self-composites, that is, by making compacts from the powders of cobalt ferrite with different initial particle sizes is found to be very effective in enhancing the magnetostriction parameters [8]. A high value of maximum magnetostriction of -315 ppm is reported in the literature, for sintered polycrystalline cobalt ferrite derived from nanocrystalline powders of size ~4 nm obtained by an autocombustion method of synthesis [9]. In another attempt, the magnitude of the maximum magnetostriction coefficient could be further enhanced upto -400 ppm after making self-composites by mixing the nanocrystalline cobalt ferrite powder synthesized by the autocombustion method and bulk cobalt ferrite powder obtained by the conventional solid state reaction method [8].

Since the trivalent metal ions substituted cobalt ferrite exhibited enhanced magnetostriction parameters, we have investigated the magnetostrictive properties of self-composites of $CoM_xFe_{2-x}O_4$ (M=Al, Ga, In, Mn) prepared by mixing nanocrystalline powder of size ~4 nm synthesized by an autocombustion method and bulk powder of the same composition of grain size ~1-3 μm prepared by the solid state reaction method.

6.2 Synthesis of $CoM_xFe_{2-x}O_4$ (x=0, 0.1; M=Al, Ga, In, Mn)

6.2.1 Synthesis of nanocrystalline powders

Different compositions in $CoM_xFe_{2-x}O_4$ (x=0, 0.1, M=Al, Ga, In, Mn) were prepared by following the procedure reported previously [7]. Stoichiometric amounts of the metal nitrates were dissolved in minimum amount of distilled water in a 1000 ml crystallizing dish followed by sonication for 15 minutes. A calculated amount of glycine (0.125 mole per mole of metal ion) was dissolved in minimum amount of distilled water in a separate 25 ml beaker. The glycine solution was mixed with the metal nitrate solution, and the resultant solution was then evaporated on a hot plate at 200 ^oC. After the evaporation of the solvent molecules, the resulting brown thick mass subsequently under went autocombustion reaction,yielding the corresponding mixed metal oxide powder.

6.2.2 Synthesis of bulk powders

Different compositions in $CoM_xFe_{2-x}O_4$ (x=0, 0.1; M=Ga, In, Mn, Al) were prepared using Fe_2O_3, Ga_2O_3, In_2O_3, Al_2O_3, MnO_2 and Co_3O_4 powders as starting precursors. Stoichiometric amounts of the corresponding metal oxides were homogeneously mixed in an agate mortar using acetone as the mixing medium. The resultant metal oxide mixture was transferred to an alumina crucible followed by heat treatment at four different temperatures (850, 1000, 1100 and 1200 ^oC) with a dwell time of 10 hours at each step with intermediate grindings.

6.2.3. Preparation of self-composites, compaction, and sintering

Self-composites were prepared by thoroughly mixing the bulk and nanosized powders of the same composition of different weight percentages in an agate motor. Later, the mixture was lubricated with 2% PVA binder and pressed into the form of cylindrical compacts at a pressure of 8 MPa and sintered at 1450 ^oC for 10 minutes with the heating and cooling rates of 5 ^oC per minute.

6.3 Characterization of powders

6.3.1 Powder XRD diffraction

Figure 6.1 shows the comparison of the powder XRD patterns of the bulk and the nanocrystalline powders of $CoFe_2O_4$ and the compositions in $CoM_{0.1}Fe_{1.9}O_4$ (M=Ga, In, Mn, Al). In the XRD patterns of the bulk powders, all peaks corresponding to the cubic spinel phase are observed and are sharp and intense indicating high degree of crystallinity whereas, in the case of the nanosized powders, only the most intense (311) peak is visible. Also, the peak is significantly broader compared to the corresponding peak of the bulk powder indicating the nanocrystalline nature of the samples. The average crystallite size of the nanocrystalline samples, calculated using the Scherrer formula, is found to be ~4 nm. The position of the (311) peak in the XRD patterns of the nanosized powders is shifted towards higher diffraction angles compared to the position of the peak in the XRD of the bulk powders. Although a large difference in the sizes of substituted ions, particular with In and Al, compared to that of Fe, the peak position of all nanocrystalline samples including unsubstituted composition is almost comparable. This is probably due to the lattice strain and stress associated with the nanocrystalline ferrite powders, as discussed in the previous chapters. A similar feature has been reported in the literature for nanocrystalline powders of different ferrites [7,9]. TEM images of the nanosized powders of $CoFe_2O_4$, and $CoM_{0.1}Fe_{1.9}O_4$ (M=Ga, In, Mn, Al) are shown in Figure 6.2. For better comparison, all the images are in same scale and magnification. It is apparent from the figure that all the compositions comprised of very small particles with size ranging from 2 to 5 nm and the particles are agglomerated in the form of small clusters, as expected for the magnetic nanocrystalline powders. For all the samples, the average crystallite size estimated from the XRD patterns is comparable with the average particles size obtained from the TEM images.

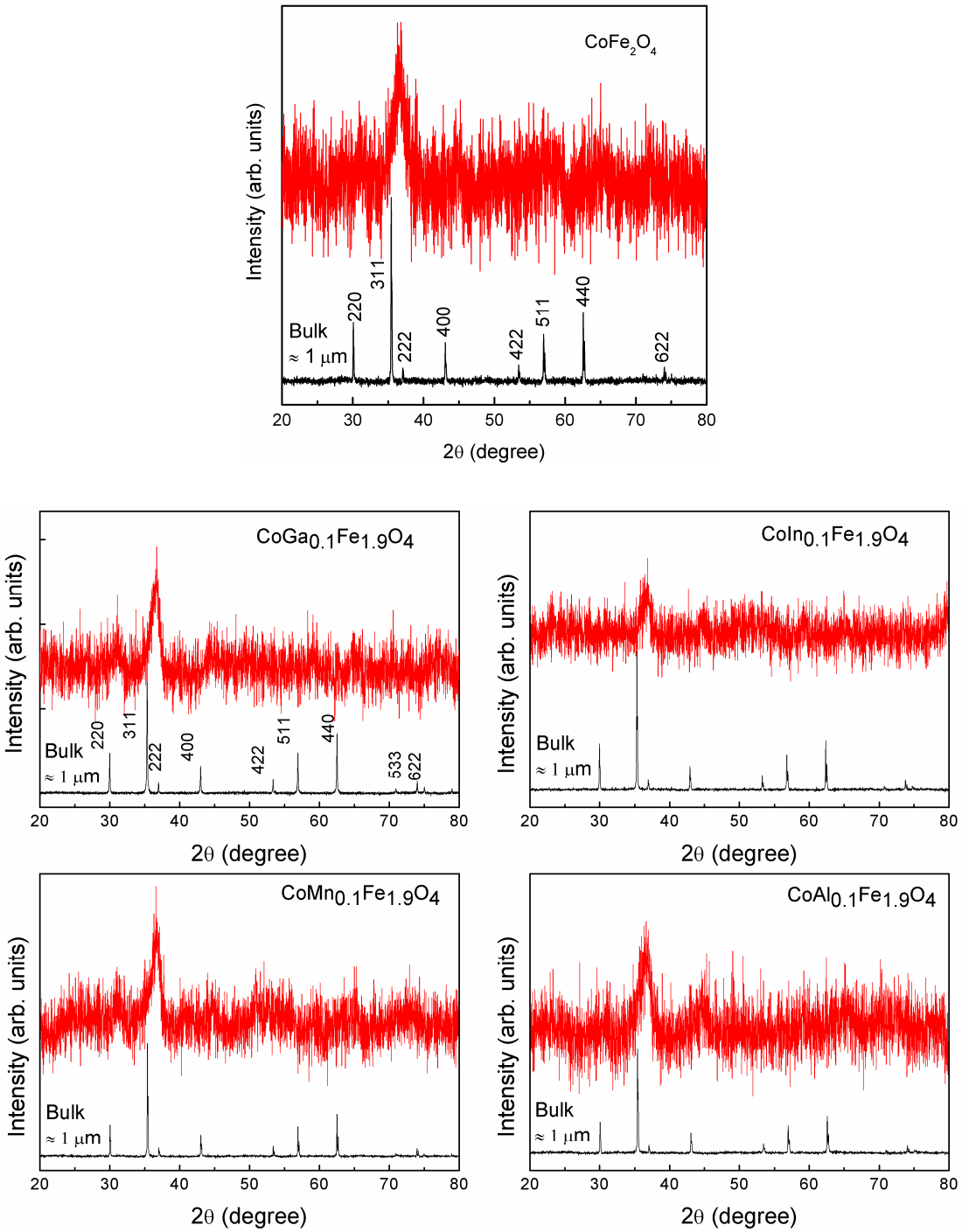

***Figure 6.1**: Comparison of the XRD patterns of the bulk and the nanocrystalline powders of $CoFe_2O_4$ and different compositions in $CoM_{0.1}Fe_{1.9}O_4$ (M=Ga, In, Mn, Al).*

6.3.2 TEM images

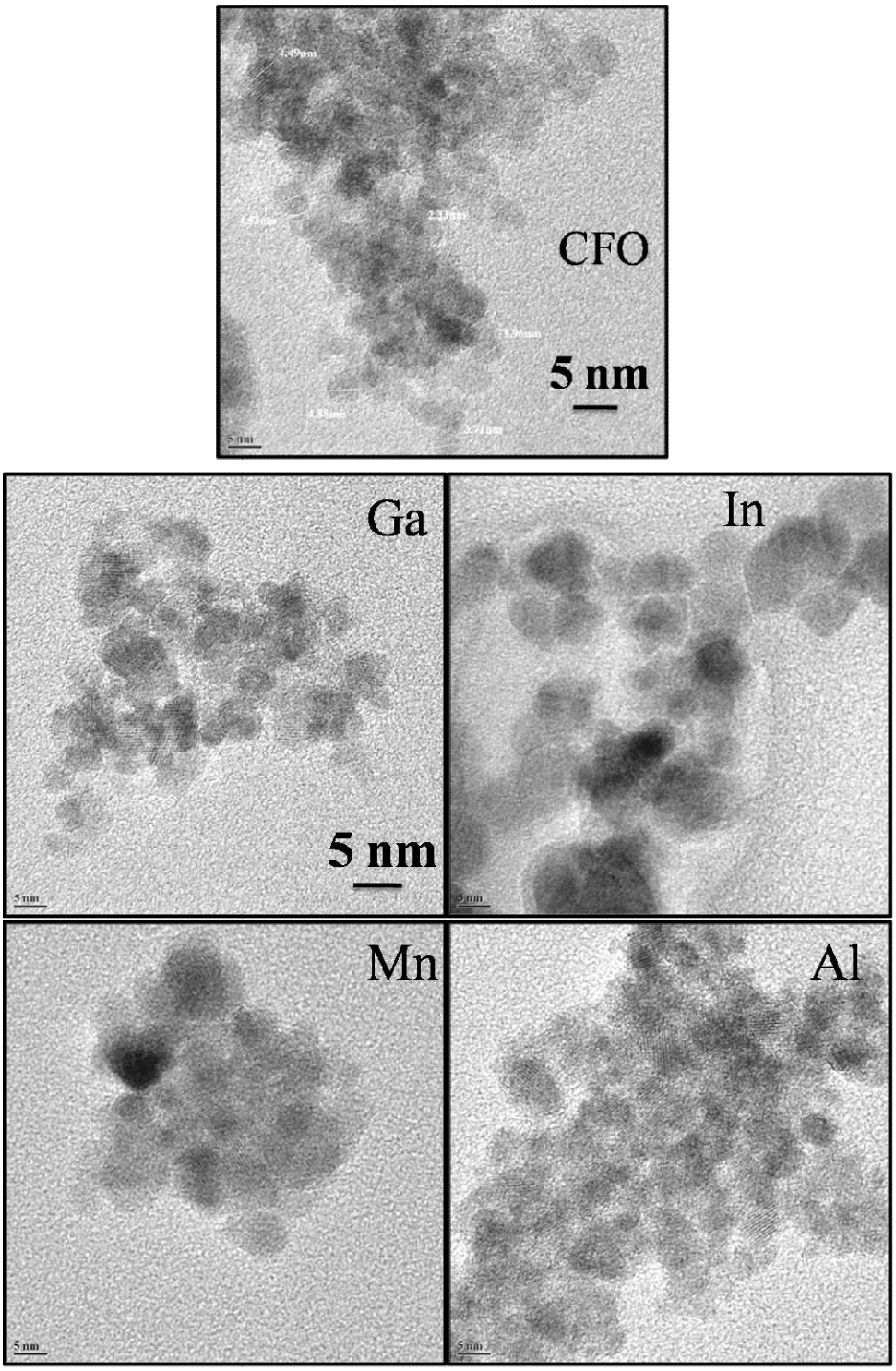

***Figure 6.2**: TEM images of cobalt ferrite (CFO) and $CoM_{0.1}Fe_{1.9}O_4$ (M=Ga, In, Mn, Al) nanoparticles. All images are in the same scale and magnification.*

6.3.3 SEM images

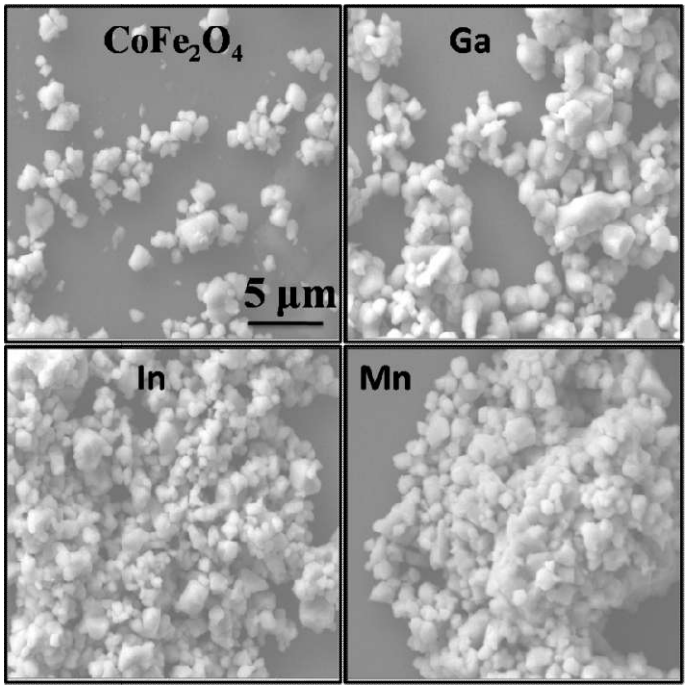

***Figure 6.3**: SEM images of the bulk powders of cobalt ferrite and $CoM_{0.1}Fe_{1.9}O_4$ (M=Ga, In, Al). All images are in the same scale and magnification.*

SEM images of the bulk powders of cobalt ferrite and $CoM_{0.1}Fe_{1.9}O_4$ (M=Ga, In, Mn) are shown in Figure 6.3. Smaller and larger grains can be seen in all the images and the average grains size is found to be ~1µm for all the compositions. Moreover, the grains are in irregular shape.

6.4 Magnetic and magnetostriction studies on sintered materials

6.4.1 $CoFe_2O_4$

Among the reported self-composites of the cobalt ferrite compacts prepared by different weight percentage of bulk and nanopowders and sintered under identical conditions, better magnetostriction characteristics, λ_{max} of ~350 nm at a field >650 kA/m, have been reported for the sintered compact made of 80% nanocrystalline and 20% bulkpowders [8]. In the present study, the experiment is repeated and the samples are synthesized and processed under identical conditions, similar to that reported in the literature [8], to verify the reproducibility of the results. The magnetostriction strain curves of cobalt ferrite sintered from the mixed nanocrystalline (80%) and bulk (20%) powders, measured along the parallel

and perpendicular directions to the applied magnetic field, are presented in Figure 6.4(a) and the corresponding strain sensitivity curves along the parallel direction are shown in Figure 6.4(b). The values of $[\lambda_{par}]_{max}$ and $[d\lambda_{par}/dH]_{max}$ of the compacts made from the bulk, nanoparticles, and the nano + bulk mixture are -172 ppm, -292 ppm and -338 ppm, respectively, and -0.87 × 10^{-9} m/A, -1.51 × 10^{-9} m/A and -2.08 × 10^{-9} m/A, respectively. Thus, the results show that higher magnetostriction and strain sensitivity can be obtained for the compact made from a mixture of nanosized and bulk powders.

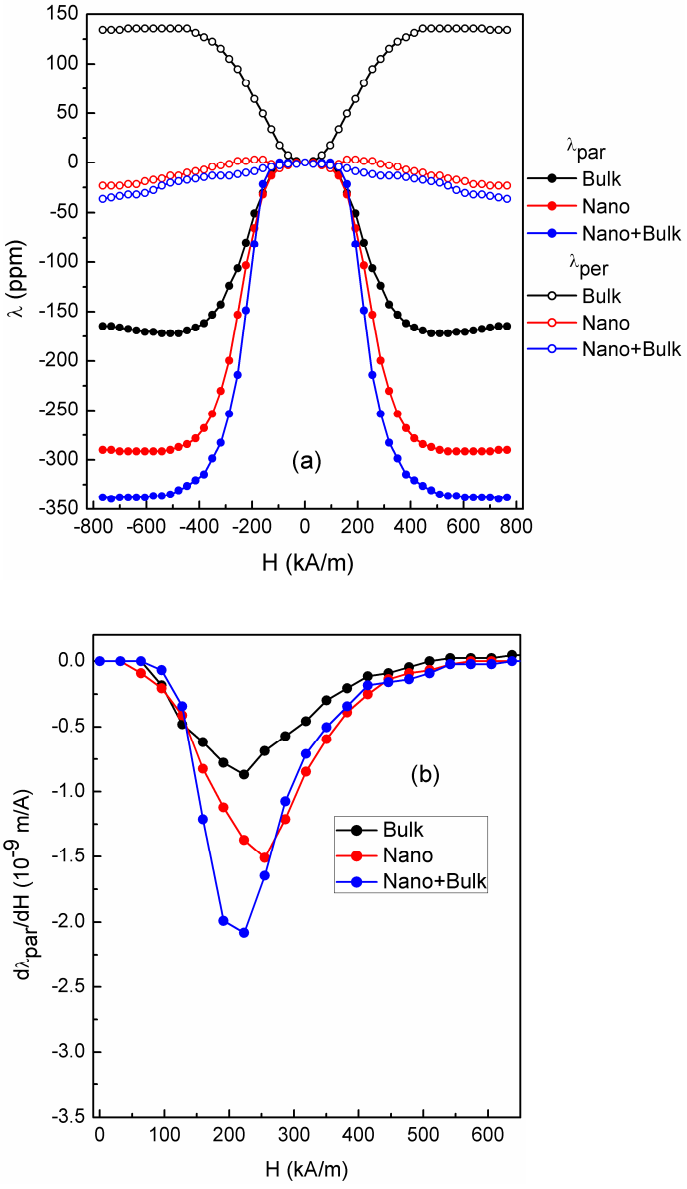

***Figure 6.4**: (a) Magnetostriction strain curves of $CoFe_2O_4$ compacts sintered from bulk, nanoparticles and mixed powders (80% nano+20% bulk), measured along the parallel (closed symbols) and perpendicular (open symbols) directions to the applied magnetic field. (b) The corresponding strain sensitivity curves along the parallel direction.*

6.4.2 $CoGa_{0.1}Fe_{1.9}O_4$

The magnetostriction strain curves of the $CoGa_{0.1}Fe_{1.9}O_4$ compacts sintered from the bulk, nanoparticles and different weight percentages of nanoparticles and bulk, measured along the parallel direction to the applied field, are shown in Figure 6.5. As can be seen from the figure, the sample sintered from the nanoparticles of size ~4 nm shows higher $[\lambda_{par}]_{max}$ with the value of -268 ppm against the value -207 ppm for the sample sintered from the bulk powder. After making the composite of 80% nanoparticles and 20% bulk, and sintered under identical conditions, the λ_{max} is increased to -326 ppm at lower magnetic fields. By increasing the percentage of bulk powder content, the amplitude of the magnetostriction coefficient is decreased. Therefore, the combination 80% nanosized and 20% bulk powders are likely to be the optimum composition of the self-composite to achieve the higher magnitude of magnetostriction. The decreasing magnetostriction with increasing the percentage bulk powder is likely to be due to changes in the microstructure.

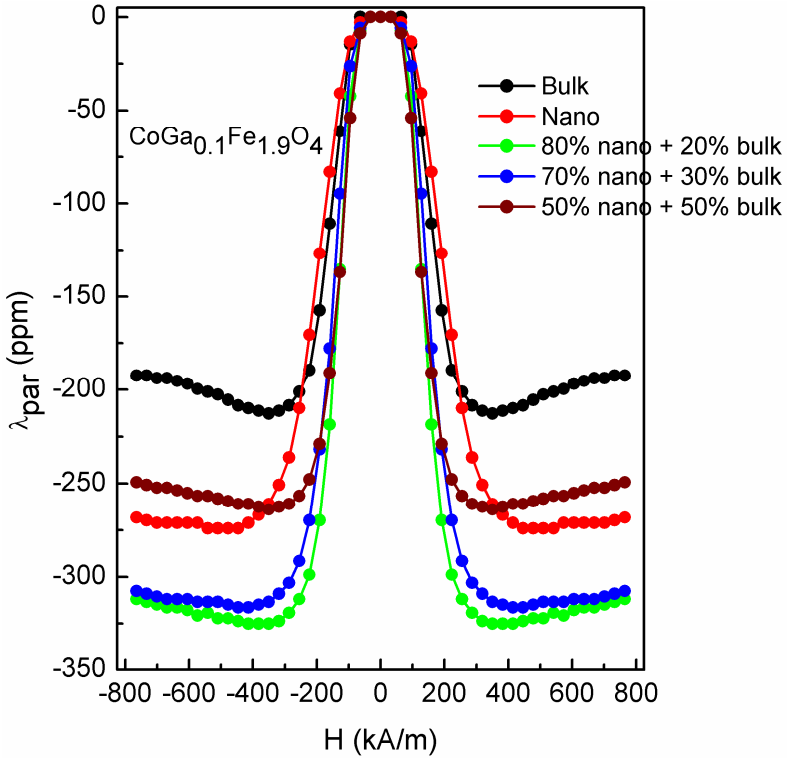

***Figure 6.5**: Magnetostriction strain curves of the samples sintered from nanoparticles, bulk and mixed nanocrystalline and bulk powders of different weight percentages, measured along the parallel direction to the applied magnetic field.*

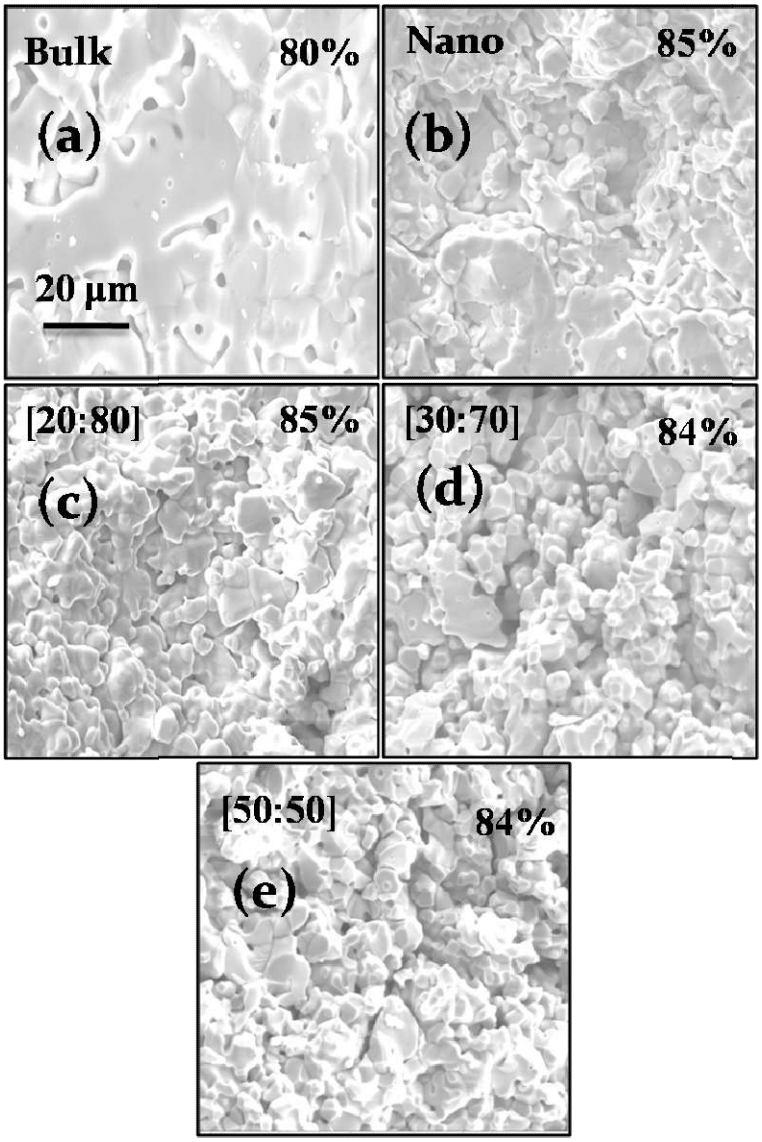

Figure 6.6*: SEM images of the $CoGa_{0.1}Fe_{1.9}O_4$ samples sintered from (a) bulk, (b) nanoparticles, and (c),(d), (e) mixed powders of different compositions. All images are in the same scale and magnification. The numbers in percentage indicate the sintered density.*

The microstructures of the sintered samples made from bulk, nanoparticles and the different percentages of the bulk and nanoparticles are shown in Figure 6.6. A distinguishable variation in the microstructures can be seen from the SEM images. The sample sintered from the bulk powder consists of larger sized grains with inter- and intragranular pores, whereas larger and relatively smaller sized grains, are observed in the sample sintered from the nanoparticles. In the case of the composite samples, nearly homogeneous distributions in the grain size with less porosity can be seen in the image of the sample sintered from 80%

nanosized and 20% bulk powders, and also number of smaller grains coexists in the form of clusters. However, with an increase in the bulk powder content in the composite, larger grainsare observed. Also, the sintered density for all the composite samples is almost comparable, and it is likely to be due to the associated porosity accompanied by relative changes in the number of smaller and larger sized grains. Although all the samples are sintered under identical conditions, such a large variation in the microstructures is most likely to be due to the difference in the kinetics of the grain growth for the bulk and nanosized powders [10-12]. The present results show that the microstructural components such as grain size, shape, and porosity of the sintered sample can effectively be controlled by making a suitable composite from the nanosized and bulk powders.

Since the composite of 80% nanosized powder and 20% bulk showed better magnetostriction characteristics, than for the individual component of the composites, and other composites, magnetic measurements were performed on the samples sintered from the bulk, nano and the composite (80% nano and 20% bulk). Initial magnetization curves of the sintered samples measured as a function of the magnetic field are shown in Figure 6.7. A marginal variation in the saturation magnetization is noticed for the samples, and the values are listed in Table 6.1.

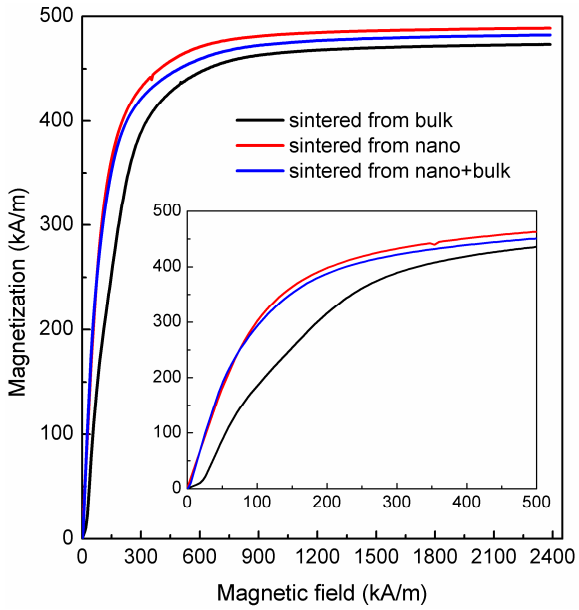

***Figure 6.7**: Initial magnetization curves of the samples sintered from the nanoparticles, bulk powder and mixture of powders [80% nano + 20% bulk]. The inset shows the enlarged view of the initial magnetization curves at low fields.*

The marginal variation of M_s is most probably due to the effect of cation distribution as well as the orientation of the grains. At lower magnetic fields (<400 kA/m), the relatively higher magnetization is observed, with almost equal magnitude, for the samples sintered from the nanoparticles and the composite powders compared to the sample sintered from the bulk powderas shown in the inset of Figure 6.7. Higher magnetization at lower magnetic fields indicates lower anisotropy of the samples, as discussed in the previous chapters.

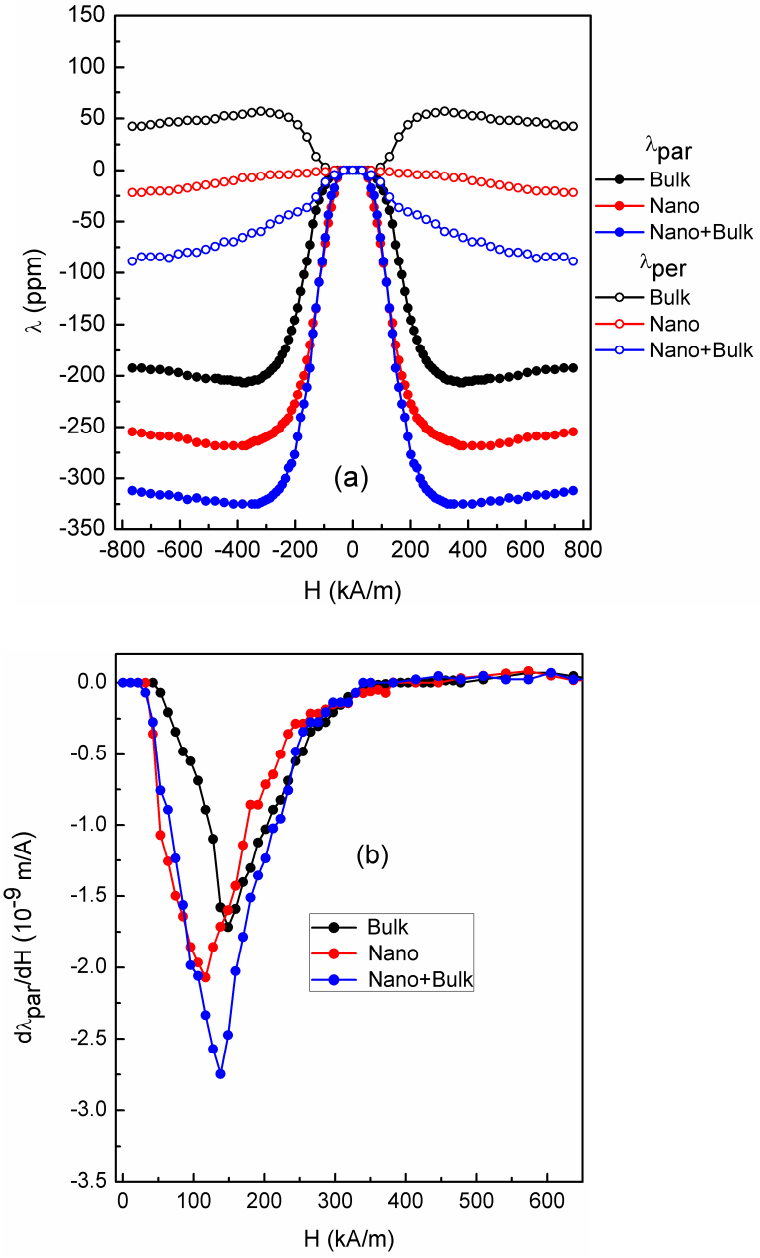

***Figure 6.8**: (a) Magnetostriction strain curves, measured along the parallel (closed circles) and perpendicular (open circles) directions to the applied magnetic field, and (b) strain sensitivity curves of the samples $CoGa_{0.1}Fe_{1.9}O_4$ sintered from bulk, nano, and mixed (80% nano + 20% bulk) powders.*

Magnetostriction strain and strain sensitivity curves of the $CoGa_{0.1}Fe_{1.9}O_4$ samples sintered from the bulk, nanoparticles and the self-composite of 80% nanosized powders and 20% bulk, measured along the parallel and perpendicular directions to the applied magnetic field are shown in Figure 6.8. Along the parallel direction, $[\lambda_{par}]_{max}$ is highest for the sample sintered from the mixed powders, with the value of -326 ppm at a field of 340 kA/m and the maximum value is nearly 57% and 22% higher than the values obtained for the samples sintered from bulk and nanosized powders, respectively. The values of $[\lambda_{par}]_{max}$ are compared in Table 6.1. The $[\lambda_{par}]_{max}$ value obtained for the self-composite in the present study is the highest magnetostriction value so far reported in the literature for any metal ions substituted sintered polycrystalline cobalt ferrite. Along the perpendicular direction, almost linear increase in the negative magnetostriction with increasing applied magnetic field is observed for the samples sintered from the nano and the composite powders, but the magnitude is highest for the composite sample. On the other hand, the sample sintered from the bulk powder shows positive magnetostriction curve having both positive and negative slopes at two different magnetic field regions. Although all three samples are sintered under identical conditions, such variation in the nature of the magnetostriction curves along the perpendicular direction for the samples sintered from different initial particle sizes is attributed to changes in the microstructural components such as grain size, grain orientation, porosity, etc.

The highest strain sensitivity is observed for the composite sample with the value of -2.74×10^{-9} m/A. The values of the magnetostriction parameters of all three compositions are listed in Table 6.1. The results indicate that it is possible to achieve very high magnetostriction parameters by sintering the green compacts prepared by mixing the nanosized and bulk powders of the same composition at a suitable proportion. Although the magnetic parameters are nearly comparable in all three samples,the main reason for the higher magnitude of magnetostriction for the sample sintered from the composite powder is themicrostructure. As explained earlier, the composite sample consists of more number of smaller grains in the form of clusterscompared to other two samples. The observed higher magnitude of the negative magnetostriction along the perpendicular direction for the composite also could be due to the contribution of the microstructure. The response of the magnetization process and the domain configuration to the applied magnetic field along two distinct directions will be different for the sample comprising of more number of smaller grains compared to the one with more number of larger sized grains.

***Table 6.1**: Magnetostriction and magnetic parameters of the samples sintered from nano sized powder, bulk and the self-composite (80% nano and 20% bulk).*

$CoGa_{0.1}Fe_{1.9}O_4$ Sintered from	**$[\lambda_{par}]_{max}$ (ppm)**	**H @ $[\lambda_{par}]_{max}$ (kA/m)**	**$[d\lambda/dH]_{max}$ (10^{-9} m/A)**	**H @ $[d\lambda/dH]_{max}$ (kA/m)**	**H_c (kA/m)**	**M_s (kA/m)**
Bulk	-207	382	-1.72	148	11.8	479
Nano	-268	371	-2.07	117	11.2	493
Nano(80%) + bulk(20%)	-326	328	-2.74	138	10.7	488

6.4.3 $CoM_{0.1}Fe_{1.9}O_4$ (M= In, Mn and Al)

The self-composite technique is extended for the other trivalent metal ion substituted cobalt ferrite samples. As discussed in Chapter 4, the compositions x=0.1 in $CoM_xFe_{2-x}O_4$ (M=Al, Ga and In) showed higher magnetostriction parameters at lower magnetic fields compared to the unsubstituted composition (x=0). For better comparison, all the samples are prepared and processed under identical conditions, similar to that of $CoGa_{0.1}Fe_{1.9}O_4$.

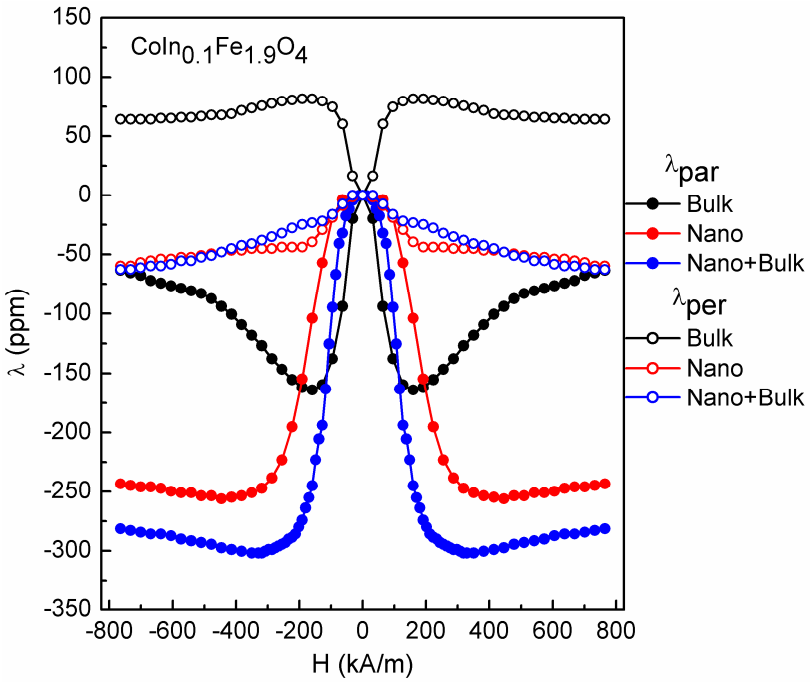

***Figure 6.9**: Magnetostriction strain curve of $CoIn_{0.1}Fe_{1.9}O_4$ samples sintered from bulk, nano and mixed (80% nano + 20% bulk) powders, measured along the parallel (closed symbols) and perpendicular (open) directions to the applied magnetic field.*

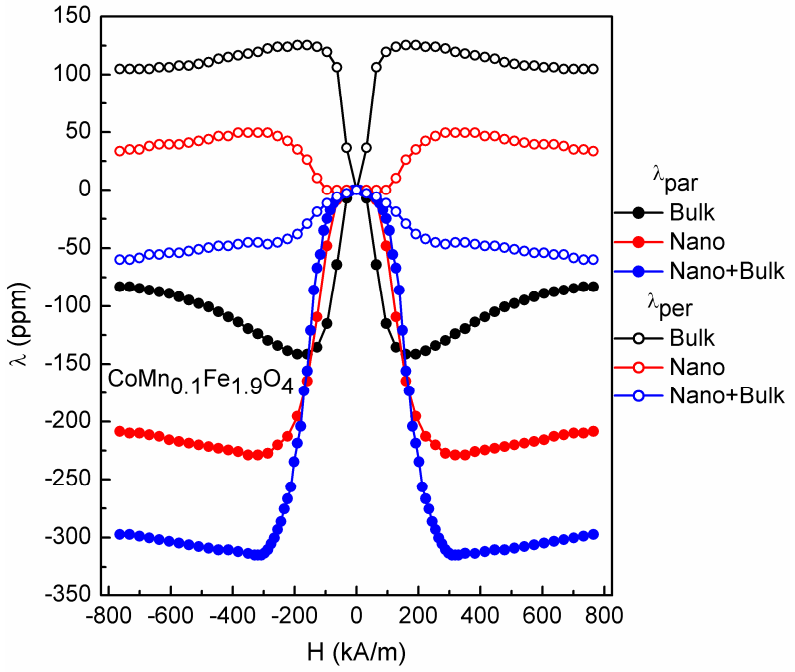

***Figure 6.10**: Magnetostriction strain curve of $CoMn_{0.1}Fe_{1.9}O_4$ samples sintered from bulk, nano and mixed (80% nano + 20% bulk) powders, measured along the parallel (closed symbols) and perpendicular (open) directions to the applied magnetic field.*

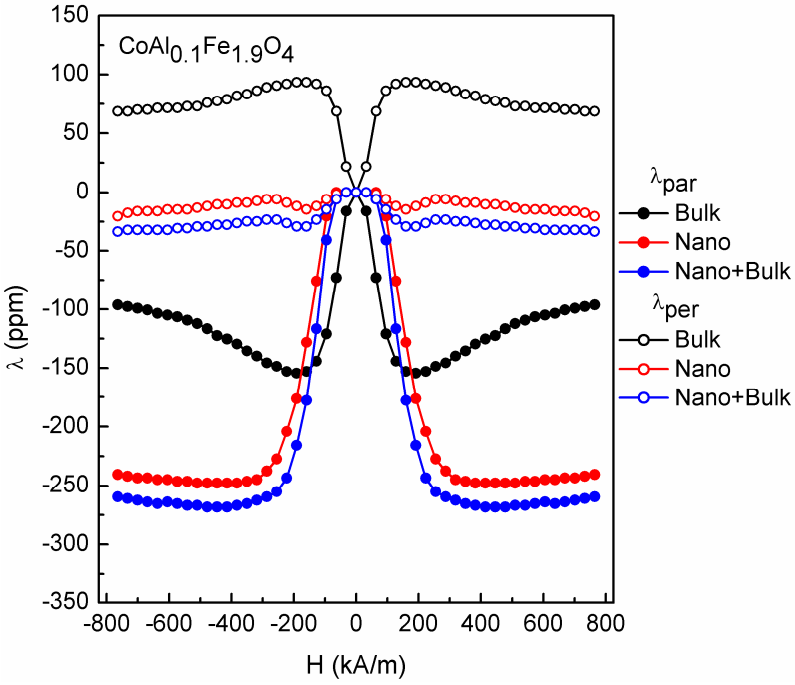

***Figure 6.11**: Magnetostriction strain curve of $CoAl_{0.1}Fe_{1.9}O_4$ samples sintered from bulk, nano and mixed (80% nano + 20% bulk) powders, measured along the parallel (closed symbols) and perpendicular (open symbols) directions to the applied magnetic field.*

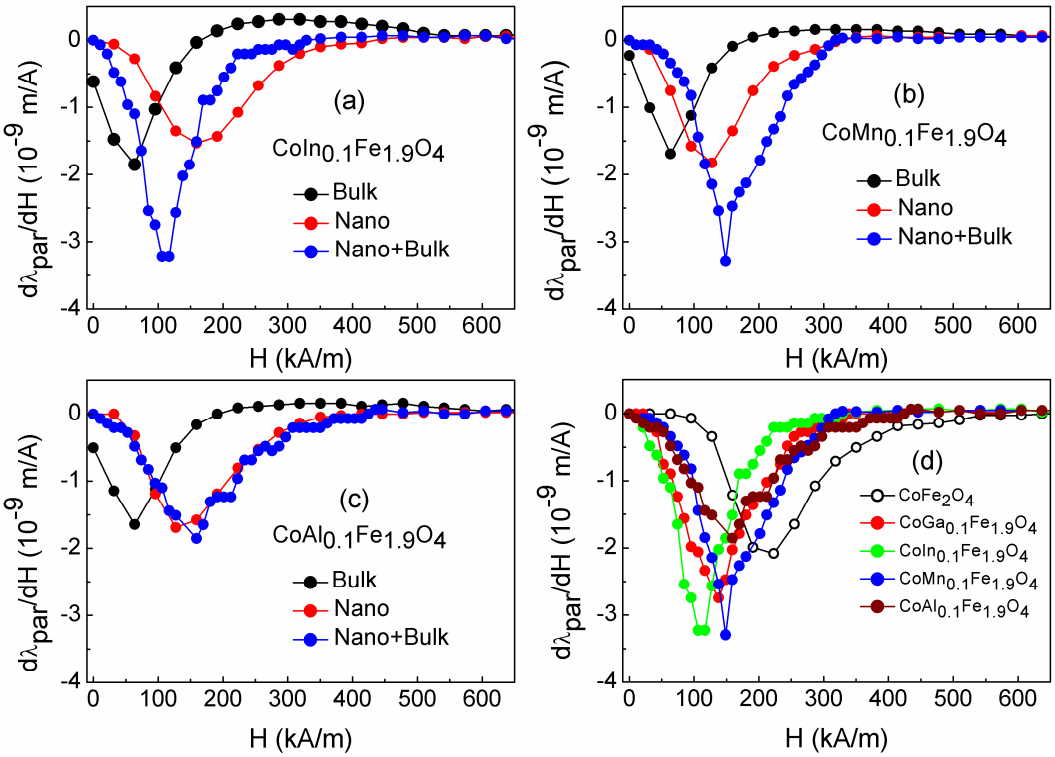

***Figure 6.12**: Comparison of the strain sensitivity curves of compacts sintered from bulk, nano and mixed (80% nano + 20% bulk) powders for (a) $CoIn_{0.1}Fe_{1.9}O_4$, (b) $CoMn_{0.1}Fe_{1.9}O_4$, (c) $CoAl_{0.1}Fe_{1.9}O_4$, and (d) shows the comparison of strain sensitivity curves of $CoM_{0.1}Fe_{1.9}O_4$ with that of $CoFe_2O_4$.*

Comparison of the magnetostriction strain curves of the $CoM_{0.1}Fe_{1.9}O_4$ (M=In, Ga and Al) compacts sintered from the bulk, nano and the mixed (80% nano + 20% bulk) powders are shown in Figures 6.9, 6.10, 6.11. Along the parallel direction, the samples sintered from the composite powders exhibit higher magnitudes of the magnetostriction compared to the samples sintered from the individual bulk and nanosized powders, for all the three different metal ion substituted compositions. The $CoIn_{0.1}Fe_{1.9}O_4$ and the $CoMn_{0.1}Fe_{1.9}O_4$ samples sintered from the composite powder show $[\lambda_{par}]_{max}$ above -300 ppm and the values are closer to that obtained for the $CoGa_{0.1}Fe_{1.9}O_4$ (-326 ppm) composite. For $CoAl_{0.1}Fe_{1.9}O_4$, the $[\lambda_{par}]_{max}$ (-268 ppm) is considerably lower than for the other compositions even though the sample was sintered from the similar combination of the bulk and nanosized powder as that of the other compositions. The results show that the Ga-, In- and Mn-substituted compositions sintered from the composite of nanosized and bulk powders are more suitable for sensors and actuators applications, due to their higher magnetostriction parameters at lower magnetic fields. Along the perpendicular direction, in all three cases, the

magnetostriction is negativefor the samples sintered from the nano and composite powders, except for the samples $CoMn_{0.1}Fe_{1.9}O_4$ sintered from the nanosized powder where the magnetostriction is positive. For the samples sintered from the bulk powder, the magnetostriction is positive with two different slopes at two different magnetic field regions, as expected. The values of the $[\lambda_{par}]_{max}$ and the field at which those values are obtained along the parallel direction for the different metal ions substituted samples sintered from composite powder are listed in Table 6.2.

The strain sensitivity curves of the compositions $CoIn_{0.1}Fe_{1.9}O_4$, $CoMn_{0.1}Fe_{1.9}O_4$,and $CoAl_{0.1}Fe_{1.9}O_4$ sintered from bulk, nano and the mixed powders are shown in Figure 6.12. Comparison of the strain sensitivity curves of the compacts sintered from the mixed powders of the metal ions substituted and unsubstituted cobalt ferrite is shown in Figure 6.12(d). $[d\lambda_{par}/dH]_{max}$ of the compositions $CoIn_{0.1}Fe_{1.9}O_4$, $CoMn_{0.1}Fe_{1.9}O_4$, sintered from mixed powder is higher than that the compacts of the individual components of the composite. However in the case of $CoAl_{0.1}Fe_{1.9}O_4$, $[d\lambda_{par}/dH]_{max}$ is almost comparable for the samples sintered from bulk, nano, and mixed powders. Similarly, $[d\lambda_{par}/dH]_{max}$ of the compositions $CoM_{0.1}Fe_{1.9}O_4$ (M=Ga, In, Mn) sintered from the mixed powders is higher than that of the unsubstituted composition even at lower magnetic fields. In the case of $CoAl_{0.1}Fe_{1.9}O_4$, $[d\lambda_{par}/dH]_{max}$ is slightly lower than that for the parent compound. The values of $[d\lambda_{par}/dH]_{max}$ and the field at which the maximum values obtained for the different compositions, including for parent compound sintered from the mixed powder are given in Table 6.2.

SEM images of the $CoM_{0.1}Fe_{1.9}O_4$ (M=Ga, In, Mn and Al) and $CoFe_2O_4$ composite samples sintered from 80% nano + 20% bulk powders are shown in Figure 6.13. Larger fused sized grains along with more number of smaller grains are observed in the case of cobalt ferrite sample whereas smaller grains in the form of clusters are observed for the Ga-, In- and Mn-substituted samples. In the case of the Al-substituted sample, more fused grains with irregular shape and orientation can be seen. Probably this difference in the microstructure of the Al-substituted self-composite is the reason for its lower magnetostriction. Sintered density is almost comparable for all the compositions and are shown on the respective images.

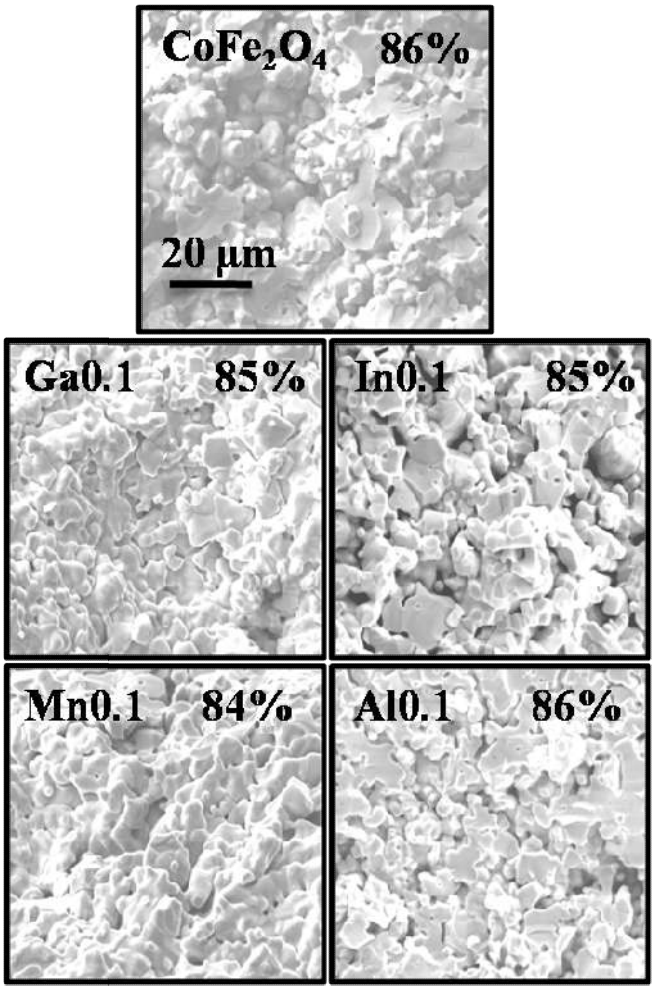

***Figure 6.13**: SEM images of the $CoM_xFe_{2-x}O_4$ (x=0, 0.1, M=Ga, In, Mn and Al) samples sintered from the mixed powders (80% nano + 20% bulk). The numbers in percentage indicate sintered densities. The scale shown is common for all images.*

The initial magnetization curves of the $CoM_xFe_{1.9}O_4$ (x=0, 0.1, M=Ga, In, Mn and Al) self-composite samples sintered from the powders of 80% nano and 20% bulk are shown in Figure 6.14. The magnetization is higher for the Ga, In, and Mn-substituted samples and lower for the Al-substituted sample compared to the unsubstituted counterpart. At lower magnetic fields (<400 kA/m), higher magnetization is obtained for the substituted compositions compared to the parent compound (inset of Figure 6.14), and this is due to the reduction in the anisotropy as well as A-O-B superexchange interactions, as described in the previous chapters. The values of the M_s and H_c of all the compositions are given in Table 6.2. Among the substituted samples, at lower magnetic fields (H<400 kA/m), Ga-, In- and Mn-substituted composite samples show higher magnetization than that for the Al-substituted sample (inset of Figure 6.14). Another interesting observation is that among the Ga-, In- and Mn-substituted composite samples, Ga-substituted sample has higher magnetization at lower

magnetic fields (<200 kA/m) and the same sample show higher magnitude of maximum magnetostriction coefficient (-326 ppm) compared to the other samples. The observations made from the magnetic and magnetostriction characterizations indicate that there is a correlation between the magnetic and magnetostrictive parameters, particularly at lower magnetic fields. For instance, λ_{max}, saturation magnetization and the magnetization at lower magnetic fields for the Al-substituted composite sample are much lower compared tothe other samples.

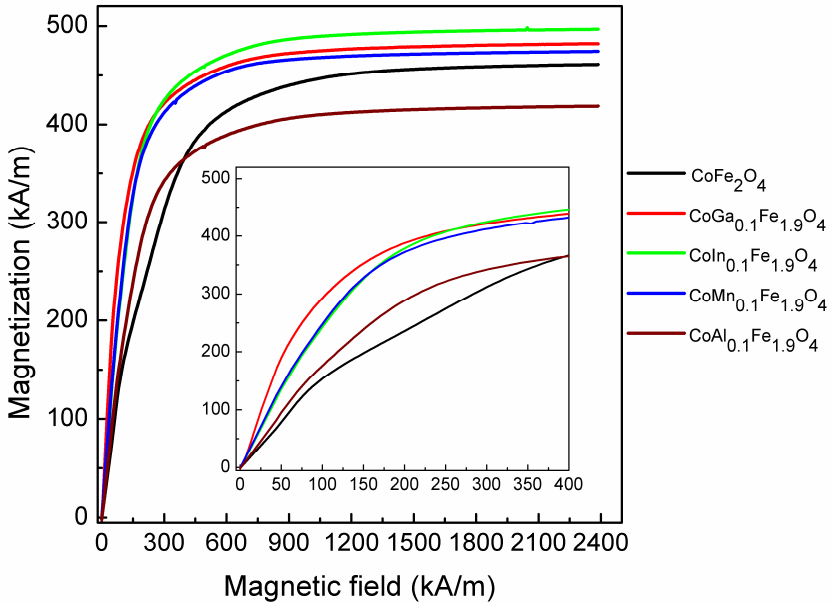

***Figure 6.14**: Initial magnetization curves of the $CoM_xFe_{2-x}O_4$ (x=0, 0.1, M=Ga, In, Mn and Al) $CoFe_2O_4$ samples sintered from the mixed powders of (80% nano + 20% bulk). The inset shows enlarged view at low magnetic field regions.*

***Table 6.2**: Magnetic and magnetostriction parameters of $CoMn_xFe_{2-x}O_4$ (x=0, 0.1, M=Ga, In, Mn, Al) sintered from the mixed powders of 80% nano and 20% bulk.*

Compositions	**$[\lambda_{par}]_{max}$ (ppm)**	**H @ $[\lambda_{par}]_{max}$ (kA/m)**	**$[d\lambda_{par}/dH]_{max}$ (10^{-9} m/A)**	**H @ $[d\lambda_{par}/dH]_{max}$ (kA/m)**	**M_s (kA/m)**	**H_c (kA/m)**
$CoFe_2O_4$	-338	605	-2.08	223	469	12.8
$CoGa_{0.1}Fe_{1.9}O_4$	-326	328	-2.74	138	488	10.7
$CoIn_{0.1}Fe_{1.9}O_4$	-302	320	-3.22	106	504	8.7
$CoMn_{0.1}Fe_{1.9}O_4$	-313	320	-3.29	148	477	9.6
$CoAl_{0.1}Fe_{1.9}O_4$	-268	446	-1.85	160	424	11.6

6.5 Magnetic field annealing

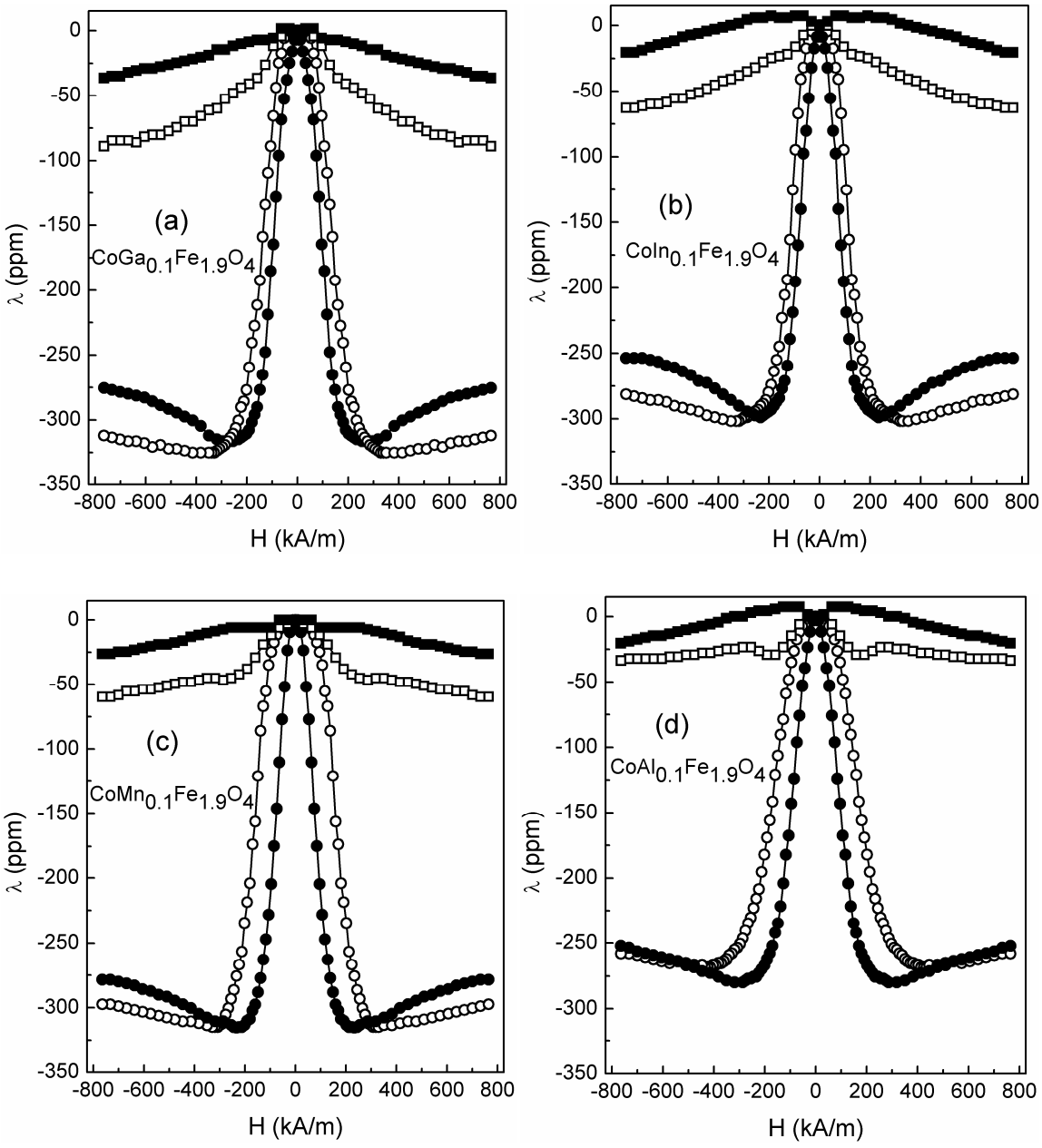

***Figure 6.15**: Magnetostriction strain curves of the sintered self-composites (80% nano + 20% bulk) of (a) $CoGa_{0.1}Fe_{1.9}O_4$, (b) $CoIn_{0.1}Fe_{1.9}O_4$, (c) $CoMn_{0.1}Fe_{1.9}O_4$ and (d) $CoAl_{0.1}Fe_{1.9}O_4$, before annealing (open symbols) and after annealing (closed symbols) in a magnetic field, measured along the parallel (circles) and perpendicular (squares) directions to the applied magnetic field.*

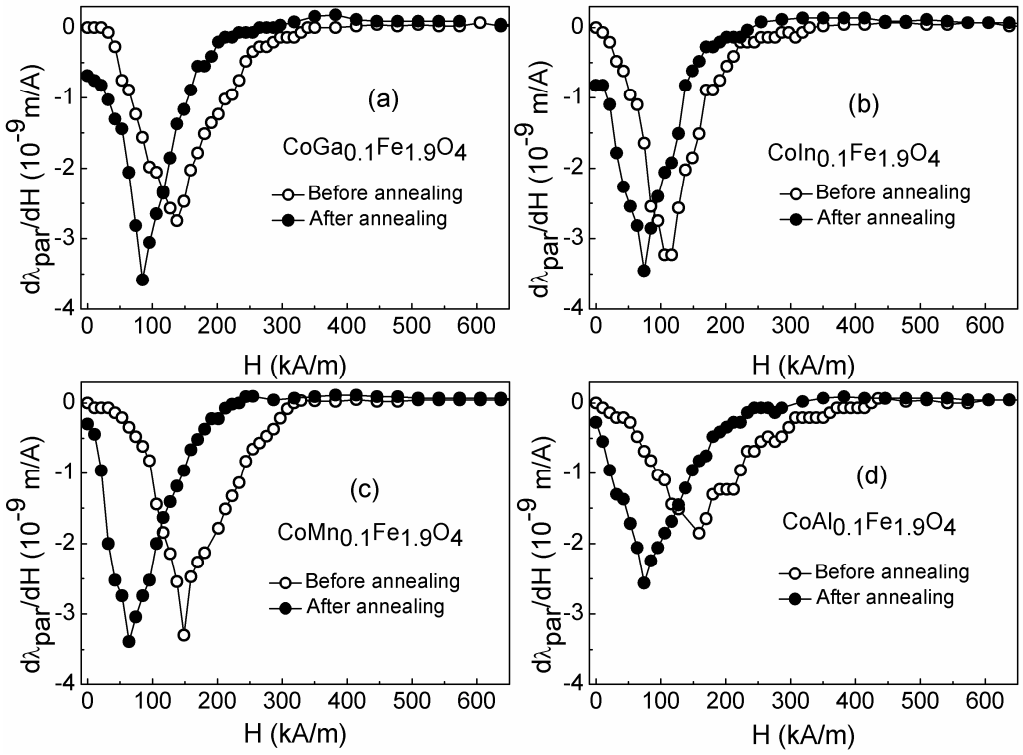

***Figure 6.16**: Comparison of the strain sensitivity curves obtained along the parallel direction for the sintered self-composites (80% nano + 20% bulk) of (a) $CoGa_{0.1}Fe_{1.9}O_4$, (b) $CoIn_{0.1}Fe_{1.9}O_4$, (c) $CoMn_{0.1}Fe_{1.9}O_4$, and (d) $CoAl_{0.1}Fe_{1.9}O_4$, before (open circles) and after (closed circles) annealing in a magnetic field.*

Comparison of the magnetostriction strain curves of the field annealed and unannealed composites of the different compositions, $CoM_{0.1}Fe_{1.9}O_4$ (M=Ga, In, Mn and Al), measured along both the directions, are shown in Figure 6.15. As seen from the Figure 6.15, even after annealing the samples in a magnetic field, no significant improvement in the magnitude of maximum magnetostriction strain is observed along the parallel direction for all the samples, except for shifting the maximum values to lower magnetic fields. The shift of $[\lambda_{par}]_{max}$ towards lower magnetic fields for the annealed samples is attributed to the induced uniaxial anisotropy along the field annealed direction and associated changes in the magnetization process and domain configurations, as reported [9,13]. The values of $[\lambda_{par}]_{max}$ and the field at which the values are obtained for the field-annealed,and unannealed samples are compared in Table 6.3. The comparable $[\lambda_{par}]_{max}$ for the field annealed and unannealed samples suggest that there is no additional contribution from induced anisotropy for the annealed samples. This is probably because the domains are already oriented in the unannealed samples because of the size, shape, and orientation of the grains in the sintered samples [8]. Smaller as well as larger grains are noticed in the microstructures of the sintered composites (Figure 6.13), and

it is possible that most of the domains are aligned away from the measuring direction so that reorientation of the magnetization of the domains from the direction of the annealing field is likely to be ineffective. However, along the perpendicular direction, a noticeable variation in the nature of the magnetostriction curves is observed. Before the field annealing, all the composites show negative magnetostriction and even after the field annealing, the sign of the curves remains the same, but the magnitude is reduced. This likely to be due to changes in the contribution of the different magnetostriction coefficients and also slight changes in the domain magnetization vectors triggered by the annealing field which changes the distribution of the magnetostriction along both the directions.

Comparison of the strain sensitivity curves of the compositions $CoM_{0.1}Fe_{1.9}O_4$ (M= Ga, In, Mn, Al) before and after annealing in a magnetic field is shown in Figure 6.16 as a function of applied magnetic field. After the field annealing, Ga and Al-substituted compositions show higher magnitude for the strain sensitivity at lower magnetic fields whereas the maximum strain sensitivity for the In- and Mn-substituted compositions is almost comparable to that of the unannealed samples, but the maximum is obtained at lower magnetic fields after annealing. The values of the maximum strain sensitivity and the field at which the maximum is obtained are tabulated in Table 6.3.

***Table 6.3**: Magnetostriction parameters for the self-composites (80% nano + 20% bulk) of the compositions $CoM_{0.1}F_{1.9}O_4$ (M=Ga, In, Mn, Al) before and after annealing the samples in a field.*

Compo -sitions	**Before Annealing**		**After Annealing**			
	$[\lambda_{par}]_{max}$ (ppm)	**$[d\lambda_{par}/dH]_{max}$ (10^{-9} m/A)**	**$[\lambda_{par}]_{max}$ (ppm)**	**H @ $[\lambda_{par}]_{max}$ (kA/m)**	**$[d\lambda_{par}/dH]_{max}$ (10^{-9} m/A)**	**H @ $[d\lambda/dH]_{max}$ (kA/m)**
Ga0.1	-326	**-2.74**	-316	240	**-3.58**	85
In0.1	-302	**-3.22**	-299	225	**-3.45**	74
Mn0.1	-313	**-3.29**	-316	223	**-3.38**	65
Al0.1	-268	**-1.85**	-280	280	**-2.56**	74

6.6 Conclusions

Sintered self-composites made by mixing and compacting nanosized and bulk powders of $CoM_{0.1}Fe_{1.9}O_4$ (M= Al, Ga, In and Mn) and the magnetostriction characteristics of the compacts are compared with the compacts sintered from the individual component powders. The composites made from the nanosized and bulk powders showed enhanced magnetostriction properties over the samples sintered from the individual components. Such a large enhancement in the magnetostriction parameters of the sample sintered from the self-composite powders of different sizes is attributed to the changes in the microstructure. Highest $[\lambda_{par}]_{max}$ and strain sensitivity of 302–326 ppm and 3.38–3.58 $\times$ 10^{-9} m/A, respectively, are obtained for the substituted compositions. The $[\lambda_{par}]_{max}$ value for $CoGa_{0.1}Fe_{1.9}O_4$ (326 ppm) sintered from the mixtures of 80% nanosized powder and 20% bulk powder is the highest magnetostriction value so far reported for any sintered polycrystalline metal ion substituted cobalt ferrite. Combining the high magnetostriction coefficient at low fields and the high strain sensitivity, these compositions are likely to be suitable for many applications.

Bibliography

[1] M. Atif, R. Sato Turtelli, R. Grossinger, and F. Kubel, *J. Appl. Phys*. **113**, 153902 (2013).

[2] K. K. Mohaideen and P. A. Joy, *Curr. Appl. Phys*. **13**, 1697 (2013).

[3] K. K. Mohaideen and P. A. Joy, *J. Eur. Ceram. Soc*. **34**, 677 (2014).

[4] S. D. Bhame and P. A. Joy, *J. Am. Ceram. Soc*., **91**, 1976 (2008).

[5] I. C. Nlebedim, N. Ranvah, P. I. Williams, Y. Melikhov, J. E. Snyder, A. J. Moses, and D. C. Jiles, *J. Magn. Magn. Mater*. **322**, 1929 (2010).

[6] I. C. Nlebedim, J. E. Snyder, A. J. Moses, D. C. Jiles, *J. Magn. Magn. Mater*. **322**, 3938 (2010).

[7] K. K. Mohaideen and P. A. Joy, *J. Magn. Magn. Mater*. **346**, 96 (2013).

[8] K. K. Mohaideen and P. A. Joy, *ACS Appl. Mater. Interfaces* **4**, 6421 (2012).

[9] K. K. Mohaideen and P. A. Joy, *Appl. Phys. Lett*. **101**, 072405 (2012).

[10] A. Rafferty, T. Prescott, D. Brabazon, *Ceram. Int*. **34**, 15 (2008).

[11] X. -H. Wang, X. -Y. Deng, Hai-Lin Bai, H. Zhou, Wei-Guo Qu, and L.-T. Li, *J. Am. Ceram. Soc*. **89**, 438 (2006).

[12] H. Naceur, A. Megriche, M. E. Maaoui, *J. Adv. Ceram*. **3**, 17 (2014).

[13] C. C. H. Lo, A. P. Ring, J. E. Snyder, D. C. Jiles, *IEEE Tran. Magn*. **41**, 3676 (2005).

Chapter 7

Conclusions

and

Future perspectives

7.1 Conclusions

There are reports in the literature on the magnetostriction studies of metal ion substituted sintered polycrystalline cobalt ferrite. However, individual studies are reported on materials prepared and processed under different conditions. Some of the results reported in the literature on metal ion substituted cobalt ferrite samples sintered from nanocrystalline powders showed enhancement in the strain sensitivity without any decrease or with higher values of magnetostriction strain at lower amounts of substitution whereas other studies on similar compositions reported decrease in the magnetostriction coefficient. There are no systematic studies reported on the role of valency, size, and site preference of the substituted metal ions in the cobalt ferrite lattice on the magnetostrictive properties. The objectives of the present work was to develop different metal ion (M) substituted cobalt ferrite compositions in $CoFe_{2-x}M_xO_4$, with high magnetostriction strain and strain sensitivity at low magnetic fields, based on the understanding of the role of some of the above mentioned factors by substituting nonmagnetic metal ions of different valencies and sizes for trivalent Fe in $CoFe_2O_4$.

Detailed studies are made to understand the effects of valency and size, amount of substitution, and site preferences of the substituted metal ions on the structural, magnetic and magnetostrictive properties of cobalt ferrite. For better comparison and correlation of the results, the compositions in the individual series described in the different chapters are synthesized and processed under identical conditions. The phase formation and purity of the synthesized nanosized powders as well as the sintered compositions are analyzed by powder X-Ray diffraction. The lattice parameters of all sintered compositions are obtained from the Rietveld refinement analysis of the XRD patterns. Detailed magnetic characterizations have been made on the sintered samples to obtain information of the magnetic parameters and also site preference of the substituted metal ions among the tetrahedral and octahedral sites of the spinel ferrites. Raman spectroscopy was exploited as a complementary tool to the magnetic characterization techniques to extract information on site preferences of the substituted metal ions in the lattice of cobalt ferrite. Magnetostriction measurements are made on the sintered compacts by applying the magnetic field parallel and perpendicular directions to the cylindrical axis of the pellet. In each chapter, the parameters (structural, magnetic and magnetostrictive) obtained are interpreted by correlating with each other. Conclusions are drawn from the studies on each series of compositions.

The effect of substitution of the divalent metal ions (Zn^{2+} and Mg^{2+}) in place of Fe^{3+} in $CoFe_2O_4$ ($CoM_xFe_{2-x}O_4$; M=Zn, Mg, $0 \leq x \leq 0.2$), has been studied, as discussed in ***chapter 3***, to understand the role of site preference of the substituted metal ions on the structural, magnetic and magnetostrictive properties. Zn^{2+} has a strong preference for the tetrahedral sites, and Mg^{2+} has the ability to occupy both the tetrahedral and octahedral sites, with larger amounts preferably at the octahedral sites. Both Zn^{2+} and Mg^{2+} have comparable ionic sizes (0.57 Å and 0.72 Å for Mg^{2+} and 0.60 Å and 0.74 Å for Zn^{2+} compared to 0.49 Å and 0.645 Å for Fe^{3+} for four-fold and six-fold coordination, respectively) both the crystallographic sites. Eventhough ionic radii of Zn^{2+} and Mg^{2+} are larger than that of Fe^{3+}, the lattice parameter was decreased non-linearly with increasing the substitution content, both cases. This is due to the conversion of high-spin Co^{2+} to low-spin Co^{3+} to maintain charge neutrality.

Saturation magnetization, M_s, is decreased with increasing Mg content whereas it is increased up to x=0.15 and decreased for x>0.15 in Zn-substituted samples, indicating that large amount of Mg has been substituted for Fe at the octahedral sites whereas Zn is substituted for Fe at the tetrahedral sites. For the same amount of substitution, lower Curie temperature (T_C) is obtained for the Zn-substituted compositions samples compared to the Mg-substituted samples, providing additional information that Zn is preferentially substituted at the A-sites. Irrespective of different site preferences of the substituents, the magnetocrystalline anisotropy (K_1) is decreased at a faster rate upto x=0.1, with almost equal magnitude, in both the cases, and found to be nearly constant for the compositions x>0.1. Raman spectral analysis also revealed the presence of Co^{3+} at the octahedral sites in the substituted compositions. Also, Raman studies indicated that Zn is substituted at the A-sites and replaced more amount of Fe from the A-sites to the B-sites whereas small fraction of Mg is substituted at the A-sites for $x \leq 0.1$. In both series, the concentration of Co^{2+} at the A-sites increases with the substitution content, but the increase is slightly higher for the Zn-substituted samples compared to that for the Mg-substituted samples. XPS analysis also revealed the presence of Co^{3+} in the substituted compositions.

Maximum magnetostriction, λ_{max}, for the compositions x=0.025 and 0.05 in the $CoMg_xFe_{2-x}O_4$ is found to be almost comparable with that of the unsubstituted composition (-221 ppm) and decreased for higher values of x. However in the case of $CoZn_xFe_{2-x}O_4$, λ_{max} decreased at a faster rate with increasing the substitution content. At lower magnetic fields (say 100 kA/m), λ_{max} increased up to x=0.1 and decreased for x>0.1. Similarly, the magnitude of the maximum strain sensitivity $[d\lambda/dH]_{max}$ increased up to x=0.1 but the increase is

marginally higher for the Zn-substituted samples compared to that for the Mg-substituted samples and decreased for x>0.1. Similar trend has been observed in the magnetization data obtained at lower magnetic fields for both the series. A fast decrease in the magnetostriction parameters for x>0.1 in both the cases is attributed to the presence of low-spin Co^{3+} at the octahedral site, and also migration of large fractions of Co^{2+} from the octahedral to the tetrahedral.

The effect of substitution of three trivalent nonmagnetic metal ions (Al^{3+}, Ga^{3+} and In^{3+}), having different sizes and site preferences, for Fe in $CoFe_2O_4$ ($CoM_xFe_{2-x}O_4$, M=Al, In, Ga) on the structural, magnetic and magnetostrictive properties has been investigated in ***chapter 4***. The ionic radii of Fe^{3+} at the tetrahedral and octahedral sites are larger than that of Al^{3+}, comparable to that of Ga^{3+} and smaller than that of In^{3+} (0.39 Å and 0.53 Å for Al^{3+}, 0.69 Å and 0.645 Å for Fe^{3+}, 0.47 Å and 0.62 Å for Ga^{3+} and 0.62 Å and 0.80 Å for In^{3+}, for four-fold and six-fold coordination, respectively). Accordingly, a large linear increase and decrease in the cubic lattice parameter has been observed for the In- and Al-substituted cobalt ferrites, respectively, whereas only a slight decrease in the same has been obtained for the Ga-substituted samples, indicating the size effect of the substituted metal ions on the structural parameter. Detailed magnetic and Raman spectral analysis provided strong evidence on the site preference of the substituted metal ions where Al is substituted at both tetrahedral and octahedral sites with large fractions at the octahedral sites whereas In and Ga are substituted at the tetrahedral sites upto x≤0.2 and at the octahedral sites for x>0.2. Eventhough structural and magnetic parameters are different for the same amount of substitution in all three series, the magnetostriction parameters (λ_{max} and $[d\lambda/dH]_{max}$) obtained for the compositions x=0.1 is almost comparable and are higher than that of the unsubstituted counterpart at lower magnetic fields. However for x>0.1, a decrease of λ_{max} is observed for all the three cases but the rate of decrease is found to be faster for the Al-substituted samples compared to the In- and Ga-substituted samples.

From a comparison of the magnetostriction parameters obtained for the divalent and trivalent nonmagnetic ion substituted cobalt ferrite, as shown in Figure 7.1, it is evident that trivalent nonmagnetic metal ions are suitable over the divalent ones for the substitution in cobalt ferrite to enhance the magnetostriction coefficient. However, comparable enhancement in the strain sensitivity is obtained for both the divalent and trivalent ion substituted compositions for x≤0.1. Even higher strain sensitivity, without considerable drop in the magnitude of λ_{max} is obtained for higher levels of substitution of the trivalent ions.

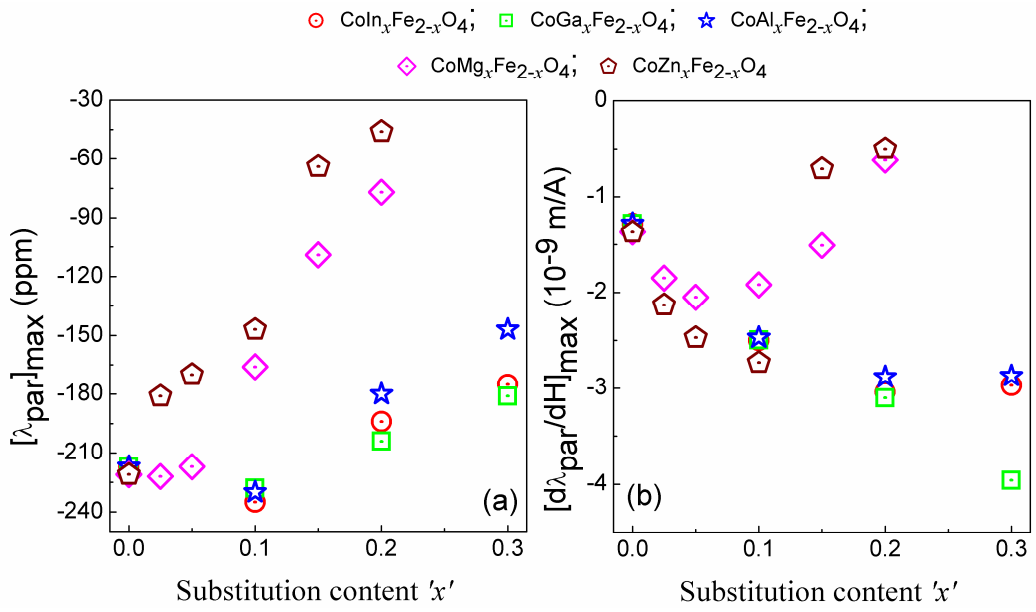

***Figure 7.1**: Comparison of the magnetostriction parameters of the sintered $CoM_xFe_{2-x}O_4$ (M=In, Ga, Al, Mg and Zn) compositions reported in chapters 3 and 4.*

In the case of divalent metal ion substituted compositions, a significant drop in the magnetostriction parameters are observed for x>0.1 and this is mainly due to the conversion of Co^{2+} into Co^{3+} to keep the systems electrically neutral.

Eventhough the site preferences of the trivalent metal ions are different, comparable magnetostriction parameters are obtained for the substituted compositions. On the other hand, effect of site preference is observed in the magnetostriction parameters of the divalent ion substituted compositions. To probe the effect of site preferences, co-substitution of different metal ions for Fe in $CoFe_2O_4$ such as $CoMg_{x/2}Zn_{x/2}Fe_{2-x}O_4$ (CMZF), $CoGa_{x/2}Mn_{x/2}Fe_{2-x}O_4$ (CGMF) and $CoGa_{x/2}Al_{x/2}Fe_{2-x}O_4$ (CGAF) on the structural, magnetic and magnetostrictive properties are studied and discussed in ***chapter 5***. The comparative studies revealed that the divalent ions co-substituted CMZF series of compositions show strong impact on the structural, magnetic and magnetostrictive properties over the other two series. Higher magnitude of magnetostriction is obtained at low magnetic fields (≤100 kA/m) for the compositions 0<x≤0.10 in CMZF compared to the similar compositions in CGMF and the CAGF. This higher magnetostriction at lower magnetic fields (100 kA/m) for x≤0.1 in the CMZF series is closely correlated with the magnetization obtained at a magnetic field 100 kA/m, as shown in Figure 7.2. The decrease in the magnetostriction at higher substitution levels is due to the presence of low-spin Co^{3+} at the octahedral sites and also migration of Co^{2+} from the octahedral sites to the tetrahedral sites. This interpretation is strongly supported

by the Raman data. There is a direct correlation between the variations of the relative area of $A_{1g}(2)$ band due to the CoO_4 vibrations and the value of $[\lambda_{par}]_{max}$ with the degree of substitution, as shown in Figures 7.2(c)&(d), for all three series. Thus, the results suggest that higher content of Co^{2+} at the octahedral sites of the spinel lattice is required to achieve higher values of $[\lambda_{par}]_{max}$. Among the threestudied different series, the CGMF series exhibits better magnetostriction parameters at higher levels of substitution, where the highest $[d\lambda_{par}/dH]_{max}$ of -3.82 × 10^{-9} m/A at a field of 37 kA/m, without significant drop in the value of $[\lambda_{par}]_{max}$, has been achieved for the CGMF series (x=0.3). An important observation is that, for all three series, the structural, Raman, magnetic and magnetostriction parameters show anomalies around the composition x=0.1, irrespective of the valency, size and site preference of the substituted ions. Thus, this is probably associated withlocal structural distortion associated with inhomogeneous distribution of the substituted metal ions in the lattice of cobalt ferrite, at this optimal composition.

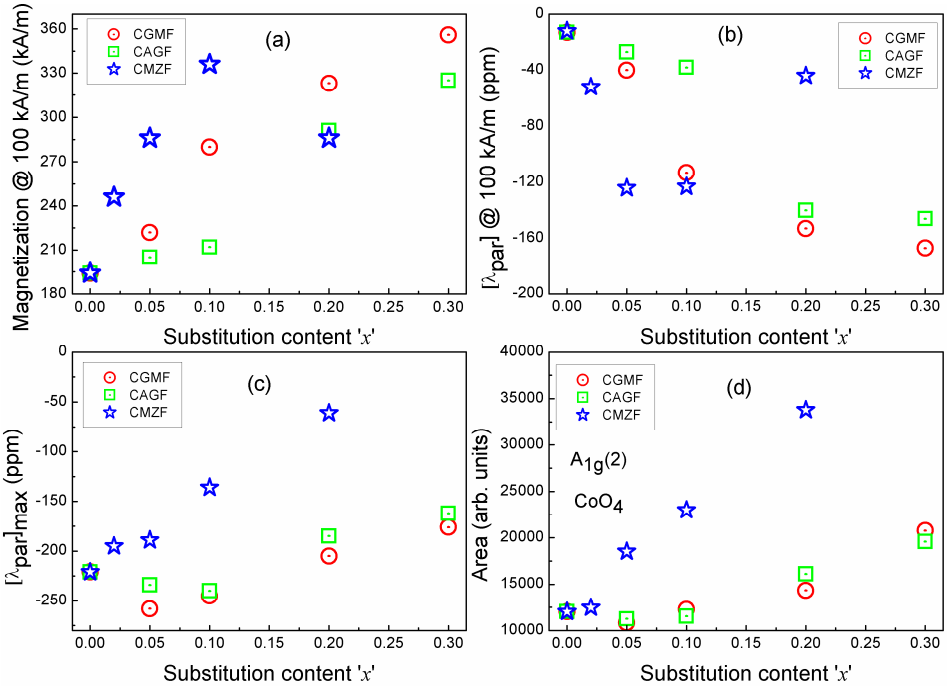

***Figure 7.2**: Variation of (a) magnetization at 100 kA/m, (b) magnetostriction at 100 kA/m, (c) maximum magnetostriction obtained along the parallel direction, and (d) area under the $A_{1g}(2)$ band, as a function of x in the CGMF, CAGF and CMZF series.*

After finding that the composition x=0.1 shows better magnetostriction parameters in the trivalent ion substituted compositions, the self-composite technique of mixing powders of the same composition with extreme particle sizes (bulk and nano) was investigated for improving the parameters by controlling the microstructure. The compositions

$CoAl_{0.1}Fe_{1.9}O_4$, $CoGa_{0.1}Fe_{1.9}O_4$, $CoMn_{0.1}Fe_{1.9}O_4$, and $CoIn_{0.1}Fe_{1.9}O_4$ are studied by mixing nanocrystalline (<5 nm) and bulk (>1 μm) powders of the same composition in the 80:20 weight ratio (based on the report in the literature as well as the finding from the weight percentage dependent studies on Ga-substituted compositions). The results are compared in Figure 7.3. Highest $[\lambda_{par}]_{max}$ of -326 ppm has been achieved for the sintered $CoGa_{0.1}Fe_{1.9}O_4$ compact and this value is comparable to that obtained for the unsubstituted cobalt ferrite prepared and processed under identical conditions, but at a much lower magnetic field and with higher strain sensitivity. More importantly, this is the highest magnetostriction value so far reported in the literature for any metal ion substituted sintered cobalt ferrite, without magnetic field annealing. The self-composites of $CoIn_{0.1}Fe_{1.9}O_4$ and $CoMn_{0.1}Fe_{1.9}O_4$ compositions showed the $[\lambda_{par}]_{max}$ above -300 ppm with the $[d\lambda_{par}/dH]_{max}$ above -3 × 10^{-9} m/A. However, in the case of $CoAl_{0.1}Fe_{1.9}O_4$ $[\lambda_{par}]_{max}$ of only -268 ppm could be achieved. The enhancement in the magnetostriction for the self-composites is well correlated with their microstructure.

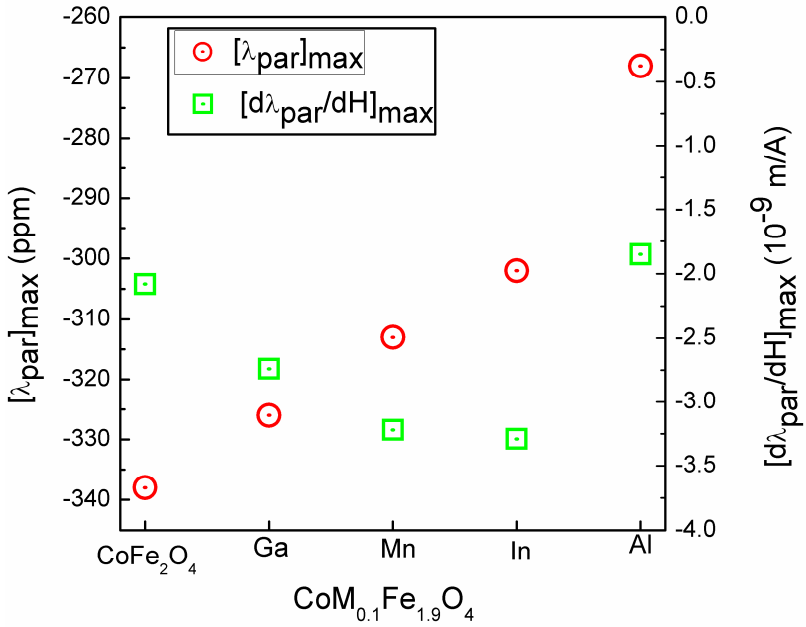

***Figure 7.3**: Comparison of the magnetostriction parameters of the sintered self-composites (80% nano + 20% bulk) of $CoFe_2O_4$ and $CoM_{0.1}Fe_{1.9}O_4$ (M= Ga, Mn, In and Al).*

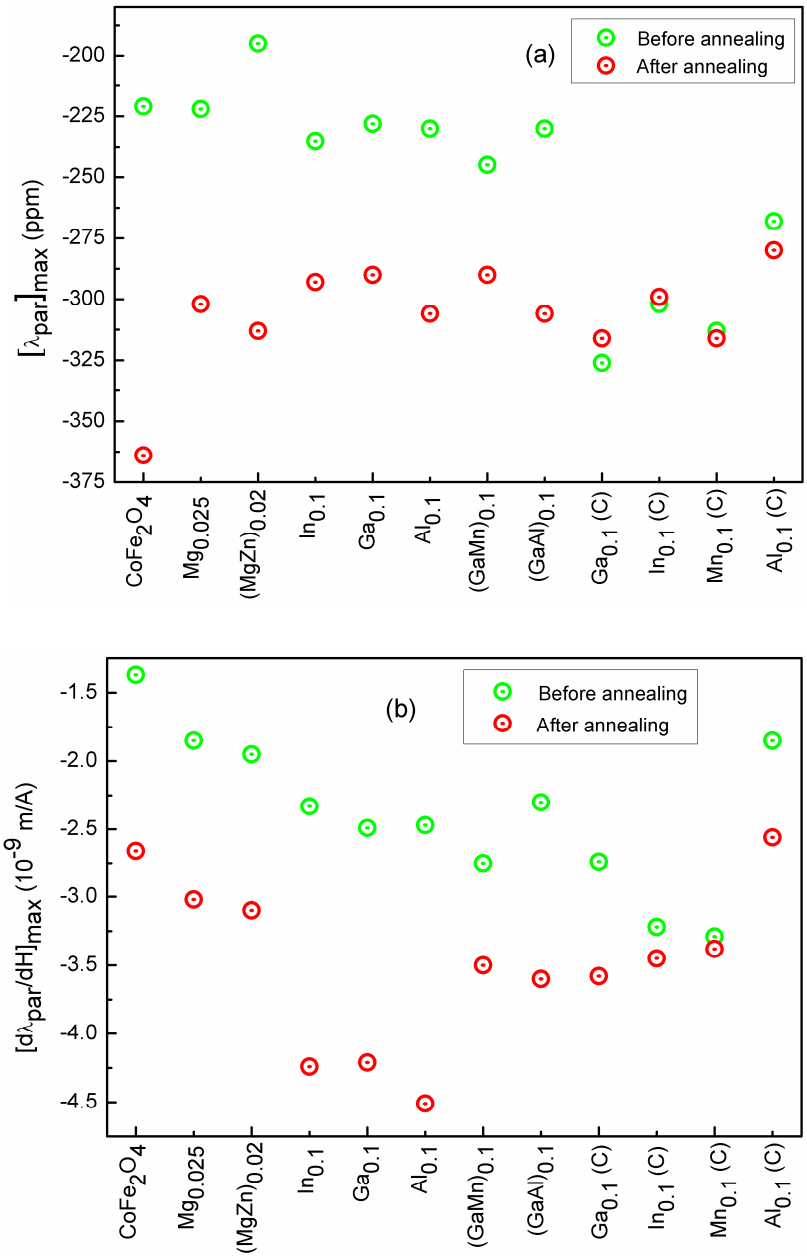

***Figure 7.4**: Comparison of the magnitude of (a) maximum magnetostriction strain obtained along the parallel direction, $[\lambda_{par}]_{max}$, and (b) maximum strain sensitivity, $[d\lambda_{par}/dH]_{max}$, for the compositions $CoM_xFe_{2-x}O_4$ (M_x=Mg, MgZn, In, Ga, Al, GaMn, GaAl) and the self-composites, before and after annealing in a magnetic field.*

Magnetic annealing studies (annealing the sintered compact in a magnetic field) suggested that the magnetostriction strain as well as the strain sensitivity can be improved considerably, by this process, for all the studied compositions. Comparison of $[\lambda_{par}]_{max}$ and $[d\lambda_{par}/dH]_{max}$ for different compositions, which showed the highest maximum magnetostriction in each series studied (x = 0.1 for the trivalent ion substituted and x= 0.05 for the divalent ion substituted compositions), before and after annealing in a magnetic field,

is shown in Figure 7.4. As can be seen in the figure, all the field-annealed samples show higher magnitude for the magnetostriction parameters compared to that of the corresponding unannealed samples. Highest $[\lambda_{par}]_{max}$ is obtained for the unsubstituted composition after field-annealing. In the case of Mg-substituted samples ($CoMg_{0.05}Fe_{1.95}O_4$), before the field annealing, the magnitudes of the $[\lambda_{par}]_{max}$ are almost comparable to that of parent compound with the value (~-220 ppm). However, after field-annealing, $[\lambda_{par}]_{max}$ is relatively lower, but with increased $[d\lambda_{par}/dH]_{max}$ compared to the parent compound. A similar feature is also observed in the case of MgZn co-substituted composition also. In the case of trivalent metal ions substituted and co-substituted cobalt ferrite compositions, before annealing, the magnitudes of $[\lambda_{par}]_{max}$ are almost comparable (~-230 ppm) and it is marginally higher than that of the parent compound. Even after the magnetic annealing, the values of $[\lambda_{par}]_{max}$ are almost comparable with the magnitude of ~-300 ppm, but lower than that of the parent compound (-364 ppm). Among all the substituted compositions, including the self-composites, highest strain sensitivity is obtained for the trivalent ions substituted compositions.

An important observation is that the magnetostriction strain of the self-composites does not vary much after the magnetic field annealing, unlike the case for the other samples where large enhancement in the strain is observed after field-annealing. Moreover, the magnetostriction strains of all the field-annealed substituted samples, except for the unsubstituted composition, are in the same range (~-300 ppm).

From the comparative studies, it is concluded that trivalent metal ions are more suitable over divalent metal ions as substituent, due to their isovalent nature with that of Fe. It is observed that the compositions around x=0.1 in $CoM_xFe_{2-x}O_4$, irrespective of the size, valence and site preferences of the substituted ions, show better magnetostriction parameters at lower magnetic fields compared to that obtained for the unsubstituted composition. The possible reason for the higher magnetostriction parameters associated with these compositions is the inhomogeneous distribution of the substituted metal ions in the unit cells of the spinel ferrite and also due to the contribution from the microstructural parameters. The inhomogeneous distribution of the substituted metal ions in the unit cells of the spinel ferrites most likely to induce local structural distortion due to changes in the bond lengths, bond angles and also number of nearest neighbours associated with each tetrahedral and octahedral site.

From the present study, it is concluded that the magnetostrictive property of sintered polycrystalline cobalt ferrite can be improved by suitable substitution for Fe by other metal ions in $CoFe_2O_4$. The valency, size, site preferences of the substituted ions in the spinel lattice of cobalt ferrite, and the amount of the substituted metal ions, apart from the microstructure, are factors deciding the magnetostriction characteristics. However, local structural distortion is very important at low levels of substitution. The self-composite technique of compacting mixed powders having particles of very small and large sizes greatly improve the magnetostriction parameters due to favourable microstructure of the sintered compacts.

7.2. Future perspectives

- The self-composite technique is very effective to achieve better magnetostriction parameters without any magnetic field annealing. The effect of compaction pressure and sintering conditions on the compacts made up of the self-composites are not investigated in the present study. It may be possible to improve the magnetostriction parameters further by optimizing these two factors.
- Sintered polycrystalline cobalt ferrite can be considered as a hard magnetostrictive material because of its higher λ_{max} and lower $[d\lambda/dH]_{max}$ obtained only at higher magnetic fields whereas metal ion substituted cobalt ferrites are soft magnetostrictive materials due to their higher $[d\lambda/dH]_{max}$ and moderate λ_{max} at low magnetic fields. Therefore, by making a suitable composite of the unsubstituted and substituted compositions, along with controlling the microstructure of the sintered compacts, it might be possible to achieve higher magnetostriction parameters at lower magnetic fields.
- Eventhough higher magnetostriction parameters are achieved at lower magnetic fields after annealing the samples in a magnetic field, the annealed samples are not suitable for use at elevated temperatures because the induced anisotropy will be lost at high temperatures. If the samples are compacted in the presence of a magnetic field and then sintered, it may lead to preferred orientation of the grains in the sintered samples which in turns may yield higher magnetostriction parameters at lower magnetic fields. Such materials can be used even at elevated temperatures for practical applications.

- For many technological devices, based on magnetostriction, thin films are required. Studies on the magnetostrictive properties of thin films of the optimised compositions of substituted cobalt ferrite are required to assess their applications.
- In magnetoelectric multiferroic composites, magnetostrictive material is one of the active components along with a piezoelectric component to obtain higher magnitude of magnetoelectric coefficient. A magnetostrictive material with higher strain and strain sensitivity at low magnetic fields is always essential to make a better magnetoelectric composite material. The materials reported in the present work are suitable candidates for multiferroic composites.

List of Publications:

[1] Magnetic and magnetostrictive properties of aluminium substituted cobalt ferrite synthesized by citrate-gel method

P. N. Anantharamaiah and P. A. Joy, *J. Mater. Sci*., 50, 6510 (2015).

[2] Enhancing the strain sensitivity of $CoFe_2O_4$ at low magnetic fields without affecting the magnetostriction coefficient by substitution of small amounts of Mg for Fe

P. N. Anantharamaiah and P. A. Joy, *Phys. Chem. Chem. Phys.,* 18, 10516 (2016).

[3] High magnetostriction parameters of sintered and magnetic field annealed Ga-substituted $CoFe_2O_4$

P. N. Anantharamaiah and P. A. Joy, *Mater. Lett.*, 192, 169 (2017).

[4] Tuning of the magnetostrictive properties of cobalt ferrite by forced distribution of substituted divalent metal ions at different crystallographic sites

P. N. Anantharamaiah and P. A. Joy, *J. Appl. Phys.*, 121, 093904 (2017).

[5] Effect of size and site preference of trivalent metal ions (Al^{3+}, Ga^{3+} and In^{3+}) substitution for Fe^{3+} on the magnetostrictive properties of sintered $CoFe_2O_4$

P. N. Anantharamaiah and P. A. Joy, *J. Phys. D: Appl. Phys. (Accepted, in press)*

[6] Role of valency and site preference of the metal ions substitution for Fe^{3+} on the magnetostrictive properties of sintered cobalt ferrite

P. N. Anantharamaiah and P. A. Joy, *(Manuscript under preparation)*

[7] Large enhancement in the magnetostriction of sintered metal substituted cobalt ferrite by making self-composites from nanocrystalline and bulk powders,

P. N. Anantharamaiah and P. A. Joy, (*Manuscript under preparation)*

Conference attended:

- International Conference on Magnetic Materials and Applications (MagMA-2013)", held at **IIT Guwahati** during December 5 - 7, 2013, and **presented the research work in the form of poster**.
- International Conference on Magnetic Materials and Applications (MagMA-2014)", held at **Pondicherry University** during September 15-17, 2014, and **received the best poster award for the research work presentation in the form of poster**.
- International Conference on Magnetic Materials and Applications (MagMA-2015)", held at **VIT Vellore** during December 2 - 4, 2015, and **delivered the oral talk**.

Workshop attended:

Participated in "**XV School on Neutrons as probes of condensed matter**" organized by UGC-DAE consortium for scientific research, Mumbai centre & solid state physics division, BARC, held at BARC, Mumbai during January 8-12, 2013.